Nature of Electrostatic Interactions in Macromolecular Systems

Thesis by
Pierre J. Walker

In Partial Fulfillment of the Requirements for the
Degree of
Doctor of Phylosophy in Chemical Engineering



CALIFORNIA INSTITUTE OF TECHNOLOGY
Pasadena, California

2027
Defended August 19 2026

© 2027

Pierre J. Walker
ORCID: 0000-0001-8628-6561

All rights reserved

Cette thèse est dédiée à Maman et Zackou.

ACKNOWLEDGEMENTS

This thesis and all the works came about over the duration of this PhD are a reflection of the many interactions I've had over the past five years with individuals within and without Caltech. To all those acknowledged here, I am eternally grateful for your support.

First and foremost, I would like to thank Prof. Zhen-Gang Wang, an ever present figure throughout my academic journey at Caltech. I chose Caltech for Zhen-Gang and, although the reasons have changed, I couldn't have picked a better advisor. Thank you for giving me the freedom to explore a broad range of topics, while also pushing for reflection into the motivations and physical questions driving the work. I am grateful for all the support you've given for my academic career. While I came into the group with an engineering mindset, I leave with a deeper appreciation for the fundamentals of polymer physics[1].

I consider myself fortunate to have joined the Wang group when it was at its largest, having had the opportunity to interact with so many talented researchers. I wish to thank Dr. Sriteja Mantha, Prof. Alejandro Gallegos and Prof. Yasemin Basdogan for their mentorship across all my projects, most of which wouldn't have succeeded without their help. I would also like to thank Prof. Shensheng Chen, Dr. Samuel Varner, Dr. Alexandros Tsamopoulos, Dr. Benjamin Ye, Dr. Andy Ylitalo, Dr. Tianyi Jin, Vignesh Bhethanabotla and Zhuolin He for the pleasure of collaborating with them on various projects. More broadly, thank you to the entire group, including Dr. Alec Glisman, Dr. Chris Balzer, Dr. Dorian Bruch, Dr. Felipe Silva Carvalho, Christopher Stewart and Jihoon Oh for creating such an enjoyable atmosphere within group, especially during our memorable group get-togethers.

I would also like to thank my thesis committee, Prof. Karthish Manthiram, Prof. Kara D. Fong and Prof. Julia R. Greer, for their guidance and support over the past few years. In particular, special thanks to Prof. Greer for her trust in my abilities to collaborate with her group. The experience of working with her many wonderful group members has been invaluable in developing my own approach to research and collaborations. I would like to thank Dr. Seola Lee, Dr. Miralem Salihovic, Seneca Velling and Cyrus Fiori for the many enriching collaborations we've had over the last few years.

[1] By my measure, I have achieved ~ 20% expertise in polymer physics.

Outside of Caltech, I've had the privilege to collaborate with a number of amazing academics. I would like to thank Prof. Richard Braatz and Prof. Allan Myerson for the opportunity to contribute to their work on lipid nanoparticles and for placing their trust in a PhD student on the other side of the continent. Thank you to Prof. Bilin Zhuang for entrusting Sam and me with her very talented undergraduate student and embarking on a project whose scope we all greatly underestimated. I am also grateful for the many insightful discussions with Dr. Simon Mueller, Prof. Christian Holm, Prof. Xiaodong Liang and Prof. Georgios Kontogeorgis over the last few years. It has been a pleasure collaborating with all of you.

Special thanks to Prof. Brad Olsen for inviting and enduring Zhen-Gang's and my contributions to their review article. I look forward to working more closely with them during my post-doctoral career.

I would also like to give a very special thanks to my undergraduate mentors at Imperial, Dr. Andrew Haslam and Prof. George Jackson, and at MIT, Dr. Yunsie Chung and Prof. Bill Green. To Andrew and George, my jump into academic research started from conversations with you both during office hours and your guidance laid the foundation for my approach to research for the years to come. I am grateful for your continued support of my academic endeavors.

In my time at Caltech, I've also had the privilege to mentor a number of undergraduate students. I thank Ananya Venkatachalam, Kelsey Fu, Matthew Cox, Michael Gadaloff and Luc Paoli for hanging in there over the course of their research experience and for their commitment to the projects we worked on together. It brings me great pride to see where you have all ended up.

Outside of my PhD work, an endeavor that I am particularly proud of is the Clapeyron.jl package, which has grown into its own self-sustaining ecosystem, enabling much of the research I've done and inviting new collaborations. This project would not have been possible without the contributions of Paul (Hon-Wa) Yew and Andrès Riedemann, for which I am grateful.

Two additional collaborators which do not fall into any of the above groups I would like to highlight are Dr. David Beyer and Dr. Pavan Inguva. Without David, two of the chapters in this thesis would not exist. I am grateful for all the stimulating discussions we've had and continue to have, which really help push my interest in the fundamentals of polymer physics over the last year. As for Pavan, he remains my longest standing collaborator dating back all the way to my time as an undergraduate.

Many of the problems we've worked on together have pushed me to rethink my approaches to research and help to keep me focused on real world issues. I look forward to our collaborations in the future, for both David and Pavan.

As someone who's never managed to live in the same place for very long, the friendships which have lasted until now are incredibly important to me, although I may not be the best at staying in touch. Dating back all the way to my time in Thailand, Johnny, Declan and Khao-Tu remain some of my closest friends and, in the moments we've managed to get together either online or in-person, have helped keep myself grounded and remember the things that matter to me outside academics. To the friends I've made at Imperial and who I suffered through COVID-19 with, Nick, Animesh, Andreas, Tianpu, Marie, Chen-Horng and Karyshma, thank you so much for the memories both during and since Imperial. And finally, to the friends I've made during my time in Los Angeles, Brian, Alex, Elena, Ailene, Ryan, James, Cyrus, Soyoung, Siya, Ester and Sonia. It's been a long time since I've lived continuously in one place for an extended period of time, and it's been an unforgettable journey to see us all grow into (slightly more) mature adults. Our Catan nights, climbing gym evenings, trips all over the world and sometimes just enjoying good food together, the time at Caltech would not have been the same. I thank you all for the memories and look forward to where the future takes us.

I would like to thank both the Walker and Jaroniak sides of my family. The last few years have not been the easiest for us, and despite being ten thousand miles away, their support from across the sea to pursue an academic career means far more to me than I can ever express in person.

I am also grateful to my partner's family, Max, Grace, Serena and Michelle, for not only entrusting me with their daughter, but also their support as we navigate the difficulties of having families and careers which span the entire globe. I look forward to spending more time together as our journey eventually brings us to Singapore.

Close to my heart is my sister, Victoria, and my Dad. We've been an international family for many years now and, in spite of the distance and through our hardships, our unconditional love for one another remains. To Vicky, thank you for your bluntness with me and never failing to remind me how silly this whole research thing is. And to my Dad, thank you for your unwavering support throughout my entire life. I can only hope to one day have the same strength against the challenges of the world that you have.

Finally, one of the most important people in my life ended up being the first person I ever met in Los Angeles, my partner Marion. You are my player two in both games and life. Loving, caring and supporting you is one of the easiest things I've had to do. We've developed a beautiful and comfortable life together, with our wonderful pets Sencha and E.G, which make life just a little bit easier by just existing. Through both good times and bad, I can rest easy knowing we'll be there to support one another. While I don't know what the future will hold, I know that together we'll be fine.

ABSTRACT

Electrostatic interactions govern the organization and motion of charged matter across molecular and macroscopic length scales. In macromolecular systems, their long-ranged and collective nature couples molecular conformation, mobile-ion organization, solvent response, chemical equilibrium, and material dynamics. Consequently, the behavior of charged materials cannot generally be inferred from charge magnitude, pair interactions, or static molecular structure alone. This thesis combines physically grounded theory with molecular simulations to isolate these couplings and establish transferable relationships between microscopic electrostatic interactions and macroscopic material behavior.

The first part maps the thermodynamic landscape of charge-containing systems. For polymer–ionic liquid mixtures, we show that electrostatic correlations produce phase-envelope asymmetries and molecular-weight scaling laws that differ from classical Flory–Huggins predictions, enabling the development of a minimal model with physically interpretable parameters. We then challenge the treatment of solvents as passive dielectric continua. An explicit-solvent liquid-state theory and molecular simulations demonstrate that dipolar polarization is an active thermodynamic degree of freedom: ion–dipole correlations alter dielectric screening, reverse the temperature dependence of effective electrostatic interactions, and generate both upper-critical-solution-temperature behavior and inverted salt partitioning in polyelectrolyte coacervates. The effects of molecular architecture are subsequently examined through charge sequence and polymer topology. For polyampholytic intrinsically disordered proteins, charge blockiness promotes salt-free coacervation, whereas net charge suppresses it through electrostatic repulsion and counterion entropy. Added salt can nevertheless screen these repulsions and induce phase separation over a broad region of sequence space. For branched polyelectrolytes, compact topologies display an enhanced propensity for coacervation, while differences in topology alone can drive multiphase separation.

The second part examines the dynamic pathways by which charge, matter, and stress move and relax within these thermodynamic states. In ionic-liquid–solvent mixtures, all-atom simulations and analytical theory reveal that ion dissociation is controlled by chemically specific short-range interactions rather than bulk dielectric constant alone. Moreover, ion-pair populations do not uniquely determine conductivity, which depends on collective relaxation, electrophoretic, viscous, and

ion-asymmetry effects. In charge-regulating polyelectrolyte hydrogels, dynamic protonation can enhance multivalent-ion diffusion by an order of magnitude through a protonation-assisted hopping mechanism, thereby decoupling ionic mobility from equilibrium binding. Finally, a multiscale framework combining quantum chemistry, thermodynamic theory, and coarse-grained simulation connects metal–ligand coordination to the phase behavior and mechanics of metallo-polyelectrolyte complexes. Their mechanical response is governed not by binding strength alone, but by competition among interchain bridges, intrachain loops, crosslink persistence, and network relaxation.

Together, these results establish that the properties of charged materials emerge from the collective organization and motion of ions, solvents, and macromolecular architectures, providing practical design principles for ionic liquids, biomolecular condensates, responsive hydrogels, and other charge-containing soft materials.

PUBLISHED CONTENT AND CONTRIBUTIONS

Published papers forming chapters of this thesis

David Beyer, Pierre J. Walker, Lena Tarrach, Zhen-Gang Wang, and Christian Holm. *How Topology Shapes the Phase Behavior of Polyelectrolytes*. arXiv:2607.15703 [cond-mat.soft]. July 2026. DOI: 10.48550/arXiv.2607.15703

> **Co-first and co-corresponding author.** P.J.W. and D.B.B. conceived and derived the theory behind this work and co-wrote the manuscript. P.J.W. implemented the code used to generate the figures within the manuscript.

Pierre J. Walker, David Beyer, Christian Holm, and Zhen-Gang Wang. *Ion Transport Enhancement in Charge-Regulating Hydrogels*. 2026. DOI: 10.26434/chemrxiv.15004897/v2

> **Co-first and co-corresponding author.** P.J.W. and D.B.B. conceived this project and co-wrote the manuscript. P.J.W. implemented the simulation protocol and performed analysis of the resulting simulations.

Pierre J. Walker and Zhen-Gang Wang. "Anomalous Phase Behavior of Polymer–Ionic Liquid Mixtures". In: *J. Phys. Chem. B* 129 (Nov. 2025). ISSN: 1520-6106. DOI: 10.1021/acs.jpcb.5c04858

> **First and co-corresponding author.** P.J.W. and Z-G.W. conceived the project and co-wrote the manuscript. P.J.W. derived and implemented the theory to generate the results in the manuscript.

Seola Lee, Pierre J. Walker, Seneca J. Velling, Amylynn Chen, Zane W. Taylor, Cyrus J. B. M. Fiori, Vatsa Gandhi, Zhen-Gang Wang, and Julia R. Greer. "Molecular control via dynamic bonding enables material responsiveness in additively manufactured metallo-polyelectrolytes". In: *Nat. Commun.* 15.1 (Aug. 2024), p. 6850. ISSN: 2041-1723. DOI: 10.1038/s41467-024-50860-6

Co-first author. S.L. and P.J.W. conceived the project and co-wrote the manuscript with S.J.V. and C.J.B.M.F. P.J.W. performed all theoretical and computational calculations, generating all results related to these calculations included in the manuscript.

Manuscripts in preparation forming chapters of this thesis

Zongpei Wu, Júlia Bonesso-Sabadini, Pierre J. Walker, Watson Loh, Zhen-Gang Wang, Sarah L. Perry, and Shensheng Chen. "Origin of the Anomalous Guest Polymer Selectivity in Complex Coacervates". In: *Submitted* (2026)

First and co-corresponding author. Z.W., J.B-S. and P.J.W. co-wrote the manuscript. P.J.W. derived the theory and implemented the code used to generate the figures within the manuscript.

Pierre J. Walker and Zhen-Gang Wang. "Explicit Solvents Reverse Electrostatic Phase Behavior in Charged Fluids". In: *In preparation* (2026)

First and co-corresponding author. P.J.W. conceived and derived the theory behind this work and co-wrote the manuscript.

Pierre J. Walker, Tianyi Jin, Alejandro Gallegos, and Zhen-Gang Wang. "Dielectric Inhomogeneity Governs Phase Behavior and Salt Partitioning in Complex Coacervates". In: *In preparation* (2026)

Co-first author. P.J.W. and T.J. conceived this project and co-wrote the manuscript. P.J.W. implemented the code and generated the results in the manuscript.

Tianyi Jin, Pierre J. Walker, Kelsey Fu, Shensheng Chen, and Zhen-Gang Wang. "Self- and salt-induced coacervation of polyampholytic intrinsically disordered proteins". In: *In preparation* (2026)

Co-first author. P.J.W. and K.F. conceived this project and co-wrote the manuscript with T.J. P.J.W. implemented the code and generated the results in the manuscript.

Pierre Walker and Zhen-Gang Wang. "Decoupling Ion Association from Conductivity in Ionic-Liquid–Solvent Mixtures". In: *In preparation* (2026)

> **First and co-corresponding author.** P.J.W. conceived the project and co-wrote the manuscript. P.J.W. performed all theoretical and computational calculations, generating all results related to these calculations included in the manuscript.

Published papers not forming chapters

Samuel Varner, Pierre J. Walker, Ananya Venkatachalam, Bilin Zhuang, and Zhen-Gang Wang. "Stockmayer fluid with a shifted dipole. II. Interfacial behavior". en. In: *J. Chem. Phys.* 164.18 (May 2026). ISSN: 0021-9606. DOI: 10.1063/5.0331066

Pierre J. Walker, Ananya Venkatachalam, Samuel Varner, Bilin Zhuang, and Zhen-Gang Wang. "Stockmayer fluid with a shifted dipole. I. Bulk behavior". In: *J. Chem. Phys.* 164.18 (May 2026), p. 184512. ISSN: 0021-9606. DOI: 10.1063/5.0331053

Vico Tenberg, Pierre J. Walker, Pavan K. Inguva, Maria del Carme Pons Royo, Andrew L. Acevedo, Vernon S. Lin, Marion Pang, Zhen-Gang Wang, Allan S. Myerson, and Richard D. Braatz. *Thermodynamic Modeling of mRNA with the Addition of Precipitants*. Oct. 2025. DOI: 10.1101/2025.10.18.683252

Pavan K. Inguva, Saikat Mukherjee, Pierre J. Walker, Vico Tenberg, Cedric Devos, Sunkyu Shin, Yanchen Wu, Srimanta Santra, Jie Wang, Shalini Singh, Mona A. Kanso, Shin Hyuk Kim, Bernhardt L. Trout, Martin Z. Bazant, Allan S. Myerson, and Richard D. Braatz. "Mechanistic modeling of lipid nanoparticle formation for the delivery of nucleic acid therapeutics". In: *Biotechnol. Adv.* 84 (Nov. 2025), p. 108643. ISSN: 0734-9750. DOI: 10.1016/j.biotechadv.2025.108643

Benjamin B. Ye, Pierre J. Walker, and Zhen-Gang Wang. "MDCraft: A Python assistant for performing and analyzing molecular dynamics simulations of soft matter systems". In: *J. Open Source Softw.* 9.100 (Aug. 2024), p. 7013. ISSN: 2475-9066. DOI: 10.21105/joss.07013

Luc T. Paoli, Pavan K. Inguva, Andrew J. Haslam, and Pierre J. Walker. "Confronting the thermodynamics knowledge gap: A short course on computational

thermodynamics in Julia". In: *Educ. Chem. Eng.* 48 (July 2024), pp. 1–14. ISSN: 1749-7728. DOI: 10.1016/j.ece.2024.03.002

Pierre J. Walker, Andrés Riedemann, and Zhen-Gang Wang. "GCIdentifier.jl: A Julia package for identifying molecular fragments from SMILES". in: *J. Open Source Softw.* 9.96 (Apr. 2024), p. 6453. ISSN: 2475-9066. DOI: 10.21105/joss.06453

Pierre J. Walker, Simon Mueller, and Irina Smirnova. "Confidence-Interval and Uncertainty-Propagation Analysis of SAFT-type Equations of State". In: *J. Chem. Eng. Data* 69.2 (Aug. 2023), pp. 495–508. ISSN: 0021-9568. DOI: 10.1021/acs.jced.3c00413

Pierre J. Walker. "Toward Advanced, Predictive Mixing Rules in SAFT Equations of State". In: *Ind. Eng. Chem. Res.* 61.49 (Dec. 2022), pp. 18165–18175. ISSN: 0888-5885. DOI: 10.1021/acs.iecr.2c03464

Andrew S. Ylitalo, Huikuan Chao, Pierre J. Walker, Jacob Crosthwaite, Thomas C. Fitzgibbons, Valeriy G. Ginzburg, Weijun Zhou, Zhen-Gang Wang, Ernesto Di Maio, and Julia A. Kornfield. "Competition between CO $_2$ -philicity and Mixing Entropy Leads to CO $_2$ Solubility Maximum in Polyether Polyols". In: *Ind. Eng. Chem. Res.* (Aug. 2022), acs.iecr.2c02396. ISSN: 0888-5885, 1520-5045. DOI: 10.1021/acs.iecr.2c02396

Pierre J. Walker, Hon-Wa Yew, and Andrés Riedemann. "Clapeyron.jl: An Extensible, Open-Source Fluid Thermodynamics Toolkit". In: *Ind. Eng. Chem. Res.* 61.20 (May 2022), pp. 7130–7153. ISSN: 0888-5885, 1520-5045. DOI: 10.1021/acs.iecr.2c00326

Manuscripts in preparation not forming chapters of this thesis

Ananya Venkatachalam, Pierre Walker, Samuel Varner, Bilin Zhuang, and Zhen-Gang Wang. "Stockmayer Fluid with a Shifted Dipole. III. Ion Solvation". In: *In preparation* (2026)

Pierre J. Walker, Hannah Uhl, Oliver Xie, Zhen-Gang Wang, and Bradley D. Olsen. "Thermodynamics of Polymer Mixtures: From Classical Theories to Data-Driven Modeling". In: *Submitted* (2026)

TABLE OF CONTENTS

Acknowledgements iv
Abstract viii
Published Content and Contributions x
Table of Contents xiii
List of Illustrations xvi
List of Tables xix
Introduction 1

I Equilibrium Behavior of Charge-Containing Macromolecular Systems 6

Chapter I: Electrostatic Origins of Anomalous Phase Behavior in Polymer–Ionic Liquid Mixtures 11
1.1 Introduction 11
1.2 Theory 13
1.3 Phase Equilibrium and Critical Point 20
1.4 Key Physical Effects 20
1.5 A Minimal Model 30
1.6 Conclusion 34
1.7 Appendix 35
Chapter II: Explicit Solvents Reverse Electrostatic Phase Behavior in Charged Fluids 48
2.1 Introduction 49
2.2 Methods 52
2.3 Results and Discussion 63
2.4 Conclusion 75
Chapter III: Self- and Salt-Induced Coacervation of Charge-Asymmetric Polyampholytes 87
3.1 Introduction 88
3.2 Methods 90
3.3 Results and Discussion 104
3.4 Conclusion 117
Chapter IV: Topology-Driven Phase Separation in Charged Polymer Solutions 126
4.1 Introduction 126
4.2 Theory 128
4.3 Results and discussion 130
4.4 Conclusion 138
4.5 Appendix 139

II Dynamic Behavior of Charge-Containing Macromolecular Systems 149

Chapter V: Decoupling Ion Association from Conductivity in Ionic-Liquid–Solvent Mixtures . . . 153
5.1 Introduction . . . 154
5.2 Methods . . . 157
5.3 Results and Discussion . . . 161
5.4 Appendix . . . 172
Chapter VI: Dynamic Charge Regulation Enhances Ion Mobility in Polyelectrolyte Networks . . . 183
6.1 Introduction . . . 183
6.2 Methods . . . 186
6.3 Results . . . 193
6.4 Conclusion and Outlook . . . 202
6.5 Appendix . . . 206
Chapter VII: From Metal–Ligand Coordination to the Mechanics of Metallo-Polyelectrolyte Complexes . . . 221
7.1 Introduction . . . 221
7.2 Metal–Ligand Binding . . . 224
7.3 Phase Behavior and Gelation . . . 228
7.4 Mechanical Properties . . . 253
7.5 Conclusions . . . 268
Concluding Remarks . . . 279

LIST OF ILLUSTRATIONS

Number *Page*

1.1 Phase behavior and critical scaling from clustering alone 23
1.2 Average cluster size vs. ion binding-site number 24
1.3 Clustering and binding contributions to the free energy of mixing . . 25
1.4 Phase behavior and critical scaling from electrostatics alone 26
1.5 Electrostatic (green) contribution to the free energy of mixing (purple) for a polymer–ionic liquid system at various temperatures. 26
1.6 PEO+[EMIM][BF_4] phase diagram across chain lengths 30
1.7 Phase diagrams for PiPGE and PnBGE ionic-liquid mixtures 31
1.8 Free-energy contributions for PEO-20+[EMIM][BF_4] at two temperatures 33
1.9 Origin of guest-polymer exclusion from host coacervates 37
2.1 Bjerrum length l_B as a function of temperature for water, methanol, acetonitrile, and acetone, calculated from experimental static-permittivity data obtained from the DETHERM databank [146]. 50
2.2 Dielectric constant and Bjerrum length vs. temperature 63
2.3 Dielectric response of pure solvent vs. added salt 64
2.4 Ion PMFs and phase diagram in an explicit dipolar solvent 67
2.5 Potential of mean force between oppositely charged ions at infinite dilution (blue) and $\phi = 0.01$ (green) with varying temperature for an explicit dipolar solvent with $\bar{\mu} = 0.15$. 68
2.6 Coacervate phase behavior in an explicit or implicit solvent 69
2.7 Polyelectrolyte PMFs and phase diagram in an explicit solvent 72
2.8 Coacervate phase behavior with added salt 73
2.9 Salt partitioning in an implicit or explicit solvent 74
3.1 Overview of the theoretical frameworks compared in this chapter . . 92
3.2 Single-chain triplet distance and radius of gyration vs. κ 104
3.3 Salt-free phase behavior across representative charge sequences . . . 107
3.4 Salt-free behavior of two sequences with matched doublets 110
3.5 Added-salt effect on representative charge sequences 112
3.6 Global IDP sequence–state diagrams, gauLS vs. RPA 115
4.1 Overview of coacervation and the polymer topologies studied 127

4.2 Phase diagrams of simple and complex coacervates by topology . . . 131
4.3 Charge–charge structure factor of a simple polyelectrolyte of varying topology with its counterion at $l_B = b$, $\sigma = 0.2$, $\phi_p = 0.01$ and $N = 200$. 132
4.4 Phase behavior of mixed-topology complex coacervates 134
4.5 Salt partitioning in a simple (a) and complex (b) coacervate as a function of salt concentration in the supernatant with varying polyelectrolyte topology. For all systems, $l_B = b$. 135
5.1 Molar conductivity and ionicity across IL–solvent mixtures 155
5.2 Ion-association structure in [BMIM][BF_4]–solvent mixtures 162
5.3 Relating ion dissociation, ionicity, and conductivity 166
5.4 Ionic conductivity σ and dynamic viscosity η on a logarithmic scale as a function of x_{IL} for various ionic liquid and solvent systems 172
5.5 Site–site radial distribution function $g(r)$ between anionic and cationic binding systems in the pure ionic liquid 173
5.6 Association fractions for additional IL–solvent systems 173
5.7 For ionic liquid + solvent systems not considered in the main text: Normalized molar conductivity, $\Lambda/\Lambda_{ref.}$, and free ion fraction, α, as functions of ionic-liquid mole fraction x_{IL}, where the reference point is the lowest simulated IL mole fraction for each system. 174
5.8 Onsager decomposition for additional IL–solvent systems 174
5.9 Onsager decomposition of [BMIM][BF_4] across four solvents 175
6.1 Overview of the simulation methodology 188
6.2 Effect of hydrogel charge density on ion transport 195
6.3 Effect of competitive binding on ion transport 197
6.4 Effect of dynamical charge regulation on ion transport 200
6.5 Design implications of charge regulation for ion transport 203
6.6 Variation in the hydrogel degree of ionization as a function of the pK_a value and for different salt concentrations and valencies 206
6.7 Cation diffusion vs. pK_a across valencies 206
6.8 Anion diffusion vs. pK_a across cation valencies 207
6.9 Unbound cation fraction vs. pK_a 207
6.10 Ion-pair relaxation time vs. pK_a 208
6.11 Nearest-neighbor polymer backbone charge autocorrelation function $\rho_q(l = 1)$ as a function of pK_a and obtained for different salt valencies and concentrations. 208

6.12 Cation diffusion vs. hydrogel ionization degree 209
6.13 Cation diffusion vs. unbound cation fraction 209
6.14 Diffusion: discrete vs. homogeneous charge distribution 210
6.15 Diffusion sensitivity to MD/MC step ratio 211
7.1 Initial configurations used in all quantum chemistry calculations to obtain binding energies between acrylate and metal ions. 224
7.2 Visual representation of the process used to obtain binding energies from quantum chemistry calculations in the case of a divalent cation. 225
7.3 QC binding energies vs. ion-dipole and Coulombic predictions . . . 226
7.4 Optimized zinc and nickel complex structures 228
7.5 Schematic of associating polymers with sticker spacing 229
7.6 Phase and gelation diagram vs. sticker spacing 231
7.7 Schematic of the proposed metal-crosslinking theory 232
7.8 Contribution of each term in the proposed theory 237
7.9 Phase diagrams for divalent and trivalent counter-ions 240
7.10 Phase diagram with added divalent and trivalent salt 243
7.11 Combined phase and gelation diagram with added salt 244
7.12 Possible association states of a weak polyelectrolyte 245
7.13 Charge sparsity vs. metal concentration and valency 248
7.14 Gel regions vs. pH and metal valency 249
7.15 Possible intra- and inter-chain crosslink configurations 250
7.16 Crosslink-type fractions vs. pH and valency 251
7.17 Simulation snapshots of a polyelectrolyte chain in the presence of divalent metal ions at different low (left) and high (right) pH values. . 255
7.18 Relaxation times of different motion modes 257
7.19 Predicted vs. simulated inter-crosslinked ion fraction 259
7.20 Stress-strain curves across valency and pH 262
7.21 Simulation snapshot of divalent (7.21a) and trivalent (7.21b) systems at approximately 500% strain, close to the point at which both systems form two separate clusters. 262
7.22 Fraction of inter-crosslinked ions during deformation. 264
7.23 Mechanical response of MPEC gels vs. ion diameter 265
7.24 Mechanical response of MPEC gels vs. applied pressure 267

LIST OF TABLES

Number *Page*

1.1 Parameters corresponding to the PEO+[EMIM][BF_4] system for the approach using a combination of the MSA + χ contribution. 32

5.1 Association parameters ($\Delta_{ij,ab}$) used within the proposed theory (equation 5.7). 165

INTRODUCTION

Electromagnetic interactions constitute one of the four fundamental interactions of nature and underpin chemical bonding, molecular organization, and many biological processes. In the electrostatic limit, these interactions are governed by Coulomb's law, first formulated more than two centuries ago[23]. The magnitude of the force between two point charges is

$$F = k_{\mathrm{e}} \frac{q_1 q_2}{r^2}\,, \tag{1}$$

where k_{e} is Coulomb's constant, q_i is the charge of entity i, r is the separation between the charges, and F is the force between them. At the time of Coulomb's work, before a molecular description of matter had been established, this law was applied primarily to macroscopic charged objects. Faraday and Maxwell's subsequent studies of dielectric polarization[24, 25] clarified how the intervening medium modifies electrostatic interactions, while the later work of Born and Landé applied Coulombic models directly to the energetics of ionic crystals[26, 27, 28], one of the first uses of Coulomb's law to describe interatomic interactions. At the microscopic level, chemical bonding and intermolecular forces ultimately arise from electromagnetic interactions among nuclei and electrons, with quantum mechanics determining how these underlying Coulombic interactions manifest as covalent bonding, polarization, hydrogen bonding, and dispersion.

Despite this common microscopic origin, electrostatic interactions occupy a distinctive position in statistical mechanics because of their exceptionally long range. Although the Coulomb force decays as r^{-2}, the corresponding pair potential decays only as r^{-1}. Consequently, a naive mean-field integration of the bare Coulomb potential over an infinite system does not converge. By contrast, many common intermolecular interactions decay sufficiently rapidly that pairwise-additive or local mean-field approximations provide a useful starting point. Electrostatic interactions must therefore be treated collectively, with the response of the surrounding charged medium included from the outset.

This collective character was first captured systematically by Debye and Hückel[29]. By solving the linearized Poisson–Boltzmann equation, they showed that an ion is surrounded by an oppositely charged ionic atmosphere that reduces its effective interaction with distant charges. The resulting phenomenon of electrostatic screening arises because a central ion responds not only to its nearest neighbors, but to the collective organization of many ions throughout the surrounding solution. Even at

relatively low concentrations, the effective interaction differs from the bare Coulomb potential. Electrostatic contributions therefore cannot, in general, be represented as an independent pairwise correction to an otherwise neutral reference system; they depend on the composition, structure, and collective response of the charged medium.

The development of analytical theories for simple ionic systems proceeded rapidly. Seminal contributions from Onsager and Fuoss extended the Debye–Hückel framework and provided foundational descriptions of ionic association, conductivity, and the correlated motion of charged species[30, 31, 32, 33]. Subsequent theories have incorporated finite ion size, short-range correlations, molecular association, solvent structure, and hydrodynamic effects, including Kirkwood's extension of dielectric theory to account for local molecular correlations in polar liquids[34]. As a result, the equilibrium and transport properties of simple electrolytes can now be described quantitatively across a broad range of conditions, although concentrated and chemically complex electrolytes continue to present important challenges.

The incorporation of electrostatic interactions into polymer physics introduces an additional hierarchy of complexity. Macromolecules possess extended conformations, internal connectivity, and characteristic length and time scales[35] that overlap with those associated with electrostatic correlations. Charges located on distant positions along the same molecule may interact directly, while the conformation of the chain controls the spatial organization of those charges. At the same time, electrostatic interactions between different chains couple molecular conformation to intermolecular organization and macroscopic material properties. Neither the polymeric nor the electrostatic degrees of freedom can therefore be treated as a passive background for the other.

Even mixtures containing uncharged macromolecules and small ions may exhibit behavior without a straightforward analogue in neutral molecular mixtures. Large disparities in molecular size, mobility, and interaction environment create competing asymmetries in both equilibrium partitioning and transport. The addition of charge further couples the motion and distribution of the small species to the organization of the macromolecules, producing thermodynamic and dynamic behavior that cannot generally be inferred from either component in isolation.

A particularly rich realization of this coupling occurs in polyelectrolytes, for which charged monomers are chemically connected along a macromolecular backbone. In these systems, long-ranged electrostatic correlations coexist with the extended length

scale and constrained architecture of the polymer chain. This coupling produces complex single-chain behavior that depends on solvent conditions, ionic strength, charge density, charge sequence, and molecular architecture. At finite concentration, overlap between chains introduces additional intermolecular correlations, while counterions and added salt reorganize in response to the polymeric charge distribution. The resulting macroscopic phase behavior and transport properties emerge from correlations spanning monomeric, molecular, and collective length scales.

Charge-containing systems are also subject to constraints that have no direct counterpart in neutral materials. Most prominent among these is electroneutrality. This condition couples species that may possess vastly different sizes, mobilities, and interaction environments, such as polyelectrolytes and their counterions or oppositely charged polymers with different charge densities and molecular architectures. Electroneutrality consequently reduces the number of independently variable compositions, constrains phase coexistence and species partitioning, and correlates the local motion of charged entities[36]. Although simple in statement, this constraint can generate nontrivial scaling behavior that is absent from either component considered independently.

A further source of complexity is charge regulation: the ability of a molecular site to alter its charge state through a reversible chemical reaction. Charge regulation is not unique to macromolecular systems, nor does chemical equilibrium itself require electrostatic interactions. Nevertheless, acid–base reactions are ubiquitous in aqueous environments[37, 38], and their equilibrium is inherently coupled to the local electrostatic potential. Within a macromolecule or polymer network, changes in protonation modify electrostatic interactions, which in turn alter molecular conformation, ion binding, and the local propensity for further protonation or deprotonation. Charge regulation therefore establishes feedback between chemical state, molecular organization, and transport, giving rise to behavior that cannot be reproduced by models with fixed charges.

This thesis examines how these defining characteristics of charge-containing systems (long-ranged correlations, molecular connectivity, electroneutrality, chemical specificity, and charge regulation) combine to determine their macroscopic behavior. Rather than attempting to reproduce the full chemical complexity of each material from the outset, the work follows a reductionist strategy in which dominant physical ingredients are isolated and examined individually. This approach makes it possible

to identify transferable mechanisms and design principles that apply across systems that may otherwise appear chemically unrelated.

The thesis is divided into two complementary parts. Part I, *Equilibrium Behavior of Charge-Containing Macromolecular Systems*, develops an equilibrium map of the states accessible to charged macromolecular materials. It examines how electrostatic correlations govern phase stability and how these correlations are reshaped by mixture composition, solvent polarization, charge sequence, and polymer topology. Across these chapters, the central objective is to determine the unique ways in which electrostatic interactions drive phase separation in each of the scenarios considered.

Part II, *Dynamic Behavior of Charge-Containing Macromolecular Systems*, considers how charge, matter, and stress move and relax within these thermodynamic states. It investigates the relationship between ion association and electrical conductivity, the coupling of charge regulation to ion transport through polymer networks, and the role of dynamic metal–ligand associations in controlling hydrogel mechanics. These chapters demonstrate that static measures such as ion-pair populations, equilibrium charge states, or crosslink densities do not uniquely determine dynamic behavior. Conductivity, diffusion, and mechanical response instead emerge from collective motion, exchange kinetics, and competition among relaxation pathways spanning multiple length and time scales.

Together, the two parts provide complementary views of charge-containing materials. The first identifies the thermodynamic landscape and the collective interactions that shape it; the second examines the pathways by which systems move, respond, and relax within that landscape. In doing so, this thesis seeks to establish a unified physical picture connecting microscopic electrostatic interactions to the equilibrium and dynamic behavior of chemically complex macromolecular systems.

References

[23] C. A. (Charles Augustin) Coulomb et al. *Mémoires sur l'électricité et la magnétisme*. Paris : Chez Bachelier, libraire ..., 1789.

[24] Michael Faraday. *Experimental Researches In Electricity Vol. 1*. Unknown. 1839.

[25] James Clerk Maxwell. *A treatise on electricity and magnetism*. eng. Oxford : Clarendon Press, 1873.

[26] M. Born and A. Landé. "Kristallgitter und Bohrsches Atommodell". de. In: *Selected Scientific Papers of Alfred Landé*. Ed. by A. O. Barut and A.

van der Merwe. Dordrecht: Springer Netherlands, 1988, pp. 65–72. ISBN: 978-94-009-3981-3. DOI: 10.1007/978-94-009-3981-3_8.

[27] M. Born and A. Landé. "Über die absolute Berechnung der Kristalleigenschaften mit Hilfe Bohrscher Atommodelle". de. In: *Selected Scientific Papers of Alfred Landé*. Ed. by A. O. Barut and A. van der Merwe. Dordrecht: Springer Netherlands, 1988, pp. 37–57. ISBN: 978-94-009-3981-3. DOI: 10.1007/978-94-009-3981-3_6.

[28] M. Born and A. Landé. "Über die Berchnung der Kompressibilität regulärer Kristalle aus der Gittertheorie". de. In: *Selected Scientific Papers of Alfred Landé*. Ed. by A. O. Barut and A. van der Merwe. Dordrecht: Springer Netherlands, 1988, pp. 58–64. ISBN: 978-94-009-3981-3. DOI: 10.1007/978-94-009-3981-3_7.

[29] P. Debye and E. Hückel. "Zur Theorie der Elektrolyte. I. Gefrierpunktserniedrigung und verwandte Erscheinungen". In: *Phys. Z.* 24 (1923), pp. 185–206.

[30] Lars Onsager. "Zur Theorie der Electrolyte. I". In: *Phys. Z.* 27 (1926), pp. 388–392.

[31] Lars Onsager. "Zur Theorie der Electrolyte. II". In: *Phys. Z.* 28 (1927), pp. 277–298.

[32] Raymond M. Fuoss and Lars Onsager. "Conductance of Unassociated Electrolytes." In: *J. Phys. Chem.* 61.5 (May 1957), pp. 668–682. ISSN: 0022-3654. DOI: 10.1021/j150551a038.

[33] Raymond M. Fuoss. "Ionic Association. I. Derivation of Constants from Conductance Data". In: *J. Am. Chem. Soc.* 79.13 (July 1957), pp. 3301–3303. ISSN: 0002-7863, 1520-5126. DOI: 10.1021/ja01570a001.

[34] John G. Kirkwood. "The Dielectric Polarization of Polar Liquids". en. In: *J. Chem. Phys.* 7.10 (Oct. 1939), pp. 911–919. ISSN: 0021-9606. DOI: 10.1063/1.1750343.

[35] Paul J. Flory. *Principles of Polymer Chemistry*. Cornell University Press, 1953. ISBN: 978-0-8014-0134-3.

[36] Gerald S. Manning. "Limiting Laws and Counterion Condensation in Polyelectrolyte Solutions I. Colligative Properties". In: *J. Chem. Phys.* 51.3 (Aug. 1969), pp. 924–933. ISSN: 0021-9606. DOI: 10.1063/1.1672157.

[37] Lawrence J. Henderson. "Concerning the relationship between the strength of acids and their capacity to preserve neutrality". In: *Am. J. Physiol.* 21.2 (Mar. 1908), pp. 173–179. ISSN: 0002-9513. DOI: 10.1152/ajplegacy.1908.21.2.173.

[38] Karl Albert Hasselbalch. *Die Berechnung der Wasserstoffzahl des Blutes aus der freien und gebundenen Kohlensäure desselben, und die Sauerstoffbindung des Blutes als Funktion der Wasserstoffzahl*. Julius Springer, 1916.

P a r t I

EQUILIBRIUM BEHAVIOR OF CHARGE-CONTAINING MACROMOLECULAR SYSTEMS

(FOCUS: ELECTROSTATIC CORRELATIONS, DIPOLAR SOLVENTS, CHARGE SEQUENCE AND POLYMER TOPOLOGY)

Introduction

Just as geographical maps help us navigate physical space, phase diagrams provide maps of thermodynamic behavior. Their utility lies in projecting a high-dimensional thermodynamic space onto a small number of experimentally or theoretically accessible control variables. For a nonreactive system in the absence of additional constraints, the dimensionality of the coexistence space is described by the Gibbs phase rule[39],

$$F = C - P + 2\,, \tag{2}$$

where F is the number of degrees of freedom, C is the number of components, and P is the number of phases. As chemical systems become increasingly complex, however, both the accurate description of their thermodynamics and the projection of their many degrees of freedom onto an easily interpretable variable space become increasingly challenging. Tackling this complexity in its entirety is often intractable and may provide few general principles that can be transferred across different classes of materials. A more productive approach is therefore to distill a system into its dominant physical ingredients and develop an understanding of the role played by each. Canonical examples of this strategy include the theories of van der Waals[40], Flory and Huggins[41, 42], and Debye and Hückel[29], each of which reduced the chemical complexity of real systems to a small number of physically interpretable parameters and thereby enabled application across a broad range of materials.

Subsequent theoretical developments extended these foundational models to account for molecular association, chemical specificity, molecular architecture, and conformational degrees of freedom. Despite this progress, electrostatic interactions remain particularly difficult to reduce to a compact set of transferable principles, especially in multicomponent macromolecular systems. As discussed in the general Introduction, the long-ranged nature of electrostatics produces collective, many-body correlations that depend strongly on composition and molecular organization. In macromolecular systems, electrostatic interactions couple many charged sites both within and between molecules, linking molecular conformation, mobile-ion organization, solvent response, and macroscopic phase stability across multiple length scales[43]. The resulting phenomenology often lies beyond simple pairwise-additive or mean-field descriptions.

Charged systems are additionally constrained by electroneutrality, which reduces the number of independently variable compositions and couples the partitioning of different ionic species. Although such constraints can be incorporated into gener-

alized forms of the Gibbs phase rule, they make the construction and interpretation of low-dimensional phase diagrams less straightforward. Moreover, electrostatic interactions may be attractive or repulsive depending on the spatial organization of charge, while their effective range and strength are modified collectively through screening and solvent polarization. The phase behavior of charged macromolecular systems therefore cannot generally be inferred from charge magnitude or pair interactions alone.

The objective of this first part is to identify how electrostatic correlations govern macroscopic phase behavior and how those correlations are reshaped by four molecular features: mixture composition, solvent polarization, charge sequence, and polymer topology. By isolating these effects in progressively more complex settings, the following chapters provide a "map" of the phase space accessible to charged macromolecular materials and establish physical principles that can be transferred across chemically distinct systems.

Motivated by the anomalous phase behavior of polymer–ionic liquid mixtures, Chapter 1 examines how electrostatic correlations affect the thermodynamic stability of mixtures containing charged species and macromolecules. The electrostatic contribution is shown to be distinct from conventional Flory–Huggins-type interactions and to produce markedly different molecular-weight and composition scaling laws. The resulting framework is then extended to polyelectrolyte coacervates[44, 45] to examine the electrostatic origins of macromolecular partitioning as a function of molecular size, charge density, and charge sequence. Although polymer–ionic liquid mixtures and polyelectrolyte coacervates are chemically distinct, isolating their electrostatic contributions reveals common physical principles applicable to both.

Chapter 2 relaxes a central assumption made in most treatments of electrostatic interactions: the representation of the solvent as a passive, homogeneous dielectric background. Using complementary analytical theories and molecular simulations, we compare explicit and implicit treatments of the solvent and demonstrate that solvent polarization can qualitatively alter the thermal response of electrostatic interactions and the resulting phase behavior. This comparison reveals the fundamental limitations of abstracting away the molecular response of the solvent in electrostatically driven systems.

In Chapter 3, we consider a more subtle manifestation of electrostatic interactions: their dependence on the sequence of charges along a macromolecular backbone. In systems such as polyampholytic intrinsically disordered proteins, numerous studies

have proposed strong connections between isolated-chain properties and macroscopic phase behavior. By developing analytical theories that explicitly account for charge sequence and validating them against molecular simulations, we find that single-chain descriptors capture only part of the accessible phase behavior. Added salt modifies collective screening and intermolecular correlations in ways that cannot be inferred from isolated-chain properties alone, producing an expanded phase space that includes both self- and salt-induced phase separation.

Finally, while the effects of chain length, charge density, and charge sequence are examined in the preceding chapters, a more subtle and comparatively underappreciated molecular variable is polymer topology. Chapter 4 demonstrates that, even at fixed chain length, charge density, and interaction parameters, changes in polymer topology alter intramolecular correlations and thereby modify macroscopic phase stability. These results highlight the counterintuitive role of molecular connectivity in determining the collective behavior of charged polymers.

Together, these four chapters provide a unified account of how electrostatic correlations are shaped by composition, solvent polarization, charge sequence, and molecular topology. They demonstrate that the phase behavior of charged macromolecular systems emerges not from charge alone, but from the collective organization of charged sites, mobile ions, solvent molecules, and molecular architecture.

References

[29] P. Debye and E. Hückel. “Zur Theorie der Elektrolyte. I. Gefrierpunktserniedrigung und verwandte Erscheinungen”. In: *Phys. Z.* 24 (1923), pp. 185–206.

[39] J. Willard (Josiah Willard) Gibbs et al. *On the equilibrium of heterogeneous substances : first [-second] part*. eng. [New Haven : Published by the Academy], 1874.

[40] Johannes Diderik van der Waals. “The Equation of State for Gases and Liquids”. In: *Nobel Lecture*. 1910.

[41] Paul J. Flory. “Thermodynamics of High Polymer Solutions”. In: *J. Chem. Phys.* 9.8 (Aug. 1941), p. 660. ISSN: 0021-9606. DOI: 10.1063/1.1750971.

[42] Maurice L. Huggins. “Solutions of Long Chain Compounds”. In: *J. Chem. Phys.* 9.5 (May 1941), p. 440. ISSN: 0021-9606. DOI: 10.1063/1.1750930.

[43] P. G. De Gennes et al. “Remarks on polyelectrolyte conformation”. en. In: *J. Phys. (Paris)* 37.12 (Dec. 1976), pp. 1461–1473. ISSN: 0302-0738, 2777-3396. DOI: 10.1051/jphys:019760037012014610O.

[44] J. T. G. Overbeek and M. J. Voorn. “Phase separation in polyelectrolyte solutions. Theory of complex coacervation”. In: *J. Cell. Comp. Physiol.* 49.S1 (1957), pp. 7–26. ISSN: 1553-0809. DOI: 10.1002/jcp.1030490404.

[45] Arthur Veis. “A review of the early development of the thermodynamics of the complex coacervation phase separation”. In: *Adv. Colloid Interface Sci.* Polyelectrolyte-Macroion Coacervation 167.1 (Sept. 2011), pp. 2–11. ISSN: 0001-8686. DOI: 10.1016/j.cis.2011.01.007.

Chapter 1

ELECTROSTATIC ORIGINS OF ANOMALOUS PHASE BEHAVIOR IN POLYMER–IONIC LIQUID MIXTURES

Polymer–ionic liquid (IL) mixtures are promising materials for applications ranging from battery electrolytes and gas separation membranes to responsive actuators and sensors, owing to their unique combination of mechanical robustness and ionic conductivity. These systems often exhibit lower critical solution temperature (LCST) behavior and more symmetric phase envelopes than anticipated from the classical Flory–Huggins theory. In this chapter, we investigate the molecular origins of this anomalous behavior by systematically incorporating clustering, polymer–cation binding and electrostatic correlations into a simple thermodynamic framework. Our analysis reveals that the formation of clusters contributes to demixing at low temperatures, contrary to both experimental observations and prior theoretical predictions. In contrast, electrostatic interactions introduce persistent asymmetries in the free energy landscape, yielding different chain-length scaling in the critical composition and interaction parameter than predicted by the Flory–Huggins theory. Based on these insights, we propose a minimal, physically grounded model incorporating only mixing entropy, temperature-dependent Flory–Huggins parameter, and electrostatic correlation. This model successfully reproduces key experimental features in systems such as PEO + [EMIM][BF_4], using a small set of interpretable parameters. These results offer a mechanistic understanding of the phase behavior of polymer–IL mixtures and provide a practical modeling framework for their design and optimization.

This chapter includes work from our previously published article: Pierre J. Walker and Zhen-Gang Wang. "Anomalous Phase Behavior of Polymer–Ionic Liquid Mixtures". In: *J. Phys. Chem. B* 129 (Nov. 2025). ISSN: 1520-6106. DOI: 10.1021/acs.jpcb.5c04858

1.1 Introduction

Polymer–ionic liquid (IL) mixtures are promising materials for a range of applications. Owing to their thermal and chemical stability, non-volatility, and high ionic conductivity, ionic liquids have been widely explored for use in battery electrolytes [46, 47, 48]. When combined with polymers, which impart mechanical strength and

structural integrity, these mixtures yield durable and efficient electrolytes [49, 50, 51]. Beyond energy storage, polymer–IL systems have also shown utility in gas and ion separation membranes [52, 53, 54, 55], soft actuators [56, 57], and chemical sensors [58, 59, 60]. Despite this versatility, the phase behavior of these mixtures remains poorly understood [61].

At first glance, polymer–IL mixtures appear to resemble conventional polymer solutions and should therefore be well described by the classical Flory–Huggins theory [42, 35], with the familiar expression for the free energy of mixing ΔF_{mix}:

$$\frac{v\Delta F_{\mathrm{mix}}}{k_B T V} = \frac{\phi}{N}\log\phi + (1-\phi)\log(1-\phi) + \chi\phi(1-\phi)\,. \tag{1.1}$$

In Eq. (1.1), v is the monomer volume (assumed to be the same as that of the solvent), V is the system volume, T the temperature, k_B the Boltzmann constant, N the chain length of the polymer, ϕ the polymer volume fraction and χ the Flory–Huggins parameter characterizing the polymer–solvent interaction. This expression has been extensively used to model polymer solutions and blends [62, 63], often with χ taken to be temperature-dependent. Notably, it predicts that the critical volume fraction and interaction parameter scale as $\phi_c = N^{-1/2}$ and $\chi_c = \frac{1}{2} + N^{-1/2}$, respectively, for large N.

However, experiments by Lee et al. [64, 65] with mixtures of poly(ethylene oxide) (PEO) and 1-ethyl-3-methylimidazolium tetrafluoroborate ([EMIM][BF_4]) revealed anomalous behavior that is very different from that anticipated from Flory–Huggins theory. Given the hydrophilic nature of PEO and the relatively hydrophobic character of [EMIM][BF_4], one would expect a positive interaction parameter χ that decreases with temperature, leading to upper critical solution temperature (UCST) behavior. Additionally, due to size asymmetry, the critical concentration would be expected to vanish as $N \to \infty$. Instead, Lee et al. observed lower critical solution temperature (LCST) phase separation with a critical composition near $\phi_c \approx 0.5$, relatively insensitive to chain length. This trend has been observed in other polymer–IL systems [66, 67, 68, 69, 70, 71, 72].

To explain this behavior, several approaches have been proposed. Molecular dynamics simulations [73, 74] have successfully reproduced the experimental trends and offered valuable insights into the phase behavior. For instance, Choi et al. [73] emphasized the importance of polymer–cation binding, particularly between the ether oxygens on PEO and the electropositive hydrogens on the imidazolium ring of $EMIM^+$. However, because molecular dynamics inherently capture all interactions

simultaneously, it can be difficult to disentangle the specific contribution of each. In this context, theoretical approaches offer a clear advantage by enabling controlled, systematic investigation of individual interactions.

White and Lipson [75] were the first to develop a theoretical approach to model polymer–IL systems. They used a lattice-based model incorporating the strong cohesive energy of ILs and their tendency to form long-lived clusters [76, 77, 78]. By making the simplifying assumption that ILs form clusters of fixed size, their model successfully reproduced the more-symmetric shape of the phase envelope.

Another major simplification in the work of White and Lipson, and in others [79, 80], is the treatment of electrostatic interactions. These studies typically assume that electrostatics are effectively captured through ion pairing or, in White and Lipson's case, through the formation of fixed-size clusters. Other approaches, such as that of Nakamura [81], incorporate electrostatic effects via solvation free energies and dielectric mismatch. However, to our knowledge, no existing theoretical model has explicitly included electrostatic correlations, which are inherently non-pairwise, in polymer–IL mixtures using even basic frameworks such as the Debye–Hückel theory [29], let alone more advanced treatments such as the mean spherical approximation (MSA) [82] or the hypernetted-chain (HNC) approach [83].

Prior work on charged polymer systems by Sing and co-workers [84, 85] has shown that including electrostatic interactions can significantly shift phase boundaries relative to neutral analogs, arising from the many-body, long-range nature of these interactions in contrast to typical solvent–polymer interactions. This suggests that the same may hold for polymer–IL systems. We therefore hypothesize that electrostatic correlations are essential to understanding the anomalous phase behavior of polymer–IL mixtures.

To test this hypothesis, we systematically examine the role of clustering, polymer–cation binding and electrostatics in determining the phase behavior. Based on this analysis, we propose a minimal model that incorporates only the essential physics yet captures the experimentally observed trends.

1.2 Theory

To model the phase behavior of polymer–ionic liquid mixtures, we extend the Flory–Huggins (FH) theory, taking inspiration from the work by Jiang and co-workers [86, 87] (later extended by Zhang et al. [88]). We express this theory in terms of the

Helmholtz free energy of mixing, ΔF_{mix}, as a sum of ideal and excess contributions:

$$\frac{\Delta F_{\text{mix}}}{k_{\text{B}}TV} = \Delta f_{\text{mix}} = \Delta f_{\text{id}} + \Delta f_{\text{ex}} \,, \tag{1.2}$$

where T is the temperature, k_B is the Boltzmann constant and V is the system volume. The ideal mixing contribution, Δf_{id}, captures the translational entropy and is formally given by:

$$\Delta f_{\text{id}} = \frac{1}{v}\left[\frac{\phi}{N}\log\phi + (1-\phi)\log(1-\phi)\right] , \tag{1.3}$$

where ϕ and N are the volume fraction and degree of polymerization of the polymer and v is the reference monomer volume.

The excess contribution, Δf_{ex}, accounting for all other non-ideal interactions, will depend on the system and the model representation. The simplest and most familiar treatment would be through the Flory–Huggins expression[89, 42], in which the interactions between pairs of species are represented by the parameter χ:

$$\Delta f_{\text{ex}} = \frac{1}{v}\chi\phi(1-\phi) \,, \tag{1.4}$$

A common extension introduces temperature dependence into χ, enabling the description of both UCST and LCST behavior[62, 90]:

$$\chi = A + \frac{B}{T} \,, \tag{1.5}$$

where A and B are the entropic and enthalpic components, respectively. Note that the specific temperature dependence of the χ parameter does not alter the scaling with chain length of the critical properties. It is more rigorous, and in many cases necessary, to explicitly account for the underlying physical interactions that give rise to the phase behavior. In this work, we consider three such interactions explicitly: clustering, polymer–cation binding, and electrostatic correlations.

Clustering

A distinguishing feature of ionic liquids, relative to inorganic salts, is their tendency to form large and long-lived aggregates or clusters[76, 77, 78]. This behavior has been proposed as a key factor underlying the atypical phase behavior of certain polymer–ionic liquid mixtures. For instance, White and Lipson [75] suggested that clustering, with a characteristic aggregate size of ten, contributed to the unusual phase behavior of PEO + [EMIM][BF_4] mixtures. Several theoretical frameworks have been developed to describe clustering in these systems [91, 92].

Building on Wertheim's thermodynamic perturbation theory (TPT1) and in a similar vein as the approach of McEldrew and co-workers [91, 92], we assume a known reference state ref. of unbound n_c species, where each species i has m_i binding sites, and the number of pairs between species i and j is given by m_{ij}. The partition function of this system is given by the following equation:

$$Z = Z_{\text{ref.}} P_{\text{comb}} W_{\text{bind}} \,, \tag{1.6}$$

where Z_{ref} is the partition of the reference system. W_{bind} is the product of the probability of all pairs ij being formed:

$$W_{\text{bind}} = \prod_{ij} \left(\frac{\lambda_{ij} v}{V} \right)^{m_{ij}} \,, \tag{1.7}$$

where λ_{ij} is the binding strength between species i and j, v is the monomer volume and V is the system volume. The number of ways to form m_{ij} pairs, P_{comb}, is given by:

$$P_{\text{comb}} = \prod_{ij} \frac{(m_i N_i)!(m_j N_j)!}{m_{ij}!(m_i N_i - \sum_k m_{ik})!(m_j N_j - \sum_k n_{jk})!} \,. \tag{1.8}$$

If we take the logarithm of the perturbative terms (W_{bind} and P_{comb}), we can obtain the binding term as:

$$\begin{aligned} \frac{F_{\text{bind}}}{k_{\text{B}} T} = -\sum_{ij} \Bigg(& \ln (m_i N_i)! + \ln (m_j N_j)! - \ln (m_{ij}!) \\ & - \ln (m_i N_i - \sum_k m_{ik})! \\ & - \ln (m_j N_j - \sum_k m_{jk})! \\ & + m_{ij} \ln \left(\frac{\lambda_{ij} v}{V} \right) \Bigg) \,. \end{aligned} \tag{1.9}$$

Minimizing with respect to m_{ij} gives:

$$\frac{m_{ij}}{(m_i N_i - \sum_k m_{ik})(m_j N_j - \sum_k m_{jk})} = \frac{\lambda_{ij} v}{V} \,, \tag{1.10}$$

re-arranging:

$$m_{ij} = (m_i N_i - \sum_k m_{ik})(m_j N_j - \sum_k m_{jk}) \frac{\lambda_{ij} v}{V} \,. \tag{1.11}$$

If we now add up all j sites, we have:

$$\sum_j m_{ij} = (m_i N_i - \sum_k m_{ik}) \sum_j (m_j N_j - \sum_k m_{jk}) \frac{\lambda_{ij} v}{V} \,. \tag{1.12}$$

Dividing by $m_i N_i$, we have (setting $N_j v/V = \phi_j$):

$$\frac{\sum_j m_{ij}}{m_i N_i} = \left(1 - \frac{\sum_k m_{ik}}{m_i N_i}\right) \sum_j \phi_j m_j \left(1 - \frac{\sum_k m_{jk}}{m_j N_j}\right) \lambda_{ij} \,. \tag{1.13}$$

If we then define:

$$X_i = 1 - \frac{\sum_j m_{ij}}{m_i N_i} \,, \tag{1.14}$$

we have:

$$1 - X_i = X_i \sum_j \phi_j m_j X_j \lambda_{ij} \,. \tag{1.15}$$

Giving us the generalized law of mass action:

$$X_i = \frac{1}{1 + \sum_j \phi_j m_j \lambda_{ij} X_j} \,. \tag{1.16}$$

Substituting this result into our expression for the Helmholtz free energy will simplify to:

$$\frac{F_{\text{bind}} v}{k_{\text{B}} T V} = f_{\text{bind}} = \sum_i \phi_i m_i \left[\ln X_i + \frac{1 - X_i}{2}\right] \,. \tag{1.17}$$

The excess contribution can be obtained by deducting the bind free energy in the pure state (denoted by the subscript 0):

$$v \Delta f_{\text{bind}} = \sum_i \phi_i m_i \left[\ln\left(\frac{X_i}{X_{i0}}\right) + \frac{X_{i0} - X_i}{2}\right] \,, \tag{1.18}$$

giving us the generalized excess free energy due to binding. In the case of the clustering term, we simply set $m_p = 0$ and only allow binding between m_+ cation sites and m_- anion sites. The excess free energy contribution due to clustering in this mixture is then given by:

$$\begin{aligned} v \Delta f_{\text{cl}} = \frac{1}{2}(1 - \phi) \Bigg\{ & m_+ \left[\log\left(\frac{X_+}{X_{+0}}\right) + \frac{1}{2}(X_{+0} - X_+)\right] \\ & + m_- \left[\log\left(\frac{X_-}{X_{-0}}\right) + \frac{1}{2}(X_{-0} - X_-)\right] \Bigg\} \,, \end{aligned} \tag{1.19}$$

where X_i and X_{i0} denote the fractions of unbound sites of species i (or equivalently, the fraction of free species i) in the mixed and pure ionic liquid, respectively. These values are obtained self-consistently from the mass action equations:

$$X_+ = \frac{1}{1 + \frac{1}{2} m_- (1 - \phi) \lambda_{\text{cl}} X_-} \,, \tag{1.20}$$

$$X_- = \frac{1}{1 + \frac{1}{2} m_+ (1 - \phi) \lambda_{\text{cl}} X_+} \,. \tag{1.21}$$

The analytical solution to this coupled set of equations is:

$$X_+ = \frac{-(1+\frac{1}{2}(1-\phi)\lambda_{\mathrm{cl}}(m_- - m_+)) + \sqrt{(1+\frac{1}{2}(1-\phi)\lambda_{\mathrm{cl}}(m_- - m_+))^2 + 2(1-\phi)m_+\lambda_{\mathrm{cl}}}}{(1-\phi)m_+\lambda_{\mathrm{cl}}} \tag{1.22}$$

$$X_- = \frac{-(1+\frac{1}{2}(1-\phi)\lambda_{\mathrm{cl}}(m_+ - m_-)) + \sqrt{(1+\frac{1}{2}(1-\phi)\lambda_{\mathrm{cl}}(m_+ - m_-))^2 + 2(1-\phi)m_-\lambda_{\mathrm{cl}}}}{(1-\phi)m_-\lambda_{\mathrm{cl}}} . \tag{1.23}$$

Note that identical expressions can be obtained following the approach by Semenov and Rubinstein[93]. The parameter λ_{cl} is the binding strength between cation and anion sites, defined as:

$$\lambda_{\mathrm{cl}} = v_{\mathrm{cl}} \exp\left(\epsilon_{\mathrm{cl}}/(k_{\mathrm{B}}T)\right), \tag{1.24}$$

where v_{cl} is a dimensionless binding volume (normalized by the monomer volume), reflecting the steric accessibility, and ϵ_{cl} is the pairwise binding energy[93].

From this framework, the average cluster size, $\langle N_c \rangle$, can be calculated as[94, 95]:

$$\langle N_c \rangle = 1 + \frac{p_{+-}p_{-+}[(m_+ - 1)p_{+-} + (m_- - 1)p_{-+}]}{\left(\frac{p_{+-}}{m_-} + \frac{p_{-+}}{m_+}\right)[1 - (m_+ - 1)(m_- - 1)p_{+-}p_{-+}]}, \tag{1.25}$$

where p_{+-} and p_{-+} denote the probabilities that a site on a cation is bound to an anion, and vice versa:

$$p_{+-} = \frac{1}{2}(1-\phi)m_-\lambda_{\mathrm{cl}}X_+X_- , \tag{1.26}$$

$$p_{-+} = \frac{1}{2}(1-\phi)m_+\lambda_{\mathrm{cl}}X_+X_- . \tag{1.27}$$

From Eq. (1.25), it follows that percolation (i.e., the formation of infinite clusters) occurs when $1 - (m_+ - 1)(m_- - 1)p_{+-}p_{-+} = 0$, which can only be satisfied when $m_+ \geq 2$ and $m_- \geq 2$. For instance, when $m_+ = m_- = 2$, infinite clusters only arise in the limit $p_{+-} = p_{-+} = 1$, corresponding to infinite binding strength and chain-like assembly. In the case of $m_+ > 2$ and/or $m_- > 2$, percolation can occur at a finite binding strength. If either species has only a single binding site ($m_i = 1$), then the maximum cluster size is finite and limited to $m_+ + m_-$.

Polymer–cation binding

In their study, Lee et al. [65] proposed (and later verified by Choi et al. [73]) that cations such as $EMIM^+$ can bind to the oxygen atoms in PEO via hydrogen bonding

interactions from the imidazolium ring. This phenomenon is very similar to the hydrogen bonding interactions in water+PEO systems[96, 97] where the introduction of PEO results in entropy loss as water is now bound to the PEO backbone. Such interactions can be modeled analogously to the clustering framework described above, by introducing binding sites on both the polymer and the cation.

For simplicity, we assume one binding site per polymer repeat unit and one per cation. Under these assumptions, the excess free energy contribution from (1.17) can be simplified to:

$$v\Delta f_{\mathrm{b}} = \frac{1}{2}(1-\phi)\left(\log X_+ + \frac{1-X_+}{2}\right) + \phi\left(\log X_p + \frac{1-X_p}{2}\right).$$

where X_+ and X_p are the fractions of unbound sites on the cation and polymer, respectively. Since binding is only considered between polymer and cation, the reference values $X_{i0} = 1$ for all species. The unbound site fractions are determined self-consistently from the following mass-action equations:

$$X_+ = \frac{1}{1+\phi\lambda_{\mathrm{b}}X_p}, \tag{1.28}$$

$$X_p = \frac{1}{1+\frac{1}{2}m_+(1-\phi)\lambda_{\mathrm{b}}X_+}, \tag{1.29}$$

where λ_{b} is the polymer–cation binding strength, defined analogously to Eq. (1.24). The analytical solution to this coupled set of equations is given by:

$$X_+ = \frac{-(1+\frac{1}{2}\lambda_{p+}(3\phi-1)) + \sqrt{(1+\frac{1}{2}\lambda_{p+}(3\phi-1))^2 + 2(1-\phi)\lambda_{p+}}}{(1-\phi)\lambda_{p+}} \tag{1.30}$$

$$X_p = \frac{-(1-\frac{1}{2}\lambda_{p+}(3\phi-1)) + \sqrt{(1-\frac{1}{2}\lambda_{p+}(3\phi-1))^2 + 4\phi\lambda_{p+}}}{2\phi\lambda_{p+}}. \tag{1.31}$$

While this model can, in principle, be extended to include both clustering and polymer–cation binding within a unified framework [91], doing so requires solving the larger coupled system of equations and introduces additional parameters, as shown in (1.16). To isolate the effects of each interaction and maintain interpretability, we consider clustering and binding contributions separately in this work.

Electrostatic correlations

To model electrostatic interactions, several theoretical approaches are available, including the Debye–Hückel theory [29] and the hypernetted-chain approximation

[83]. Consistent with our previous work [88, 90, 4], we employ the mean spherical approximation (MSA), as developed by Blum and co-workers [82, 98], which provides a favorable balance between analytical tractability and quantitative accuracy. The generalized form of the MSA free energy requires solving a self-consistent set of equations. However, in the special case of equal size for all ions, the free energy can be simplified to give an analytical expression:

$$\Delta f_{\text{ele}} = \frac{1}{\pi}\left[(1-\phi)\Gamma_0^3\left(\frac{2}{3}+\Gamma_0\sigma\right) - \Gamma^3\left(\frac{2}{3}+\Gamma\sigma\right)\right],$$

where σ is the ion diameter and the inverse screening length, Γ, is related to the inverse Debye screening length, κ, as:

$$\Gamma(1+\Gamma\sigma) = \frac{\kappa}{2}, \tag{1.32}$$

where $\kappa^2 = \frac{4\pi l_{\text{B}}}{v}(1-\phi)$ for monovalent ions. Here, $l_{\text{B}} = e^2/(4\pi\epsilon_0\epsilon_{\text{r}}k_{\text{B}}T)$, is the Bjerrum length which characterizes the distance where the electrostatic interaction between two elementary charges in a medium equals the thermal energy. The constant e is the elementary charge, ϵ_0 is the vacuum permittivity and ϵ_{r} is the relative static permittivity of the medium. Γ_0 is the screening length of a pure ionic liquid. There is some debate in the literature as to what the relative static permittivity should depend on. For most pure solvents, the relative static permittivity is expected to decrease with increasing temperature. This inverse relationship often results in an increase in the Bjerrum length, and therefore the strength of electrostatic interactions. However, it is also known that the introduction of charged species to the medium can also lead to a decrement in the relative static permittivity[99, 100, 101]. A true first-principles theory would have to account for both these effects, which is clearly beyond the scope of this work. The value of the relative dielectric permittivity used in the model should best be interpreted as representing some average value across the range of compositions and temperatures considered.

We note that comparable behavior can be captured using the full Debye–Hückel free energy, where the two treatments converge in the dilute limit. Specifically, the Debye–Hückel limiting law is recovered by taking the point-charge limit ($\sigma \to 0$), which yields $f_{\text{ele}} \to -\kappa^3/(12\pi)$. This corresponds to a Voorn–Overbeek-like treatment of charged systems[44]. However, in contrast to models incorporating finite-sized ions, the Debye–Hückel limiting law permits a divergence of the electrostatic free energy with increasing ion concentration. This behavior is unphysical at high packing fractions, where excluded volume effects limit ion overlap and lead

to saturation of electrostatic contributions. Therefore, for dense systems such as polymer–ionic liquid mixtures, the use of MSA is essential for a realistic description.

1.3 Phase Equilibrium and Critical Point

In the previous sections, all equations were defined in terms of the polymer volume fraction, ϕ, where the composition of each ion can be obtained as $\phi_- = \phi_+ = \frac{1}{2}(1-\phi)$, as dictated by electroneutrality.

At a fixed temperature, the condition for coexistence between phases α and β is given by:

$$\left.\frac{\partial \Delta f_{\text{mix}}}{\partial \phi}\right|_{\alpha} = \left.\frac{\partial \Delta f_{\text{mix}}}{\partial \phi}\right|_{\beta}, \tag{1.33}$$

$$\left.\left(\Delta f_{\text{mix}} - \phi\frac{\partial \Delta f_{\text{mix}}}{\partial \phi}\right)\right|_{\alpha} = \left.\left(\Delta f_{\text{mix}} - \phi\frac{\partial \Delta f_{\text{mix}}}{\partial \phi}\right)\right|_{\beta}, \tag{1.34}$$

The first condition ensures equality of (exchange) chemical potential, while the second ensures equality of osmotic pressure. We note that, when the critical point is near $\phi \approx 1$, it is sometimes best to solve Eq. (1.33) and Eq. (1.34) in terms of $1-\phi$ rather than ϕ. Additional numerical stability can be achieved by solving for the logarithm of the compositions instead.

The critical point of the system is obtained from the condition:

$$\frac{\partial^2 \Delta f_{\text{mix}}}{\partial \phi^2} = 0, \tag{1.35}$$

$$\frac{\partial^3 \Delta f_{\text{mix}}}{\partial \phi^3} = 0, \tag{1.36}$$

which is solved simultaneously to determine the critical composition ϕ_c and temperature T_c. All thermodynamic derivatives in this work are evaluated numerically using ForwardDiff.jl [102], a Julia package that implements forward-mode automatic differentiation.

1.4 Key Physical Effects

We shall now consider the effect of each interaction introduced in the previous section on the phase behavior of a polymer–ionic liquid mixture, before proposing a minimal model to reproduce the experimental results.

Clustering

We begin by examining the role of clustering, as shown by the solid curves in Figure 1.1, where temperature is normalized by the binding energy. In these calculations, we set $m_+ = 3$ and $m_- = 4$, corresponding to the number of putative binding sites on $EMIM^+$ and BF_4^-, respectively.[91] By itself, clustering will favor demixing as it acts to reduce the translational entropy of the solvent. For sufficiently strong binding strength, clustering can induce phase separation if both m_+ and m_- exceed two. We can demonstrate this analytically if one considers the limit of infinite binding strength. For simplicity, we only consider $m_+ = m_- = m$, where our solutions for the association fractions simplify substantially:

$$X_+ = X_- = X = \frac{-1 + \sqrt{1 + 2(1-\phi)m\lambda_{\mathrm{cl}}}}{(1-\phi)m\lambda_{\mathrm{cl}}} \,. \tag{1.37}$$

In the case of the excess free energy, we are interested in two quantities: the difference between X and X_0, and their ratios. In the limit of infinite binding energy, it is easy to see that:

$$\lim_{\lambda_{\mathrm{cl}}\to\infty} X = \lim_{\lambda_{\mathrm{cl}}\to\infty} X_0 = 0 \,. \tag{1.38}$$

As such:

$$\lim_{\lambda_{\mathrm{cl}}\to\infty} X - X_0 = 0 \,. \tag{1.39}$$

However, the limit of the ratios is more interesting:

$$\lim_{\lambda_{\mathrm{cl}}\to\infty} \frac{X}{X_0} = \lim_{\lambda_{\mathrm{cl}}\to\infty} \frac{-1 + \sqrt{1 + 2(1-\phi)m\lambda_{\mathrm{cl}}}}{-1 + \sqrt{1 + 2m\lambda_{\mathrm{cl}}}} \frac{1}{1-\phi} = \frac{1}{\sqrt{1-\phi}} \,. \tag{1.40}$$

Substituting these solutions into our expression for the mixing free energy gives:

$$\Delta f_{\mathrm{mix}} = \frac{\phi}{N} \log\phi + \left(1 - \frac{m}{2}\right)(1-\phi)\log(1-\phi) \,. \tag{1.41}$$

We can now test different values of m and examine the maximum effect of clustering on the free energy of mixing. In the case of $m = 1$, our expression for the free energy of mixing simplifies to:

$$\Delta f_{\mathrm{mix}} = \frac{\phi}{N} \log\phi + \frac{1-\phi}{2} \log(1-\phi) \,, \tag{1.42}$$

which is equivalent to the mixing free energy when the solvent is of size $N = 2$. This makes sense as with $m = 1$, the maximum cluster size will be a dimer. In this case, the cluster contribution to the mixing free energy is simply a correction to the entropy of mixing.

In the limit of $m = 2$, where percolation becomes possible, our expression simplifies to:

$$\Delta f_{\text{mix}} = \frac{\phi}{N} \log \phi \,, \tag{1.43}$$

which is equivalent to the mixing free energy when the solvent is of infinite chain length. This makes sense as with $m = 2$, we can form continuous chains. This does highlight that, even at infinite binding strength, it is impossible to induce a phase split when $m = 2$ through clustering alone as the contribution to the mixing free energy is simply a correction to the mixing entropy.

Finally, for $m > 2$, the second term of this equation becomes positive, favoring demixing and leading to a phase split. One of these phases will be the polymer-rich phase whose composition is $\phi = 1$, which also corresponds to the spinodal. The composition of the other spinodal will be given by:

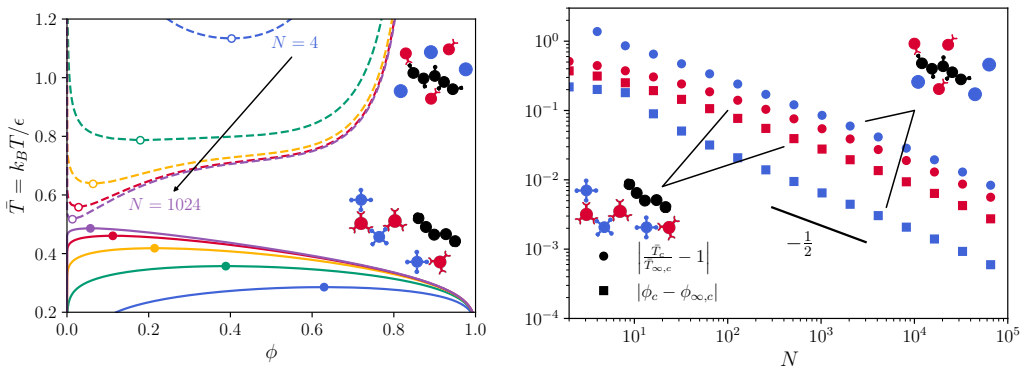
$$\phi^{\text{sp.}} = \frac{1}{N(\frac{m}{2} - 1) + 1} \,. \tag{1.44}$$

And the composition of the binodal is:

$$\phi^{\text{bi.}} = -\frac{1}{c} W(-ce^{-c}) \,, \quad c = N\left(\frac{m}{2} - 1\right) + 1 \,, \tag{1.45}$$

where $W(x)$ is the Lambert W function. It is easy to verify that the 'critical point' will occur when $m_c = 2$ and $\phi_c = 1$. We can see that the composition of the binodal and spinodal are finite, only approaching zero when $N \to \infty$. This highlights that, although infinite clusters do form at these conditions, mixing entropy of the polymer is still sufficient to allow it to dissolve within the clusters. The only time this will not be the case is when N is infinite.

With this understanding, we can now examine the resulting phase behavior for finite λ_{cl}, which exhibits upper critical solution temperature (UCST) behavior. As shown in Figure 1.1a, the critical point initially lies near polymer-rich compositions but shifts toward polymer-dilute regions with increasing chain length. White and Lipson [75] previously argued that clustering increases the effective size of ionic species, thereby reducing the size asymmetry with the polymer and shifting the critical point toward polymer-rich compositions. This trend is partially reflected in our results. However, at sufficiently large polymer chain lengths, the critical point shifts back toward the polymer-dilute region, consistent with Flory–Huggins theory for mixtures with unfavorable polymer–solvent interactions. Indeed, this model recovers the classic Flory–Huggins scaling of the critical point with chain length, $N^{-1/2}$, as shown by the red markers in Figure 1.1b.



(a) (b)

Figure 1.1: Phase behavior (a) and critical scaling (b) of a polymer + ionic liquid mixture only including the effect of clustering. The solid lines (a) and blue symbols (b) are the results obtained using clustering where $\epsilon_{\text{cl}} = 1.0$, $v_{\text{cl}} = 10^{-1}$ and $m_+ = 3, m_- = 4$. The dashed lines (a) and red symbols (b) are the results obtained using cation-polymer binding where $\epsilon_{\text{b}} = 1.0$, $v_{\text{b}} = 1.0$ and $m_+ = m_p = 1$, with an athermal $\chi = 1.95$. Square symbols in (b) correspond to the critical volume fraction of the polymer while the circular symbols correspond to the critical temperature.

These trends can be rationalized by examining the average cluster size, shown in Figure 1.2. In pure ionic systems, cluster size is determined by the number of binding sites per ion and the binding strength (via Eq. (1.24)). For example, at low temperatures, systems with $m_+ = m_- = 2$ form moderately large clusters, and systems with $m_+ = 3$ and $m_- = 4$ exhibit a divergence in cluster size with decreasing polymer volume fractions, indicating the onset of percolation. In both cases, increasing either the polymer volume fraction, disrupting cluster formation, or the temperature, weakening the binding interactions, leads to a reduction in average cluster size. This behavior is independent of polymer chain length.

At low polymer chain lengths, the mixing entropy is relatively large, resulting in a decreased critical temperature. Under these conditions, clustering plays a more significant role in the free energy of mixing, as seen from the solid red curve in Figure 1.3. Here, clustering effectively acts as a correction to the entropy of mixing, accounting for the increased effective size of the ionic species. This correction is skewed toward polymer-rich compositions, leading to a shift in the critical point toward higher polymer concentrations.

As the polymer chain length increases, the mixing entropy decreases, leading to a higher critical temperature. At these higher temperatures, clusters are both smaller and more easily disrupted, reducing their contribution to the free energy of mixing.

This is reflected in the dashed and dotted red curves in Figure 1.3, which show a smaller and more symmetric excess contribution, resembling that of the standard Flory–Huggins interaction. As a result, the critical point shifts toward polymer-dilute compositions, recovering the characteristic $N^{-1/2}$ scaling behavior of Flory–Huggins theory, as shown in Figure 1.1b.

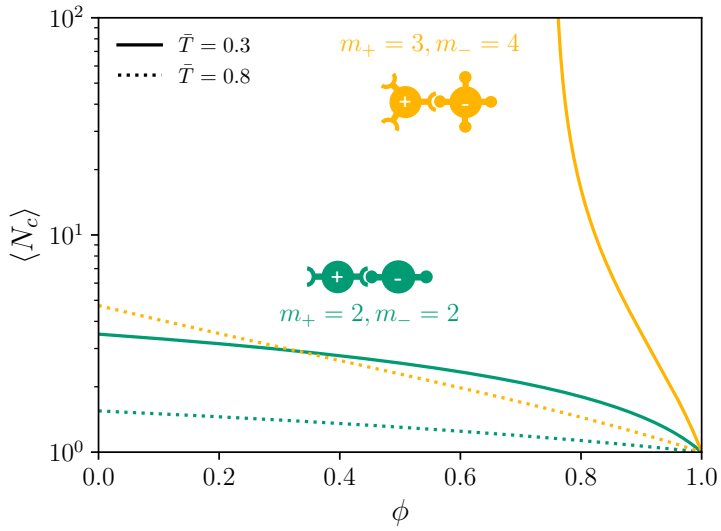


Figure 1.2: Average cluster size, obtained using Eq. (1.25), in a polymer–ionic liquid mixture varying number of sites on the ions (shown through the illustrations) at $\bar{T} = 0.3$ (solid line) and $\bar{T} = 0.8$ (dotted line). These results are independent from the chain length of the polymer. Parameters for clustering are identical to those used in Figure 1.1.

These results suggest that clustering among ionic liquids alone is insufficient to explain the experimentally observed phase behavior of polymer–ionic liquid systems.

Polymer–cation binding

An important interaction in IL–polymer mixtures is the reversible binding between cations and the polymer backbone. Lee et al. [65] proposed, and Choi et al.[73] confirmed using molecular dynamics simulations, that cations such as $EMIM^+$ can form hydrogen bonds with the ether oxygens in PEO via the electropositive hydrogens on the imidazolium ring. We model this interaction using Eq. (1.28), where, because $X_+, X_p \leq 1$, the binding contribution to the free energy of mixing is always negative. This indicates that polymer–cation binding enhances miscibility as illustrated by the blue curves in Figure 1.3. Note that, as temperature decreases, the minimum of the binding contribution shifts toward $\phi = \frac{1}{3}$, corresponding to the case where the number of cations equals the number of binding sites on the polymer.

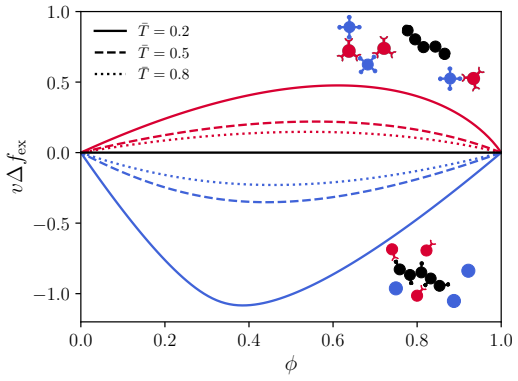


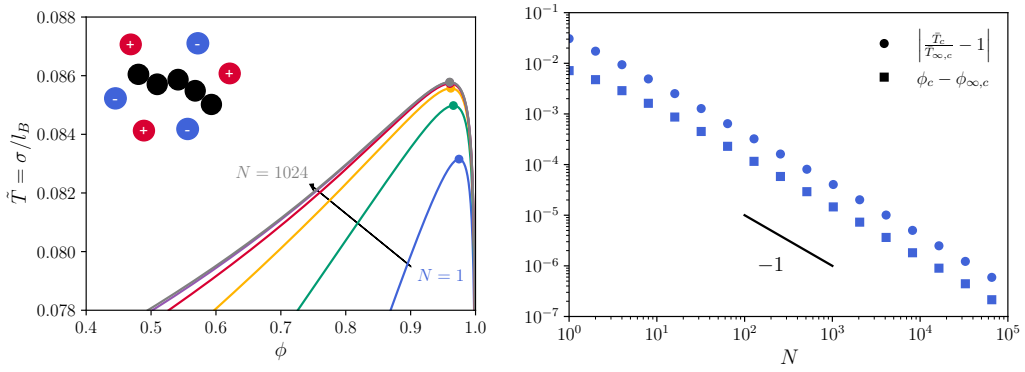
Figure 1.3: Contribution of clustering (red curves) and cation-polymer binding (blue curves) to the free energy of mixing for a polymer + ionic liquid system at various temperatures, with parameters corresponding to those used in Figure 1.1.

To recover the experimentally observed LCST behavior, we can introduce an athermal, positive Flory–Huggins interaction parameter χ to account for the unfavorable mixing between hydrophilic polymers and hydrophobic ionic liquid moieties. At high temperatures, binding is weak and unfavorable χ interactions dominate, driving phase separation. Because this mechanism does not involve clustering or aggregation, the LCST is shifted toward the polymer-dilute compositions, and the critical scaling follows the Flory–Huggins prediction of $N^{-1/2}$, as shown by the red markers in Figure 1.1b. Moreover, the binding contribution, being skewed toward polymer-dilute compositions (Figure 1.3), may actually enhance this shift at lower chain lengths.

While the inclusion of explicit polymer–cation binding offers mechanistic insight and a more physically grounded treatment, the same qualitative features, particularly LCST-type demixing, can be captured using a temperature-dependent χ parameter. In this sense, the binding model serves to justify such a dependence. Indeed, the binding free energy can be algebraically rewritten in a form resembling Eq. (1.5), with effective parameters $A \sim -\log v_b$ and $B \sim -\epsilon_b$, highlighting the connection between reversible binding and the phenomenological χ parameter.

Electrostatic correlations

In modeling ionic liquids, many prior studies have neglected electrostatic interactions [79, 75, 80], often arguing that ion pairing and clustering effectively render the system neutral, allowing the cation–anion pair to be treated as a single, uncharged species. However, as discussed in the previous section, clusters are dynamic entities. Their size and stability depend strongly on temperature and concentration,



(a) (b)

Figure 1.4: Phase behavior (a) and critical scaling (b) of a polymer–ionic liquid mixture only including electrostatic interactions. Square symbols in (b) correspond to the critical volume fraction of the polymer while the circular symbols correspond to the critical temperature.

and under many conditions, ionic liquids predominantly consist of dissociated ions. Consequently, we argue that electrostatic interactions are a fundamental feature of ionic liquids and must be retained in any physically consistent model. In this work, we account for these interactions using the mean spherical approximation (MSA), as detailed in Section 1.2. Electrostatic correlations manifest as effective attractions between the ions that are inherently many-body in nature. Such effective attractions are disrupted when diluted by another neutral solvent, including polymeric solvent. This is evident by the positive contribution to the mixing free energy shown in Figure 1.5, providing the driving force for phase separation, even in the absence of other energetic interactions[103, 104].

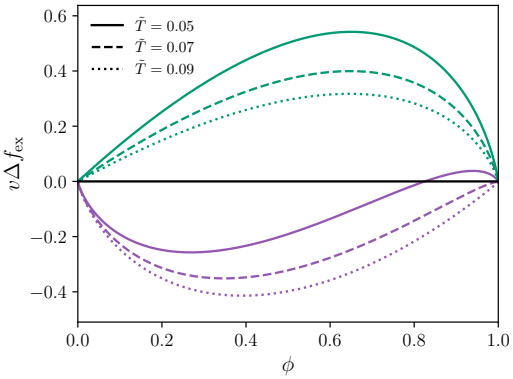


Figure 1.5: Electrostatic (green) contribution to the free energy of mixing (purple) for a polymer–ionic liquid system at various temperatures.

Figure 1.4 shows the phase diagrams for the polymer–IL mixture at several chain

lengths with only electrostatic interactions, where the temperature axis is normalized using the Bjerrum length. For reference, assuming a dielectric constant $\epsilon_r \approx 6 - 15$ at $T = 298.15\,\mathrm{K}$ for PEO, this corresponds to a reduced temperature range of $\tilde{T} \approx 0.04 - 0.10$, with $\sigma = 0.4\,\mathrm{nm}$.

Due to the effective repulsion between the polymer and the ionic species, as the polymer disrupts favorable electrostatic interactions, a polymer–IL mixture with only electrostatic interactions exhibits UCST behavior. However, unlike classical Flory–Huggins systems, the critical concentration remains consistently skewed toward polymer-rich compositions, even at large chain lengths, and approaches a finite value as $N \to \infty$. These features contrast sharply with the behavior observed in Figure 1.1, and is consistent with known trends in charged systems[104], including polyelectrolytes [105, 106, 107, 88]. To understand this shift, we consider the scaling of the inverse screening length, which follows:

$$\Gamma \sim (1 - \phi)^{\frac{1}{2}}\,, \tag{1.46}$$

at low ionic strengths. As such, Γ decreases sharply as $\phi \to 1$, resulting in weaker electrostatic interactions at high polymer concentrations. This asymmetry is reflected in the electrostatic contribution to the free energy of mixing (Figure 1.5), which is positive and skewed toward polymer-rich compositions. Importantly, this skewness persists even at elevated temperatures, with the maximum in the excess free energy occurring around $\phi \approx 0.65$. Note that when the mixing entropy is included, the combined free energy produces a composition of the polymer-rich phase at coexistence close to $\phi \approx 1$; see Figure 1.5.

Although increasing chain length modifies the entropy of mixing and introduces a competing asymmetry, this contribution diminishes with increasing N. As a result, the electrostatic contribution dominates, and the critical concentration remains near the polymer-rich region, as shown in Figure 1.5.

An additional noteworthy result is the scaling of the critical parameters, shown in Figure 1.4b. We find that both the critical temperature and concentration scale as N^{-1}, in contrast to the $N^{-1/2}$ scaling predicted by Flory–Huggins theory. To our knowledge, this scaling has not been reported in experiments or simulations. However, this is not entirely surprising. The experiments of Lee et al. [65], for example, involve multiple competing interactions, making it impossible to isolate the effects of electrostatics. Furthermore, our result is derived using a reduced temperature based on the Bjerrum length, which incorporates the dielectric constant. As ϵ_r

typically decreases with increasing temperature, direct experimental validation of this scaling will be challenging. However, simulations could be designed to isolate electrostatic effects and verify this scaling. We note that a version of the theory presented in section 1.2 which incorporates a temperature-dependent dielectric constant has shown that this decrease in dielectric constant can induce LCST behavior by itself.[90]

Another striking finding from our analysis is the behavior of the inverse screening length at the critical point. Following tedious algebra, we find that the spinodal condition, when expressed in terms of the screening length Γ, is given by:

$$v\frac{\partial^2 \Delta f_{\text{mix}}}{\partial \phi^2} = \frac{1}{N\phi} + \frac{1}{1-\phi} - \frac{vQ(\Gamma)}{(1-\phi)^2}, \tag{1.47}$$

where:

$$Q(\Gamma) = \frac{\Gamma^3(1+\Gamma\sigma)}{2\pi(1+2\Gamma\sigma)}. \tag{1.48}$$

Imposing the second constraint for the critical point, we find:

$$v\frac{\partial^3 \Delta f_{\text{mix}}}{\partial \phi^3} = \frac{1}{N\phi^2} - \frac{1}{(1-\phi)^2} + \frac{vQ(\Gamma)r(\Gamma)}{(1-\phi)^3}, \tag{1.49}$$

where:

$$r(\Gamma) = \frac{10\Gamma^2\sigma^2 + 8\Gamma\sigma + 1}{2(1+2\Gamma\sigma)^2}. \tag{1.50}$$

Introducing:

$$x = \frac{\phi}{1-\phi}, \qquad \phi = \frac{x}{1+x}, \tag{1.51}$$

gives:

$$vQ(\Gamma) = \frac{x(N+x)}{N(1+x)}. \tag{1.52}$$

from (1.47), and:

$$x^2 + r(\Gamma)x + N(r(\Gamma) - 1) = 0. \tag{1.53}$$

from (1.49). We can then obtain the following solutions at the critical point:

$$N(\Gamma) = \frac{\pi v\Gamma^3(1+\Gamma\sigma)\left(10\Gamma^2\sigma^2 + 8\Gamma\sigma + 1\right)^2}{(1+2\Gamma\sigma)(1-2\Gamma^2\sigma^2)\left[2\pi(1+2\Gamma\sigma) - v\Gamma^3(1+\Gamma\sigma^2)\right]^2}, \tag{1.54}$$

$$1 - \phi_c(\Gamma) = \frac{v\Gamma^3(1+\Gamma\sigma)\left(10\Gamma^2\sigma^2 + 8\Gamma\sigma + 1\right)}{4\pi(1+2\Gamma\sigma)^3 - v\Gamma^3(1+\Gamma\sigma)(1-2\Gamma^2\sigma^2)}, \tag{1.55}$$

and:

$$l_{\text{B,c}}(\Gamma) = \frac{(1+\Gamma\sigma)\left[4\pi(1+2\Gamma\sigma)^3 - v\Gamma^3(1+\Gamma\sigma)(1-2\Gamma^2\sigma^2)\right]}{8\pi\Gamma\left(10\Gamma^2\sigma^2 + 8\Gamma\sigma + 1\right)}. \tag{1.56}$$

The limit $N \to \infty$ can only be achieved for physical values of Γ when

$$\lim_{N\to\infty} (1 - 2\Gamma^2\sigma^2) \to 0. \tag{1.57}$$

The limiting critical value is therefore

$$\Gamma_{c,\infty}\sigma = \frac{1}{\sqrt{2}}. \tag{1.58}$$

Performing an expansion around $\Gamma_{c,\infty}\sigma$ such that:

$$\Gamma_c\sigma = \Gamma_{c,\infty}\sigma - \delta\,, \tag{1.59}$$

where $0 < \delta^2 \ll 1$. Substituting into (1.54), (1.55) and (1.56) gives the scaling relationships:

$$\lim_{N\to\infty} \Gamma_c\sigma = \frac{1}{\sqrt{2}} - \frac{4\pi(4+3\sqrt{2})}{(8\pi-1)^2}\frac{1}{N} + O\left(N^{-2}\right), \tag{1.60}$$

$$\lim_{N\to\infty} (1-\phi_c) = \frac{1}{8\pi} - \frac{72\pi + 48\sqrt{2}\pi - 1}{8\pi(8\pi-1)^2}\frac{1}{N} + O\left(N^{-2}\right), \tag{1.61}$$

$$\lim_{N\to\infty} \frac{l_{B,c}}{\sigma} = \left(\frac{3}{4} + \frac{1}{\sqrt{2}}\right)\left(1 + \frac{1}{8\pi - 1}\frac{1}{N} + O\left(N^{-2}\right)\right), \tag{1.62}$$

all of which are in good agreement with the results from Figure 1.4b. These results are also all of similar magnitude to the limit predicted by the restricted primitive model studied by Luijten et al. [104], though our values are slightly smaller. We hypothesize that the limiting behavior of the screening parameter Γ_c may reflect optimal ion packing in the condensed phase under strong electrostatic correlations. A detailed exploration of this hypothesis is beyond the scope of this work and is left for future investigation.

More broadly, while the mean spherical approximation (MSA) captures long-range electrostatic interactions, it has also been argued that it implicitly accounts for short-range clustering [108, 109]. This interpretation has important modeling implications: combining an explicit clustering free energy with an MSA-based electrostatic term risks double counting the same physical effect. Since the MSA approach alone reproduces the experimentally observed shift in critical concentration (Figure 1.4), we contend that it provides a more parsimonious and physically grounded basis for modeling ionic liquid–polymer mixtures. For cases where a more explicit treatment of ion pairing is desired, extensions such as binding-MSA [110, 111] may offer a systematic and rigorous framework, though less interpretable.

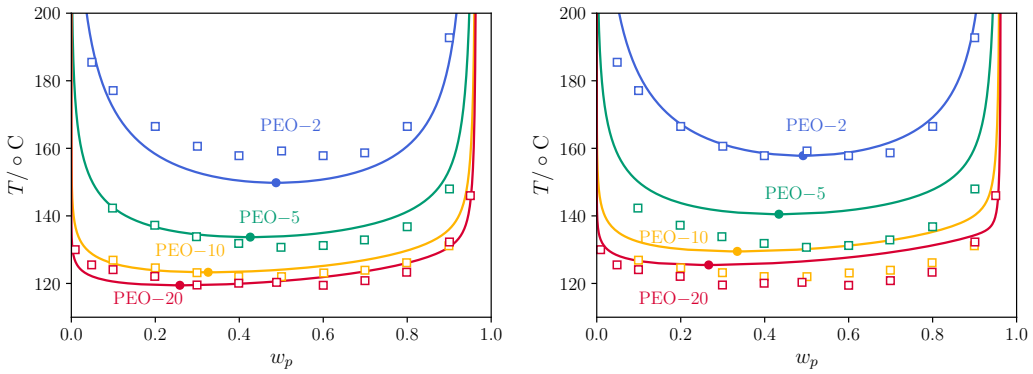


Figure 1.6: Phase diagram for PEO+[EMIM][BF_4] at various PEO chain lengths (color) where solid curves represent fittings obtained using a combination of MSA + χ contributions when fitted to PEO-20 (a) and PEO-2 (b). Model parameters are given in table 1.1. w_p is the weight fraction of the polymer. Data are taken from Ref. [65] where i in the notation PEO-i denotes the approximate kg/mol of the polymer chain.

1.5 A Minimal Model

Building on the insights developed in the preceding sections, we now introduce a minimal model for polymer–ionic liquid mixtures.

If one were to attempt rigorously accounting for all interactions present in a polymer–IL system, it would require combining clustering, polymer–cation binding, electrostatic and χ interactions. Aside from introducing significant model complexity, these contributions are all temperature-dependent and can become intertwined, leading to parameter degeneracy and ambiguity in interpretation [17]. An example of this has already been hinted at in section 1.4 where the effects of polymer–cation binding could be convoluted with a temperature-dependent χ parameter. For these reasons, a more pragmatic and robust modeling strategy may be to omit polymer-cation binding altogether and absorb their effects into a temperature-dependent χ with both enthalpic and entropic contributions (leading to an LCST). As electrostatic correlations cannot be captured by an effective χ parameter, and the mean spherical approximation implicitly accounts for clustering, the MSA contribution will be retained where we set $\sigma = 0.4\,\text{nm}$, as we have done in our prior work[90].

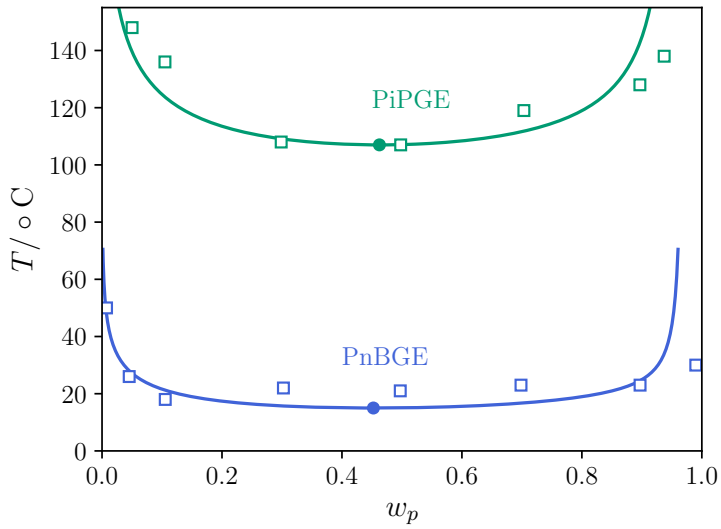


Figure 1.7: Phase diagram for poly(isopropyl glycidyl ether) (green, PiPGE) and poly(n-butyl glycidyl ether) (blue, PnBGE) with 1-hexyl-3-methylimidazolium bis(trifluoromethylsulfonyl)imide ([HMIM][NTf_2]) where solid curves represent fittings obtained using a combination of MSA + χ contributions. The model parameters are given in Table 1.1. w_p is the weight fraction of the polymer. Data are taken from Bentley et al. [69].

The resulting expression is given by:

$$\Delta f_{\text{mix}} = \frac{1}{v}\left[\frac{\phi}{N}\log\phi + (1-\phi)\log(1-\phi) + \chi\phi(1-\phi)\right] + \frac{1}{\pi}\left[(1-\phi)\Gamma_0^3\left(\frac{2}{3}+\Gamma_0\sigma\right) - \Gamma^3\left(\frac{2}{3}+\Gamma\sigma\right)\right], \tag{1.63}$$

where each term, its parameters and influence on the free energy of mixing has been discussed in the previous section. This expression only departs slightly from the classical Flory–Huggins theory, but retains the key physical ingredients necessary to reproduce the thermodynamic behavior of these systems. Specifically, we propose that the mixing free energy requires only three contributions: entropy of mixing, polymer–ion interactions (captured via a temperature-dependent Flory–Huggins parameter given by Eq. (1.5)), and electrostatics treated using the mean spherical approximation (MSA). To avoid overfitting, an all-too-common pitfall[112, 17], we deliberately restrict ourselves to just four adjustable parameters: the molecular weight per effective monomer, the coefficients A and B in χ between the polymer and cation, and a single dielectric constant.

For the purposes of this section, we will focus on the PEO-[EMIM][BF_4] system studied by Lee et al.[65], although we have applied our model to two other polymer–

ionic liquid mixtures. The resulting phase diagrams are shown in Figure 1.6 and Figure 1.7, with the fitted values of the parameters given in Table 1.1. It is important to note that the fitting is dependent on which data set is used, as demonstrated in Figure 1.6 where we fit either to the longest (Figure 1.6a) or shortest (Figure 1.6b) PEO chain length, with all other chains representing predictions. In this comparison, we see that the PEO-20 fit provides much better predictions than the PEO-2 fit. This is likely due to the fact that shorter PEO chains are expected to have different dielectric constants[113]. We also note that, as discussed by Lee et al.[65], large uncertainties are to be expected in the measurements of cloud points. As such, small disagreements between predictions and experimental data, such as that for PEO-2 and PEO-5 mixtures, can be partially attributed to this. As such, for the remainder of this section, we will focus on the PEO-20 parameters and Figure 1.6a where the close agreement between the theoretical predictions and the experimental data highlights the model's extrapolative power and physical grounding, achieved using a minimal set of well-motivated parameters.

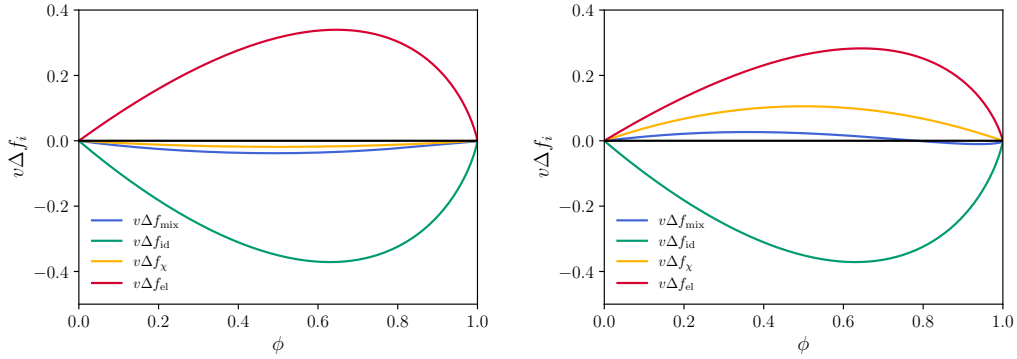
Table 1.1: Parameters corresponding to the PEO+[EMIM][BF_4] system for the approach using a combination of the MSA + χ contribution.

Parameter	**PEO-20 Fit**	**PEO-2 Fit**	**PiPGE Fit**	**PnBGE Fit**	**Units**
M_w/N	237.2	237.2	760.6	447.41	g/mol
A	2.509	2.411	2.577	2.677	-
B	-923.3	-970.4	-764.1	-977.6	K
ϵ_r	9.228	8.356	9.158	11.883	-

We now briefly discuss the parameter values obtained from our model for the PEO-20 fitting. If we consider the polymer chain length predicted in Table 1.1 and our prescribed value for σ, it suggests that each coarse-grained segment corresponds to approximately five PEO monomers, which is consistent with the large Kuhn length of PEO [114]. Note that while M_w/N is expected to be degenerate with σ, as both quantify the size of the chain, it is expected that this correspondence should remain the same.

The fitted interaction parameters between the ions and the polymer are similarly reasonable. They are intended to reflect the temperature-dependent balance between favorable ion–polymer binding at low temperatures and unfavorable hydrophilic–hydrophobic interactions at higher temperatures. The magnitudes are comparable to those used for systems with similar lower critical solution temperature (LCST) behavior, such as water + PEO mixtures [96, 97]. The condition $A > 0$

and $B < 0$ induces the LCST, as observed in Figure 1.6.



(a) (b)

Figure 1.8: Electrostatic (red), χ (yellow) and ideal (green) contributions to the free energy of mixing (blue) for PEO-20+[EMIM][BF_4] at 90°C (left) and 170°C (right). Parameters match those obtained from the PEO-20 fitting given in table 1.1.

Crucially, the inclusion of electrostatic interactions is necessary to capture the observed shift in critical concentration. Without them, the coexistence curve would be skewed toward polymer-dilute compositions. This arises from the inherent skew in the electrostatic contribution compensating for the skew present in the entropy of mixing, shown visually in Figure 1.8. The fitted dielectric constant falls between the known values for PEO (5-10)[113] and for common ionic liquids (5-20)[115], lending further physical credibility to the model. Note that this value is expected to depend on the specific polymer–ionic liquid mixture. We also assume the dielectric constant is independent of temperature, although it is known to generally decrease with increasing temperature. Therefore, we interpret this value as an effective average over the temperature range considered. We note that, in our previous work[90], the inclusion of this dielectric decrement by itself can induce LCST behavior in aqueous polyelectrolytes. In polymer+IL systems, even if the decrement in relative static permittivity with increasing temperature had been captured explicitly, due to the already low value in the dielectric constant, this would be insufficient to drive such behavior.

An interesting feature in Figure 1.6 is that the critical composition shifts toward polymer-dilute regions with increasing chain length. Experimentally, while Lee et al.[65] did not explicitly report the critical point, we note that the experimental coexistence curves near criticality are relatively flat, making the precise location of the critical point difficult to extract. Within this model, the trend arises because,

for the two-phase region to close at lower temperatures, the favorable χ interactions must eventually outweigh the electrostatic contributions. Consequently, the critical behavior becomes dominated by the entropy of mixing, which naturally drives the critical point toward the polymer-dilute limit as chain length increases. However, if the dielectric decrement with temperature is sufficiently strong so as to lead to an LCST driven by electrostatic correlations alone, then based on the limited shift in critical composition in Fig 1.4a, we would observe minimal shifts in critical composition as the chain length increases.

Overall, the results presented in Figure 1.6 and Figure 1.7 demonstrate that even a system as complex as polymer + ionic liquid systems, involving a convolution of electrostatic and clustering interactions, can be accurately and transparently modeled using a minimal set of physically motivated parameters.

1.6 Conclusion

In this chapter, we have developed a physically motivated framework for modeling the phase behavior of polymer–ionic liquid mixtures, with particular emphasis on understanding the role of clustering, polymer–cation binding, and electrostatic correlations. Starting from Flory–Huggins theory, we incorporated key non-ideal effects through excess contribution to the mixing free energy expression. Through systematic analysis of each contribution, we clarified the distinct and competing roles they play in determining the phase behavior.

Our results demonstrate that although clustering leads to phase separation which skews slightly towards the polymer-rich compositions, it cannot by itself account for the experimentally observed lower critical solution temperature (LCST) behavior in systems. Conversely, explicit modeling of cation–polymer binding, combined with an unfavorable entropic Flory–Huggins interaction, can capture the LCST behavior and yields critical scaling consistent with Flory–Huggins predictions. However, this effect alone does not reproduce the shape of the coexistence curve with increasing molecular weight observed experimentally in polymer–ionic liquid systems.

Importantly, we find that electrostatic interactions, often neglected in prior treatments, have a profound and persistent influence on the phase behavior. The MSA treatment captures not only the many-body, long-range nature of electrostatic interactions but also implicitly reflects the tendency of ions to form clusters, eliminating the need for a separate clustering term. The inclusion of this contribution leads to a complete transposition of the critical concentration towards the polymer-rich com-

positions, something that cannot be explained using a simple Flory–Huggins-type theory. Interestingly, the critical concentration now approaches a finite value close to $\phi = 1$, in contrast to the typical result from Flory–Huggins theory. The change in the critical temperature and concentration (from the infinite chain-length limit) both scale as N^{-1}, as opposed to the $N^{-1/2}$ scaling from the Flory–Huggins theory.

Finally, we propose a minimal model that combines only three ingredients (mixing entropy, temperature-dependent χ interactions, and electrostatics) yet reproduces key features of experimental phase behavior using a minimal set of physically interpretable parameters. This model highlights how a carefully constrained theoretical framework can yield quantitative predictions while avoiding the pitfalls of overfitting and parameter degeneracy. Good agreement with experimental data on several polymer–ionic liquid mixtures demonstrates the broad applicability of this model.

Together, these findings offer a unified and extensible framework for the thermodynamic modeling of polymer–ionic liquid systems, with implications for both fundamental understanding and materials. A brief example of this is shown in the appendix for a chemically-different system, polyelectrolyte coacervates, where the same physical model can be used to illustrate the origins of another anomalous phenomena.

1.7 Appendix

Guest Polymer Selectivity in Complex Coacervates

This section contains work currently in preparation: Zongpei Wu, Júlia Bonesso-Sabadini, Pierre J. Walker, Watson Loh, Zhen-Gang Wang, Sarah L. Perry, and Shensheng Chen. “Origin of the Anomalous Guest Polymer Selectivity in Complex Coacervates”. In: *Submitted* (2026)

Complex coacervates are charge-rich liquid phases formed through the association of oppositely charged macromolecules. Their ability to selectively concentrate proteins, nucleic acids, and synthetic polymers is central to their biological function and to proposed applications in artificial cells, therapeutic delivery, and nanoreactors [116, 117, 118]. However, guest uptake is often strongly dependent on molecular size, charge density, and charge sequence. For example, coacervates may absorb small neutral solutes while excluding chemically similar neutral polymers [119, 120, 121]. Charged guests likewise exhibit selectivity that cannot be explained solely by macroscopic charge compensation: proteins containing localized charge patches can partition more strongly than proteins with comparable net charge but more

disordered charge distributions [122, 123]. These observations suggest that guest partitioning is governed by how the guest perturbs the electrostatic correlations that stabilize the host coacervate.

Here, we apply the theory developed earlier in this chapter for polymer–ionic-liquid mixtures to describe guest polymers in complex coacervates. Only minor modifications are required because the theory is already formulated for arbitrary multicomponent mixtures. For an incompressible mixture of equal-sized segments, the free energy is written as

$$\Delta f_{\mathrm{mix}} = \Delta f_{\mathrm{FH}} + \Delta f_{\mathrm{el.}} + \Delta f_{\mathrm{ch.}}, \tag{1.64}$$

where Δf_{FH} is the Flory–Huggins free energy mixing, $\Delta f_{\mathrm{el.}}$ is the electrostatic correlation contribution obtained from the mean-spherical approximation [82, 98], and Δf_{ch} is the free-energy contribution associated with connecting charged beads into chains [124]. This latter term is the only new contribution required. More details given in Sections 2.2 and 3.2.

In our treatment, it is assumed the coacervate host is made up of oppositely charged polyelectrolyte ($N_h = 50$), guests of varying composition and the remainder being comprised of monomeric, neutral solvent. All χ interactions have been set to zero to isolate the effects of electrostatic interactions. Neutral guests are represented by chains of uncharged beads. For partially charged polyelectrolytes, a fraction f of the guest beads is assigned a charge and the corresponding neutralizing counterions are included explicitly. For polyampholytes or intrinsically disordered proteins (IDPs), the bead charges are assigned according to the prescribed sequence, so that the chain contribution distinguishes between like-charged and oppositely charged neighboring segments. The electrostatic free-energy expression itself is unchanged. Thus, the differences between the guest classes enter through the species composition, the required counterions, and the statistics of the bonded charge pairs rather than through the introduction of an additional phenomenological interaction parameter.

Global phase equilibria are obtained by enforcing equality of the chemical potentials and pressure between all coexisting phases [20] as described in section 1.3. Figure 1.9 shows representative phase diagrams in terms of the total host and guest volume fractions, ϕ_h and ϕ_g. The dashed gray path corresponds to replacing solvent with guest at fixed host content, as in the accompanying simulations. An intersection of this path with the two-phase region therefore indicates that the guest is expelled from the host-rich coacervate.

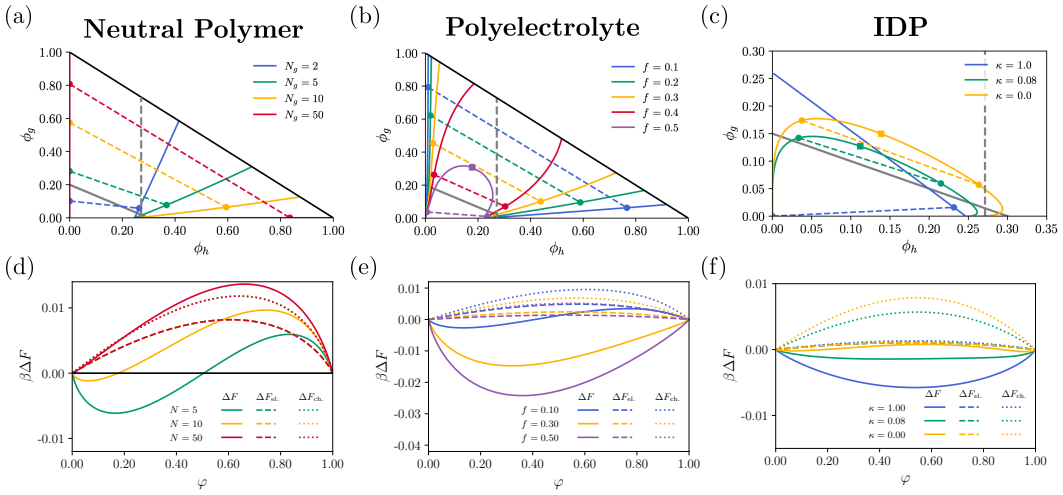


Figure 1.9: The physical origin of the exclusion of guest polymers and its consequence on the guest encapsulation efficiency. (a) to (c), Phase diagrams of the host (ϕ_h, $N_h = 50$) + guest (ϕ_g, $N_g = 50$, unless indicated otherwise) for each guest considered in this work. Areas enclosed by the solid colored lines represent the two-phase regions where, if the composition of our systems enters this region, a phase split is expected to occur where the composition of the coexisting phases lies on a tie line (examples given by the colored dashed lines). The dashed gray lines represent the process of substituting solvent with guest species, as done in our earlier work. If this line enters the two-phase region, the guest is expelled from the coacervate phase. The solid gray line represents the specific tie line over which the mixing free energies in figures (d), (e), and (f) are obtained. Not included for simplicity is the three-phase region present in (b), which occurs at low ϕ_g. (d) to (f), Free energies of mixing, and their respective electrostatic and chain contributions, obtained when traversing the phase diagrams along the solid gray line, where φ denotes the path along the tie line, for each guest considered. Conditions correspond exactly to those used in figures (a) to (c).

For neutral guests, increasing chain length widens the two-phase region; when $N_g = 50$, nearly the entire diagram lies within the two-phase domain, as shown in Figure 1.9(a). Along the gray path, the point at which phase separation occurs shifts to progressively smaller guest fractions as N_g increases. This aligns with simulation results[125]: for $N_g = 10$, $\phi_g = 0.01$ remains in the one-phase region, whereas for $N_g = 50$ the system expels almost all guests, as indicated by the red tie line linking a guest-free coacervate to a host-free supernatant.

To identify the driving forces, we compute the free-energy change along an arbitrary path (black line in Figure 1.9(a)) between a guest-free coacervate ($\varphi = 0$) and a coacervate-free mixture ($\varphi = 1$). Note that, even if a tangent line can be drawn along this projection, the compositions along this path do not necessarily correspond

to the true, globally optimal phases. While we could have chosen a path that connects coexisting phases, doing so in a fair comparison between all systems is unfeasible. Further, this approach allows us to decompose the free energy (Figure 1.9(d)) into the electrostatic correlation contribution ΔF_{el} and the chain-formation contribution ΔF_{ch}, where both are strongly unfavorable as N_g increases. Introducing neutral guest dilutes the charge concentration, thereby weakening electrostatic attractions, an energetically costly effect which favors demixing, as discussed in section 1.2. Moreover, chain formation among like charges is more extended relative to a neutral chain due to electrostatic repulsions. Such conformations are entropically favorable and diluting the charged environment reduces this effect and produces an unfavorable contribution to ΔF.

Both mechanisms are insensitive to the guest's chain length and thus behave analogously to the "enthalpic" term in a Flory–Huggins description, but with the crucial distinction that electrostatic interactions are inherently many-body and cannot be captured by a single χ-parameter [103, 104, 107], as discussed earlier. These contributions compete with the entropy of mixing, which decreases with increasing chain length of either component. Consequently, once both host or guest chain length exceeds a certain chain length (N_g, $N_h > 50$), the mixing entropy becomes too small to offset the unfavorable electrostatic correlation and chain formation contributions, and neutral guests are universally expelled.

When the guest carries a small charge fraction f, the phase behavior changes qualitatively (Figure 1.9(b)). Introducing a weak polyelectrolyte necessarily introduces counterions as well; ϕ_g therefore represents the combined volume fraction of the guest beads and their neutralizing counterions. As f increases, the two-phase region shrinks, and for $f = 0.50$ the gray path no longer intersects the two-phase domain, consistent with simulations, where higher-charge-density guests readily mix with the coacervate.

The free-energy decomposition along the black path in Figure 1.9(b) (plotted in Figure 1.9(e)) confirms that both $\Delta F_{\text{el.}}$ and $\Delta F_{\text{ch.}}$ are reduced relative to the neutral case. This is because the guest now introduces some charge, reducing the dilution of the electrostatic interactions. Moreover, the accompanying counterions contribute strongly to the entropy of mixing, further incentivizing mixing. Together, these effects suppress the exclusion of the charged guest observed for neutral guests.

The behavior of intrinsically disordered proteins (IDPs) is more nuanced. The two-phase region is much smaller overall, requiring a zoomed-in axis in Figure 1.9(c).

More ordered sequences ($\kappa = 1.0$) can even self-coacervate in the absence of host polymer ($\phi_h = 0$). Because these IDPs gain electrostatic cohesion from contacts within their own chains, they mix favorably with the host coacervate, as reflected by the positive-slope tie lines. Only when the sequence becomes sufficiently disordered does the two-phase region begin to expand, and the tie lines invert to indicate expulsion rather than mixing. The more disordered sequences ($\kappa = 0.08$ and 0.00) exhibit a re-entrant-like behavior: the two-phase region grows at low guest fractions but closes again at larger ones. The gray path intersects the two-phase domain only when the sequence is fully disordered ($\kappa = 0.00$), consistent with the simulation results.

The free energy change contributions in Figure 1.9(f) show that, unlike the previous two cases, the electrostatic contribution ΔF_{el} is nearly negligible across all IDP sequences. Because the guest introduces fully charged species (even though the net charge is zero), the overall charge density is not diluted, and electrostatic correlations remain largely unchanged. Exclusion of the guest is therefore driven almost entirely by the chain-formation term ΔF_{ch}.

IDPs differ from standard polyelectrolytes because they form both like-charged and oppositely-charged neighboring pairs. Unlike polyelectrolytes, which only contain like-charged neighbors, IDPs experience favorable local electrostatic attractions that promote locally collapsed conformations, reducing chain entropy. More disordered sequences (smaller κ) contain more such unlike-charge contacts and therefore incur a larger entropic penalty upon forming chains. This penalty is only sufficient to drive phase separation when the sequence is highly disordered, and even then the driving force is weak; a slight increase in charge concentration would increase screening and eliminate the effect, restoring a single-phase system. This explains the re-entrant behavior observed in Figure 1.9(c). Note that the approach used only considers pair-wise interactions. As such, we do not account for any long-range, intramolecular interactions within IDPs. Such effects are considered in more detail within Chapter 3.

Thus, using a very similar theoretical approach, we identify a common physical origin for the selectivity of neutral, charged, and sequence-defined guests: guest incorporation perturbs the long-range, many-body electrostatic and conformational correlations of the host coacervate. The particular free-energy contribution responsible for exclusion depends on the guest architecture, but no change to the underlying theory is required, demonstrating the generalizability of such coarse grained models.

References

[4] Seola Lee et al. “Molecular control via dynamic bonding enables material responsiveness in additively manufactured metallo-polyelectrolytes”. In: *Nat. Commun.* 15.1 (Aug. 2024), p. 6850. ISSN: 2041-1723. DOI: 10.1038/s41467-024-50860-6.

[5] Zongpei Wu et al. “Origin of the Anomalous Guest Polymer Selectivity in Complex Coacervates”. In: *Submitted* (2026).

[17] Pierre J. Walker, Simon Mueller, and Irina Smirnova. “Confidence-Interval and Uncertainty-Propagation Analysis of SAFT-type Equations of State”. In: *J. Chem. Eng. Data* 69.2 (Aug. 2023), pp. 495–508. ISSN: 0021-9568. DOI: 10.1021/acs.jced.3c00413.

[20] Pierre J. Walker, Hon-Wa Yew, and Andrés Riedemann. “Clapeyron.jl: An Extensible, Open-Source Fluid Thermodynamics Toolkit”. In: *Ind. Eng. Chem. Res.* 61.20 (May 2022), pp. 7130–7153. ISSN: 0888-5885, 1520-5045. DOI: 10.1021/acs.iecr.2c00326.

[29] P. Debye and E. Hückel. “Zur Theorie der Elektrolyte. I. Gefrierpunktserniedrigung und verwandte Erscheinungen”. In: *Phys. Z.* 24 (1923), pp. 185–206.

[35] Paul J. Flory. *Principles of Polymer Chemistry*. Cornell University Press, 1953. ISBN: 978-0-8014-0134-3.

[42] Maurice L. Huggins. “Solutions of Long Chain Compounds”. In: *J. Chem. Phys.* 9.5 (May 1941), p. 440. ISSN: 0021-9606. DOI: 10.1063/1.1750930.

[44] J. T. G. Overbeek and M. J. Voorn. “Phase separation in polyelectrolyte solutions. Theory of complex coacervation”. In: *J. Cell. Comp. Physiol.* 49.S1 (1957), pp. 7–26. ISSN: 1553-0809. DOI: 10.1002/jcp.1030490404.

[46] Andrzej Lewandowski and Agnieszka Świderska-Mocek. “Ionic liquids as electrolytes for Li-ion batteries—An overview of electrochemical studies”. In: *J. Power Sources* 194.2 (Dec. 2009), pp. 601–609. ISSN: 0378-7753. DOI: 10.1016/j.jpowsour.2009.06.089.

[47] Kexin Liu et al. “Ionic liquids for high performance lithium metal batteries”. In: *J. Energy Chem.* 59 (Aug. 2021), pp. 320–333. ISSN: 2095-4956. DOI: 10.1016/j.jechem.2020.11.017.

[48] Wenjun Zhou et al. “Recent Advance in Ionic-Liquid-Based Electrolytes for Rechargeable Metal-Ion Batteries”. In: *Adv. Sci.* 8.13 (2021), p. 2004490. ISSN: 2198-3844. DOI: 10.1002/advs.202004490.

[49] Jianmei Lu, Feng Yan, and John Texter. “Advanced applications of ionic liquids in polymer science”. In: *Prog. Polym. Sci.* 34.5 (May 2009), pp. 431–448. ISSN: 0079-6700. DOI: 10.1016/j.progpolymsci.2008.12.001.

[50] Irene Osada et al. “Ionic-Liquid-Based Polymer Electrolytes for Battery Applications”. In: *Angew. Chem., Int. Ed.* 55.2 (2016), pp. 500–513. ISSN: 1521-3773. DOI: 10.1002/anie.201504971.

[51] Sharmin Sultana et al. “Ionic Liquid-Based Gels for Applications in Electrochemical Energy Storage and Conversion Devices: A Review of Recent Progress and Future Prospects”. In: *Gels* 8.1 (Jan. 2022), p. 2. ISSN: 2310-2861. DOI: 10.3390/gels8010002.

[52] Jason E. Bara et al. “Synthesis and Performance of Polymerizable Room-Temperature Ionic Liquids as Gas Separation Membranes”. In: *Ind. Eng. Chem. Res.* 46.16 (Aug. 2007), pp. 5397–5404. ISSN: 0888-5885. DOI: 10.1021/ie0704492.

[53] Yuanyan Gu and Timothy P. Lodge. “Synthesis and Gas Separation Performance of Triblock Copolymer Ion Gels with a Polymerized Ionic Liquid Mid-Block”. In: *Macromolecules* 44.7 (Apr. 2011), pp. 1732–1736. ISSN: 0024-9297. DOI: 10.1021/ma2001838.

[54] Mahinder Ramdin, Theo W. de Loos, and Thijs J.H. Vlugt. “State-of-the-Art of CO $_2$ Capture with Ionic Liquids”. In: *Ind. Eng. Chem. Res.* 51.24 (June 2012), pp. 8149–8177. ISSN: 0888-5885, 1520-5045. DOI: 10.1021/ie3003705.

[55] Shuaifei Zhao et al. “Ionic liquid-based polymer inclusion membranes for metal ions extraction and recovery: Fundamentals, considerations, and prospects”. In: *Chem. Eng. J.* 481 (Feb. 2024), p. 148792. ISSN: 1385-8947. DOI: 10.1016/j.cej.2024.148792.

[56] Takeshi Ueki. “Stimuli-responsive polymers in ionic liquids”. In: *Polym. J.* 46.10 (Oct. 2014), pp. 646–655. ISSN: 1349-0540. DOI: 10.1038/pj.2014.37.

[57] Timothy P. Lodge and Takeshi Ueki. “Mechanically Tunable, Readily Processable Ion Gels by Self-Assembly of Block Copolymers in Ionic Liquids”. In: *Acc. Chem. Res.* 49.10 (Oct. 2016), pp. 2107–2114. ISSN: 0001-4842. DOI: 10.1021/acs.accounts.6b00308.

[58] Matthew D. Bennett and Donald J. Leo. “Ionic liquids as stable solvents for ionic polymer transducers”. In: *Sens. Actuators, A* 115.1 (Sept. 2004), pp. 79–90. ISSN: 0924-4247. DOI: 10.1016/j.sna.2004.03.043.

[59] Abdul Rehman and Xiangqun Zeng. “Interfacial composition, structure, and properties of ionic liquids and conductive polymers for the construction of chemical sensors and biosensors: a perspective”. In: *Curr. Opin. Electrochem.* Electrocatalysis • Sensors and Biosensors 23 (Oct. 2020), pp. 47–56. ISSN: 2451-9103. DOI: 10.1016/j.coelec.2020.03.010.

[60] Ahmet Cetinkaya et al. “The role and the place of ionic liquids in molecularly imprinted polymer-based electrochemical sensors development for sensitive drug assay”. In: *TrAC, Trends Anal. Chem.* 147 (Feb. 2022), p. 116512. ISSN: 0165-9936. DOI: 10.1016/j.trac.2021.116512.

[61] Tong Gao et al. “Polarization of ionic liquid and polymer and its implications for polymerized ionic liquids: An overview towards a new theory and simulation”. In: *J. Polym. Sci.* (Aug. 2021), pol.20210330. ISSN: 2642-4150, 2642-4169. DOI: 10.1002/pol.20210330.

[62] Michael Rubinstein and Ralph H. Colby. *Polymer Physics*. Oxford, New York: Oxford University Press, Aug. 2003. ISBN: 978-0-19-852059-7.

[63] Pavan K. Inguva et al. “Continuum-scale modelling of polymer blends using the Cahn–Hilliard equation: transport and thermodynamics”. In: *Soft Matter* 17.23 (2021), pp. 5645–5665. ISSN: 1744-683X, 1744-6848. DOI: 10.1039/D1SM00272D.

[64] Hau-Nan Lee and Timothy P. Lodge. “Lower Critical Solution Temperature (LCST) Phase Behavior of Poly(ethylene oxide) in Ionic Liquids”. In: *J. Phys. Chem. Lett.* 1.13 (July 2010), pp. 1962–1966. ISSN: 1948-7185, 1948-7185. DOI: 10.1021/jz100617t.

[65] Hau-Nan Lee et al. “Unusual Lower Critical Solution Temperature Phase Behavior of Poly(ethylene oxide) in Ionic Liquids”. In: *Macromolecules* 45.8 (Apr. 2012), pp. 3627–3633. ISSN: 0024-9297, 1520-5835. DOI: 10.1021/ma300335p.

[66] Zhilin Xiao et al. “Unusual phase separation and rheological behavior of poly(ethylene oxide)/ionic liquid mixtures with specific interactions”. In: *Soft Matter* 12.36 (Sept. 2016), pp. 7613–7623. ISSN: 1744-6848. DOI: 10.1039/C6SM01220E.

[67] Mika Kobayashi and Hajime Tanaka. “The reversibility and first-order nature of liquid–liquid transition in a molecular liquid”. In: *Nat. Commun.* 7.1 (Dec. 2016), p. 13438. ISSN: 2041-1723. DOI: 10.1038/ncomms13438.

[68] Huan Luo et al. “Phase separation kinetics and rheological behavior of Poly(ethylene oxide)/ionic liquid mixtures with large dynamic asymmetry”. In: *Polymer* 123 (Aug. 2017), pp. 290–300. ISSN: 0032-3861. DOI: 10.1016/j.polymer.2017.07.023.

[69] Caitlin L. Bentley et al. “Modes of Interaction in Binary Blends of Hydrophobic Polyethers and Imidazolium Bis(trifluoromethylsulfonyl)imide Ionic Liquids”. In: *Macromolecules* 53.15 (Aug. 2020), pp. 6519–6528. ISSN: 0024-9297. DOI: 10.1021/acs.macromol.0c01155.

[70] Aakriti Kharel et al. “Dilute Solution Properties of Poly(benzyl methacrylate) in Ionic Liquids”. In: *Macromolecules* 53.3 (Feb. 2020), pp. 885–894. ISSN: 0024-9297. DOI: 10.1021/acs.macromol.9b02618.

[71] Brian R. Carrick, Claire L. Seitzinger, and Timothy P. Lodge. "Unusual Lower Critical Solution Temperature Phase Behavior of Poly(benzyl methacrylate) in a Pyrrolidinium-Based Ionic Liquid". In: *Molecules* 26.16 (Jan. 2021), p. 4850. ISSN: 1420-3049. DOI: 10.3390/molecules26164850.

[72] Claire L. Seitzinger, Cecilia C. Hall, and Timothy P. Lodge. "Photoreversible Order–Disorder Transitions in Block Copolymer/Ionic Liquid Solutions". In: *Macromolecules* 55.10 (May 2022), pp. 3811–3820. ISSN: 0024-9297. DOI: 10.1021/acs.macromol.2c00397.

[73] Eunsong Choi and Arun Yethiraj. "Entropic Mechanism for the Lower Critical Solution Temperature of Poly(ethylene oxide) in a Room Temperature Ionic Liquid". In: *ACS Macro Lett.* 4.7 (July 2015), pp. 799–803. DOI: 10.1021/acsmacrolett.5b00355.

[74] Hyuntae Jung and Arun Yethiraj. "Phase Behavior of Poly(ethylene oxide) in Room Temperature Ionic Liquids: A Molecular Simulation and Deep Neural Network Study". In: *J. Phys. Chem. B* 124.41 (Oct. 2020), pp. 9230–9238. ISSN: 1520-6106, 1520-5207. DOI: 10.1021/acs.jpcb.0c06510.

[75] Ronald P. White and Jane E. G. Lipson. "Origins of Unusual Phase Behavior in Polymer/Ionic Liquid Solutions". In: *Macromolecules* 46.14 (July 2013), pp. 5714–5723. ISSN: 0024-9297, 1520-5835. DOI: 10.1021/ma400710z.

[76] B. L. Bhargava and Michael L. Klein. "Aqueous solutions of imidazolium ionic liquids: molecular dynamics studies". In: *Soft Matter* 5.18 (Sept. 2009), pp. 3475–3480. ISSN: 1744-6848. DOI: 10.1039/B908046E.

[77] Shimou Chen et al. "Ionic liquid clusters: structure, formation mechanism, and effect on the behavior of ionic liquids". In: *Phys. Chem. Chem. Phys.* 16 (Mar. 2014), pp. 5893–5906. DOI: 10.1039/C3CP53116C.

[78] Jesse G. McDaniel and Chang Yun Son. "Ion Correlation and Collective Dynamics in BMIM/BF_4-Based Organic Electrolytes: From Dilute Solutions to the Ionic Liquid Limit". In: *J. Phys. Chem. B* 122.28 (July 2018), pp. 7154–7169. ISSN: 1520-6106, 1520-5207. DOI: 10.1021/acs.jpcb.8b04886.

[79] Xiaoyan Ji, Christoph Held, and Gabriele Sadowski. "Modeling imidazolium-based ionic liquids with ePC-SAFT". In: *Fluid Phase Equilib.* 335 (Dec. 2012), pp. 64–73. ISSN: 03783812. DOI: 10.1016/j.fluid.2012.05.029.

[80] Yichun Dong et al. "SAFT-γ Mie model for ionic liquids". In: *AIChE J.* 68.6 (Apr. 2022), e17697. ISSN: 0001-1541, 1547-5905. DOI: 10.1002/aic.17697.

[81] Issei Nakamura. "Effects of Dielectric Inhomogeneity and Electrostatic Correlation on the Solvation Energy of Ions in Liquids". In: *J. Phys. Chem. B* 122.22 (June 2018), pp. 6064–6071. ISSN: 1520-6106. DOI: 10.1021/acs.jpcb.8b01465.

[82] L. Blum. "Mean spherical model for asymmetric electrolytes". In: *Mol. Phys.* 30.5 (Nov. 1975), pp. 1529–1535. ISSN: 0026-8976. DOI: 10.1080/00268977500103051.

[83] Jean-Pierre Hansen and I. R. McDonald. *Theory of Simple Liquids*. Amsterdam Boston: Academic Press, 2007. ISBN: 978-0-12-370535-8.

[84] Charles E. Sing, Jos W. Zwanikken, and Monica Olvera de la Cruz. "Ion Correlation-Induced Phase Separation in Polyelectrolyte Blends". In: *ACS Macro Lett.* 2.11 (Nov. 2013), pp. 1042–1046. DOI: 10.1021/mz400511r.

[85] Charles E. Sing, Jos W. Zwanikken, and Monica Olvera de la Cruz. "Electrostatic control of block copolymer morphology". In: *Nat. Mater.* 13.7 (July 2014), pp. 694–698. ISSN: 1476-4660. DOI: 10.1038/nmat4001.

[86] Jianwen Jiang et al. "A molecular-thermodynamic model for polyelectrolyte solutions". In: *J. Chem. Phys.* 108.2 (Jan. 1998), pp. 780–784. ISSN: 0021-9606. DOI: 10.1063/1.475438.

[87] Tao Jiang and Jianzhong Wu. "Ionic Effects in Collapse of Polyelectrolyte Brushes". In: *J. Phys. Chem. B* 112.26 (July 2008), pp. 7713–7720. ISSN: 1520-6106. DOI: 10.1021/jp801911a.

[88] Pengfei Zhang et al. "Salting-Out and Salting-In of Polyelectrolyte Solutions: A Liquid-State Theory Study". In: *Macromolecules* 49.24 (Dec. 2016), pp. 9720–9730. ISSN: 0024-9297, 1520-5835. DOI: 10.1021/acs.macromol.6b02160.

[89] Paul J. Flory. "Thermodynamics of Dilute Solutions of High Polymers". en. In: *J. Chem. Phys.* 13.11 (Nov. 1945), pp. 453–465. ISSN: 0021-9606, 1089-7690. DOI: 10.1063/1.1723978.

[90] Andrew S. Ylitalo et al. "Electrostatic Correlations and Temperature-Dependent Dielectric Constant Can Model LCST in Polyelectrolyte Complex Coacervation". In: *Macromolecules* 54.24 (Dec. 2021), pp. 11326–11337. ISSN: 0024-9297, 1520-5835. DOI: 10.1021/acs.macromol.1c02000.

[91] Michael McEldrew et al. "Theory of ion aggregation and gelation in superconcentrated electrolytes". In: *J. Chem. Phys.* 152.23 (June 2020), p. 234506. ISSN: 0021-9606, 1089-7690. DOI: 10.1063/5.0006197.

[92] Michael McEldrew et al. "Ion Clusters and Networks in Water-in-Salt Electrolytes". In: *J. Electrochem. Soc.* 168.5 (May 2021), p. 050514. ISSN: 0013-4651, 1945-7111. DOI: 10.1149/1945-7111/abf975.

[93] Alexander N. Semenov and Michael Rubinstein. "Thermoreversible Gelation in Solutions of Associative Polymers. 1. Statics". In: *Macromolecules* 31.4 (Feb. 1998), pp. 1373–1385. ISSN: 0024-9297, 1520-5835. DOI: 10.1021/ma970616h.

[94] Walter H. Stockmayer. "Molecular distribution in condensation polymers". In: *J. Polym. Sci.* 9.1 (1952), pp. 69–71. ISSN: 1542-6238. DOI: 10.1002/pol.1952.120090106.

[95] Christopher W. Macosko and Douglas R. Miller. "A New Derivation of Average Molecular Weights of Nonlinear Polymers". In: *Macromolecules* 9.2 (Mar. 1976), pp. 199–206. ISSN: 0024-9297. DOI: 10.1021/ma60050a003.

[96] Stefan Bekiranov, Robijn Bruinsma, and Philip Pincus. "Solution behavior of polyethylene oxide in water as a function of temperature and pressure". In: *Phys. Rev. E* 55.1 (Jan. 1997), pp. 577–585. DOI: 10.1103/PhysRevE.55.577.

[97] Piotr Knychała et al. "*50th Anniversary Perspective* : Phase Behavior of Polymer Solutions and Blends". In: *Macromolecules* 50.8 (Apr. 2017), pp. 3051–3065. ISSN: 0024-9297, 1520-5835. DOI: 10.1021/acs.macromol.6b02619.

[98] L. Blum and J. S. Hoeye. "Mean spherical model for asymmetric electrolytes. 2. Thermodynamic properties and the pair correlation function". In: *J. Phys. Chem.* 81.13 (June 1977), pp. 1311–1316. ISSN: 0022-3654, 1541-5740. DOI: 10.1021/j100528a019.

[99] Bjørn Maribo-Mogensen, Georgios M. Kontogeorgis, and Kaj Thomsen. "Comparison of the Debye–Hückel and the Mean Spherical Approximation Theories for Electrolyte Solutions". In: *Ind. Eng. Chem. Res.* 51.14 (Apr. 2012), pp. 5353–5363. ISSN: 0888-5885. DOI: 10.1021/ie2029943.

[100] Pierre J. Walker, Xiaodong Liang, and Georgios M. Kontogeorgis. "Importance of the Relative Static Permittivity in electrolyte SAFT-VR Mie Equations of State". In: *Fluid Phase Equilib.* 551 (Jan. 2022), p. 113256. ISSN: 03783812. DOI: 10.1016/j.fluid.2021.113256.

[101] Gabriel M. Silva, Xiaodong Liang, and Georgios M. Kontogeorgis. "How to account for the concentration dependency of relative permittivity in the Debye–Hückel and Born equations". In: *Fluid Phase Equilib.* 566 (Mar. 2023), p. 113671. ISSN: 0378-3812. DOI: 10.1016/j.fluid.2022.113671.

[102] Jarrett Revels, Miles Lubin, and Theodore Papamarkou. *Forward-Mode Automatic Differentiation in Julia*. July 2016.

[103] Michael E. Fisher and Yan Levin. "Criticality in ionic fluids: Debye-Hückel theory, Bjerrum, and beyond". In: *Phys. Rev. Lett.* 71.23 (Dec. 1993), pp. 3826–3829. ISSN: 0031-9007. DOI: 10.1103/PhysRevLett.71.3826.

[104] Erik Luijten, Michael E. Fisher, and Athanassios Z. Panagiotopoulos. "Universality Class of Criticality in the Restricted Primitive Model Electrolyte". In: *Phys. Rev. Lett.* 88.18 (Apr. 2002), p. 185701. ISSN: 0031-9007, 1079-7114. DOI: 10.1103/PhysRevLett.88.185701.

[105] M. Muthukumar. “Phase Diagram of Polyelectrolyte Solutions: Weak Polymer Effect”. In: *Macromolecules* 35.24 (Nov. 2002), pp. 9142–9145. ISSN: 0024-9297. DOI: 10.1021/ma021456z.

[106] A. V. Ermoshkin and M. Olvera de la Cruz. “A Modified Random Phase Approximation of Polyelectrolyte Solutions”. In: *Macromolecules* 36.20 (Oct. 2003), pp. 7824–7832. ISSN: 0024-9297. DOI: 10.1021/ma034148p.

[107] G. Orkoulas, Sanat K. Kumar, and Athanassios Z. Panagiotopoulos. “Monte Carlo Study of Coulombic Criticality in Polyelectrolytes”. In: *Phys. Rev. Lett.* 90.4 (Jan. 2003), p. 048303. DOI: 10.1103/PhysRevLett.90.048303.

[108] H. Krienke and J. Barthel. “Association concepts in electrolyte solutions”. In: *J. Mol. Liq.* 78.1-2 (Aug. 1998), pp. 123–138. ISSN: 01677322. DOI: 10.1016/S0167-7322(98)00087-7.

[109] Gabriel M. Silva, Xiaodong Liang, and Georgios M. Kontogeorgis. “Ion–ion association is lost by linearizing the Poisson–Boltzmann equation when deriving the Debye–Hückel equation”. In: *J. Chem. Phys.* 160.3 (Jan. 2024), p. 034506. ISSN: 0021-9606. DOI: 10.1063/5.0184269.

[110] L. Blum and O. Bernard. “The general solution of the binding mean spherical approximation for pairing ions”. In: *J. Stat. Phys.* 79.3 (May 1995), pp. 569–583. ISSN: 1572-9613. DOI: 10.1007/BF02184871.

[111] O. Bernard and L. Blum. “Binding mean spherical approximation for pairing ions: An exponential approximation and thermodynamics”. In: *J. Chem. Phys.* 104.12 (Mar. 1996), pp. 4746–4754. ISSN: 0021-9606. DOI: 10.1063/1.471168.

[112] Freeman Dyson. “A meeting with Enrico Fermi”. In: *Nature* 427.6972 (Jan. 2004), pp. 297–297. ISSN: 1476-4687. DOI: 10.1038/427297a.

[113] R. J. Sengwa, Kulvinder Kaur, and Rakhee Chaudhary. “Dielectric properties of low molecular weight poly(ethylene glycol)s”. In: *Polym. Int.* 49 (2000), pp. 599–608. ISSN: 1097-0126.

[114] Ralf Everaers et al. “Kremer–Grest Models for Commodity Polymer Melts: Linking Theory, Experiment, and Simulation at the Kuhn Scale”. In: *Macromolecules* 53.6 (Mar. 2020), pp. 1901–1916. ISSN: 0024-9297, 1520-5835. DOI: 10.1021/acs.macromol.9b02428.

[115] Tejwant Singh and Arvind Kumar. “Static Dielectric Constant of Room Temperature Ionic Liquids: Internal Pressure and Cohesive Energy Density Approach”. In: *J. Phys. Chem. B* 112.41 (Oct. 2008), pp. 12968–12972. ISSN: 1520-6106. DOI: 10.1021/jp8059618.

[116] Charles E. Sing and Sarah L. Perry. “Recent progress in the science of complex coacervation”. In: *Soft Matter* 16.12 (Mar. 2020), pp. 2885–2914. ISSN: 1744-6848. DOI: 10.1039/D0SM00001A.

[117] Artem M. Rumyantsev, Nicholas E. Jackson, and Juan J. de Pablo. "Polyelectrolyte Complex Coacervates: Recent Developments and New Frontiers". en. In: *Annu. Rev. Condens. Matter Phys.* 12.Volume 12, 2021 (Mar. 2021), pp. 155–176. ISSN: 1947-5454, 1947-5462. DOI: 10.1146/annurev-conmatphys-042020-113457.

[118] Alexander B. Cook, Sebastian Novosedlik, and Jan C. M. van Hest. "Complex Coacervate Materials as Artificial Cells". In: *Acc. Mater. Res.* 4.3 (Feb. 2023), pp. 287–298. ISSN: 2643-6728. DOI: 10.1021/accountsmr.2c00239.

[119] A. M. Marianelli, B. M. Miller, and C. D. Keating. "Impact of macromolecular crowding on RNA/spermine complex coacervation and oligonucleotide compartmentalization". In: *Soft Matter* 14.3 (Jan. 2018), pp. 368–378. ISSN: 1744-683X. DOI: 10.1039/c7sm02146a.

[120] Shanta Biswas et al. "Understanding the Impacts of Molecular and Macromolecular Crowding Agents on Protein–Polymer Complex Coacervates". In: *Biomacromolecules* 24.11 (Oct. 2023), pp. 4771–4782. ISSN: 1525-7797. DOI: 10.1021/acs.biomac.3c00545.

[121] Nicolette G. Moreau et al. "Spontaneous membrane-less multi-compartmentalization via aqueous two-phase separation in complex coacervate micro-droplets". In: *Chem. Commun.* 56.84 (Oct. 2020), pp. 12717–12720. ISSN: 1359-7345. DOI: 10.1039/d0cc05399f.

[122] Allie C. Obermeyer et al. "Complex coacervation of supercharged proteins with polyelectrolytes". In: *Soft Matter* 12.15 (Apr. 2016), pp. 3570–3581. ISSN: 1744-6848. DOI: 10.1039/C6SM00002A.

[123] Whitney C. Blocher McTigue and Sarah L. Perry. "Design rules for encapsulating proteins into complex coacervates". In: *Soft Matter* 15.15 (Apr. 2019), pp. 3089–3103. ISSN: 1744-683X. DOI: 10.1039/c9sm00372j.

[124] J. W. Jiang et al. "Thermodynamic properties and phase equilibria of charged hard sphere chain model for polyelectrolyte solutions". In: *Mol. Phys.* 99.13 (July 2001), pp. 1121–1128. ISSN: 0026-8976. DOI: 10.1080/00268970110043414.

[125] Zongpei Wu and Shensheng Chen. *Electrostatic Depletion Force in Complex Coacervates*. arXiv:2508.01328 [cond-mat.soft]. Aug. 2025. DOI: 10.48550/arXiv.2508.01328.

Chapter 2

EXPLICIT SOLVENTS REVERSE ELECTROSTATIC PHASE BEHAVIOR IN CHARGED FLUIDS

Coacervation in charged polymer solutions underlies the formation of many functional materials and biological condensates. Most existing theories treat the solvent implicitly as a homogeneous dielectric continuum with a prescribed dielectric constant, thereby neglecting both the coupling between ionic and dipolar degrees of freedom and differences in dielectric response between coexisting phases. In this chapter, we combine molecular dynamics simulations with an explicit-solvent liquid-state theory that incorporates the orientational polarization of dipolar solvent molecules directly into the thermodynamics of electrolyte and polyelectrolyte solutions. The dielectric response is determined self-consistently from the temperature and local composition, allowing the coacervate and supernatant to develop distinct dielectric constants and Bjerrum lengths. At finite charge concentrations, many-body ion–dipole correlations suppress local dipolar screening and reverse the temperature dependence of effective electrostatic interactions. This collective effect, which is inaccessible to pairwise implicit-solvent descriptions, produces upper-critical-solution-temperature behavior in direct contrast to the lower-critical-solution-temperature behavior predicted by conventional implicit-solvent electrostatic theories. When applied to complex coacervation with added salt, the theory further predicts an experimentally observed inversion of salt partitioning arising from competition among dielectric-mediated electrostatic stabilization, electrostatic screening, and mobile-ion mixing entropy. These results identify solvent polarization as an active thermodynamic degree of freedom and demonstrate that phase-dependent dielectric environments can fundamentally control phase separation and ion partitioning in charged polymer solutions.

This chapter includes work currently in preparation: Pierre J. Walker and Zhen-Gang Wang. "Explicit Solvents Reverse Electrostatic Phase Behavior in Charged Fluids". In: *In preparation* (2026)

Pierre J. Walker, Tianyi Jin, Alejandro Gallegos, and Zhen-Gang Wang. "Dielectric Inhomogeneity Governs Phase Behavior and Salt Partitioning in Complex Coacervates". In: *In preparation* (2026)

2.1 Introduction

As shown in Chapter 1, treating electrostatic correlations explicitly already captures phase behavior that pairwise, Flory–Huggins-type theories miss; the present chapter asks how the remaining implicit-solvent approximation used there may change the resulting phase behavior.

Much of our understanding of electrolyte and polyelectrolyte solutions is based on the use of implicit solvent models, in which the solvent is represented as a dielectric continuum, with polarization and dipolar degrees of freedom subsumed into a single parameter, the dielectric constant, which rescales Coulomb interactions as[1]

$$\beta\phi_{\mathrm{el}}(r) = \frac{q_i q_j}{4\pi\epsilon_0\epsilon_{\mathrm{r}} k_{\mathrm{B}} T r} = Z_i Z_j \frac{l_{\mathrm{B}}}{r}, \tag{2.1}$$

where q_i and q_j are the particle charges, Z_i and Z_j their valencies, and $l_{\mathrm{B}} = e^2/(4\pi\epsilon_0\epsilon_{\mathrm{r}} k_{\mathrm{B}} T)$ is the Bjerrum length, a measure of the strength of electrostatic interaction relative to thermal energy.

The dielectric-continuum framework played a central role in the classical theories of Gouy–Chapman [126, 127], Debye–Hückel [29], Wagner [128], and Onsager [30, 31]. These developments established many of the foundational concepts in the physics of ionic solutions, including electrostatic screening, ionic correlations, and the structure of the electrical double layer. Subsequent treatments incorporated the finite hard-core size of ions, leading to the primitive model, whose analysis remains a central component of liquid-state theory and underpins a large fraction of modern computer simulations of electrolyte systems.

The same implicit-solvent description forms the basis of most contemporary theories of polyelectrolyte phase separation. Of particular interest is complex coacervation, a liquid–liquid phase-separation process in which a solution containing charged macromolecules separates into a dense, polymer-rich coacervate and a dilute, polymer-poor supernatant. Coacervation plays an important role in materials science [116] and is increasingly recognized as a driving force for the formation of biomolecular condensates and membraneless organelles, which provide spatial organization for numerous cellular processes.

Theoretical approaches have been instrumental in identifying the molecular mechanisms governing coacervation and establishing general design principles for charged

[1] The first instance of this formulation is believed to appear in Maxwell's "A Treatise on Electricity and Magnetism".

macromolecular systems [44, 36]. Modern theories describe the competition among electrostatic correlations, chain connectivity, excluded-volume interactions, and the translational entropy of polymers and mobile ions [88, 129, 130, 106, 131, 105, 132, 133, 124, 134, 12, 135]. These frameworks have subsequently been extended to describe the effects of charge asymmetry [136, 137], counterion valency [4, 131], salt partitioning [138, 139], charge regulation [140, 141, 142, 143], and polymer charge sequence [144, 145, 130].

Despite their considerable success, most of these theories assume that the solvent can be represented as a spatially homogeneous dielectric medium with a prescribed dielectric constant. The consequence of this is better understood by examining the effect of the temperature-dependence of the dielectric constant on the phase behavior. If the dielectric constant is fixed, increasing the temperature decreases the Bjerrum length and weakens electrostatic interactions. In strongly polar solvents, however, increasing temperature also disrupts dipolar correlations and reduces ϵ_r. This reduction can be sufficiently strong that the Bjerrum length increases with temperature, as illustrated for several common polar solvents in Figure 2.1. Electrostatic interactions may therefore be interpreted as strengthening upon heating, in contrast to most conventional attractive intermolecular interactions.

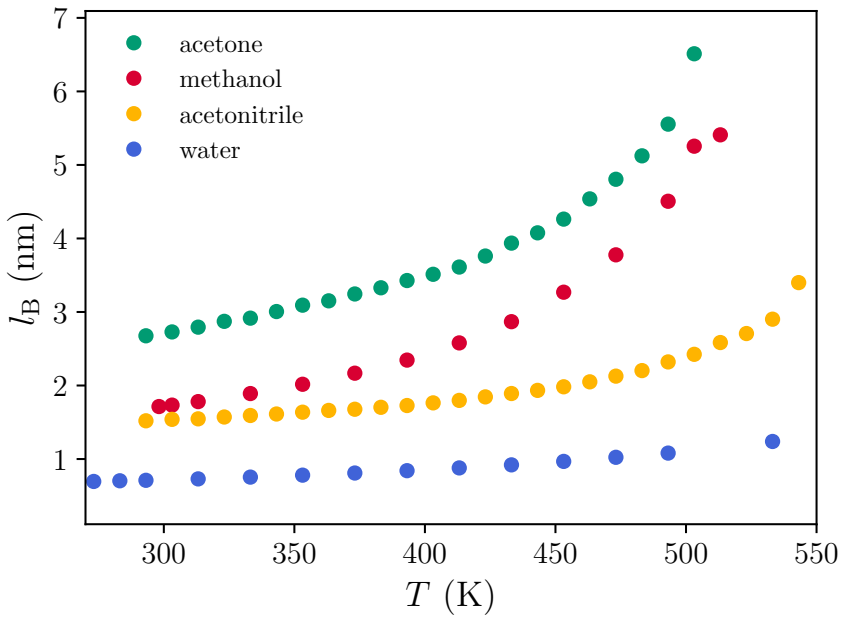


Figure 2.1: Bjerrum length l_B as a function of temperature for water, methanol, acetonitrile, and acetone, calculated from experimental static-permittivity data obtained from the DETHERM databank [146].

Within an implicit-solvent theory employing the dielectric response of the pure solvent, this behavior suggests that electrostatic correlations should promote phase separation at elevated temperatures and therefore produce lower-critical-solution-temperature (LCST) behavior. This mechanism has been invoked to explain experimentally observed LCST behavior in aqueous polyelectrolyte complexation [147, 90]. However, it cannot provide a general account of electrolyte phase behavior. In particular, it is difficult to reconcile with the frequently observed increase in simple-salt solubility with temperature or with the upper-critical-solution-temperature (UCST) behavior reported for several polyelectrolyte systems [148, 149, 150].

The limitation arises because the dielectric constant is not solely a property of the pure solvent and cannot, in general, be prescribed independently of the ionic composition. Ion–dipole interactions partially align and saturate the solvent molecules surrounding an ion, reducing their ability to respond to an external electric field. The resulting decrease in the dielectric constant with ionic concentration is the well-known dielectric decrement [151, 152, 153]. Direct ion–dipole interactions also generate solvent-mediated, effective many-body interactions between ions that cannot be represented by the pairwise Coulomb potential in Eq. 2.1. The solvent therefore does more than passively rescale electrostatic interactions: its polarization is coupled directly to the local charge concentration and contributes to the thermodynamics of the solution.

This coupling becomes particularly important in phase-separated systems. Conventional continuum theories assign the same dielectric constant to the coacervate and supernatant even though the two phases differ substantially in polymer, salt, and solvent composition [154]. In reality, their different charge concentrations should produce distinct solvent-polarization responses and, consequently, distinct dielectric constants and Bjerrum lengths. The electrostatic correlations stabilizing each phase then modify the local composition, which further alters the dielectric response. This feedback between composition, solvent polarization, and electrostatic interactions cannot be captured when ϵ_{r} is treated as a fixed external parameter.

Recent studies have begun to relax this assumption by introducing explicit dipolar solvent molecules or by incorporating the measured temperature dependence of the dielectric constant [155, 147, 156, 157]. Mean-field treatments of dipolar solvents, for example, account explicitly for dipole–dipole and ion–dipole interactions [155, 147], whereas other approaches prescribe $\epsilon_{\mathrm{r}}(T)$ using empirical correlations for bulk

water [158]. The latter introduces an additional temperature-dependent contribution to electrostatic interactions that is sometimes described as electrostatic entropy [159].

In this chapter, we develop an explicit-solvent liquid-state theory that incorporates the orientational polarization of dipolar solvent molecules directly into the thermodynamic description of electrolyte and polyelectrolyte solutions. The theory builds upon the mean-spherical-approximation treatments of dipolar and ion–dipole fluids developed by Blum and others [82, 98, 160, 161, 124]. We employ a minimal molecular model in which solvent molecules are represented as hard spheres carrying point dipoles, while ions or charged polyelectrolyte monomers are represented as hard spheres carrying discrete charges. This model retains the orientational degrees of freedom of the solvent while remaining sufficiently simple to permit an analytical thermodynamic treatment. We corroborate these findings using molecular dynamics simulations of an equivalent system.

2.2 Methods

We take this opportunity to discuss the appropriate normalization of the variables present in the theory. As with previous treatments[88, 138, 3], the bead diameter, σ, provides a simple normalization for the densities ($\phi_i = \rho_i \sigma^3$). Normalizing temperature is more subtle. In most treatments of electrostatics, a common metric used to characterize the strength of electrostatic interactions is a reduced Bjerrum length:

$$\bar{l}_\mathrm{B} = \frac{l_\mathrm{B}}{\sigma} = \frac{e_c^2}{4\pi\epsilon_0\epsilon_\mathrm{r} k_\mathrm{B} T \sigma}\,, \tag{2.2}$$

where e_c is the elementary charge, ϵ_0 is the vacuum permittivity, ϵ_r is the dielectric constant of the medium, k_B is the Boltzmann constant and T is the temperature. Inherently, $\bar{l}_\mathrm{B}$ is the inverse dimensionless temperature. However, in the explicit solvent treatment, the dielectric constant also becomes dependent on composition, making $\bar{l}_\mathrm{B}$ an inappropriate measure to characterize temperature. As such, we will instead define the temperature scale relative to the Bjerrum length of a vacuum, $l_{\mathrm{B},0}$, eliminating the dielectric constant from our temperature length scale:

$$\bar{T} = \frac{4\pi\epsilon_0 k_\mathrm{B} T \sigma}{e_c^2} = \frac{\sigma}{l_{\mathrm{B},0}}\,. \tag{2.3}$$

By a similar token, we normalize the dipole strength by the electrostatic energy:

$$\bar{\mu} = \frac{\mu}{e_c \sigma}\,. \tag{2.4}$$

As a reference, assuming $\sigma = 3\,\text{Å}$ and $T = 300\,\text{K}$, $\bar{T} \approx 0.005$. For most dipolar solvents in the liquid phase (such as water), the dipole strength can range from 2-4 D, which, rescaling to account for the electronic polarizability of most solvents ($\epsilon_\infty \approx 2$), would give a range of $\bar{\mu} \approx 0.15$-0.4.

Theory

We describe both the implicit- and explicit-solvent models within a common liquid-state-theory framework[124, 88]. Due to the mathematical complexity of these terms, unlike the previous chapter, the theory will expressed in terms of the total Helmholtz free energy, rather than the mixing function. Maintaining a consistent set of dimensionless variables, we define the reduced Helmholtz free-energy density as

$$f = \frac{F}{V k_\text{B} T} = f_\text{id.} + f_\text{hs} + f_\text{ele.} + f_\text{chain}\,. \tag{2.5}$$

The four contributions account for the ideal translational entropy, hard-sphere excluded volume, electrostatic correlations, and chain formation, respectively. The ideal contribution accounts for the translational entropy of each species,

$$f_\text{id.} = \sum_i \frac{\rho_i}{N_i}\left[\ln\left(\frac{\rho_i \Lambda_i^3}{N_i}\right) - 1\right], \tag{2.6}$$

where Λ_i is the thermal de Broglie wavelength of species i. Excluded-volume interactions between disconnected beads are described using the Boublík–Mansoori–Carnahan–Starling–Leland (BMCSL) equation of state [162, 163]. For equal bead diameters, this reduces to the Carnahan–Starling expression,

$$f_\text{hs} = \frac{6\eta^2(4-3\eta)}{\pi\sigma^3(1-\eta)^2}\,. \tag{2.7}$$

where

$$\eta = \frac{\pi}{6}\sum_i \rho_i \sigma^3\,. \tag{2.8}$$

is the total packing fraction. Under the incompressibility constraint imposed below the packing fraction is fixed at $\eta = \pi/6$. The hard-sphere term is therefore retained for formal completeness but does not affect phase equilibrium for the equal-diameter incompressible systems considered here.

The implicit- and explicit-solvent descriptions differ in the treatment of electrostatic correlations and, consequently, in the reference contact correlations entering the chain contribution. These terms are developed separately below. The implicit-solvent electrostatic contribution is identical to the one used in Chapter 1 and Chapter 3, although we now place more emphasis on the derivation of the this term.

We note that, unlike prior works where the solvent is treated entirely implicit, only contributing through the dielectric constant, for consistency between both implicit and explicit solvent treatments, the solvent within the implicit solvent treatment will also be included as a neutral hard-sphere satisfying the incompressibility constraint:

$$\sum_i \rho_i \sigma^3 = \sum_i \phi_i = 1\,. \tag{2.9}$$

This also accounts for any differences in packing effects between the two treatments.

Implicit Solvent

In the primitive-model mean-spherical approximation developed by Blum and co-workers[82, 98], ions are represented as charged hard spheres embedded in a dielectric continuum. The pair interaction is:

$$u_{ij}^{\text{ion}}(r) = \begin{cases} \infty\,, & r < \sigma \\ \frac{Z_i Z_j e_c^2}{4\pi\epsilon_0\epsilon_\text{r} r}\,, & r \geq \sigma \end{cases} \tag{2.10}$$

where Z_i is the valence of species i and r is the separation distance between beads i and j. The solvent enters the electrostatic reference system only through the prescribed relative permittivity ϵ_r. By solving the Ornstein–Zernike[164] equations under the MSA closure, Blum[82, 98] obtain the following central equation:

$$2\Gamma(1 + \Gamma\sigma) = \kappa\,, \tag{2.11}$$

where Γ is the MSA inverse screening length and $\kappa^2 = \frac{e_c^2}{\epsilon_0\epsilon_\text{r} k_\text{B} T} \sum_i \rho_i Z_i^2$ is the Debye inverse screening length. From this result, Blum also derived the free-energy contribution from electrostatic interactions as:

$$f_\text{ele.} = -\frac{\Gamma^3(2/3 + \Gamma\sigma)}{\pi}\,. \tag{2.12}$$

In this form, only disconnected charged beads are accounted for. The free energy change when disconnected beads are assembled into chains can be accounted for by invoking Wertheim's first-order perturbation theory[165, 166, 167, 168], which gives:

$$f_\text{chain} = -\sum_i \rho_i \left(1 - \frac{1}{N_i}\right) \ln\left[g_{ii}(\sigma) e^{\beta u_{ii}(\sigma)}\right], \tag{2.13}$$

where $g_{ij}(\sigma)$ and $u_{ij}(\sigma)$ are the contact pair distribution function and interaction potential between beads i and j. While both can be obtained from the MSA treatment

for charge hard spheres, it is known that $g_{ij}^{\mathrm{MSA}}(\sigma)$ can give erroneous predictions (namely $g_{ij}^{\mathrm{MSA}}(\sigma) < 0$) which would result in unphysical values of f_{chain}. Because of this, the EXP approximation[169, 170, 171, 172] is typically invoked, where:

$$g_{ij}^{\mathrm{EXP}}(\sigma) = g_{ij}^{\mathrm{HS}}(\sigma) \exp\left(g_{ij}^{\mathrm{MSA}}(\sigma) - g_{ij}^{\mathrm{HS}}(\sigma)\right), \tag{2.14}$$

where the hard-sphere radial distribution function at contact, $g^{\mathrm{HS}}(\sigma)$, is given by[173]:

$$g_{ij}^{\mathrm{HS}}(\sigma) = \frac{2+\eta}{2(1-\eta)^2}, \tag{2.15}$$

and:

$$g_{ij}^{\mathrm{MSA}}(\sigma) - g_{ij}^{\mathrm{HS}}(\sigma) = -\frac{l_{\mathrm{B}} Z_i Z_j}{\sigma(1+\sigma\Gamma)^2}. \tag{2.16}$$

The contact interaction potential is simply:

$$\beta u_{ij}(\sigma) = Z_i Z_j \frac{l_{\mathrm{B}}}{\sigma}. \tag{2.17}$$

Explicit Solvent

The explicit solvent treatment proposed in this work is based upon the work developed by Blum and Wei[160, 161] and subsequent works by Simonin[174, 175] which aided in clarifying many of the ambiguities in the former. Here, "explicit solvent" denotes a molecular-level reference model in which each solvent molecule is represented as a hard sphere carrying a central point dipole. The model therefore resolves ion–dipole and dipole–dipole correlations explicitly, while retaining a coarse-grained representation of molecular structure. As a result, the ion–ion interaction no longer require the dielectric constant in its definition:

$$u_{ij}^{\mathrm{ion}}(r) = \begin{cases} \infty, & r < \sigma \\ \frac{Z_i Z_j e_c^2}{4\pi\epsilon_0 r}, & r \geq \sigma. \end{cases} \tag{2.18}$$

Subsequently, ion–dipole interactions are also included:

$$u_{ij}^{\text{ion-dipole}} = \begin{cases} \infty, & r < \sigma \\ \frac{Z_i e_c}{4\pi\epsilon_0 r^3} \boldsymbol{\mu}_j \cdot \mathbf{r}, & r \geq \sigma, \end{cases} \tag{2.19}$$

where $\boldsymbol{\mu}_j$ is the dipole vector of species j and $\mathbf{r}$ is the separation vector between species i and j. Finally, dipole–dipole interactions are also included:

$$u_{ij}^{\text{dipole-dipole}} = \begin{cases} \infty, & r < \sigma \\ \frac{1}{4\pi\epsilon_0 r^3}\left[\boldsymbol{\mu}_i \cdot \boldsymbol{\mu}_j - \frac{3(\boldsymbol{\mu}_i \cdot \mathbf{r})(\boldsymbol{\mu}_j \cdot \mathbf{r})}{r^2}\right], & r \geq \sigma. \end{cases} \tag{2.20}$$

Because the dielectric response is generated by the explicit dipoles, we introduce the bare Debye parameter

$$\kappa_0^2 = \frac{e_c^2}{\epsilon_0 k_B T} \sum_i \rho_i Z_i^2, \qquad \overline{\kappa}_0 = \kappa_0 \sigma, \tag{2.21}$$

where the sum again extends over charged species. The dipolar coupling is characterized by

$$\chi = \frac{\rho_{\text{solv}} \mu^2}{3\epsilon_0 k_B T}. \tag{2.22}$$

Using an invariant expansion with spherical harmonics[176, 177] and following a similar procedure to the implicit solvent approach, Blum and Wei[160, 161] obtained the following three central equations, each corresponding to the ion–ion, ion–dipole and dipole–dipole correlations. To the best of our ability, for a system in which all beads have the same diameter, we obtain a simplified set of equations:

$$(1+\Gamma\sigma)^2\,\Gamma^2 + (1-D)(1+\Gamma\sigma)^2(1+\lambda+\Gamma\sigma)^2 = \frac{D^2\kappa_0^2}{4}\,, \tag{2.23}$$

$$\sqrt{D-1}\frac{1+\Gamma\sigma}{3}\left[D(1+\lambda+\Gamma\sigma)^2(3+\lambda+\Gamma\sigma) - (1+\Gamma\sigma)(1+\lambda)(3+2\lambda+2\Gamma\sigma)\right] = \frac{D^2\kappa_0\sigma\sqrt{\chi}}{2}\,, \tag{2.24}$$

$$\frac{9(1+\lambda)^4}{16(2+\lambda)^2}\left((1-\rho_{\text{solv.}}K^{11})^2 + \frac{(1+\Gamma\sigma)^2(D-1)}{9D^2}\,(3+\lambda+\Gamma\sigma)^2\right) = \epsilon_{\text{r}}\,, \tag{2.25}$$

where D and λ are measures of the ion–dipole and dipole–dipole interaction strength. The auxiliary quantity K^{11} is given by

$$\begin{aligned} 1-\rho_{\text{solv.}}K^{11} = {} & \frac{\lambda(2+\lambda)}{3D} \\ & + \frac{D-1}{3D}(1+\lambda+\Gamma\sigma)\,(3+\lambda+\Gamma\sigma)\,, \end{aligned} \tag{2.26}$$

and the dielectric constant is related to χ and λ through:

$$\epsilon_{\text{r}} = 1 + \frac{9(1+\lambda)^4}{16(2+\lambda)^2}\chi\,. \tag{2.27}$$

Thus, unlike the implicit-solvent model, the dielectric response is predicted from the density and dipole moment of the solvent together with the ion-induced changes

in the MSA scaling parameters. From these equations, the free energy contribution from electrostatic interactions is given by:

$$f_{\text{ele.}} = \frac{1}{12\pi}\left[\frac{\kappa^2}{\sigma}\left(\frac{D-1-\Gamma\sigma}{1+\Gamma\sigma}+\frac{(D-1)}{2+\lambda}\right) - \sqrt{\chi(D-1)}\frac{\kappa}{\sigma^2}\right] - J' \,, \tag{2.28}$$

where the full expression for J' involves three contributions:

$$J' = J'_{\text{ion-ion}} + 2J'_{\text{ion-solv.}} + J'_{\text{solv.-solv.}} \,, \tag{2.29}$$

where:

$$J'_{\text{ion-ion}} = \frac{\pi\sigma^3}{3}\sum_{ij}\rho_i\rho_j\left(h_{\text{ion-ion},ij}(\sigma)\right)^2 \,, \tag{2.30}$$

where:

$$h_{\text{ion-ion},ij}(\sigma) = \frac{2+\eta}{2(1-\eta)^2} - Z_iZ_j\frac{4l_{\text{B},0}}{D\kappa^2\sigma^3}\left(\frac{3(D-1)}{2+\lambda}+(\Gamma\sigma)^2\right) \,. \tag{2.31}$$

For $J'_{\text{ion-solv.}}$:

$$J'_{\text{ion-solv.}} = \frac{\pi\sigma^3}{3}\sum_{i\in\text{ion}}\sum_{j\in\text{solv.}}\rho_i\rho_j\left(h_{\text{ion-solv.},ij}(\sigma)\right)^2 \,, \tag{2.32}$$

where:

$$h_{\text{ion-solv.},ij}(\sigma) = -4\sqrt{3}Z_i\frac{\sqrt{\rho_j(D-1)}}{D\sqrt{I}}(\lambda+\Gamma\sigma(1+\lambda+\Gamma\sigma)) \,. \tag{2.33}$$

And for $J'_{\text{solv.-solv.}}$:

$$J'_{\text{solv.-solv.}} = \frac{\pi\sigma^3}{3}\left(\left(h_{\text{solv.-solv.},1}(\sigma)\right)^2+\frac{\left(h_{\text{solv.-solv.},2}(\sigma)\right)^2}{5}\right)\sum_{ij\in\text{solv.}}\rho_i\rho_j \,, \tag{2.34}$$

where:

$$h_{\text{solv.-solv.},1}(\sigma) = \frac{Q'^{11}+2q'}{2\sqrt{3}\pi\sigma} \,, \tag{2.35}$$

$$h_{\text{solv.-solv.},2}(\sigma) = \sqrt{10}\frac{Q'^{11}-2q'}{2\sqrt{3}\pi\sigma} \,, \tag{2.36}$$

and:

$$Q'^{11} = \frac{2\lambda}{D\rho_{\text{solv.}}\sigma^3}(\lambda+(D-1)(1+\lambda+\Gamma\sigma))+2\frac{(D-1)}{D}(1+\Gamma\sigma)(1+\lambda+\Gamma\sigma)-\frac{2}{\rho_{\text{solv.}}\sigma^3} \tag{2.37}$$

$$q' = -6\frac{(\lambda-1)(\lambda+3)}{(2+\lambda)(1+\lambda)^2} \tag{2.38}$$

The dipole-free limit is obtained for $\chi \to 0$, $D \to 1$, and $\lambda \to 1$. In this limit, Eqs. (2.23) and (2.28) reduce to the primitive-model MSA with a vacuum dielectric background, $\epsilon_r = 1$, and $J' = \Gamma^3/(3\pi)$. Conversely, in the ion-free limit, $\kappa_0 = \Gamma = 0$ and $D = 1$, such that Eq. (2.25) becomes

$$\frac{\lambda^2(1+\lambda)^4}{16} = \epsilon_r \,. \tag{2.39}$$

Combined with equation 2.27, this gives the expression for Wertheim's dielectric constant[178].

By using the same EXP approximation used in the previous section, we can obtain the free energy change when forming chains of charged beads in the explicit solvent treatment. In this case, we have:

$$\begin{aligned} g_{ij}^{\mathrm{MSA}}(\sigma) - g_{ij}^{\mathrm{HS}}(\sigma) = \\ - Z_i Z_j \frac{4 l_{\mathrm{B},0}}{D\kappa^2\sigma^3}\left(\frac{3(D-1)}{2+\lambda} + (\Gamma\sigma)^2\right) . \end{aligned} \tag{2.40}$$

In the limit of no dipoles, equation 2.40 recovers equation 2.16 by substituting equation 2.11 with $\epsilon_r = 1$.

Within the electrostatic reference fluid, charged beads enter through their densities irrespective of whether they are free ions or segments of a polyelectrolyte. Polymer connectivity enters separately through the chain term. Consequently, the predicted dielectric response depends on the density of charged beads but does not distinguish salt ions from chemically identical charged polymer segments at the level of the MSA electrostatic term.

With this, all equations necessary to model polyelectrolyte phase behavior in an explicit solvent have been defined. As noted earlier, equations 2.23-2.25 must be solved simultaneously for Γ, D and λ. This must be done with an iterative solver where, for reliable solutions, we recommend using the initial values obtained from both the ion-free and dipole-free limits (D can be initialized at unity).

Phase Equilibrium and Criticality

All systems are treated as incompressible,

$$\sum_i \phi_i = 1, \tag{2.41}$$

which allows the solvent volume fraction to be eliminated. We consider symmetric mixtures of oppositely charged polyelectrolytes with equal chain lengths and equal-magnitude valences. Local electroneutrality is imposed in each bulk phase, such that

$$\phi_{\mathrm{p}+} = \phi_{\mathrm{p}-} = \frac{\phi_{\mathrm{p}}}{2}. \tag{2.42}$$

For a symmetric monovalent salt, we similarly set

$$\phi_{\mathrm{s}+} = \phi_{\mathrm{s}-} = \frac{\phi_{\mathrm{s}}}{2}. \tag{2.43}$$

The solvent fraction is therefore

$$\phi_{\mathrm{solv}} = 1 - \phi_{\mathrm{p}} - \phi_{\mathrm{s}}. \tag{2.44}$$

For co-existence to exist between a supernatant and coacervate phase, we must have:

$$\mu_i^{\mathrm{sup.}} = \mu_i^{\mathrm{co.}}, \quad \forall i \in \{\mathrm{p}, \mathrm{s}\}, \tag{2.45}$$

$$\Pi^{\mathrm{sup.}} = \Pi^{\mathrm{co.}}, \tag{2.46}$$

where the chemical potential, μ_i, is obtained by:

$$\mu_i = \left(\frac{\partial f}{\partial \phi_i}\right)_{T,\phi_{j\neq i}}, \tag{2.47}$$

and the osmotic pressure is given by:

$$\Pi = -f + \sum_i \phi_i \mu_i \,. \tag{2.48}$$

For the salt-free system, incompressibility and electroneutrality leave ϕ_{p} as the only independent composition variable. The critical point therefore satisfies

$$\left(\frac{\partial^2 f}{\partial \phi_{\mathrm{p}}^2}\right)_T = 0, \tag{2.49}$$

$$\left(\frac{\partial^3 f}{\partial \phi_{\mathrm{p}}^3}\right)_T = 0. \tag{2.50}$$

All calculations in this work are performed using Clapeyron.jl[20] where partial derivatives are obtained using the ForwardDiff.jl[102] package.

Molecular Dynamics Simulations

All simulations are performed using LAMMPS[179] with an NVT ensemble where temperature was maintained at $\tilde{T}$ in Lennard-Jones (LJ) units using a Nosé–Hoover thermostat which accounts for the rotational degrees of freedom of dipolar particles with a relaxation time $\tau = 100\Delta t$ (where Δt is the timestep) and a constant total reduced density ($\rho\sigma^3$) of 0.8 was set for all conditions. [180, 181] The solvent was treated as a spherical bead with a permanent point dipole of magnitude $\tilde{\mu}$, while charged particles were treated using the Coulombic potential with charge $\pm\tilde{q}$. Both interactions are evaluated in real space up to a cutoff distance of r_c, dependent on the system, beyond which the interactions are evaluated in Fourier space using the particle–particle particle–mesh (PPPM) method for long–range dipolar interactions [182] with a target force accuracy of 10^{-4}. To emulate hard-sphere interactions so as to closely mimic the theoretical predictions, all particles also interact through the Weeks–Chandler–Adams (WCA) potential:

$$U_{\mathrm{WCA}}(r) = \begin{cases} 4\epsilon\left[\left(\frac{\sigma}{r}\right)^{12} - \left(\frac{\sigma}{r}\right)^{6} + \frac{1}{4}\right], & \text{if } r \le 2^{\frac{1}{6}}\sigma \\ 0, & \text{if } r > 2^{\frac{1}{6}}\sigma \end{cases} \tag{2.51}$$

where ϵ is the Lennard-Jones energy parameter which provides the normalization for the temperature in LJ units, $\tilde{T} = T/(k_{\mathrm{B}}\epsilon)$. When considering polyelectrolytes, adjacent monomers were connected using the finite extensible nonlinear elastic (FENE) potential[183],

$$U_{\mathrm{FENE}}(r) = -0.5kR_0^2 \ln\left[1 - \left(\frac{r}{R_0}\right)^2\right] \tag{2.52}$$

with $k = 30\epsilon/\sigma^2$ and $R_0 = 1.5\sigma$.

Although we use the LJ unit system within LAMMPS as it does not natively support the dimensionless unit system used within the explicit solvent liquid state theory proposed earlier, we map the LJ temperatures ($\tilde{T}$), dipoles ($\tilde{\mu}$) and charges ($\tilde{q}$) to the desired units through the following relationships:

$$\bar{T} = \frac{\tilde{T}}{4\pi\tilde{q}^2}, \quad \bar{\mu} = \frac{\tilde{\mu}}{\tilde{q}}, \quad \bar{q} = \pm 1.0\,. \tag{2.53}$$

This provided the benefit that the simulations used values of $O(1)$ in LJ units for the temperature ($\tilde{T} \sim 1.0{-}3.0$), charges ($\tilde{q} \sim 3.0{-}11.5$) and dipole strengths ($\tilde{\mu} \sim 0.3{-}1.7$), resulting in numerical stability.

All systems were initialized using Packmol[184] followed energy minimization using the conjugate-gradient algorithm until both the energy and force tolerances reached 10^{-5}. Particle velocities were then initialized from a Maxwell–Boltzmann distribution at the specified reduced temperature with zero net linear momentum.

Unlike the theoretical calculations for polyelectrolytes, rather than using a homopolyelectrolyte, we use chains with alternating neutral and charged blocks, where all chains start and terminate with a neutral bead. This was done due to the fact that, with an explicit solvent, polyelectrolyte beads no longer represent entire monomers. More appropriately, they now represent functional groups, where neutral groups would be separating the charged groups. Keeping with the simplified representation, we only consider a linear chain. Furthermore, due to the more polarizable nature of functional groups in polyelectrolytes compared to simple electrolytes, we must account for the larger electronic polarizability contribution to the dielectric constant. In conventional forcefields, this is done through rescaling of the charges.[185] For simplicity, we rescale all charges by $\sqrt{\epsilon_\infty}$ where $\epsilon_\infty = 2$.

All simulations used a timestep $\Delta t = 0.005\tau_0$ where $\tau_0 = \sqrt{m\sigma^2/\epsilon}$.

Bulk Simulations

In order to compute dielectric properties of dipolar solvent with varying temperature, dipole strength and simple electrolyte composition, we perform bulk, isotropic simulations with 5000 total particles. A real-space cutoff of 7σ for electrostratic interactions. Systems were equilibrated for 10^5 timesteps followed by 2×10^6 timesteps for production. We compute the dielectric constant, ϵ_r, from equilibrium polarization fluctuations using the Kirkwood fluctuation formula,[186, 152]

$$\epsilon_\mathrm{r} = 1 + \frac{4\pi\rho}{3k_\mathrm{B}T}(\langle\mathbf{M}^2\rangle - \langle\mathbf{M}\rangle^2)\,, \tag{2.54}$$

where the total system dipole moment is:

$$\mathbf{M} = \sum_i \boldsymbol{\mu}_i\,, \tag{2.55}$$

making use of MDAnalysis[187] and MDCraft[14] to parse the simulation trajectories. Block averaging was used to compute dielectric constant errors.

Slab Simulations

In order to determine the composition of co-existing phases, we perform slab simulations where, initializing the coacervate as pure electrolyte and the supernatant as

pure solvent, the compositions are allowed to equilibrate over the duration of the simulation. In the case of simple electrolytes, a box of $10\sigma \times 10\sigma \times 97.5\sigma$ with 6000 solvent particles and 900 ion pairs. In the case of polyelectrolyte coacervates, a box of $15\sigma \times 15\sigma \times 148\sigma$ with 18000 solvent particles, 270 polyelectrolyte pairs and equivalent composition of ion pairs. For simple electrolytes and polyelectrolytes, a real space cutoff of 8σ and 14σ were used, respectively, to evaluate the electrostatic interactions using PPPM.

We initialize the coacervate / charge dense slab by first introducing charged species in the system, and dragging them to the center of the box over 10^5 timesteps. Subsequently, solvent is added to the remaining box volume. After an additional energy minimization step, the two domains are allowed to equilibrate and reach the equilibrium density. While not all system conditions required it, equilibrium compositions were typically reached after 10^7 timesteps.

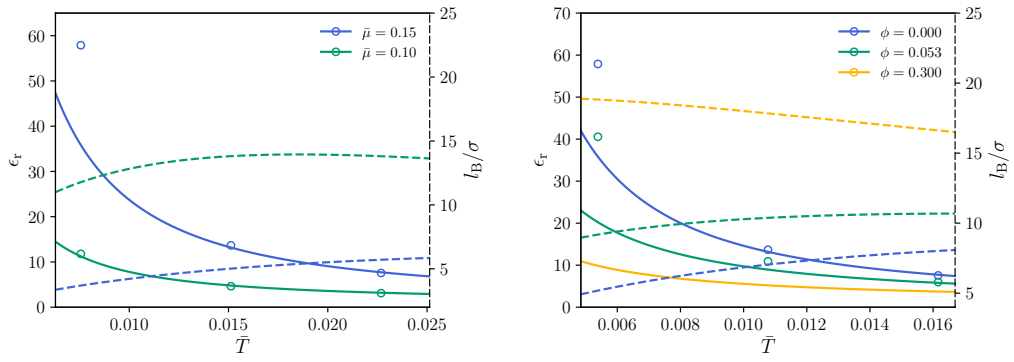
Compositions of the coexisting phases were determined by obtaining the density profiles using MDCraft[14].

Potentials of Mean Force

To examine the effects of temperature, dipole strength, charge concentration and degree of polymerization, we compute PMFs between oppositely charged monovalent ions and oppositely charged polyelectrolyte chains using the adaptive biasing force (ABF) method[188, 189] implemented in the Colvars module [190].

For simple electrolytes, a box of $18.42\sigma \times 18.42\sigma \times 18.42\sigma$ was initialized with 5000 total particles, with at least one ion pair. The ion separation distance is treated as a collective variable and is varied over the interval 1σ to 9.21σ. The system is initially equilibrated for 10^5 timesteps followed by 10^7 timesteps for production. A real space cutoff of 7σ to evaluate the electrostatic interactions using PPPM.

For complex polyelectrolytes, a box of $40\sigma \times 40\sigma \times 40\sigma$ was initialized with 48000 total particles, with one pair of polyelectrolytes with their counterions. The chain center-of-mass separation distance is treated as a collective variable and is varied over the interval 0σ to 20σ divided into five intervals. The system is initially equilibrated for 10^5 timesteps followed by 2×10^7 timesteps for production. A real space cutoff of 14σ to evaluate the electrostatic interactions using PPPM.



(a) (b)

Figure 2.2: Temperature dependence of the dielectric constant (solid lines and symbols, left axis) and Bjerrum length (dashed lines, right axis) for a pure solvent (a) and solvent + salt mixture (b). Lines denote results obtained from the explicit solvent theory while symbols denote results obtained from simulations.

2.3 Results and Discussion

Dielectric constant

The strength of electrostatic interactions is often characterized by the Bjerrum length, l_B, defined as the separation at which the Coulomb interaction between two elementary charges equals the thermal energy, $k_B T$. The Bjerrum length is therefore given by $l_B = e_c^2/[4\pi\epsilon_0\epsilon_r(T)k_B T]$, where its magnitude can be interpreted as a measure of the electrostatic driving force. In this expression, the temperature dependence enters in two places: through the explicit $1/T$ dependence and through the dielectric constant, $1/\epsilon_r(T)$, which accounts for the orientational response of the solvent dipoles. Consequently, understanding the temperature dependence of the Bjerrum length requires simultaneous consideration of both thermal and dipolar fluctuations.

We first consider the simple case of a pure solvent in the absence of ions. To first establish the validity of the mean-spherical approximation in modeling explicit solvent systems, consider Figure 2.2 where the theory predictions are compared to simulation results. Examining the pure solvent behavior first in Figure 2.2a, one can see that, for both dipole strengths considered, remarkable agreement is achieved between theory and simulations. The exception to this is for $\bar{\mu} = 0.15$ at the lowest temperature. This is somewhat to be expected as, according to Blum and others[161, 160, 191, 174], it is in this very regime of strong dipolar correlations where the linear approximations within the MSA approach are expected to manifest. Nonetheless, the explicit solvent approach adequately accounts for the qualitative behavior of

the dielectric constant and Bjerrum length of a pure dipolar solvent, predicting an increasing Bjerrum length with temperature, as expected from real polar fluids (see Figure 2.1).

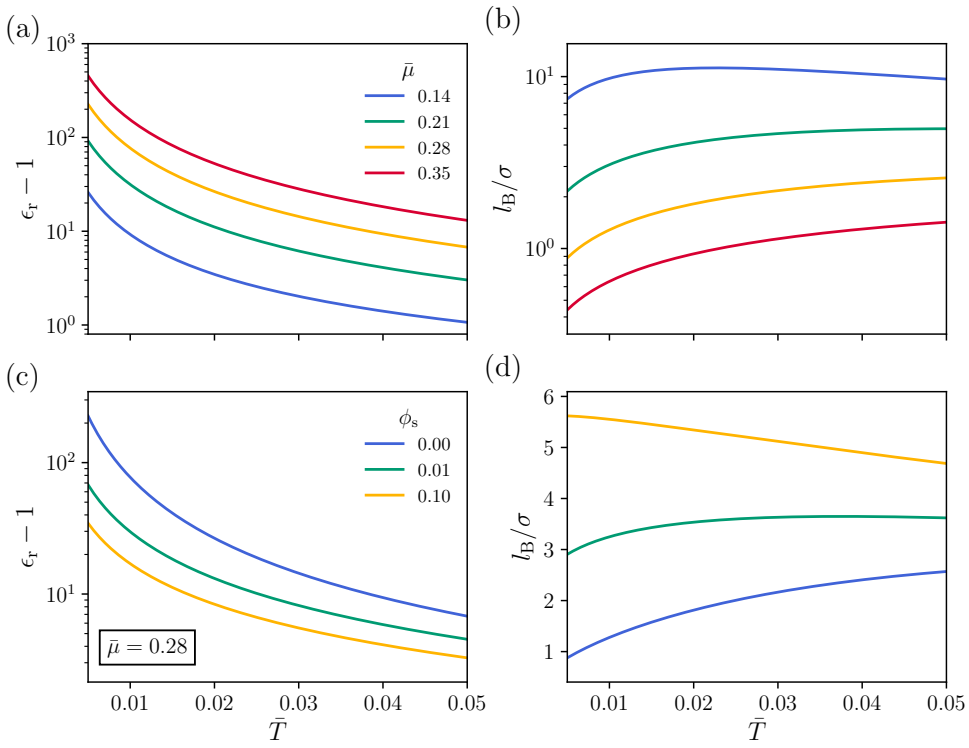


Figure 2.3: Temperature dependence of (a), (c) the dielectric constant and (b), (d) Bjerrum length of (a), (b) a pure dipolar solvent with varying dipole strength and (c), (d) a single dipolar solvent ($\bar{\mu} = 0.28$) with varying salt concentration. In (a) and (b), varying colors denote the different dipole strengths, corresponding to the legend in (a). In (c) and (d), varying colors denote the different salt concentrations, corresponding to the legend in (c).

Extending our analysis to mixtures of dipolar fluids and salts in Figure 2.2b, similar qualitative agreement is achieved. To maximize the concentration range over which ions are soluble within the solvent, we have only considered $\bar{\mu} = 0.15$. As a result, the limited agreement in Figure 2.2a permeates to Figure 2.2b. In spite of this, the explicit solvent MSA approach does qualitatively capture the dielectric decrement upon addition of salt. When examined in terms of the Bjerrum length, this results in a weakening in the sensitivity to temperature.

Having established the validity of the theoretical approach against simulations, we can now leverage its cheaper computational cost to better understand the effects of dipole strength, salt concentration and temperature on the dielectric constant and

the strength of electrostatic interactions through the Bjerrum length. Figures 2.3(a) and (b) show the dielectric constant and Bjerrum length, respectively, for varying solvent dipole moments, $\bar{\mu}$ obtained from theory. Considering the dielectric constant first, increasing the temperature monotonically decreases the dielectric constant in all cases, as thermal fluctuations weaken the orientational correlations between permanent dipoles. Increasing the dipole strength enhances the dielectric response of the solvent and therefore produces a larger dielectric constant. On a logarithmic scale, the decay of the dielectric constant with temperature is similar for the different dipole strengths.

The corresponding Bjerrum lengths in Figure 2.3(b) reveal the competition between thermal energy and solvent polarization. At low temperatures, the dielectric constant decreases rapidly for all dipole strengths. This reduction is sufficiently large to outweigh the explicit $1/T$ dependence, causing the Bjerrum length to initially increase with temperature. Most polar solvents are expected to have a dipole strength of approximately $\bar{\mu} \geq 0.2$ within the present coarse-grained description. Thus, over the temperature range considered, the implicit-solvent picture would predict that the electrostatic driving force strengthens with increasing temperature. Similar behavior has been discussed in previous works [147, 90].

As the temperature increases further, however, the sensitivity of the dielectric constant to temperature weakens, such that the explicit $1/T$ dependence eventually becomes dominant. This competition produces a broad maximum in the Bjerrum length, followed by a gradual decrease. The crossover is most evident for weakly polar solvents, such as the case with $\bar{\mu} = 0.15$. If a broader temperature range were considered, the Bjerrum length would eventually decrease for all dipole strengths. These results demonstrate the competition between thermal and dipolar fluctuations. For most of the dipole strengths and temperatures considered here, the explicit $1/T$ dependence is outweighed by the decrease in dielectric constant, resulting in an increasing Bjerrum length and, consequently, strengthening electrostatic interactions.

These results reflect the typical temperature dependence of the Bjerrum length, and therefore of the effective electrostatic driving force, within an implicit-solvent treatment. However, the addition of ions to a dipolar solvent can itself influence the dielectric response. Following Debye's theory of polar dielectrics, the dielectric constant reflects the collective orientational polarization of the solvent dipoles. Dissolved ions perturb this orientational response through ion–dipole interactions and solvation, giving rise to the well-known dielectric decrement observed experimen-

tally [151], computationally[152, 192] and theoretically [193, 153, 194, 195]. Figure 2.3(c) illustrates this effect for a solvent with a fixed dipole strength, $\bar{\mu} = 0.28$, at three salt concentrations. Increasing the salt concentration systematically lowers the dielectric constant over the entire temperature range, demonstrating the suppression of the dielectric response by the addition of salt.

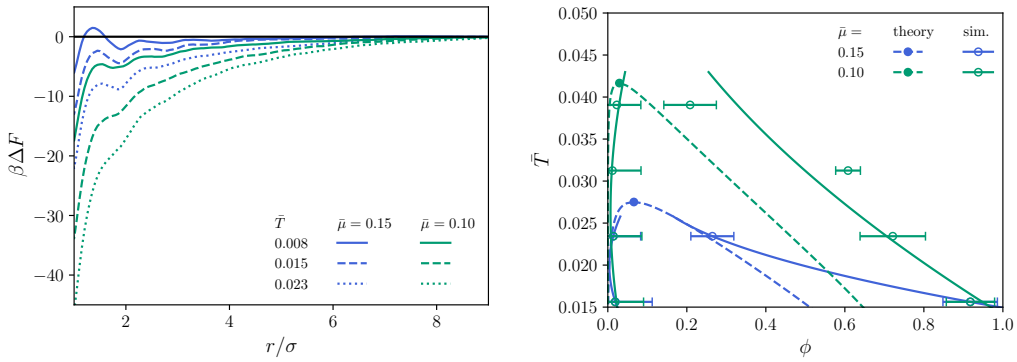
The reduction in the dielectric constant has a direct consequence for the effective strength of electrostatic interactions, as shown in Figure 2.3(d). At low temperatures, the lower dielectric constant at higher salt concentrations results in an increased Bjerrum length. However, this reduction in the dielectric constant is accompanied by a weaker temperature dependence. At sufficiently high salt concentrations, the dielectric constant becomes sufficiently insensitive to temperature that the explicit $1/T$ dependence becomes dominant. This results in an eventual decrease in the Bjerrum length with increasing temperature, implying a weakening of the effective electrostatic driving force.

Within implicit-solvent treatments, the physical picture is comparatively simple: an increasing Bjerrum length strengthens electrostatic interactions and can therefore enhance the driving force for phase separation, resulting in lower-critical-solution-temperature (LCST) behavior. However, when the dielectric constant is determined explicitly by the concentrations of ions and dipoles, the Bjerrum length and its temperature dependence can differ substantially between the two phases. These trends may even oppose one another under some conditions. As a result, Figure 2.3 alone is insufficient to determine the resulting phase behavior of an electrostatically driven system. The complete phase diagram must instead be obtained by explicitly solving the phase-equilibrium conditions.

We briefly note that, although a dielectric decrement upon the addition of simple salts is generally expected for polar solvents, dielectric increments can occur when ion pairing is substantial [196] or, in the case of polyatomic ions, when electronic polarizability contributes significantly to the dielectric response [197]. Such behavior is most commonly observed in weakly polar or non-polar solvents. In studies of polyelectrolyte coacervates [198, 149, 148, 150], however, the solvent of primary interest is typically water, for which the dipolar contribution to the dielectric constant is substantial.

Simple electrolyte phase behavior

Before examining more complex systems, we next examine the phase behavior of simple electrolyte systems. As the proposed theory only considers fluid phases, it is more appropriate to consider these systems as being most similar to ionic liquid + polar solvent mixtures, rather than the typical simple, monoatomic electrolytes which typically precipitate out of solution into a solid phase. This section intends to provide the initial intuitions needed to understand the effects of an explicit solvent on ion–ion interactions. Later sections will more directly consider the qualitative differences between implicit and explicit solvent approaches.



(a) (b)

Figure 2.4: (a) Potentials of mean force between oppositely charged ions in an explicit solvent of varying dipole strength (color) with varying temperature (line styles) obtained from simulations (b) Phase diagram for a mixture of dipolar solvent and monomeric ions with varying dipole strength (color) obtained from simulations (solid lines and empty symbols) and theory (dashed lines and solid symbols). Empty symbols denote simulations results whilst the lines serve as visual aids. Filled symbols denote critical points.

Before examining the macroscopic phase behavior, it is useful to first consider the potential of mean force between pairs of oppositely charged ions with varying temperature in order to examine the effects of an explicit solvent on the two-body ion–ion interactions, shown in Figure 2.4a. Across the range of dipole strengths and temperatures examined, pair interactions strengthen with increasing temperature. Consistent with Eq. 2.1 and prior work[193], decreasing dipole strength lowers the dielectric response and deepens the attractive well. At $\bar{\mu} = 0.15$, the PMF between monomeric ions exhibits short-ranged oscillations associated with solvation-shell structure once dipolar screening substantially weakens direct ion–ion interactions. These observations are all consistent with the typical implicit solvent picture of electrostatic interactions. However, as shown in Figure 2.4b, the true phase behavior

results in the closure of the two-phase region at higher temperatures, implying that the ion–ion interactions should weaken within increasing temperatures.

The origins of this discrepancy are partly explained by the results in the previous section where, within the charge-dense phase in which ion–ion interactions dominate, the Bjerrum length decreases with increasing temperature, implying weakening interaction strength. However, this result is more correlative in nature rather than causal. The latter can be better understood by revisiting the PMF, now considering the effects of added salt.

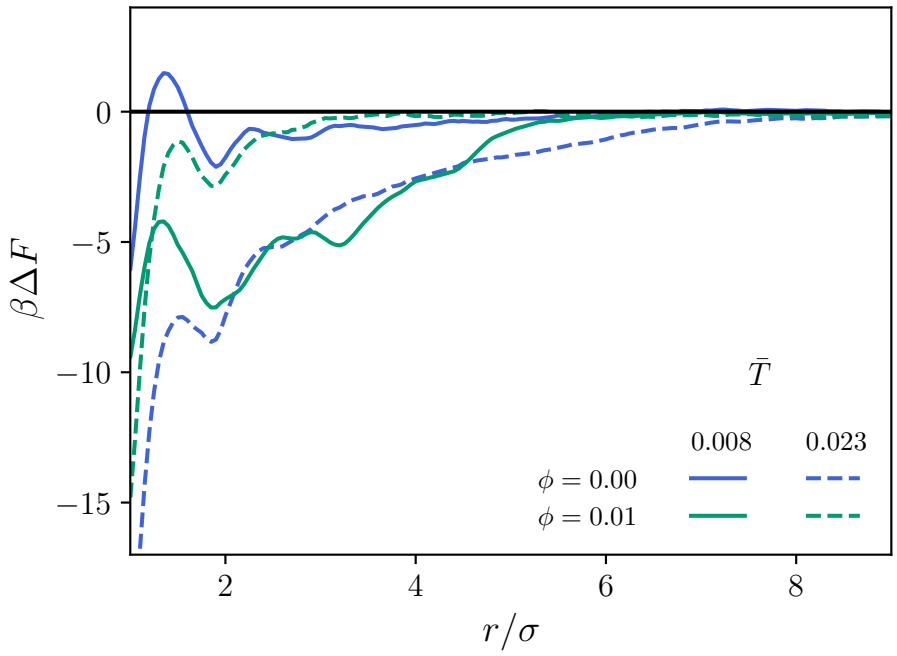


Figure 2.5: Potential of mean force between oppositely charged ions at infinite dilution (blue) and $\phi = 0.01$ (green) with varying temperature for an explicit dipolar solvent with $\bar{\mu} = 0.15$.

As shown in Figure 2.5(a), introducing a small ion fraction ($\phi = 0.01$, corresponding to approximately 0.2 M for $\sigma = 0.4$ nm) produces two effects. First, ionic screening shortens the interaction range relative to the infinite-dilution limit[29, 84, 3]. Second, and more importantly, the thermal response reverses: pair interactions now weaken with increasing temperature. This reversal correlates with the dielectric decrement discussed in the previous section[152, 153]. Crucially, simulations show that this reversal emerges at substantially lower concentrations ($\phi < 0.01$ in Figure 2.5) than would be inferred from the macroscopic dielectric response alone ($\phi \geq 0.3$ in Figure 2.2b). This reflects the distinction between bulk dielectric behav-

ior and the local environment governing ion–ion interactions: dipoles within ionic solvation shells are perturbed far more strongly than those in the bulk, leading to a larger reduction in local dielectric screening and a more pronounced reversal of the thermal response[199, 200, 201]. This effect is naturally captured in MSA-ID and simulations through the explicit coupling between ionic and dipolar degrees of freedom.

In essence, the mechanism is a crossover from solvent-controlled electrostatics at infinite dilution to ion-induced suppression of local dipolar screening at finite concentration, reversing the thermal response of electrostatic interactions and ultimately producing UCST phase behavior.

Polyelectrolyte salt-free phase behavior

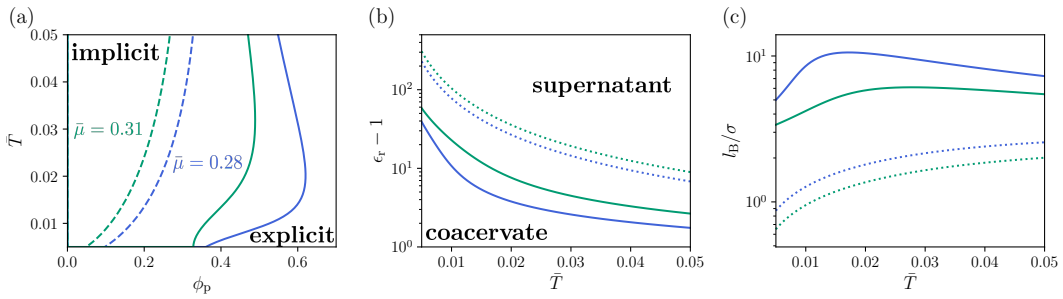


Figure 2.6: Phase behavior of a pure complex polyelectrolyte coacervate ($N = 50$) with varying temperature and solvent dipole strength. (a) Phase boundary of an explicit solvent (solid lines) and implicit solvent (dashed lines), where the implicit solvent assumes the same temperature-dependent dielectric constant of a pure dipolar solvent. (b) Dielectric constant and (c) Bjerrum length in the coacervate (solid lines) and supernatant (dotted lines) in the explicit solvent systems. The temperature dependence in implicit solvent systems would follow approximately that of the supernatant phase in explicit solvent systems.

With the intuitions developed in the previous section, we now consider the phase behavior of a complex polyelectrolyte in the presence of implicit and explicit solvents, as shown in Figure 2.6. To enable a direct comparison between the two approaches, the dielectric constant in the implicit-solvent model is assigned the same temperature dependence as that of the pure dipolar solvent in the explicit-solvent treatment. Thus, within this comparison, the principal difference is that the explicit-solvent model additionally accounts for the dependence of the dielectric response on charge concentration. We elect not to show the complete phase diagrams because the lower- and upper-critical solution temperatures occur at either unphysically low or unphysically high temperatures. The temperature range shown therefore better represents

physically relevant conditions.

As shown in Figure 2.6(a), the two theories predict qualitatively different phase behavior. In both cases, decreasing the molecular dipole moment lowers the dielectric constant and weakens the ion–dipole interactions, thereby enlarging the coexistence region without substantially changing its overall shape. As expected from the discussion in the previous section and Figure 2.3(b), the pure-solvent Bjerrum length increases with temperature over the range considered. Within the implicit-solvent treatment, this strengthens the electrostatic driving force for coacervation and gives rise to lower-critical-solution-temperature (LCST)-like behavior, consistent with previous work [147, 90].

In contrast, the explicit-solvent treatment predicts more complex behavior, with the two-phase region initially widening before narrowing again at higher temperatures. We have observed closure of the coexistence region only at high temperatures, and not at low temperatures. However, as noted by Blum and Wei[160, 161] in their original work, the low-temperature regime corresponds to very strong electrostatic correlations, under which the theory can begin to produce unrealistic predictions. Nonetheless, over the physically relevant temperature range, the explicit-solvent treatment predicts UCST-like and, in some cases, looping phase behavior in complex polyelectrolytes.

To understand the origin of this behavior, we first examine the dielectric constants of the coexisting phases in Figure 2.6(b). The supernatant is composed predominantly of dipolar solvent molecules and contains only a low concentration of polyelectrolytes. Consequently, its dielectric constant closely follows that of the corresponding pure dipolar solvent shown in Figure 2.3(a), decreasing monotonically with increasing temperature as the orientational polarization of the solvent weakens. This trend is nearly identical to the dielectric constant imposed in the implicit-solvent treatment. Examining the corresponding Bjerrum length in Figure 2.6(c), the resulting phase behavior is consistent with the conventional Bjerrum-length interpretation: the rapid decrease in dielectric constant causes the Bjerrum length to increase, thereby strengthening electrostatic interactions and promoting phase separation.

The polymer-rich coacervate, by contrast, exhibits a consistently lower dielectric constant than the supernatant throughout the coexistence region. This is expected because the coacervate contains a higher concentration of charged species and a lower concentration of dipolar solvent. The lower dielectric constant also contributes

to the high polymer concentration of the coacervate at low temperatures, as it strengthens ion–ion interactions and enhances the driving force for phase separation.

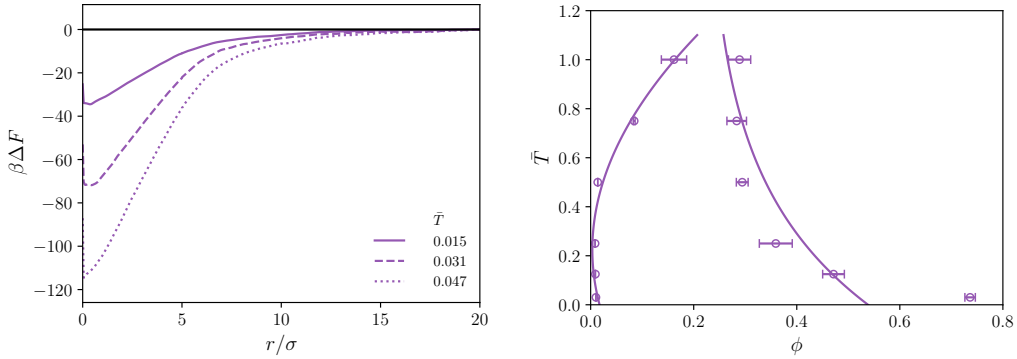
Like that of the supernatant, the dielectric constant of the coacervate decreases monotonically with increasing temperature. However, the resulting temperature dependence of the Bjerrum length is more complex. At low temperatures, the dielectric constant of the coacervate decreases more rapidly than that of the supernatant. This behavior arises from two coupled effects. First, increasing temperature weakens the orientational response of the dipoles, directly reducing the dielectric constant. Second, the resulting reduction in dielectric constant strengthens ion–ion interactions and promotes further phase separation. The associated increase in polymer concentration further lowers the dielectric constant by reducing the concentration of dipolar solvent and increasing the disruption of the solvent dielectric response. Together, these effects produce the rapid decrease in dielectric constant and the corresponding rapid increase in Bjerrum length at low temperatures.

At a crossover temperature that depends on the solvent dipole strength, the dipolar contribution has been sufficiently weakened so that the dielectric constant is now weakly dependent on temperature. Further reductions in the dielectric constant are then unable to compensate for the explicit increase in thermal energy, and the Bjerrum length begins to decrease with increasing temperature. As the effective electrostatic interactions weaken, the driving force for coacervation is reduced, leading to a decrease in the polymer concentration of the coacervate. At sufficiently high temperatures, this driving force becomes too weak to sustain phase separation, and the two-phase region closes.

The qualitative variation of the Bjerrum length in Figure 2.6(c) closely follows the phase behavior shown in Figure 2.6(a), supporting a central conclusion of this work: the coacervation behavior of an electrostatically driven system is governed by the dielectric environment within the coacervate, which correlates poorly, if at all, with the dielectric environment of the supernatant.

To ensure the validity of this analysis, we now briefly consider a comparison to coarse-grained simulations, given in Figure 2.7. First consider the potential of mean force given in Figure 2.7a where, much like the previous section, with increasing temperature, we observe a deepening potential. At face value, like the implicit solvent model, one would expect LCST-type phase behavior. However, as shown in Figure 2.7b, one actually observes a UCST, in good agreement with the findings of the previous section and Figure 2.6. Figure 2.7 is a demonstration of the clear

disconnect between the two-body image often used to characterize polyelectrolyte interactions[159] and the macroscopic phase behavior arising from the long-range, many-body nature of electrostatic interactions.



(a) (b)

Figure 2.7: (a) Potentials of mean force between oppositely charged polyelectrolytes in an explicit solvent ($\bar{\mu} = 0.15$) and counterions with varying temperature (line styles) obtained from simulations (b) Phase diagram for a mixture of dipolar solvent and oppositely charged polyelectrolytes obtained from simulations (solid lines and empty symbols). Empty symbols denote simulations results whilst the lines serve as visual aids.

The elevated critical temperatures in Figures 2.6 and 2.7, relative to ambient conditions, and the depth of the PMFs in Figure 2.7 reflect a deliberate simplification of the model, in which polyelectrolytes are treated as assemblies of strongly interacting charges. Rather than providing a quantitative description of a specific material, this minimal representation isolates electrostatics as a singular driving force and thereby exposes its intrinsic thermodynamic tendency. In real systems, both solvent and polymers contain polarizable groups and intrinsic dipoles, giving rise to a dielectric response comprising a weakly temperature-dependent electronic contribution and a strongly temperature-dependent orientational contribution. Electronic polarizability has been approximately incorporated through a rescaling of charges[185], which preserves both the inversion in the Bjerrum length and the UCST behavior found here. When the dielectric response is dominated by electronic polarizability (e.g., in non-polar solvents or ionic liquids) such that the effect on ion–ion interactions amounts to a rescaling of the charges, the implicit-solvent picture is appropriate[202]. For most polyelectrolytes in highly polar solvents such as water, however, dipolar contributions dominate and this approximation breaks down.

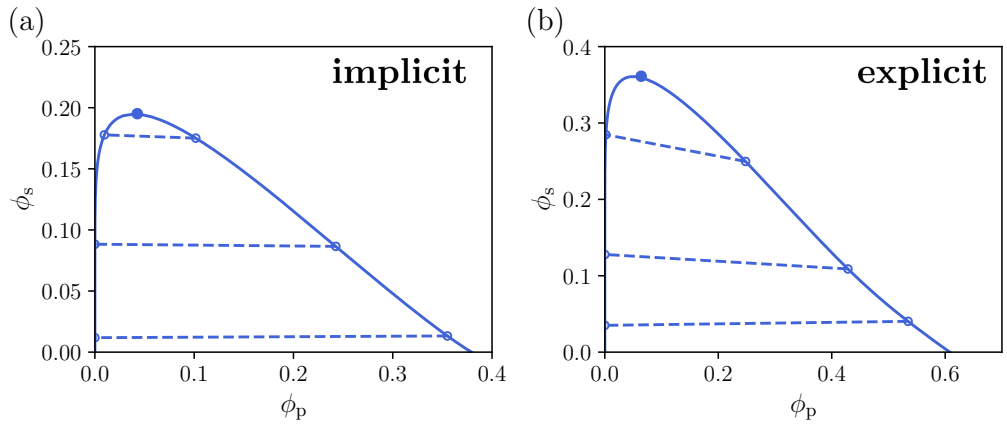


Figure 2.8: Phase behavior for a polyelectrolyte complex ($N = 50$) with varying salt concentration and a dipolar solvent ($\bar{\mu} = 0.28$) at $\bar{T} = 0.015$ for an (a) implicit and (b) explicit solvent system. The implicit solvent phase diagram is obtained assuming the dielectric constant is unchanged from the charge-free limit. Solid lines denote the two-phase boundary. Dashed lines connecting empty square symbols denote tie lines connecting co-existing phases. Solid markers denote the critical points.

Polyelectrolyte added-salt phase behavior

We next investigate the effect of added salt on the phase behavior of complex coacervates at a fixed temperature, $\bar{T} = 0.015$. As shown in Figure 2.8, both the implicit- and explicit-solvent theories predict that increasing the salt concentration progressively suppresses phase separation, causing the coexistence region to shrink and eventually close at sufficiently high salt concentrations. This behavior reflects the well-established screening effect of added salt, which weakens the electrostatic correlations responsible for coacervation.

Although the overall phase boundaries predicted by the two theories are qualitatively similar, the theories predict different salt-partitioning behavior, as indicated by the tie lines. As shown in Figure 2.8(a), the implicit-solvent treatment predicts nearly horizontal tie lines throughout the coexistence region, indicating only weak salt partitioning between the coacervate and supernatant. This behavior follows from the assumption of a compositionally uniform dielectric constant, leaving only a relatively weak balance between electrostatic and mixing-entropy contributions to salt partitioning. These effects are sufficiently small that they do not produce a visually significant slope in the tie lines.

In contrast, the explicit-solvent theory predicts a pronounced evolution of the tie-line slopes, as shown in Figure 2.8(b). At low salt concentrations, the tie lines have positive slopes, indicating preferential accumulation of salt within the coacervate.

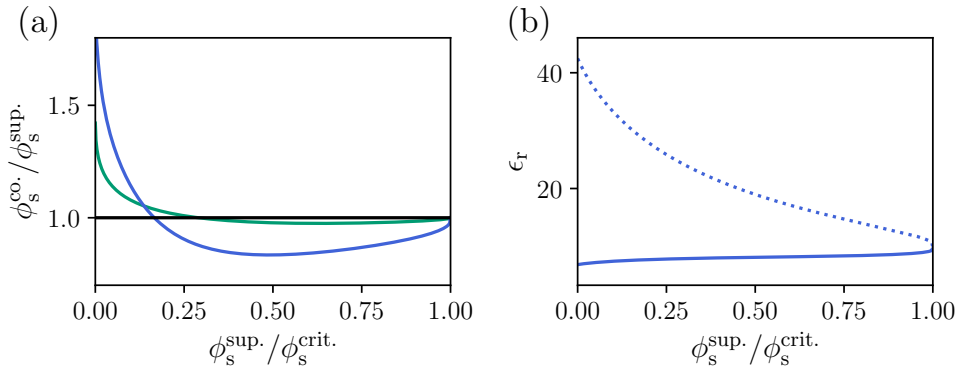


Figure 2.9: (a) Salt partition coefficient with varying salt concentration in the supernatant phase from the phase diagrams in 2.8 for implicit (green) and explicit (blue) solvent treatments. (b) Dielectric constants in the coacervate (solid) and supernatant (dotted) phases for the explicit solvent systems. Implicit solvent systems assume a dielectric constant of ≈ 42 for all conditions.

As the overall salt concentration increases, the tie-line slope gradually decreases and eventually becomes negative near the critical point. The corresponding salt partition coefficient, ϕ_s^{co}/ϕ_s^{sup}, is shown in Figure 2.9(a) for both treatments. The explicit-solvent theory predicts a transition from salt enrichment in the coacervate, $\phi_s^{co}/\phi_s^{sup} > 1$, at low salt concentrations to preferential partitioning into the supernatant, $\phi_s^{co}/\phi_s^{sup} < 1$, at intermediate salt concentrations, before the partition coefficient approaches unity at the critical point. In contrast, the implicit-solvent theory predicts only weak deviations from unity throughout the coexistence region. The slight enrichment of salt in the coacervate predicted by the implicit-solvent treatment at low salt concentrations arises from the initial enhancement of electrostatic correlations upon the addition of salt, before screening becomes dominant [138]. The explicit-solvent treatment, however, predicts substantially larger variations in the partition coefficient, similar to those observed experimentally[203, 204, 205, 206, 207, 208, 209].

The physical origin of this behavior is illustrated in Figure 2.9(b). Throughout the coexistence region, the coacervate possesses a substantially lower dielectric constant than the supernatant because of its higher charge concentration and its correspondingly lower concentration of dipolar solvent. At low salt concentrations, this large dielectric contrast produces a substantially larger Bjerrum length in the coacervate, making it energetically favorable for ions to partition into the coacervate despite the stronger electrostatic screening within this phase.

As additional salt is introduced, the dielectric decrement in the supernatant reduces the dielectric contrast between the coexisting phases, while electrostatic screening simultaneously weakens the ion correlations. Consequently, the energetic advantage associated with ion accumulation in the coacervate diminishes. Mixing entropy and the weaker electrostatic screening in the supernatant then become increasingly important, leading to preferential salt partitioning into the supernatant [210].

These results demonstrate that dielectric heterogeneity provides an additional thermodynamic driving force for ion partitioning. By allowing the dielectric constant to evolve self-consistently with the local composition, the present theory captures the pronounced evolution of salt partitioning that is absent from continuum treatments employing a homogeneous dielectric medium.

2.4 Conclusion

In this chapter, we used molecular simulations and explicit-solvent liquid-state theory to examine how ion–dipole coupling governs the temperature-dependent phase behavior of charged fluids and complex coacervates. In contrast to conventional implicit-solvent descriptions, in which the solvent is reduced to a spatially uniform dielectric background, the present framework retains dipolar solvent fluctuations as an explicit thermodynamic degree of freedom. The dielectric response therefore emerges self-consistently from the temperature and local composition, allowing regions with different charge concentrations to possess distinct dielectric constants and Bjerrum lengths.

This self-consistent treatment reveals that the electrostatic response of a dipolar solvent is governed by competition between thermal disruption of dipolar correlations and the many-body suppression of dipolar shielding by charged species. Although the dielectric constant of the bulk solvent decreases upon heating, this macroscopic response alone does not determine the thermodynamics of phase separation. Implicit-solvent theories that prescribe the temperature-dependent dielectric constant of the pure solvent predict that electrostatic correlations strengthen upon heating and consequently favor LCST behavior. Explicitly accounting for ion–dipole coupling instead produces a concentration-dependent reversal of this thermal response and leads intrinsically to UCST behavior. The local electrostatic environment controlling ionic correlations can therefore differ qualitatively from that inferred from the dielectric properties of the bulk solvent[199, 200, 201].

When applied to complex coacervation, this dielectric feedback allows the coacer-

vate and supernatant to develop different dielectric environments. Phase separation modifies the local concentrations of polymer, ions, and dipolar solvent, which changes the dielectric response and, in turn, alters the electrostatic correlations stabilizing the coexisting phases. The resulting dielectric inhomogeneity provides a mechanism for UCST behavior that is absent from theories employing a compositionally uniform dielectric constant. Our analysis further shows that phase stability is governed predominantly by the Bjerrum length within the polymer-rich coacervate. This quantity is not constrained to follow the Bjerrum length of the supernatant, as is necessarily assumed in an implicit-solvent description.

The extension of the theory to coacervates containing added salt further demonstrates the central role of dielectric inhomogeneity in ion partitioning. At low salt concentrations, the lower dielectric constant of the coacervate strengthens electrostatic correlations sufficiently to overcome the greater degree of electrostatic screening within the dense phase, leading to preferential salt accumulation in the coacervate. As the salt concentration increases, the difference in dielectric contrast between the phases diminishes, while screening and the translational entropy of the mobile ions become increasingly important. The balance between these contributions ultimately reverses the direction of salt partitioning. The theory therefore provides a unified thermodynamic explanation for the evolution and inversion of tie-line slopes across the phase diagram.

More generally, these results demonstrate that the phase behavior of charged fluids cannot be inferred from isolated pair interactions alone. Potentials of mean force between two charges are frequently used as proxies for phase-separation propensity, yet they neglect the collective reorganization of the surrounding dipolar solvent. Consequently, an increase in the effective attraction between an isolated pair of charges upon heating does not necessarily imply LCST behavior. Phase separation is instead controlled by the coupling of electrostatic interactions to many-body solvent-mediated correlations, which can reverse the trend suggested by the pair potential.

These findings also illustrate both the utility and the limitations of reducing complex charged systems to a simplified set of interactions. By isolating electrostatics, we find that explicit ion–dipole coupling establishes an intrinsic tendency towards UCST behavior. The occurrence of both UCST and LCST behavior across different experimental polyelectrolyte systems likely reflects competition between this electrostatic baseline and additional chemistry-specific interactions, including hy-

drophobic association and hydrogen bonding, which may favor LCST behavior [12, 3]. Electrostatics thus provides a baseline thermodynamic driving force, while short-range interactions fine-tune the balance between different classes of phase behavior.

Overall, this work establishes dipolar solvent fluctuations as an active component of the thermodynamics rather than a passive dielectric background. Incorporating explicit ion–dipole coupling and dielectric feedback substantially extends the predictive capabilities of liquid-state theories and provides a common framework for understanding critical behavior, dielectric inhomogeneity, and ion partitioning in charged polymer solutions. These results point to a growing need for explicit-solvent descriptions in quantitative models of real polyelectrolyte systems [211, 156, 157]. The framework may be extended naturally to sequence-defined polyelectrolytes, intrinsically disordered proteins, multivalent electrolytes, and biological condensates, in which spatial variations in solvent polarization may be similarly important.

References

[3] Pierre J. Walker and Zhen-Gang Wang. "Anomalous Phase Behavior of Polymer–Ionic Liquid Mixtures". In: *J. Phys. Chem. B* 129 (Nov. 2025). ISSN: 1520-6106. DOI: 10.1021/acs.jpcb.5c04858.

[4] Seola Lee et al. "Molecular control via dynamic bonding enables material responsiveness in additively manufactured metallo-polyelectrolytes". In: *Nat. Commun.* 15.1 (Aug. 2024), p. 6850. ISSN: 2041-1723. DOI: 10.1038/s41467-024-50860-6.

[6] Pierre J. Walker and Zhen-Gang Wang. "Explicit Solvents Reverse Electrostatic Phase Behavior in Charged Fluids". In: *In preparation* (2026).

[7] Pierre J. Walker et al. "Dielectric Inhomogeneity Governs Phase Behavior and Salt Partitioning in Complex Coacervates". In: *In preparation* (2026).

[12] Vico Tenberg et al. *Thermodynamic Modeling of mRNA with the Addition of Precipitants*. Oct. 2025. DOI: 10.1101/2025.10.18.683252.

[14] Benjamin B. Ye, Pierre J. Walker, and Zhen-Gang Wang. "MDCraft: A Python assistant for performing and analyzing molecular dynamics simulations of soft matter systems". In: *J. Open Source Softw.* 9.100 (Aug. 2024), p. 7013. ISSN: 2475-9066. DOI: 10.21105/joss.07013.

[20] Pierre J. Walker, Hon-Wa Yew, and Andrés Riedemann. "Clapeyron.jl: An Extensible, Open-Source Fluid Thermodynamics Toolkit". In: *Ind. Eng. Chem. Res.* 61.20 (May 2022), pp. 7130–7153. ISSN: 0888-5885, 1520-5045. DOI: 10.1021/acs.iecr.2c00326.

[29] P. Debye and E. Hückel. “Zur Theorie der Elektrolyte. I. Gefrierpunktserniedrigung und verwandte Erscheinungen”. In: *Phys. Z.* 24 (1923), pp. 185–206.

[30] Lars Onsager. “Zur Theorie der Electrolyte. I”. In: *Phys. Z.* 27 (1926), pp. 388–392.

[31] Lars Onsager. “Zur Theorie der Electrolyte. II”. In: *Phys. Z.* 28 (1927), pp. 277–298.

[36] Gerald S. Manning. “Limiting Laws and Counterion Condensation in Polyelectrolyte Solutions I. Colligative Properties”. In: *J. Chem. Phys.* 51.3 (Aug. 1969), pp. 924–933. ISSN: 0021-9606. DOI: 10.1063/1.1672157.

[44] J. T. G. Overbeek and M. J. Voorn. “Phase separation in polyelectrolyte solutions. Theory of complex coacervation”. In: *J. Cell. Comp. Physiol.* 49.S1 (1957), pp. 7–26. ISSN: 1553-0809. DOI: 10.1002/jcp.1030490404.

[82] L. Blum. “Mean spherical model for asymmetric electrolytes”. In: *Mol. Phys.* 30.5 (Nov. 1975), pp. 1529–1535. ISSN: 0026-8976. DOI: 10.1080/00268977500103051.

[84] Charles E. Sing, Jos W. Zwanikken, and Monica Olvera de la Cruz. “Ion Correlation-Induced Phase Separation in Polyelectrolyte Blends”. In: *ACS Macro Lett.* 2.11 (Nov. 2013), pp. 1042–1046. DOI: 10.1021/mz400511r.

[88] Pengfei Zhang et al. “Salting-Out and Salting-In of Polyelectrolyte Solutions: A Liquid-State Theory Study”. In: *Macromolecules* 49.24 (Dec. 2016), pp. 9720–9730. ISSN: 0024-9297, 1520-5835. DOI: 10.1021/acs.macromol.6b02160.

[90] Andrew S. Ylitalo et al. “Electrostatic Correlations and Temperature-Dependent Dielectric Constant Can Model LCST in Polyelectrolyte Complex Coacervation”. In: *Macromolecules* 54.24 (Dec. 2021), pp. 11326–11337. ISSN: 0024-9297, 1520-5835. DOI: 10.1021/acs.macromol.1c02000.

[98] L. Blum and J. S. Hoeye. “Mean spherical model for asymmetric electrolytes. 2. Thermodynamic properties and the pair correlation function”. In: *J. Phys. Chem.* 81.13 (June 1977), pp. 1311–1316. ISSN: 0022-3654, 1541-5740. DOI: 10.1021/j100528a019.

[102] Jarrett Revels, Miles Lubin, and Theodore Papamarkou. *Forward-Mode Automatic Differentiation in Julia*. July 2016.

[105] M. Muthukumar. “Phase Diagram of Polyelectrolyte Solutions: Weak Polymer Effect”. In: *Macromolecules* 35.24 (Nov. 2002), pp. 9142–9145. ISSN: 0024-9297. DOI: 10.1021/ma021456z.

[106] A. V. Ermoshkin and M. Olvera de la Cruz. “A Modified Random Phase Approximation of Polyelectrolyte Solutions”. In: *Macromolecules* 36.20 (Oct. 2003), pp. 7824–7832. ISSN: 0024-9297. DOI: 10.1021/ma034148p.

[116] Charles E. Sing and Sarah L. Perry. “Recent progress in the science of complex coacervation”. In: *Soft Matter* 16.12 (Mar. 2020), pp. 2885–2914. ISSN: 1744-6848. DOI: 10.1039/D0SM00001A.

[124] J. W. Jiang et al. “Thermodynamic properties and phase equilibria of charged hard sphere chain model for polyelectrolyte solutions”. In: *Mol. Phys.* 99.13 (July 2001), pp. 1121–1128. ISSN: 0026-8976. DOI: 10.1080/00268970110043414.

[126] M. Gouy. “Sur la constitution de la charge électrique à la surface d’un électrolyte”. fr. In: *J. Phys. Théor. Appl.* 9.1 (1910), pp. 457–468. ISSN: 0368-3893, 2507-6485. DOI: 10.1051/jphystap:019100090045700.

[127] David Leonard Chapman. “LI. A contribution to the theory of electrocapillarity”. In: *Philos. Mag.* 25.148 (Apr. 1913), pp. 475–481. ISSN: 1941-5982. DOI: 10.1080/14786440408634187.

[128] Carl Wagner. “Theorie der Alterung von Niederschlägen durch Umlösen (Ostwald-Reifung)”. de. In: *Z. Elektrochem. Ber. Bunsenges. Phys. Chem.* 65.7-8 (1961), pp. 581–591. ISSN: 0005-9021. DOI: 10.1002/bbpc.19610650704.

[129] Artem M. Rumyantsev et al. “Controlling Complex Coacervation via Random Polyelectrolyte Sequences”. In: *ACS Macro Lett.* (Sept. 2019). DOI: 10.1021/acsmacrolett.9b00494.

[130] Artem M. Rumyantsev, Alexey A. Gavrilov, and Albert Johner. “Complete Diagram of Conformational Regimes for Polyampholytic Disordered Proteins”. In: *Macromolecules* 57.11 (June 2024), pp. 5533–5544. ISSN: 0024-9297. DOI: 10.1021/acs.macromol.4c00429.

[131] Chi-Lun Lee and Murugappan Muthukumar. “Phase behavior of polyelectrolyte solutions with salt”. In: *J. Chem. Phys.* 130.2 (Jan. 2009), p. 024904. ISSN: 0021-9606. DOI: 10.1063/1.3054140.

[132] M. Muthukumar. “Electrostatic correlations in polyelectrolyte solutions”. In: *Polym. Sci., Ser. A* 58.6 (Nov. 2016), pp. 852–863. ISSN: 1555-6107. DOI: 10.1134/S0965545X16060146.

[133] M. Muthukumar. “Theory of counter-ion condensation on flexible polyelectrolytes: Adsorption mechanism”. In: *J. Chem. Phys.* 120.19 (May 2004), pp. 9343–9350. ISSN: 0021-9606. DOI: 10.1063/1.1701839.

[134] Kris T. Delaney and Glenn H. Fredrickson. “Theory of polyelectrolyte complexation—Complex coacervates are self-coacervates”. In: *J. Chem. Phys.* 146.22 (June 2017), p. 224902. ISSN: 0021-9606. DOI: 10.1063/1.4985568.

[135] Kevin Shen and Zhen-Gang Wang. “Electrostatic correlations and the polyelectrolyte self energy”. In: *J. Chem. Phys.* 146.8 (Feb. 2017), p. 084901. ISSN: 0021-9606. DOI: 10.1063/1.4975777.

[136] Pengfei Zhang et al. “Polyelectrolyte complex coacervation: Effects of concentration asymmetry”. In: *J. Chem. Phys.* 149.16 (July 2018), p. 163303. ISSN: 0021-9606. DOI: 10.1063/1.5028524.

[137] Xu Chen, Er-Qiang Chen, and Shuang Yang. “Multiphase Coacervation of Polyelectrolytes Driven by Asymmetry of Charged Sequence”. In: *Macromolecules* 56.1 (Jan. 2023), pp. 3–14. ISSN: 0024-9297. DOI: 10.1021/acs.macromol.2c01205.

[138] Pengfei Zhang et al. “Salt Partitioning in Complex Coacervation of Symmetric Polyelectrolytes”. In: *Macromolecules* 51.15 (Aug. 2018), pp. 5586–5593. ISSN: 0024-9297. DOI: 10.1021/acs.macromol.8b00726.

[139] Scott P. O. Danielsen et al. “Small ion effects on self-coacervation phenomena in block polyampholytes”. In: *J. Chem. Phys.* 151.3 (July 2019), p. 034904. ISSN: 0021-9606. DOI: 10.1063/1.5109045.

[140] Ashley R. Knoerdel, Whitney C. Blocher McTigue, and Charles E. Sing. “Transfer Matrix Model of pH Effects in Polymeric Complex Coacervation”. In: *J. Phys. Chem. B* 125.31 (Aug. 2021), pp. 8965–8980. ISSN: 1520-6106. DOI: 10.1021/acs.jpcb.1c03065.

[141] Alejandro Gallegos and Jianzhong Wu. “Charge Regulation of Natural Amino Acids in Aqueous Solutions”. In: *J. Chem. Eng. Data* 65.12 (Dec. 2020), pp. 5630–5642. ISSN: 0021-9568. DOI: 10.1021/acs.jced.0c00625.

[142] Alejandro Gallegos and Jianzhong Wu. “Hierarchical Model of Weak Polyelectrolytes with Ionization and Conformation Consistency”. In: *Macromolecules* 56.12 (June 2023), pp. 4760–4772. ISSN: 0024-9297, 1520-5835. DOI: 10.1021/acs.macromol.2c01910.

[143] David Beyer, Christian Holm, and Zhen-Gang Wang. “A Sequence-Specific Theory for Charge-Regulating IDPs”. In: *ChemRxiv* 2026.0202 (). DOI: 10.26434/chemrxiv.10001808/v1.

[144] James McCarty et al. “Complete Phase Diagram for Liquid–Liquid Phase Separation of Intrinsically Disordered Proteins”. In: *J. Phys. Chem. Lett.* 10.8 (Apr. 2019), pp. 1644–1652. DOI: 10.1021/acs.jpclett.9b00099.

[145] Artem M. Rumyantsev and Albert Johner. “Salt-Added Solutions of Markov Polyampholytes: Diagram of States, Antipolyelectrolyte Effect, and Self-Coacervate Dynamics”. en. In: *Macromolecules* 56.13 (July 2023), pp. 5201–5216. ISSN: 0024-9297, 1520-5835. DOI: 10.1021/acs.macromol.3c00512.

[146] David F. Ilten. “DETHERM: Thermophysical property data for the optimization of heat-transfer equipment”. In: *J. Chem. Inf. Comput. Sci.* 31.1 (Feb. 1991), pp. 160–167. ISSN: 0095-2338. DOI: 10.1021/ci00001a029.

[147] Sabin Adhikari, Vivek M. Prabhu, and Murugappan Muthukumar. “Lower Critical Solution Temperature Behavior in Polyelectrolyte Complex Coacervates”. In: *Macromolecules* 52.18 (Sept. 2019), pp. 6998–7004. ISSN: 0024-9297. DOI: 10.1021/acs.macromol.9b01201.

[148] Komol Kanta Sharker et al. “Upper Critical Solution Temperature (UCST) Behavior of Polystyrene-Based Polyampholytes in Aqueous Solution”. In: *Polymers* 11.2 (Feb. 2019), p. 265. ISSN: 2073-4360. DOI: 10.3390/polym11020265.

[149] Seung-Hwan Oh and Soo-Hyung Choi. “Upper Critical Solution Temperature (UCST) Behavior of Polyguanidinium in Aqueous Media”. In: *Macromolecules* 57.15 (Aug. 2024), pp. 7449–7461. ISSN: 0024-9297. DOI: 10.1021/acs.macromol.4c01095.

[150] Minglun Li et al. “Salt-Induced Liquid–Liquid Phase Separation: Combined Experimental and Theoretical Investigation of Water–Acetonitrile–Salt Mixtures”. In: *J. Am. Chem. Soc.* 143.2 (Jan. 2021), pp. 773–784. ISSN: 0002-7863, 1520-5126. DOI: 10.1021/jacs.0c09420.

[151] J. B. Hasted, D. M. Ritson, and C. H. Collie. “Dielectric Properties of Aqueous Ionic Solutions. Parts I and II”. In: *J. Chem. Phys.* 16 (Jan. 1948). ADS Bibcode: 1948JChPh..16....1H, pp. 1–21. ISSN: 0021-9606. DOI: 10.1063/1.1746645.

[152] Cameron J. Shock et al. “Molecular dynamics simulations of the dielectric constants of salt-free and salt-doped polar solvents”. In: *J. Chem. Phys.* 159.13 (Oct. 2023), p. 134507. ISSN: 0021-9606. DOI: 10.1063/5.0165481.

[153] Bjørn Maribo-Mogensen, Georgios M. Kontogeorgis, and Kaj Thomsen. “Modeling of Dielectric Properties of Aqueous Salt Solutions with an Equation of State”. In: *J. Phys. Chem. B* 117.36 (Sept. 2013), pp. 10523–10533. ISSN: 1520-6106, 1520-5207. DOI: 10.1021/jp403375t.

[154] Charles E. Sing and Jian Qin. “Bridging Field Theory and Ion Pairing in the Modeling of Polyelectrolytes and Complex Coacervation”. In: *Macromolecules* (July 2023). DOI: 10.1021/acs.macromol.3c01020.

[155] Sabin Adhikari, Michael A. Leaf, and Murugappan Muthukumar. “Polyelectrolyte complex coacervation by electrostatic dipolar interactions”. en. In: *J. Chem. Phys.* 149.16 (Oct. 2018), p. 163308. ISSN: 0021-9606, 1089-7690. DOI: 10.1063/1.5029268.

[156] Michael Beckinghausen and Andrew J. Spakowitz. “Interplay of Polymer Structure, Solvent Ordering, and Charge Fluctuations in Polyelectrolyte Solution Thermodynamics”. In: *Macromolecules* 56.1 (Jan. 2023), pp. 136–152. ISSN: 0024-9297. DOI: 10.1021/acs.macromol.2c01826.

[157] Kayley Alonso et al. “An explicit solvent model of coacervate structure and thermodynamics”. In: *J. Chem. Phys.* 164.2 (Jan. 2026), p. 024904. ISSN: 0021-9606. DOI: 10.1063/5.0305035.

[158] C.G. Malmberg and A.A. Maryott. "Dielectric constant of water from 0 to 100 C". en. In: *J. Res. Natl. Bur. Stand.* 56.1 (Jan. 1956), p. 1. ISSN: 0091-0635. DOI: 10.6028/jres.056.001.

[159] Shensheng Chen and Zhen-Gang Wang. "Driving force and pathway in polyelectrolyte complex coacervation". In: *Proc. Natl. Acad. Sci. U.S.A.* 119.36 (Sept. 2022), e2209975119. DOI: 10.1073/pnas.2209975119.

[160] L. Blum and D. Q. Wei. "Analytical solution of the mean spherical approximation for an arbitrary mixture of ions in a dipolar solvent". In: *J. Chem. Phys.* 87.1 (July 1987), pp. 555–565. ISSN: 0021-9606. DOI: 10.1063/1.453604.

[161] Dongqing Wei and Lesser Blum. "The mean spherical approximation for an arbitrary mixture of ions in a dipolar solvent: Approximate solution, pair correlation functions, and thermodynamics". In: *J. Chem. Phys.* 87.5 (Sept. 1987), pp. 2999–3007. ISSN: 0021-9606. DOI: 10.1063/1.453036.

[162] Tomáš Boublík. "Hard-Sphere Equation of State". In: *J. Chem. Phys.* 53.1 (July 1970), pp. 471–472. ISSN: 0021-9606, 1089-7690. DOI: 10.1063/1.1673824.

[163] G. A. Mansoori et al. "Equilibrium Thermodynamic Properties of the Mixture of Hard Spheres". In: *J. Chem. Phys.* 54.4 (Feb. 1971), pp. 1523–1525. ISSN: 0021-9606, 1089-7690. DOI: 10.1063/1.1675048.

[164] L.S. Ornstein and F. Zernike. "Accidental deviations of density and opalescence at the critical point of a single substance". In: *Proc. K. Ned. Akad. Wet., Ser. B: Phys. Sci.* 17 (Jan. 1914). ADS Bibcode: 1914KNAB...17..793., pp. 793–806.

[165] M. S. Wertheim. "Fluids with highly directional attractive forces. I. Statistical thermodynamics". In: *J. Stat. Phys.* 35.1-2 (Apr. 1984), pp. 19–34. ISSN: 0022-4715, 1572-9613. DOI: 10.1007/BF01017362.

[166] M. S. Wertheim. "Fluids with highly directional attractive forces. II. Thermodynamic perturbation theory and integral equations". In: *J. Stat. Phys.* 35.1-2 (Apr. 1984), pp. 35–47. ISSN: 0022-4715, 1572-9613. DOI: 10.1007/BF01017363.

[167] M. S. Wertheim. "Fluids with highly directional attractive forces. III. Multiple attraction sites". In: *J. Stat. Phys.* 42.3-4 (Feb. 1986), pp. 459–476. ISSN: 0022-4715, 1572-9613. DOI: 10.1007/BF01127721.

[168] M. S. Wertheim. "Fluids with highly directional attractive forces. IV. Equilibrium polymerization". In: *J. Stat. Phys.* 42.3-4 (Feb. 1986), pp. 477–492. ISSN: 0022-4715, 1572-9613. DOI: 10.1007/BF01127722.

[169] David Chandler and Hans C. Andersen. "Optimized Cluster Expansions for Classical Fluids. II. Theory of Molecular Liquids". In: *J. Chem. Phys.* 57.5 (Sept. 1972), pp. 1930–1937. ISSN: 0021-9606. DOI: 10.1063/1.1678513.

[170] Hans C. Andersen, David Chandler, and John D. Weeks. "Optimized Cluster Expansions for Classical Fluids. III. Applications to Ionic Solutions and Simple Liquids". In: *J. Chem. Phys.* 57.7 (Oct. 1972), pp. 2626–2631. ISSN: 0021-9606. DOI: 10.1063/1.1678641.

[171] Suzanne Hudson and Hans C. Andersen. "Optimized cluster expansions for classical fluids. IV. Primitive model electrolyte solutions". In: *J. Chem. Phys.* 60.5 (Mar. 1974), p. 2188. ISSN: 0021-9606. DOI: 10.1063/1.1681337.

[172] Hans C. Andersen, David Chandler, and John D. Weeks. "Roles of Repulsive and Attractive Forces in Liquids : The Equilibrium Theory of Classical Fluids". en. In: *Advances in Chemical Physics*. _eprint: https://onlinelibrary.wiley.com/doi/pdf/10.1002 John Wiley & Sons, Ltd, 1976, pp. 105–156. ISBN: 978-0-470-14253-0. DOI: 10.1002/9780470142530.ch2.

[173] M. S. Wertheim. "Exact Solution of the Percus-Yevick Integral Equation for Hard Spheres". en. In: *Phys. Rev. Lett.* 10.8 (Apr. 1963), pp. 321–323. ISSN: 0031-9007. DOI: 10.1103/PhysRevLett.10.321.

[174] Jean-Pierre Simonin. "On the solution of the mean-spherical approximation (MSA) for ions in a dipolar solvent in the general case". In: *AIP Adv.* 10.9 (Sept. 2020), p. 095213. ISSN: 2158-3226. DOI: 10.1063/5.0022864.

[175] Jean-Pierre Simonin and Johan S. Høye. "Full solution to the mean spherical approximation (MSA) for an arbitrary mixture of ions in a dipolar solvent". In: *J. Chem. Phys.* 155.11 (Sept. 2021), p. 114502. ISSN: 0021-9606, 1089-7690. DOI: 10.1063/5.0064188.

[176] L. Blum and A. J. Torruella. "Invariant Expansion for Two-Body Correlations: Thermodynamic Functions, Scattering, and the Ornstein—Zernike Equation". In: *J. Chem. Phys.* (1972). DOI: 10.1063/1.1676864.

[177] L. Blum. "Invariant expansion III: The general solution of the mean spherical model for neutral spheres with electostatic interactions". In: *J. Chem. Phys.* 58.8 (Apr. 1973), pp. 3295–3303. ISSN: 0021-9606. DOI: 10.1063/1.1679655.

[178] M. S. Wertheim. "Exact Solution of the Mean Spherical Model for Fluids of Hard Spheres with Permanent Electric Dipole Moments". In: *J. Chem. Phys.* 55.9 (Nov. 1971), pp. 4291–4298. ISSN: 0021-9606. DOI: 10.1063/1.1676751.

[179] Aidan P. Thompson et al. "LAMMPS - a flexible simulation tool for particle-based materials modeling at the atomic, meso, and continuum scales". In: *Comput. Phys. Commun.* 271 (Feb. 2022), p. 108171. ISSN: 0010-4655. DOI: 10.1016/j.cpc.2021.108171.

[180] Shūichi Nosé. "A molecular dynamics method for simulations in the canonical ensemble". In: *Mol. Phys.* 52.2 (June 1984), pp. 255–268. ISSN: 0026-8976. DOI: 10.1080/00268978400101201.

[181] William G. Hoover. "Canonical dynamics: Equilibrium phase-space distributions". In: *Phys. Rev. A* 31.3 (Mar. 1985), pp. 1695–1697. DOI: 10.1103/PhysRevA.31.1695.

[182] Juan J. Cerdà et al. "P3M algorithm for dipolar interactions". In: *J. Chem. Phys.* 129.23 (Dec. 2008), p. 234104. ISSN: 0021-9606. DOI: 10.1063/1.3000389.

[183] Kurt Kremer and Gary S. Grest. "Dynamics of entangled linear polymer melts: A molecular-dynamics simulation". In: *J. Chem. Phys.* 92.8 (Apr. 1990), pp. 5057–5086. ISSN: 0021-9606, 1089-7690. DOI: 10.1063/1.458541.

[184] L. Martínez et al. "PACKMOL: A package for building initial configurations for molecular dynamics simulations". In: *J. Comput. Chem.* 30.13 (Oct. 2009), pp. 2157–2164. ISSN: 01928651, 1096987X. DOI: 10.1002/jcc.21224.

[185] E. Duboué-Dijon et al. "A practical guide to biologically relevant molecular simulations with charge scaling for electronic polarization". In: *J. Chem. Phys.* 153.5 (Aug. 2020), p. 050901. ISSN: 0021-9606. DOI: 10.1063/5.0017775.

[186] Martin Neumann. "Dipole moment fluctuation formulas in computer simulations of polar systems". In: *Mol. Phys.* 50.4 (Nov. 1983), pp. 841–858. ISSN: 0026-8976, 1362-3028. DOI: 10.1080/00268978300102721.

[187] Naveen Michaud-Agrawal et al. "MDAnalysis: A toolkit for the analysis of molecular dynamics simulations". In: *J. Comput. Chem.* 32.10 (July 2011), pp. 2319–2327. ISSN: 01928651. DOI: 10.1002/jcc.21787.

[188] Eric Darve, David Rodríguez-Gómez, and Andrew Pohorille. "Adaptive biasing force method for scalar and vector free energy calculations". In: *J. Chem. Phys.* 128.14 (Apr. 2008), p. 144120. ISSN: 0021-9606. DOI: 10.1063/1.2829861.

[189] Jérome Hénin et al. "Exploring Multidimensional Free Energy Landscapes Using Time-Dependent Biases on Collective Variables". In: *J. Chem. Theory Comput.* 6.1 (Jan. 2010), pp. 35–47. ISSN: 1549-9618. DOI: 10.1021/ct9004432.

[190] Giacomo Fiorin, Michael L. Klein, and Jérôme Hénin. "Using collective variables to drive molecular dynamics simulations". In: *Mol. Phys.* 111.22-23 (Dec. 2013). _eprint: https://doi.org/10.1080/00268976.2013.813594, pp. 3345–3362. ISSN: 0026-8976. DOI: 10.1080/00268976.2013.813594.

[191] P. T. Cummings and L. Blum. "Dielectric constant of dipolar hard sphere mixtures". In: *J. Chem. Phys.* 85.11 (Dec. 1986), pp. 6658–6667. ISSN: 0021-9606. DOI: 10.1063/1.451447.

[192] Chunyi Zhang et al. “Why Dissolving Salt in Water Decreases Its Dielectric Permittivity”. In: *Phys. Rev. Lett.* 131.7 (Aug. 2023), p. 076801. DOI: 10.1103/PhysRevLett.131.076801.

[193] Samuel Varner, Christopher Balzer, and Zhen-Gang Wang. “Entropic Origin of Ionic Interactions in Polar Solvents”. In: *J. Phys. Chem. B* 127.19 (May 2023), pp. 4328–4337. ISSN: 1520-6106. DOI: 10.1021/acs.jpcb.3c00588.

[194] Amir Levy, David Andelman, and Henri Orland. “Dielectric Constant of Ionic Solutions: A Field-Theory Approach”. In: *Phys. Rev. Lett.* 108.22 (May 2012), p. 227801. DOI: 10.1103/PhysRevLett.108.227801.

[195] Sachin Raj Pandey, Matthias Ballauff, and Roland R. Netz. “Counterion-release versus dielectric entropy: insights from the Gouy-Chapman model for a uniformly charged plate”. en. In: *Colloid Polym. Sci.* 304.4 (Apr. 2026), pp. 715–725. ISSN: 1435-1536. DOI: 10.1007/s00396-025-05424-5.

[196] Ram M. Adar, Tomer Markovich, and David Andelman. “Bjerrum pairs in ionic solutions: A Poisson-Boltzmann approach”. In: *J. Chem. Phys.* 146.19 (May 2017), p. 194904. ISSN: 0021-9606. DOI: 10.1063/1.4982885.

[197] Douglas J. Grzetic, Kris T. Delaney, and Glenn H. Fredrickson. “Contrasting Dielectric Properties of Electrolyte Solutions with Polar and Polarizable Solvents”. In: *Phys. Rev. Lett.* 122.12 (Mar. 2019), p. 128007. DOI: 10.1103/PhysRevLett.122.128007.

[198] Samim Ali, Markus Bleuel, and Vivek M. Prabhu. “Lower Critical Solution Temperature in Polyelectrolyte Complex Coacervates”. In: *ACS Macro Lett.* 8.3 (Mar. 2019), pp. 289–293. DOI: 10.1021/acsmacrolett.8b00952.

[199] Buyukdagli Sahin and Blossey Ralf. “Nonlocal and nonlinear electrostatics of a dipolar Coulomb fluid”. en. In: *J. Phys.: Condens. Matter* 26.28 (June 2014), p. 285101. ISSN: 0953-8984. DOI: 10.1088/0953-8984/26/28/285101.

[200] Ralf Blossey and Rudolf Podgornik. “Continuum theories of structured dielectrics”. en. In: *Europhys. Lett.* 139.2 (July 2022), p. 27002. ISSN: 0295-5075. DOI: 10.1209/0295-5075/ac7d0a.

[201] Ralf Blossey and Rudolf Podgornik. “Field theory of structured liquid dielectrics”. en. In: *Phys. Rev. Res.* 4.2 (Apr. 2022), p. 023033. ISSN: 2643-1564. DOI: 10.1103/PhysRevResearch.4.023033.

[202] Minjung Lee, Sarah L. Perry, and Ryan C. Hayward. “Complex Coacervation of Polymerized Ionic Liquids in Non-aqueous Solvents”. In: *ACS Polym. Au* 1.2 (Oct. 2021), pp. 100–106. ISSN: 2694-2453, 2694-2453. DOI: 10.1021/acspolymersau.1c00017.

[203] Qifeng Wang and Joseph B. Schlenoff. "The Polyelectrolyte Complex/Coacervate Continuum". In: *Macromolecules* 47.9 (May 2014), pp. 3108–3116. ISSN: 0024-9297. DOI: 10.1021/ma500500q.

[204] Jingcheng Fu, Hadi M. Fares, and Joseph B. Schlenoff. "Ion-Pairing Strength in Polyelectrolyte Complexes". In: *Macromolecules* 50.3 (Feb. 2017), pp. 1066–1074. ISSN: 0024-9297. DOI: 10.1021/acs.macromol.6b02445.

[205] Ramy A. Ghostine, Rabih F. Shamoun, and Joseph B. Schlenoff. "Doping and Diffusion in an Extruded Saloplastic Polyelectrolyte Complex". In: *Macromolecules* 46.10 (May 2013), pp. 4089–4094. ISSN: 0024-9297. DOI: 10.1021/ma4004083.

[206] Joseph B. Schlenoff et al. "Ion Content of Polyelectrolyte Complex Coacervates and the Donnan Equilibrium". In: *Macromolecules* 52.23 (Dec. 2019), pp. 9149–9159. ISSN: 0024-9297. DOI: 10.1021/acs.macromol.9b01755.

[207] Lu Li et al. "Phase Behavior and Salt Partitioning in Polyelectrolyte Complex Coacervates". In: *Macromolecules* 51.8 (Apr. 2018), pp. 2988–2995. ISSN: 0024-9297, 1520-5835. DOI: 10.1021/acs.macromol.8b00238.

[208] Sean Friedowitz et al. "Looping-in complexation and ion partitioning in nonstoichiometric polyelectrolyte mixtures". In: *Sci. Adv.* 7.31 (July 2021), eabg8654. DOI: 10.1126/sciadv.abg8654.

[209] Angelika E. Neitzel et al. "Polyelectrolyte Complex Coacervation across a Broad Range of Charge Densities". In: *Macromolecules* (July 2021). DOI: 10.1021/acs.macromol.1c00703.

[210] Zhaoyang Ou and M. Muthukumar. "Entropy and enthalpy of polyelectrolyte complexation: Langevin dynamics simulations". In: *J. Chem. Phys.* 124.15 (Apr. 2006), p. 154902. ISSN: 0021-9606. DOI: 10.1063/1.2178803.

[211] Bilin Zhuang et al. "Like dissolves like: A first-principles theory for predicting liquid miscibility and mixture dielectric constant". In: *Sci. Adv.* 7.7 (Feb. 2021), eabe7275. ISSN: 2375-2548. DOI: 10.1126/sciadv.abe7275.

Chapter 3

SELF- AND SALT-INDUCED COACERVATION OF CHARGE-ASYMMETRIC POLYAMPHOLYTES

In aqueous environments, polyampholyte-like intrinsically disordered proteins (IDPs) can undergo liquid–liquid phase separation, forming a protein-rich condensate phase coexisting with a dilute supernatant phase. Previous studies have primarily focused on charge-symmetric sequences where IDPs carry an equal amount of positive and negative charges. Real-world IDPs typically possess finite net charge. Consequently, the combined influence of charge patterning and salt concentration on coacervation of charge-asymmetric IDPs remains poorly understood. In this chapter, we use a hierarchy of theoretical approaches, including a new hybrid Liquid-State Theory — gauLS — and molecular dynamics simulations to systematically investigate the phase behavior of polyampholyte-like IDPs. We demonstrate that gauLS accurately reproduces the single-chain conformation obtained from MD simulations. We show that charge blockiness is the primary molecular descriptor governing salt-free self-coacervation, whereas net charge suppresses phase separation through electrostatic repulsion and the higher translational entropy of the accompanying counterions. The addition of salt produces two competing effects: it screens the attractive electrostatic correlations responsible for coacervation while simultaneously reducing long-range repulsive interactions. Consequently, salt monotonically suppresses phase separation in charge-neutral IDPs but can initially enhance, and even induce, coacervation of moderately charge-asymmetric IDPs before eventually suppressing their phase separations at higher salt concentrations. We construct a global sequence–state diagram spanning charge blockiness and net charge, revealing that salt-induced coacervation occupies a substantial region of sequence space and is likely to be far more prevalent than previously appreciated. The predictions of gauLS show good agreement with MD simulations across the representative sequences examined. These results establish a predictive framework for understanding and designing sequence-dependent biomolecular phase behavior across a broad range of chemical and biological systems.

This chapter includes work currently in preparation: Tianyi Jin, Pierre J. Walker, Kelsey Fu, Shensheng Chen, and Zhen-Gang Wang. “Self- and salt-induced coacervation of polyampholytic intrinsically disordered proteins”. In: *In preparation*

(2026)

3.1 Introduction

Intrinsically disordered proteins (IDPs) can undergo liquid–liquid phase separation in aqueous environments, giving rise to protein-rich condensates that coexist with dilute supernatant phases. This ubiquitous phenomenon underlies the formation of membraneless organelles and plays a central role in numerous cellular processes [212, 213, 214]. Beyond their biological importance, the principles governing IDP coacervation have inspired the design of functional soft materials for applications including drug delivery, biomolecular encapsulation, and stimuli-responsive materials [116]. The stability of these condensates is highly sensitive to environmental conditions such as temperature, pH, pressure, and ionic strength, all of which alter the balance between attractive and repulsive intermolecular interactions. Consequently, relatively small environmental changes can induce substantial shifts in phase behavior and, in some cases, give rise to re-entrant phase separation, in which condensates form only over a finite range of conditions before redissolving [215, 216, 217, 218].

Among the molecular factors governing IDP phase behavior, the distribution of charged residues along the amino-acid sequence is particularly important. Numerous experimental, simulation, and theoretical studies have demonstrated that charge patterning strongly influences both single-chain conformations and phase separation [219, 220, 221, 222]. In particular, McCarty et al. [144] showed that sequences with highly segregated charged domains exhibit a substantially greater propensity for coacervation than sequences with randomly distributed charges. Experimental studies have likewise demonstrated that altering charge patterning can significantly modify the critical conditions for phase separation. However, most previous studies focused on charge-symmetric polyampholytes containing equal numbers of positively and negatively charged residues. Natural IDPs, in contrast, typically possess finite net charges [223, 222]. The net charge can introduce nontrivial electrostatic effects, as it brings additional electrostatic repulsions that compete with the attractive correlations responsible for coacervation. Consequently, the combined influence of charge blockiness, charge asymmetry, and salt concentration on IDP phase behavior remains poorly understood. Charge sequence is one of several molecular-architecture variables — alongside chain topology, examined in Chapter 4 — that can reshape intramolecular correlations without changing net charge or chain length.

Theoretical and computational approaches have been instrumental in elucidating the molecular mechanisms governing IDP phase separation and establishing sequence-dependent design principles [224, 225, 144, 139, 226]. Rather than providing a comprehensive review, we refer the reader to several recent reviews and meta-reviews [224, 117, 154]. Existing computational methods include field-theoretic methods [227, 228], the polymer reference interaction site model (PRISM) [229], the Random Phase Approximation (RPA) [230, 231, 232] and molecular dynamics (MD) simulations[233, 234, 235, 4, 236, 237, 238, 239]. Among these, RPA has become popular because of its analytical simplicity and its ability to explicitly incorporate sequence information [221]. However, its Gaussian-chain assumption often leads to an overestimation of electrostatic correlations [135]. Liquid-State (LS) theories provide a complementary framework by explicitly accounting for local packing and electrostatic correlations, but conventional implementations typically retain only nearest-neighbor connectivity (LS) [88, 136, 90, 4], thereby underestimating higher-order sequence effects. There therefore remains a need for theoretical approaches that simultaneously capture local sequence-dependent interactions and long-range conformational correlations, which can be important for charge-asymmetric IDPs.

In this work, we first extend Liquid-State Theory by incorporating explicit triplet correlations (LS-T) before introducing a hybrid embedded-chain framework, gauLS, which couples local triplet conformations to the long-range electrostatic environment of the surrounding chain. Using LS, LS-T, gauLS, and RPA, together with extensive molecular dynamics simulations, we systematically investigate how charge blockiness and salt concentration determine the coacervation of charge-asymmetric IDPs. The theoretical framework enables us to map the phase behavior of $12,741$ distinct sequences spanning the space of charge patterning and net charge.

Our results demonstrate that while charge blockiness is the primary sequence descriptor governing salt-free self-coacervation, net charge acts as an important modifier through long-range electrostatic repulsion and the introduction of small ions with high translational entropy. We identify a broad region of sequence space in which phase separation occurs only upon the addition of salt, revealing that salt-induced coacervation is not a rare phenomenon but a common outcome for moderately charge-asymmetric sequences. Together, these results establish a comprehensive sequence–state diagram for polyampholyte-like IDPs and provide a predictive framework for understanding how sequence architecture and ionic environment cooperate to regulate biomolecular condensate formation.

3.2 Methods

Sequence descriptors

Throughout this work, we consider intrinsically disordered proteins (IDPs) with a degree of polymerization of $N = 50$, similar to previous studies[219, 144]. Each sequence is characterized using two quantitative descriptors: the normalized net charge, $|Z_{\text{net}}|/N$, and the degree of charge blockiness, κ.

The normalized net charge is defined as the absolute net charge of a sequence divided by its chain length,

$$\frac{|Z_{\text{net}}|}{N}. \tag{3.1}$$

The second descriptor, κ, quantifies the degree of charge blockiness and is defined as [219]

$$\kappa_{\text{g}} = \frac{\bar{\delta}_{\text{obs},g} - \bar{\delta}_{\text{alt},g}}{\bar{\delta}_{\text{blk},g} - \bar{\delta}_{\text{alt},g}}\,. \tag{3.2}$$

Here, $\delta_{*,g}$ denotes the local charge asymmetry evaluated within a sliding window of length g. The subscripts "obs", "alt", and "blk" correspond to the sequence of interest, a maximally mixed (alternating) sequence, and a maximally blocky sequence, respectively, all having the same overall charge composition. The local charge asymmetry is given by

$$\delta_{*,g} = (f_+ - f_-)^2\,, \tag{3.3}$$

where f_+ and f_- denote the fractions of positively and negatively charged residues within the sliding window, respectively. The quantity $\bar{\delta}_{*,g}$ appearing in the definition of κ_g is obtained by averaging $\delta_{*,g}$ over all sliding windows along the sequence. Throughout this work, we use the conventional window size of $g = 5$, corresponding approximately to the blob size [219]. Unless otherwise stated, we omit the subscript and simply write κ.

For charge-neutral sequences, this definition reduces to the original descriptor proposed by Das and Pappu [219], since $\bar{\delta}_{\text{alt},g} = 0$ for a perfectly alternating sequence. By construction, κ is bounded between 0 and 1, with larger values corresponding to increasingly blocky charge patterns. For real IDP sequences containing neutral residues, the reference "alternating" and "blocky" sequences are determined through optimization by minimizing and maximizing $\bar{\delta}_{*,g}$ [240]. Neutral residues are treated as non-charged spacers when calculating the local charge asymmetry, $\delta_{*,g}$.

Furthermore, κ is approximately monotonically correlated with the normalized sequence charge decoration (nSCD) introduced by Sawle and Ghosh [241], which

has become a widely used measure of charge patterning in polyampholytes and intrinsically disordered proteins [242, 243].

It is important to note that $|Z_{\mathrm{net}}|/N$ and κ are not independent descriptors. For example, a perfectly alternating sequence ($\kappa = 0$) with an even chain length must necessarily be charge neutral. Moreover, both descriptors are many-to-one mappings: multiple distinct sequences may share identical values of $|Z_{\mathrm{net}}|/N$ and κ while exhibiting different charge arrangements.

In following sections, we examine representative sequences by systematically varying $|Z_{\mathrm{net}}|/N$ and κ. All representative sequences are listed in the Supporting Information (SI), together with their corresponding coacervation classifications. In general, three classes of sequences are considered: (1) diblock sequences; (2) triblock sequences consisting of oppositely charged terminal blocks separated by a central alternating-charge block; and (3) multiblock sequences with systematically varied charge block lengths. Finally, we consider a total of 12,741 unique sequences spanning a range of $|Z_{\mathrm{net}}|/N$, up to 0.24 (corresponding to $Z_{\mathrm{net}} = 12$) and κ, to construct the global sequence-state diagram. Larger net charges introduce substantial intra- and interchain electrostatic repulsion, which generally suppresses self-coacervation and instead favors finite-size aggregates rather than macroscopic phase separation [244]. Consequently, sequences with $Z_{\mathrm{net}} > 12$ are excluded from the present study. We also note that, under our model, sequences related by a global sign inversion (i.e., exchanging all positive and negative charges) or by sequence reversal are physically equivalent. Therefore, only one representative from each equivalence class is included in the dataset.

Theory

To investigate the phase behavior of intrinsically disordered proteins, we consider a series of complementary theoretical descriptions that differ in how they treat electrostatics interactions and chain conformations, as summarized schematically in Figure 3.1. These include the Random Phase Approximation (RPA) [232], which treats collective density fluctuations at the Gaussian level while also representing intramolecular correlations using ideal Gaussian-chain statistics ; Liquid-State Theory [124, 88] combined with Wertheim's first-order thermodynamic perturbation theory (TPT1) [165, 166, 167, 168], hereafter referred to as LS; an extension to account for next-nearest-neighbor (triplet) interactions (LS-T); and a hybrid approach developed in this work that combines the local structural description of LS-T with long-range

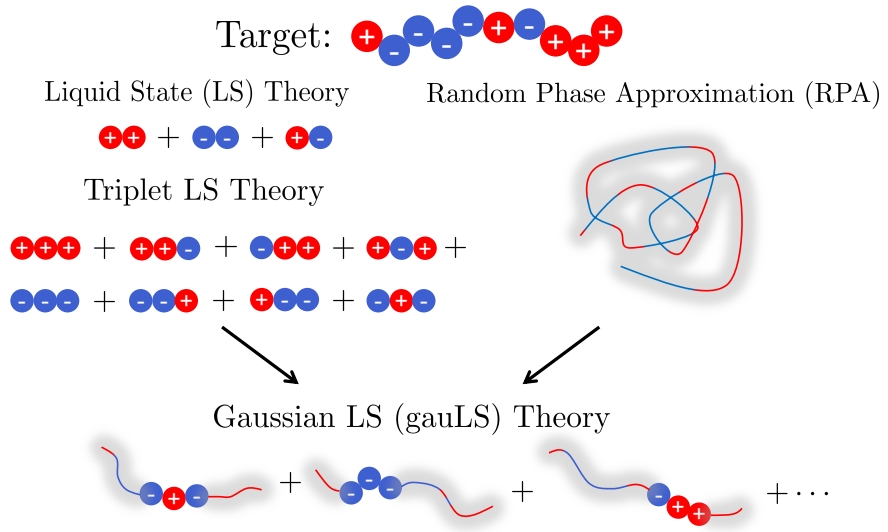


Figure 3.1: Schematic illustration of the theoretical frameworks considered in this work. The theories differ in the treatment of correlations they consider: doublet correlations are included in LS, LS-T, and gauLS; triplet correlations are included in LS-T, and gauLS; and a fixed Gaussian-chain conformation is assumed in RPA and gauLS. Throughout this work, anionic monomers are shown in blue and cationic monomers in red.

Gaussian-chain conformational statistics. We refer to this hybrid model as *gauLS*, reflecting its integration of Gaussian-chain conformations with Liquid-State Theory.

All four approaches provide an expression for the Helmholtz free energy of the system as a function of the monomer densities, $\boldsymbol{\rho}$, and the Bjerrum length, l_B,

$$\frac{F}{Vk_\mathrm{B}T} = f(\boldsymbol{\rho}, l_\mathrm{B}), \tag{3.4}$$

where f denotes the reduced free-energy density, V is the system volume, k_B is the Boltzmann constant, and T is the absolute temperature. The Bjerrum length is defined as

$$l_\mathrm{B} = \frac{\beta e^2}{4\pi\epsilon_0\epsilon_r}, \tag{3.5}$$

where $\beta = 1/(k_\mathrm{B}T)$, e is the elementary charge, ϵ_0 is the vacuum permittivity, and ϵ_r is the relative dielectric permittivity of the solvent. Physically, the Bjerrum length corresponds to the separation at which the electrostatic interaction between two elementary charges is equal to the thermal energy, $k_\mathrm{B}T$. Throughout this work, all monomers, small ions, and solvent molecules are assumed to have the same diameter, σ. The volume fraction of species i is therefore given by

$$\phi_i = \rho_i\sigma^3. \tag{3.6}$$

All theoretical models were implemented using Clapeyron.jl [20]. The source code used to reproduce all calculations is publicly available on GitHub.

Random Phase Approximation

The Random Phase Approximation (RPA) is one of the most widely used theoretical frameworks for describing electrostatic interactions and phase separation. RPA captures many qualitative trends in sequence-dependent phase behavior for polyelectrolytes [129, 245, 234, 246], polyampholytes [226, 247] with added salts [139, 145], and IDPs [221, 248]. Within RPA, concentration fluctuations are treated at the quadratic (Gaussian) level, while polymer chains are assumed to adopt Gaussian conformations that are independent of sequence, polymer concentration and salt concentration. Under these assumptions, the reduced free energy is written as the sum of an ideal mixing contribution and an electrostatic contribution,

$$f = f_{\mathrm{FH}} + f_{\mathrm{ele.}}, \tag{3.7}$$

where the subscripts FH and ele. denote the Flory–Huggins mixing and electrostatic contributions, respectively.

The Flory–Huggins contribution is

$$f_{\mathrm{FH}} = \sum_i \frac{\rho_i}{N_i} \ln \rho_i, \tag{3.8}$$

where N_i is the degree of polymerization of species i. This expression is evaluated subject to the incompressibility constraint

$$\sum_i \rho_i \sigma^3 = \sum_i \phi_i = 1. \tag{3.9}$$

The electrostatic contribution, adapted from Kudlay and Olvera de la Cruz [232], is expressed in Fourier space as

$$f_{\mathrm{ele.}} = \frac{1}{2} \int \mathrm{d}q \left[\ln \left(1 + u(q) \sum_i \rho_i g_i(q) \right) \right. \tag{3.10}$$

$$\left. - u(q) \sum_{i \neq \mathrm{p}} \rho_i \right]. \tag{3.11}$$

where the subscript p denotes the polymer species.

The electrostatic kernel,

$$u(q) = \frac{4\pi l_{\mathrm{B}}}{q^2(1 + \sigma^2 q^2)}, \tag{3.12}$$

accounts for the finite size of ions. At separations larger than the particle diameter, it reduces to the Coulomb potential, whereas at $r < \sigma$ the interaction saturates at the Coulomb contact energy.

For polymeric species, the sequence-dependent intramolecular structure factor is

$$g_{\mathrm{p}}(q) = \frac{1}{N} \sum_{i=1}^{N} \sum_{j=1}^{N} Z_i Z_j \exp\left[-\frac{q^2\sigma^2}{6}|i-j|\right], \tag{3.13}$$

where Z_i denotes the charge carried by monomer i. This expression corresponds to the Debye structure factor of an ideal Gaussian chain and therefore neglects any conformational changes arising from electrostatic interactions or excluded-volume effects.

Its assumption of Gaussian-chain conformations neglects chain contraction, chain expansion, and screening-induced conformational changes, leading to an overestimation of electrostatic correlations, particularly at high polymer concentrations and large Bjerrum lengths [135]. This limitation of RPA is more significant for charge-asymmetric IDPs due to intra-chain repulsions[135]

An additional limitation of RPA becomes evident in the polymer-free limit. For point ions (introduced here for analytical simplicity), the electrostatic free energy reduces to the Debye–Hückel expression. In the limit $\kappa_{\mathrm{D}}\sigma \to 0$, where

$$\kappa_{\mathrm{D}} = \left(4\pi l_{\mathrm{B}} \rho_{\mathrm{s}}\right)^{1/2}, \tag{3.14}$$

is the inverse Debye screening length, the free energy becomes

$$f = -\frac{\kappa_{\mathrm{D}}^3}{12\pi} + \rho_{\mathrm{s}} \ln \rho_{\mathrm{s}} + (1-\rho_{\mathrm{s}}) \ln(1-\rho_{\mathrm{s}}). \tag{3.15}$$

This expression predicts a critical Bjerrum length of approximately $l_{\mathrm{B}}/\sigma = 2.05$, above which a simple electrolyte undergoes phase separation. Such behavior is not observed experimentally under ambient aqueous conditions, illustrating the well-known tendency of RPA and Debye–Hückel theory to overestimate electrostatic correlations.

Liquid-State Theory

Liquid-State Theory (LS) provides a complementary description to RPA by explicitly accounting for local packing and electrostatic correlations between particles.

Following the work of Zhang *et al.* [88], we extend this framework to sequence-specific IDPs. The reduced free energy is decomposed into four contributions,

$$f = \frac{F}{V k_{\mathrm{B}} T} = f_{\mathrm{id.}} + f_{\mathrm{hs}} + f_{\mathrm{ele.}} + f_{\mathrm{chain}} \,, \tag{3.16}$$

where the subscripts id., hs, ele., and chain denote the ideal, hard-sphere, electrostatic, and chain formation contributions, respectively. The ideal contribution accounts for the translational entropy of each species,

$$f_{\mathrm{id.}} = \sum_i \frac{\rho_i}{N_i} \left[\ln\left(\frac{\rho_i \Lambda_i^3}{N_i} \right) - 1 \right] , \tag{3.17}$$

where Λ_i is the thermal de Broglie wavelength of species i. Since the present work focuses on phase equilibria rather than thermodynamic properties involving molecular momenta, only the translational contribution is retained. Excluded-volume interactions between disconnected beads are described using the Boublík–Mansoori–Carnahan–Starling–Leland (BMCSL) equation of state [162]. For particles of equal diameter,

$$f_{\mathrm{hs}} = \frac{6\eta^2(4 - 3\eta)}{\pi\sigma^3(1 - \eta)^2} \,. \tag{3.18}$$

where the packing fraction is

$$\eta = \frac{\pi}{6} \sum_i \rho_i \sigma^3 \,, \tag{3.19}$$

Electrostatic interactions between disconnected charged beads are described using the restricted primitive model obtained through the mean spherical approximation (MSA) of Blum and Hoeye [98],

$$f_{\mathrm{ele.}} = -\frac{\Gamma^3(2/3 + \Gamma\sigma)}{\pi} \,. \tag{3.20}$$

where the MSA screening parameter, Γ, satisfies

$$\Gamma(1 + \Gamma\sigma) = \frac{\kappa_{\mathrm{D}}}{2} \,. \tag{3.21}$$

Unlike RPA, the electrostatic contribution in LS is formulated in real space and naturally incorporates excluded-volume effects through the finite size of the constituent particles. The remaining contribution accounts for the free-energy change associated with forming polymer chains from disconnected monomers. Within Wertheim's thermodynamic perturbation theory, this contribution can formally be written as

$$f_{\mathrm{chain}} = -\sum_i \frac{\rho_i}{N_i} \left\langle \ln\left[g_i(\mathbf{r}_i^N) \exp\left(\beta U(\mathbf{r}_i^N) \right) \right] \right\rangle_{\mathbf{r}_i^N} , \tag{3.22}$$

where $g_i(\mathbf{r}_i^N)$ is the single-chain conformational distribution function, $\mathbf{r}_i^N$ denotes the coordinates of all beads within a chain, and $U(\mathbf{r}_i^N)$ is the corresponding intramolecular potential energy. Although formally exact, direct evaluation of this expression is impractical because the conformational distribution function is not known analytically and the multidimensional configurational average is computationally intractable. Consequently, successive approximations are introduced to evaluate f_{chain}, beginning with Wertheim's first-order thermodynamic perturbation theory.

The simplest approximation to the chain contribution is Wertheim's first-order thermodynamic perturbation theory (TPT1), which assumes that chain formation is governed solely by nearest-neighbor correlations. Under this approximation, the conformational distribution is factorized into a product of pair distribution functions at contact,

$$\langle \ln[g_i(\mathbf{r}_i^N) \exp\Big(\beta U(\mathbf{r}_i^N)\Big)]\rangle \approx \sum_{j=1}^{N_i-1} \ln[g_{j,j+1}(\sigma) \exp\big(\beta u_{j,j+1}(\sigma)\big)], \tag{3.23}$$

where $u_{j,j+1}(\sigma)$ is the electrostatic interaction between two bonded monomers separated by one particle diameter. Substituting this approximation into the exact chain free energy yields

$$f_{\text{chain}} = -\sum_i \frac{\rho_i}{N_i} \sum_{j=1}^{N_i-1} \ln\left[g_{j,j+1}(\sigma) e^{\left(\frac{l_B Z_{i,j} Z_{i,j+1}}{\sigma}\right)}\right]. \tag{3.24}$$

The pair distribution function at contact for charged beads is given by[124, 170, 169, 172]

$$g_{i,j}(\sigma) = \frac{2+\eta}{(1-\eta)^2} \exp\left(-\frac{l_B Z_i Z_j}{\sigma(1+\Gamma\sigma)^2}\right). \tag{3.25}$$

where the first term corresponds to the hard-sphere cavity function and the exponential accounts for screened electrostatic interactions within the MSA.

Since TPT1 only retains nearest-neighbor correlations, there are only three possible bonded charge combinations: $(++)$, $(--)$, and $(+-)$. Because the $(++)$ and $(--)$ interactions are equivalent, the chain free energy can be simplified to

$$\begin{aligned} f_{\text{chain}} = -\sum_i \frac{\rho_i}{N_i} \Bigg[& (N_i - N_{i,\pm} - 1) \ln\left(g_{\pm,\pm}(\sigma_i) e^{l_B/\sigma_i}\right) \\ & + N_{i,\pm} \ln\left(g_{+,-}(\sigma_i) e^{-l_B/\sigma_i}\right) \Bigg], \end{aligned} \tag{3.26}$$

where $N_{i,\pm}$ denotes the number of unlike nearest-neighbor pairs within the sequence. The TPT1 approximation therefore reduces the sequence dependence to a single structural descriptor, $N_{i,\pm}$, together with the net charge of the chain. Consequently, distinct sequences sharing the same values of these quantities are predicted to exhibit identical thermodynamic behavior. Furthermore, because only nearest-neighbor correlations are retained, long-range intrachain electrostatic interactions are neglected, preventing the theory from describing electrostatically induced chain contraction or expansion.

The nearest-neighbor approximation inherent to TPT1 neglects correlations between successive bonds and therefore provides only a limited description of sequence-dependent conformations. Motivated by the philosophy of second-order thermodynamic perturbation theory (TPT2)[249, 250, 251, 252], we extend the TPT1 framework by explicitly incorporating triplet correlations through next-nearest-neighbor interactions. Rather than deriving the full second-order perturbation expansion, we approximate the chain conformational distribution using triplet distribution functions, thereby retaining the dominant local three-body correlations while preserving a computationally tractable theory. Specifically, we approximate the conformational distribution as

$$g_i(\mathbf{r}_i^N)\exp\left(\beta U(\mathbf{r}_i^N)\right) \approx \tag{3.27}$$

$$\prod_{j=2}^{N_i-1} g_{j-1,j,j+1}(\sigma,\sigma,r_j)\exp\left[\beta u_{j-1,j,j+1}(\sigma,\sigma,r_j)\right], \tag{3.28}$$

where r_j denotes the separation between beads $j-1$ and $j+1$, and $g_{j-1,j,j+1}$ is the triplet distribution function describing three consecutive monomers. To obtain an analytical expression for the triplet distribution function, we adopt the approximation proposed by Müller and Gubbins [253, 254] for hard-sphere fluids,

$$g_{j-1,j,j+1}(\sigma,\sigma,r_j) = g_{j-1,j}(\sigma)g_{j,j+1}(\sigma)g_j^{(3)}(r_j), \tag{3.29}$$

where $g_j^{(3)}(r_j)$ accounts for the remaining triplet correlation not captured by the pair distribution functions. Electrostatic interactions are then incorporated by Boltzmann weighting the hard-sphere distribution, giving

$$f_{\text{chain}} = -\sum_i \frac{\rho_i}{N_i}\Bigg\{\sum_{j=1}^{N_i-1}\ln\left[g_{j,j+1}(\sigma_i)e^{l_{\text{B}}Z_{i,j}Z_{i,j+1}/\sigma_i}\right] + \sum_{j=2}^{N_i-1}\left\langle\ln\left[g_j^{(3)}(r_j)e^{l_{\text{B}}Z_{i,j-1}Z_{i,j+1}/r_j}\right]\right\rangle_{r_j}\Bigg\}, \tag{3.30}$$

where $\langle \cdots \rangle_{r_j}$ denotes a Boltzmann average over the separation r_j. By explicitly accounting for next-nearest-neighbor interactions, this triplet approach, referred to herein as LS-T, distinguishes a substantially larger number of sequences than the standard TPT1 approach and provides a more accurate description of local chain conformations. Nevertheless, the theory remains inherently local: electrostatic interactions beyond three consecutive beads influence the chain only indirectly through the bulk screening length. Although incorporating triplet correlations improves the description of local structure, LS-T remains fundamentally a local theory. Consider, for example, an otherwise polycationic chain containing a single negatively charged monomer. LS-T predicts that the attractive interaction between this monomer and its neighboring cationic beads produces a locally collapsed, hairpin-like structure. In reality, the long-range electrostatic repulsion between the remaining positively charged monomers largely prevents such a collapse, leading instead to an almost fully extended chain with only a slight local distortion. Local conformations are determined solely by the geometry of neighboring triplets and therefore cannot respond to the electrostatic environment generated by the rest of the chain. Consequently, LS-T cannot capture the feedback between global chain conformation and local electrostatic interactions which becomes increasingly important for highly heterogeneous sequences. This limitation motivates the incorporation of long-range Gaussian-chain conformational statistics in the hybrid gauLS framework.

Though the triplet correlation introduced above improves upon TPT1 by explicitly incorporating local three-body correlations, it remains a local theory where electrostatic interactions beyond three consecutive monomers enter only through the bulk screening length. However, evaluating the chain distribution in LS through Eq. 3.22 is computationally intractable, motivating an approximate treatment using local correlation. On the other hand, The Random Phase Approximation provides the complementary limit. RPA naturally incorporates long-range intrachain electrostatic correlations through Gaussian-chain statistics, but it lacks an accurate description of local packing and short-range electrostatic correlations. This motivates an embedded-chain approximation in which local triplet correlations are treated explicitly using Liquid-State Theory, while the remaining degrees of freedom are represented by an effective Gaussian chain assumed in the RPA framework, which together captures the feedback between the chain conformation and local sequence information. We refer to this hybrid framework as gauLS.

In this approach, each triplet of consecutive monomers is treated as an explicit

charged hard-sphere cluster embedded within the rest of the chain. The explicit triplet consists of monomers $j-1$, j, and $j+1$, while all remaining monomers are represented by Gaussian-chain statistics. The Gaussian-chain contribution explicitly excludes the monomers belonging to the triplet, thereby avoiding double counting of the electrostatic interactions included in the local triplet term. For a fixed terminal separation r_j between monomers $j-1$ and $j+1$, we define an effective triplet free energy,

$$\beta H_j(r_j) = \beta U_j^{\text{triplet}}(r_j) - \ln g_{j-1,j,j+1}(\sigma,\sigma,r_j) + \beta F_j^{\text{G}}(r_j), \tag{3.31}$$

where the explicit triplet electrostatic energy is

$$\beta U_j^{\text{triplet}}(r_j) = \frac{l_{\text{B}} Z_{j-1} Z_{j+1}}{r_j}. \tag{3.32}$$

The term $g_{j-1,j,j+1}(\sigma,\sigma,r_j)$ is the hard-sphere triplet distribution function introduced above, while $F_j^{\text{G}}(r_j)$ is the conformational free energy of the remaining chain, conditioned on the fixed separation r_j of the explicit triplet. The Gaussian-chain contribution is defined through the restricted configurational partition function

$$e^{-\beta F_j^{\text{G}}(r_j)} = \int \mathcal{D}\mathbf{R}(s) \exp\left[-\beta H_j^{\text{G}}[\mathbf{R}(s); r_j]\right], \tag{3.33}$$

where the functional integral is taken over all conformations of the chain segments outside the explicit triplet, subject to the constraint imposed by the terminal separation r_j. The Gaussian-chain Hamiltonian is approximated as

$$\begin{aligned}\beta H_j^{\text{G}} &= \frac{3}{2\sigma} \int_{s\notin j} \left(\frac{\partial \mathbf{R}(s)}{\partial s}\right)^2 ds \\ &+ l_{\text{B}} \int_{s\notin j} \int_{s'\notin j} ds\, ds' \frac{Z(s)Z(s')}{|\mathbf{R}(s)-\mathbf{R}(s')|} e^{-\kappa_{\text{D}}|\mathbf{R}(s)-\mathbf{R}(s')|}.\end{aligned} \tag{3.34}$$

Here, $s \notin j$ denotes all contour positions outside the explicit triplet. The first term is the elastic free energy of the effective Gaussian chain, and the second term accounts for screened electrostatic interactions between the remaining monomers. The Debye screening parameter κ_{D} is determined by the bulk ionic environment, consistent with the MSA description used in the Liquid-State Theory. Thus, local triplet interactions are treated explicitly, while the rest of the chain contributes through a screened, mean-field electrostatic environment.

Analytical expressions for the Gaussian-chain contribution can be obtained from the variational treatment of Sawle and Ghosh [241]. The effective triplet free energy

$H_j(r_j)$ therefore defines a potential of mean force for the local triplet geometry, conditioned on the sequence-dependent electrostatic environment of the surrounding chain. The Boltzmann distribution of triplet separations is

$$P_j(r_j) = \frac{e^{-\beta H_j(r_j)}}{\int_\sigma^{2\sigma} dr_j \, e^{-\beta H_j(r_j)}}, \tag{3.35}$$

where the integration limits reflect the geometrically accessible range of the terminal separation for three tangent hard spheres. The corresponding chain-formation contribution is then approximated as

$$f_{\text{chain}} = -\sum_i \frac{\rho_i}{N_i} \frac{1}{N_i - 2} \sum_{j=2}^{N_i-1} \left\langle \beta H_j(r_j) \right\rangle_{P_j(r_j)}. \tag{3.36}$$

The gauLS framework should therefore be viewed as an embedded-chain approximation rather than a rigorous higher-order perturbation expansion. Its purpose is to retain the local packing and electrostatic correlations captured by Liquid-State Theory while allowing the local triplet geometry to respond to the long-range, sequence-dependent electrostatic environment of the full chain. In this way, gauLS provides a computationally efficient route to incorporate both local and non-local sequence effects without requiring the full single-chain conformational distribution.

Phase Equilibrium and Criticality

For a given Bjerrum length, l_B, the thermodynamic state of the system is fully specified by the vector of monomer densities, $\boldsymbol{\rho}$. Before determining phase coexistence, we first assess the local stability of the homogeneous phase. Local stability is governed by the Hessian matrix of the Helmholtz free energy,

$$\mathbf{H}_{ij} = \frac{\partial^2 F}{\partial \rho_i \partial \rho_j}, \tag{3.37}$$

evaluated at the homogeneous composition. For charged systems, however, not all concentration fluctuations are physically admissible. Since macroscopic charge separation is prohibited, only fluctuations that preserve electroneutrality are considered,

$$\sum_i \frac{Z_{\text{net},i}}{N_i} \delta\rho_i = 0. \tag{3.38}$$

Accordingly, the local stability analysis is performed on the Hessian projected onto the electroneutral subspace. The homogeneous phase is locally stable when the

projected Hessian is positive definite, while the onset of spinodal decomposition is identified when its smallest eigenvalue vanishes,

$$\lambda_{\min}\left(\mathbf{H}_{\mathrm{P}}\right) = 0, \tag{3.39}$$

where $\mathbf{H}_{\mathrm{P}}$ denotes the Hessian restricted to fluctuations satisfying the electroneutrality constraint. Within the spinodal region, infinitesimal concentration fluctuations grow spontaneously, whereas outside this region any phase separation must proceed through nucleation and growth.

Assuming the system separates into two homogeneous phases with monomer densities $\boldsymbol{\rho}_\alpha$ and $\boldsymbol{\rho}_\beta$, the total Helmholtz free energy is

$$F_T = \varphi F(\boldsymbol{\rho}_\alpha, l_{\mathrm{B}}) + (1-\varphi) F(\boldsymbol{\rho}_\beta, l_{\mathrm{B}}), \tag{3.40}$$

where φ is the volume fraction of phase α. Conservation of mass requires

$$\rho_{i,0} = \varphi \rho_{i,\alpha} + (1-\varphi)\rho_{i,\beta}, \qquad \forall i, \tag{3.41}$$

where $\rho_{i,0}$ denotes the overall monomer density of species i. Since the initial state is electrically neutral, electroneutrality need only be imposed on one of the coexisting phases,

$$\sum_i \frac{\rho_{i,\alpha}}{N_i} Z_{\mathrm{net},i} = 0, \tag{3.42}$$

the corresponding condition for the second phase following automatically from the mass balance. The coexistence conditions are obtained by minimizing the total free energy subject to the mass-balance and electroneutrality constraints. Introducing Lagrange multipliers μ_i and ψ gives

$$\begin{aligned} \mathcal{L} =& \varphi F(\boldsymbol{\rho}_\alpha, l_{\mathrm{B}}) + (1-\varphi) F(\boldsymbol{\rho}_\beta, l_{\mathrm{B}}) \\ &+ \sum_i \mu_i \left[\rho_{i,0} - \varphi\rho_{i,\alpha} - (1-\varphi)\rho_{i,\beta}\right] \\ &+ \psi\varphi \sum_i \frac{\rho_{i,\alpha}}{N_i} Z_{\mathrm{net},i}, \end{aligned} \tag{3.43}$$

whose stationary point determines the equilibrium phase compositions. Minimization with respect to $\boldsymbol{\rho}_\alpha$ and $\boldsymbol{\rho}_\beta$ yields the equality of electrochemical potentials,

$$\mu_i = \left(\frac{\partial F}{\partial \rho_i}\right)_\alpha + \psi \frac{Z_{\mathrm{net},i}}{N_i} = \left(\frac{\partial F}{\partial \rho_i}\right)_\beta. \tag{3.44}$$

Minimization with respect to φ gives equality of osmotic pressure,

$$0 = F(\boldsymbol{\rho}_\alpha, l_{\mathrm{B}}) - F(\boldsymbol{\rho}_\beta, l_{\mathrm{B}}) - \sum_i \mu_i(\rho_{i,\alpha} - \rho_{i,\beta}), \tag{3.45}$$

while minimization with respect to the Lagrange multipliers recovers the mass-balance and electroneutrality constraints.

For a single, charge-neutral IDP, the critical point is obtained by simultaneously satisfying

$$\left(\frac{\partial^2 F}{\partial \rho^2}\right)_{l_\mathrm{B}} = 0, \tag{3.46}$$

$$\left(\frac{\partial^3 F}{\partial \rho^3}\right)_{l_\mathrm{B}} = 0. \tag{3.47}$$

All first-, second-, and third-order derivatives of the free energy are evaluated using automatic differentiation through ForwardDiff.jl.

Molecular Dynamics Simulation

Coarse-grained molecular dynamics (MD) simulations were performed using LAMMPS [179] following the simulation protocol of Chen and Wang [159]. IDPs were modeled using the Kremer–Grest force field with explicit electrostatic interactions. Each polymer consisted of a linear chain of charged beads, with every monomer carrying a unit charge of $\pm e$. Monovalent counterions were added to ensure overall electroneutrality, while added salt was represented by monovalent ions with interaction parameters identical to those of the counterions. All particles were assigned identical mass m and diameter σ, and all quantities are reported in reduced Lennard-Jones units.

Adjacent monomers were connected using the finite extensible nonlinear elastic (FENE) potential,

$$U_\mathrm{FENE}(r) = -0.5 k R_0^2 \ln\left[1 - \left(\frac{r}{R_0}\right)^2\right] \tag{3.48}$$

with $k = 30\epsilon/\sigma^2$ and $R_0 = 1.5\sigma$.

Excluded-volume interactions between all non-bonded particles were described by the purely repulsive Weeks–Chandler–Andersen (WCA) potential,

$$U_\mathrm{WCA}(r) = \begin{cases} 4\epsilon\left[\left(\frac{\sigma}{r}\right)^{12} - \left(\frac{\sigma}{r}\right)^{6} + \frac{1}{4}\right], & \text{if } r \le 2^{\frac{1}{6}}\sigma \\ 0, & \text{if } r > 2^{\frac{1}{6}}\sigma \end{cases} \tag{3.49}$$

where ϵ is the Lennard-Jones energy parameter. In the absence of electrostatic interactions, this corresponds to good-solvent conditions for neutral polymers. To

provide reference conformations in later parts, θ-solvent conditions were approximated using a Lennard-Jones potential with cutoff 2.5σ and interaction strength $\epsilon_{\mathrm{LJ}} = 0.3\epsilon$.

Electrostatic interactions were modeled using the Coulomb potential,

$$U_{\mathrm{coul.}}(r) = \frac{q_1 q_2}{4\pi\epsilon_0\epsilon_r r}, \tag{3.50}$$

with a real-space cutoff of 10σ. Long-range electrostatic interactions were evaluated using the particle–particle particle–mesh (PPPM) method with a target force accuracy of 10^{-4}.

All simulations were first undergo energy minimization using the conjugate-gradient algorithm until both the energy and force tolerances reached 10^{-5}. Particle velocities were then initialized from a Maxwell–Boltzmann distribution at the reduced temperature $T^* = k_{\mathrm{B}}T/\epsilon = 1.0$ with zero net linear momentum. Production simulations were performed in the canonical ensemble using a Langevin thermostat with damping parameter 7.01τ and the velocity-Verlet integration algorithm with timestep 0.005τ, where

$$\tau = \sqrt{\frac{m\sigma^2}{\epsilon}}. \tag{3.51}$$

Single-chain simulations

Single-chain simulations were performed to characterize the equilibrium conformations of individual IDPs through the radius of gyration, R_{g}, and the average separation of next-nearest neighbors. Simulations employed a cubic simulation box of dimensions $50\sigma \times 50\sigma \times 50\sigma$, followed by 10^6 equilibration timesteps and 3×10^7 production timesteps. Radii of gyration were calculated using MDAnalysis [187] together with MDCraft [14].

Two-chain simulation

Two-chain simulations were performed to quantify intermolecular interactions through the potential of mean force (PMF) as a function of the center-of-mass separation between two IDPs. The PMF was obtained using the adaptive biasing force (ABF) method [188, 189] implemented through the Colvars module [190]. The reaction coordinate was divided into four windows spanning separations from 0σ to 20σ, with each window sampled for 10^8 timesteps. The propensity for self-coacervation

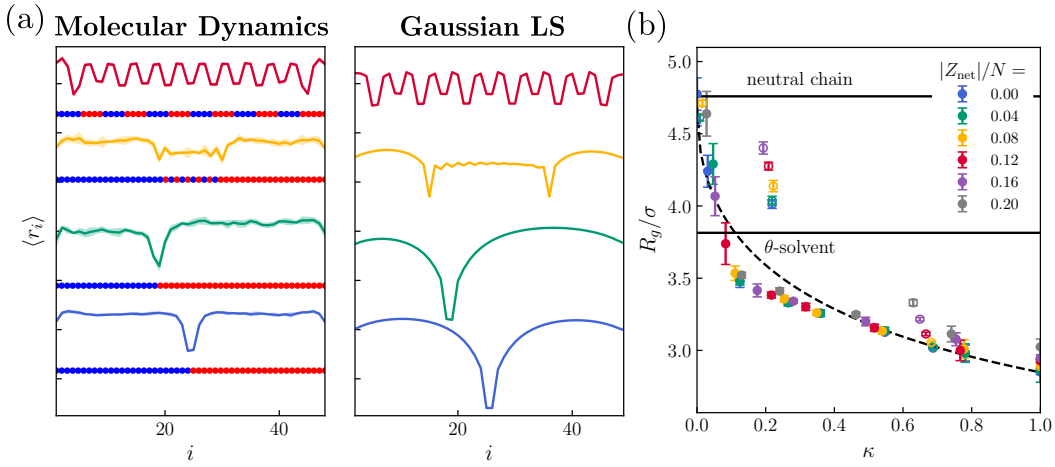


Figure 3.2: (a) Average distance between opposing beads of a triplet, $\langle r_i \rangle$, for four representative sequences obtained from MD simulations and the hybrid theory, gauLS. (b) Radius of gyration (R_g) of single-chain polyampholyte with changes of κ and $\frac{|Z_{net}|}{N}$. The R_g values corresponding to a neutral chain in a good solvent and a θ-solvent are shown as horizontal reference lines. Multiblock sequences are shown in hollow markers.

was quantified using the osmotic second virial coefficient,

$$B_2 = -2\pi \int_0^\infty [\exp(-\beta F(r)) - 1]\, r^2\, dr, \tag{3.52}$$

where $F(r)$ is the PMF. Negative values of B_2 correspond to a net attractive interaction between two chains and were therefore used to classify sequences as self-coacervating. Although direct coexistence simulations provide a more rigorous determination of phase behavior[239, 237], the second virial coefficient offers a computationally efficient metric that has been shown to correlate well with liquid–liquid phase separation[238].

3.3 Results and Discussion

To systematically investigate the effects of charge sequence, charge asymmetry, and salt concentration on IDP coacervation, we carried out more than 100 molecular dynamics simulations and theoretical calculations spanning over 10,000 distinct sequences. For clarity, we first examine a representative subset of these results to develop physical intuition regarding single-chain conformations, intermolecular interactions and phase behavior, before discussing the complete sequence phase space.

Single-chain behavior

Single-chain conformations provide valuable insight into the phase behavior of intrinsically disordered proteins and offer a stringent test of the gauLS framework developed in this work. We therefore begin by examining two microscopic quantities: the average separation between the terminal monomers of each triplet, $\langle r_i \rangle$, which directly probes the local conformations predicted by gauLS, and the radius of gyration, R_g, which characterizes the overall chain dimensions.

Within the triplet approximation (LS-T), $\langle r_i \rangle$ depends only on the local charge arrangement, resulting in only two possible values corresponding to like- and oppositely-charged terminal monomers. Conversely, RPA assumes Gaussian-chain statistics and therefore predicts a uniform value of $\langle r_i \rangle$ independent of sequence. In contrast, gauLS allows long-range electrostatic interactions to modify local triplet conformations, giving rise to sequence-dependent variations in $\langle r_i \rangle$. As shown in Figure 3.2(a), the MD simulations reveal that $\langle r_i \rangle$ varies substantially along the chain and depends strongly on the charge sequence. The predictions of gauLS reproduce these spatial variations well, demonstrating that the theory captures the influence of long-range electrostatic interactions on local chain conformations while retaining the local steric description of Liquid-State Theory.

One of the most prominent features reproduced by gauLS is the pronounced reduction in $\langle r_i \rangle$ at the interfaces between oppositely charged blocks, reflecting local charge collapse driven by electrostatic attraction. The magnitude of this collapse increases with block size, as seen by comparing the fully diblock sequence with the sequence composed of four-residue blocks. Conversely, uniformly charged domains exhibit larger values of $\langle r_i \rangle$ owing to intrablock electrostatic repulsion, with longer charged domains producing greater local extension. The theory also captures more subtle features, including the reduced extension near chain ends and the alternating degree of collapse between successive charge-block interfaces.

Overall, gauLS reproduces the sequence-dependent variation in local conformations, including the location and relative magnitude of local collapses and extensions. Nevertheless, the predicted amplitudes of $\langle r_i \rangle$ exhibit noticeable quantitative deviations from the simulations. These discrepancies arise from the assumption of gauLS that the remainder of the chain follows fixed Gaussian statistics, preventing the surrounding conformational ensemble from adapting to local sequence heterogeneity and electrostatic interactions. Addressing this limitation by incorporating a more self-consistent description of chain conformations, such as renormalized Gaussian

fluctuation (RGF) theory [135], is a promising direction for sequence-dependent polyampholytes.

The radius of gyration has been shown to correlate strongly with the phase behavior of IDPs [255, 243]. We therefore examine the dependence of R_g on the two sequence descriptors introduced in Section 3.2. As shown in Figure 3.2(b), the radius of gyration decreases nearly monotonically with increasing charge blockiness. Larger values of κ promote intrachain collapse through stronger attraction between extended oppositely charged domains, whereas more uniformly mixed sequences remain comparatively expanded, approaching the dimensions of a neutral polymer in a good solvent.

A small group of exceptions is observed near $\kappa \approx 0.2$, corresponding to multiblock sequences with a block length of four residues (hollow markers in Figure 3.2(b)). This deviation arises from the definition of κ, which employs a conventional sliding window of $g = 5$, larger than the underlying block length. When characterized using the normalized sequence charge decoration (nSCD), these sequences recover the expected monotonic trend [241, 255].

For a fixed κ, increasing the normalized net charge, $|Z_{net}|/N$, generally leads to larger values of R_g as the excess like-charged residues introduce additional intrachain electrostatic repulsion that opposes chain collapse. This effect is most pronounced for weakly blocky sequences, where attractive interactions are relatively weak. As κ approaches unity, however, the influence of net charge becomes progressively less important because the strong attraction between oppositely charged domains dominates the chain conformation. Consequently, charge blockiness is the primary determinant of chain compactness, while net charge acts as a secondary modifier that shifts the balance between attractive and repulsive electrostatic interactions, and has a more pronounced effect for sequences with low-to-moderate κ.

From a mean-field, single-chain perspective, one might therefore expect sequences that are more compact than a neutral polymer under θ-solvent conditions (indicated by the lower reference line in Figure 3.2(c)) to undergo macroscopic phase separation through sufficiently strong intrachain attraction [62]. Based solely on the single-chain conformations, one would conclude that charge blockiness is the dominant factor controlling self-coacervation. This picture, however, neglects both interchain electrostatic repulsion and the inherently many-body nature of electrostatic interactions[3, 85], where repulsive interactions can be substantially reduced through screening by neighboring chains and added salt. As shown in the follow-

ing sections, these collective effects fundamentally alter the relationship between single-chain conformations and macroscopic phase behavior, particularly for charge-asymmetric sequences.

Salt-free phase behavior

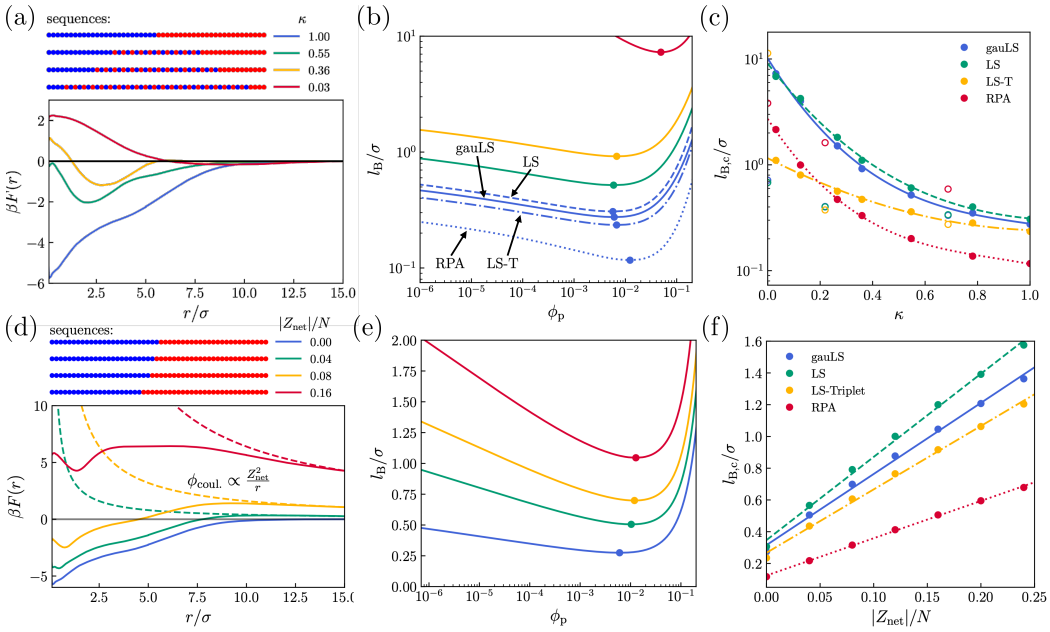


Figure 3.3: Salt-free phase behavior of representative sequences. Panels (a-c) correspond to net charge-neutral sequences ($\frac{|Z_{\text{net}}|}{N} = 0$), progressively increasing the length of alternating charge block in the center of the sequence, and panels (d-f) examine the effect of net charge ($\frac{|Z_{\text{net}}|}{N}$) for diblock sequences with $\kappa = 1$. The potentials of mean force (PMFs), $\beta F(r)$, obtained from MD simulations are shown in panels (a) and (d), together with sequence schematics and their color codes. The long-range electrostatic repulsion follows the Coulombic interaction, shown as dashed lines. Phase diagrams corresponding to the same sequences are presented in panels (b) and (e), where critical Bjerrum lengths (l_{Bc}) are denoted by circular markers. Except for the diblock sequence with $\kappa = 1$ in panel (b), for which results from all four theoretical approaches are shown, only gauLS predictions are included in the phase diagrams. The $l_{\text{B,c}}$s of selected sequences in panel (a) and additional multiblock sequences are summarized in panels (c) and (f), where predictions from all theoretical approaches are compared. The multiblock sequences (hollow markers) correspond to charge block lengths of 2, 4, and 8 residues, yielding κ values of 0.00, 0.22, and 0.69, respectively. The fitted curves are polynomial fits, with line styles corresponding to the blue set shown in panel (b). The line styles correspond to the different theoretical approaches: solid lines denote gauLS, dashed lines denote LS, dash-dotted lines denote LS-T, and dotted lines denote RPA.

We next examine the self-coacervation of IDPs in the absence of added salt, such that

the system consists only of the IDPs and the counterions required to maintain electroneutrality. We first investigate the role of charge blockiness using charge-neutral sequences (Figures 3.3(a)–(c)), before examining the effects of charge asymmetry in the following section.

The potentials of mean force (PMFs) obtained from the molecular dynamics simulations are shown in Figure 3.3(a). As the charge blockiness decreases, the PMFs become progressively less attractive, eventually developing a short-range repulsive barrier for the most alternating sequences. Physically, this reflects the increasing cancellation of neighboring opposite charges, reducing the net electrostatic attraction between chains. In contrast, the diblock sequence ($\kappa = 1$) exhibits a strongly attractive PMF across the entire separation range, highlighting the favorable interactions between large oppositely charged domains.

These microscopic interactions translate directly into the predicted phase behavior shown in Figure 3.3(b). Considering the gauLS predictions, increasing charge blockiness shifts the coexistence envelope towards lower Bjerrum lengths, indicating that more blocky sequences phase separate under weaker electrostatic interactions. This trend is in excellent agreement with the PMFs. At $l_B = \sigma$, only the three most blocky sequences possess negative second virial coefficients and are therefore expected to self-coacervate, consistent with the corresponding phase diagrams.

The diblock sequence also provides a useful benchmark for comparing the four theoretical approaches, as they differ fundamentally in their treatment of electrostatic interactions and chain conformations. The predicted critical Bjerrum lengths follow the ordering: LS $\leq$ gauLS $<$ LS-T $<$ RPA, reflecting progressively stronger predicted electrostatic correlations. LS considers only nearest-neighbor interactions and therefore predicts the weakest. At the opposite extreme, RPA assumes Gaussian-chain conformations throughout, leading to an overestimation of long-range electrostatic correlations. The two intermediate theories both incorporate higher-order sequence information but differ in their treatment of chain conformations. Whereas LS-T explicitly accounts for next-nearest-neighbor (triplet) interactions, gauLS embeds these local conformations to the long-range electrostatic environment of the surrounding chain. This coupling moderates the local electrostatic correlations, yielding predictions intermediate between LS and LS-T.

The broader trends are summarized in Figure 3.3(c). All four theories predict that the critical Bjerrum length generally decreases with increasing charge blockiness, confirming that segregating opposite charges promotes self-coacervation. For highly

blocky sequences ($\kappa \geq 0.3$), the relative ordering of the theories remains unchanged. As the sequences become increasingly disordered, however, the predictions begin to diverge. In particular, LS-T predicts a considerably weaker dependence of $l_{B,c}$ on κ than the other approaches. This behavior is consistent with the local nature of the approximation. In highly alternating sequences, each triplet contains oppositely charged next-nearest neighbors, which favors locally collapsed conformations within the triplet description. Because LS-T treats these triplets independently of the remainder of the chain, this local stabilization is not influenced by the longer-range electrostatic environment. By contrast, gauLS embeds each triplet within the Gaussian chain, allowing the local conformations to respond to the surrounding electrostatic environment while retaining the description of local structure. This additional coupling provides a possible explanation for why gauLS predicts a stronger dependence on κ than LS-T while remaining less sensitive than RPA.

Although the dependence of $l_{B,c}$ on κ is approximately monotonic, Figure 3.3(c) also reveals several notable outliers corresponding to multiblock sequences (hollow markers). These sequences exhibit substantially different critical Bjerrum lengths despite possessing similar values of κ. Their behavior cannot therefore be understood solely from the overall degree of charge blockiness. To understand the origin of these deviations, we compare in Figure 3.4 two representative sequences that contain the same number of unlike nearest-neighbor pairs but differ in their overall charge arrangement.

The PMFs obtained from MD simulations, shown in Figure 3.4(a), reveal that both sequences are capable of self-coacervation ($B_2 < 0$), but their intermolecular interactions differ substantially. The triblock sequence exhibits a deeper potential minimum at short separations, whereas the multiblock sequence displays a broader attractive well extending to larger intermolecular distances. These differences arise directly from the distinct single-chain conformations shown in Figure 3.2 and visually in the simulation snapshots of Figure 3.4(a). The triblock sequence adopts a compact conformation, favoring strong short-range interchain contacts, while the more extended multiblock sequence can establish favorable electrostatic interactions over a larger range of separations.

These microscopic differences are reflected in the predicted phase diagrams shown in Figure 3.4(b). RPA predicts a significantly larger critical Bjerrum length for the multiblock sequence than for the triblock sequence because the Gaussian-chain approximation effectively averages the alternating charge blocks into a more homo-

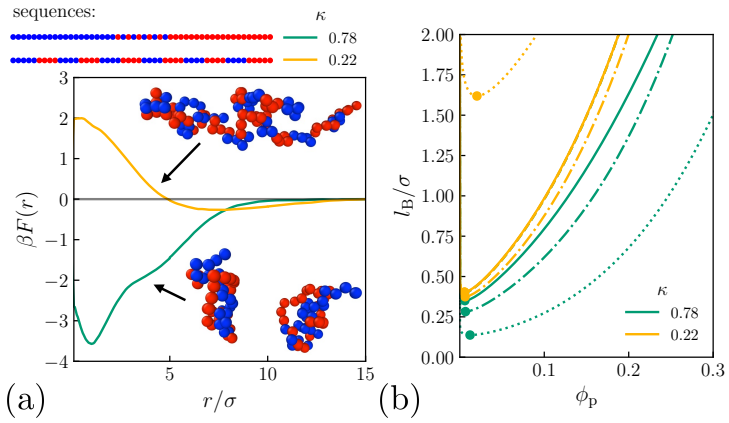


Figure 3.4: Salt-free behavior of a selected pair of sequences containing the same number of charge doublets. The potentials of mean force (PMFs), $\beta F(r)$, obtained from MD simulations are shown, together with sequences schematics and their color codes (left panel). Corresponding phase diagrams are presented in the right panel, where critical Bjerrum lengths (l_{Bc}) are shown by dots. The line styles correspond to the different theoretical approaches: solid lines denote gauLS, dashed lines denote LS, dash-dotted lines denote LS-T, and dotted lines denote RPA. The LS results for both sequences are identical and are in close proximity with the gauLS predictions for the chain with $\kappa = 0.22$.

geneous charge distribution, thereby underestimating the favorable local electrostatic correlations. In contrast, both gauLS and LS-T correctly predict that the multiblock sequence exhibits only a slightly weaker tendency towards phase separation than the triblock sequence. Figure 3.4 also illustrates the fundamental limitations of local sequence descriptors. Since the two sequences possess the same number of unlike nearest-neighbor pairs, LS predicts identical phase behavior for both sequences. This demonstrates that nearest-neighbor statistics alone are insufficient to characterize sequence-dependent self-coacervation. Incorporating triplet and long-range conformational correlations substantially improves the predictions. These results therefore demonstrate that the global organization of charge along the chain, rather than local charge statistics alone, plays a decisive role in determining intermolecular interactions and phase behavior.

Having established how charge patterning influences salt-free self-coacervation, we next examine the effect of charge asymmetry. For clarity, we restrict our discussion to diblock sequences ($\kappa = 1$), although the same qualitative trends are observed for more disordered charge patterns.

The PMFs obtained from the MD simulations are shown in Figure 3.3(d). Introducing a net charge produces a long-range Coulombic repulsion between chains, giving

rise to the expected $\beta F(r) \propto Z_{\text{net}}^2/r$ behavior at large separations. At short distances, however, attractive interactions between oppositely charged blocks remain, resulting in a local attractive minimum even for highly charge-asymmetric sequences. As the net charge increases, this minimum becomes progressively shallower because contacts between oppositely charged domains become less favorable.

These changes are reflected directly in the phase diagrams predicted by gauLS (Figure 3.3(e)). Increasing the normalized net charge systematically shifts the coexistence envelope towards larger Bjerrum lengths, demonstrating that progressively stronger electrostatic interactions are required to overcome the increasing interchain repulsion. The qualitative agreement with the PMFs is excellent: sequences with sufficiently large charge asymmetry retain short-range attractive interactions but are no longer able to undergo macroscopic phase separation.

This observation also highlights an important distinction between single-chain and many-body behavior. Although the most highly charged sequences remain more compact than a neutral polymer under θ-solvent conditions (Figure 3.2(b)), they nevertheless fail to phase separate. Single-chain collapse alone is therefore insufficient to predict self-coacervation. Macroscopic phase behavior additionally depends on the balance between attractive interchain correlations, long-range electrostatic repulsion, and the entropy of the accompanying counterions.

The complete dependence of the critical Bjerrum length on charge asymmetry is summarized in Figure 3.3(f). All four theoretical approaches predict a monotonic increase in $l_{\text{B},c}$ with increasing $|Z_{\text{net}}|/N$, consistent with the reduced propensity for phase separation as the excess charge increases. Although the quantitative predictions differ, the relative ordering of the theories remains unchanged, LS $\leq$ gauLS $<$ LS-T $<$ RPA, indicating that the treatment of intrachain electrostatic correlations remains the primary source of the quantitative differences between the theories.

Interestingly, the dependence of $l_{\text{B},c}$ on charge asymmetry is considerably weaker than its dependence on charge blockiness. While increasing the net charge suppresses phase separation through long-range interchain repulsion and the increasing translational entropy of the counterions required to maintain electroneutrality, charge blockiness directly controls the magnitude of the attractive electrostatic correlations responsible for self-coacervation. Consequently, the sequence patterning of charged residues emerges as the dominant molecular descriptor governing salt-free phase behavior, with net charge acting primarily as a secondary perturbation.

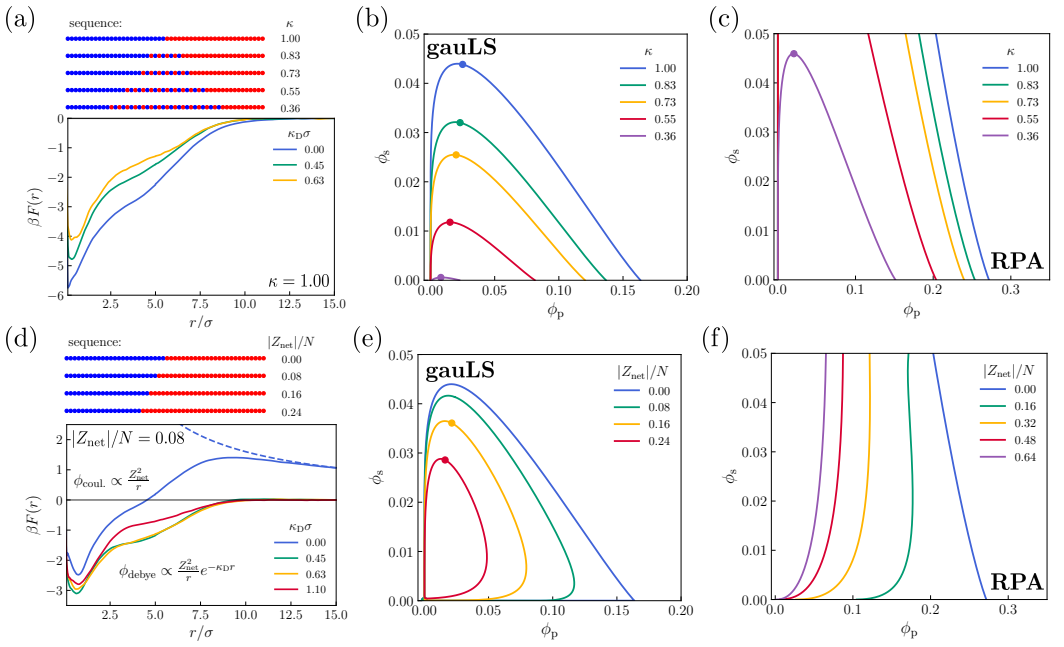


Figure 3.5: Added-salt effect on representative sequences. Panels (a-c) correspond to charge-symmetric sequences ($\frac{|Z_{\text{net}}|}{N} = 0$) with progressively increasing the length of alternating charge block in the center of the sequence, and panels (d-f) examine the effect of net charge ($\frac{|Z_{\text{net}}|}{N}$) for diblock sequences with $\kappa = 1$. The potentials of mean force (PMFs), $\beta F(r)$, obtained from MD simulations with salt concentrations (shown here as an increasing inverse screening length $\kappa_D\sigma$), are shown in panels (a) for a diblock sequence with $\frac{|Z_{\text{net}}|}{N} = 0$, and (d) for a diblock sequence with $\frac{|Z_{\text{net}}|}{N} = 0.08$. The long-range electrostatic repulsion follows the Coulombic interaction, shown as dashed lines. With added salt, the long-range attractive interactions now follow Debye screened interactions. Corresponding phase diagrams are presented in panels (b-c) and (d-e), where critical points are shown by circular markers. Results obtained by gauLS are shown in panels (b) and (e), while results obtained by RPA are shown in panels (c) and (f).

Effect of added salt

The previous section considered salt-free systems containing only the IDP and the counterions required to maintain electroneutrality. In practice, however, biological and experimental systems typically contain substantially higher salt concentrations. The effect of added salt is considerably more complicated because electrostatic screening simultaneously weakens both the attractive and repulsive interactions responsible for self-coacervation. To isolate these competing mechanisms, we again separately consider charge-neutral and charge-asymmetric sequences.

We first examine the effect of salt on a charge-neutral diblock sequence. The corresponding PMFs obtained from MD simulations are shown in Figure 3.5(a). Increas-

ing the salt concentration progressively weakens the attractive interactions between oppositely charged domains, leading to a shallower potential well. Consequently, the propensity for self-coacervation decreases monotonically with increasing salt concentration. This microscopic behavior is reflected directly in the phase diagrams predicted by both gauLS and RPA (Figures 3.5(b,c)). In both theories, increasing the salt concentration progressively contracts the coexistence region until phase separation is completely suppressed at sufficiently high salt concentrations. Sequences with weaker charge blockiness require considerably less salt to eliminate phase separation because their electrostatic attractions are already relatively weak in the salt-free limit.

Although the qualitative trends predicted by gauLS and RPA are identical, the quantitative predictions differ substantially. RPA consistently predicts significantly higher critical salt concentrations than gauLS. This difference originates from the stronger electrostatic contribution of the mobile ions within RPA compared with the MSA treatment employed in Liquid-State Theory. Consequently, greater salt concentrations are required in RPA before electrostatic screening becomes sufficient to suppress phase separation.

The behavior changes qualitatively once the sequence carries a net charge. Figure 3.5(d) shows the PMFs for a diblock sequence with $|Z_{\mathrm{net}}|/N = 0.08$. In the absence of added salt, the interaction is dominated by long-range Coulombic repulsion arising from the excess charge on each chain, preventing self-coacervation despite the presence of attractive interactions between oppositely charged domains. The addition of salt initially screens this long-range repulsion, allowing the attractive block-block interactions to dominate and producing a pronounced attractive minimum in the PMF. As the salt concentration increases further, however, these attractive interactions are themselves progressively screened, resulting in a shallower potential well. Thus, added salt first enhances and subsequently suppresses intermolecular attraction, similar to the salting-in and salting-out transition in the complex coacervation of asymmetric polycations and polyanions[88, 256, 234].

This competition produces the re-entrant phase behavior shown in Figures 3.5(e,f). At low salt concentrations, screening of the long-range repulsion enlarges the coexistence region and can even induce phase separation in sequences that remain homogeneous in the salt-free limit. Beyond an intermediate salt concentration, however, screening of the attractive electrostatic correlations becomes dominant, causing the coexistence region to contract before eventually disappearing altogether. The non-

monotonic dependence of phase behavior on salt concentration is therefore a direct consequence of the competing effects of electrostatic screening.

The extent of this re-entrant behavior differs markedly between the two theories. While gauLS predicts that re-entrant phase behavior is restricted to moderately charge-asymmetric sequences ($|Z_{\mathrm{net}}|/N \leq 0.24$), RPA predicts that it persists for highly charged sequences approaching homopolyelectrolytes. This discrepancy reflects the limitations of the Gaussian-chain approximation, together with the stronger electrostatic contribution of the mobile ions within RPA, both of which exaggerate the stabilizing effect of screening at low salt concentrations.

It is important to distinguish the present mechanism from the re-entrant phase behavior commonly discussed in the IDP literature [216, 218, 208]. In many experimental systems, phase separation occurs in both the low- and high-salt limits, with the intermediate homogeneous region arising from competition between electrostatic and hydrophobic interactions. In contrast, the systems considered here remain homogeneous in both the salt-free and high-salt limits, while phase separation occurs only at intermediate salt concentrations. The re-entrant behavior therefore arises entirely from electrostatic screening and does not require additional attractive interactions such as hydrophobicity.

A qualitatively similar non-monotonic response to added salt has recently been reported for isolated polyampholyte chains, where the radius of gyration exhibits a minimum at intermediate salt concentrations [130]. The present results demonstrate that the corresponding phase behavior is fundamentally a many-body phenomenon. While added salt modifies single-chain conformations, its dominant effect on coacervation arises through the collective screening of intermolecular electrostatic interactions. Consequently, the influence of salt cannot be inferred from single-chain properties alone.

Global phase behavior

Having established the individual roles of charge blockiness, charge asymmetry, and added salt, we now combine these effects to construct the global phase behavior of polyampholyte-like IDPs in terms of the sequence descriptors κ and $|Z_{\mathrm{net}}|/N$. Sequences are classified into three categories: those that undergo self-coacervation under salt-free conditions, those that coacervate only upon the addition of salt, and those that remain homogeneous regardless of salt concentration. Within the molecular dynamics simulations, this classification is based on the sign of the

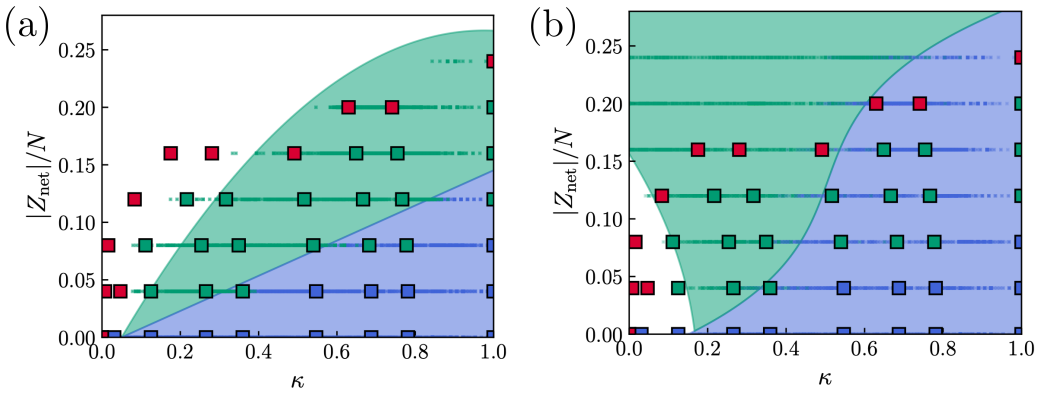


Figure 3.6: Global phase diagrams of IDP sequences using (a) gauLS and (b) RPA. Blue points denote sequences that self-coacervate under salt-free conditions, and green points denote sequences that remain homogeneous under salt-free conditions but undergo salt-induced phase separation. White regions (sequences not shown) correspond to sequences that remain homogeneous regardless of salt concentration. The MD results, quantified through the second virial coefficient (B_2), are shown as squares, where red squares denote sequences which do not coacervate under any condition.

second virial coefficient (B_2) under both salt-free and added-salt conditions. For the theoretical approaches, self-coacervation is identified by determining whether the critical Bjerrum length satisfies $l_{\text{B},c} \leq \sigma$. Sequences that do not satisfy this criterion are subsequently examined at finite salt concentration to determine whether electrostatic screening induces a spinodal instability. While the molecular dynamics simulations were limited to 30 representative sequences at three salt concentrations, the efficiency of the theoretical models enabled more than 10,000 distinct sequences to be examined.

The resulting phase maps are shown in Figure 3.6, with the predictions of gauLS and RPA presented in Figures 3.6(a) and (b), respectively. Blue regions correspond to sequences that undergo self-coacervation under salt-free conditions, green regions denote sequences that phase separate only in the presence of added salt, and the remaining white regions correspond to sequences that remain homogeneous irrespective of salt concentration. The molecular dynamics results are shown as square markers.

The molecular dynamics simulations reveal that salt-free self-coacervation is limited to sequences possessing either sufficiently large charge blockiness or sufficiently small net charge. For neutral sequences, self-coacervation persists down to approximately $\kappa \approx 0.05$, while increasing the normalized net charge progressively

suppresses phase separation, producing an approximately linear trade-off between charge blockiness and charge asymmetry. These trends are reproduced well by gauLS, which slightly overestimates the extent of the self-coacervating region. In contrast, RPA predicts that self-coacervation remains possible for sequences with substantially larger net charges, extending to $|Z_{\mathrm{net}}|/N \approx 0.30$, reflecting its systematic overestimation of electrostatic correlations.

The influence of added salt is even more striking. The green region occupies a substantial fraction of the phase diagram, demonstrating that many sequences incapable of self-coacervation under salt-free conditions can nevertheless undergo phase separation at intermediate salt concentrations through electrostatic screening. The molecular dynamics simulations indicate that, compared to the salt-free case, added salt approximately doubles the maximum net charge compatible with phase separation. Importantly, this salt-induced region remains bounded by the underlying self-coacervation boundary: if a neutral sequence cannot phase separate, introducing a net charge and screening it with salt is insufficient to induce coacervation. gauLS captures both the overall size and shape of this region, although it modestly overestimates its extent. RPA, however, predicts a substantially larger salt-induced region, incorrectly suggesting that salt can induce phase separation even for sequences whose neutral counterparts remain entirely homogeneous. This behavior originates from the combined effects of the Gaussian-chain approximation and the overestimation of the electrostatic contribution of the mobile ions.

These results demonstrate that salt-induced coacervation is not a rare phenomenon but rather occupies a substantial region of sequence space, particularly for moderately charge-asymmetric IDPs. Previous theoretical studies have largely focused on self-coacervation, whereas the present results show that many sequences lie close to the boundary separating salt-free and salt-induced phase separation. This observation has important biological implications. Ionic strength varies substantially across cellular compartments and can change in response to environmental and physiological stimuli. A preliminary analysis of 1,301 human IDP sequences extracted from the DisProt database [257] indicates that the majority cluster around $\kappa \approx 0.2$ and $|Z_{\mathrm{net}}|/N \approx 0.05$–$0.10$, placing them close to the predicted phase boundaries. Consequently, many naturally occurring IDPs may exist near the threshold of coacervation, where relatively small changes in ionic strength are sufficient to induce either condensate formation or dissolution. These results therefore suggest that changes in the local ionic environment provide a general mechanism for regulating

biomolecular phase separation without requiring modifications to the underlying amino-acid sequence.

3.4 Conclusion

In this chapter, we have systematically investigated the effects of charge blockiness, charge asymmetry, and salt concentration on the coacervation of intrinsically disordered proteins using molecular dynamics simulations and a hierarchy of theoretical approaches. To overcome the limitations of existing Liquid-State and Random Phase Approximation theories, we introduced gauLS, an embedded-chain framework that combines explicit local triplet correlations with a Gaussian-chain description of long-range electrostatic interactions. Comparison with molecular dynamics simulations demonstrated that gauLS accurately captures sequence-dependent single-chain conformations and substantially improves predictions of phase behavior across a broad range of charge sequences.

Using this framework, we mapped the phase behavior of 12,741 polyampholyte sequences in terms of charge blockiness, net charge, and salt concentration. We showed that charge blockiness is the primary molecular descriptor governing salt-free self-coacervation, while net charge acts as a secondary modifier through long-range electrostatic repulsion and the entropy of the accompanying counterions. Most importantly, we identified a broad region of sequence space in which phase separation occurs only upon the addition of salt. This salt-induced coacervation arises from the competition between screening of long-range repulsive interactions and screening of the attractive electrostatic correlations responsible for condensate formation, demonstrating that salt can both promote and suppress phase separation depending on the sequence architecture and ionic environment.

Beyond providing a predictive theoretical framework, these results establish a comprehensive sequence–state diagram for polyampholyte-like IDPs and reveal that salt-induced coacervation is likely to be far more prevalent than previously appreciated. Given that many naturally occurring IDPs possess both finite net charge and operate in environments with varying ionic strength, our findings suggest that changes in the local ionic environment may provide a general mechanism for regulating biomolecular condensate formation without requiring modifications to the underlying amino-acid sequence. More broadly, the gauLS framework provides a foundation for extending predictive theories of biomolecular phase separation to increasingly realistic systems, including charge regulation [143], heterogeneous

interaction chemistries [258], multicomponent condensates, and explicit solvent effects.

References

[3] Pierre J. Walker and Zhen-Gang Wang. "Anomalous Phase Behavior of Polymer–Ionic Liquid Mixtures". In: *J. Phys. Chem. B* 129 (Nov. 2025). ISSN: 1520-6106. DOI: 10.1021/acs.jpcb.5c04858.

[4] Seola Lee et al. "Molecular control via dynamic bonding enables material responsiveness in additively manufactured metallo-polyelectrolytes". In: *Nat. Commun.* 15.1 (Aug. 2024), p. 6850. ISSN: 2041-1723. DOI: 10.1038/s41467-024-50860-6.

[8] Tianyi Jin et al. "Self- and salt-induced coacervation of polyampholytic intrinsically disordered proteins". In: *In preparation* (2026).

[14] Benjamin B. Ye, Pierre J. Walker, and Zhen-Gang Wang. "MDCraft: A Python assistant for performing and analyzing molecular dynamics simulations of soft matter systems". In: *J. Open Source Softw.* 9.100 (Aug. 2024), p. 7013. ISSN: 2475-9066. DOI: 10.21105/joss.07013.

[20] Pierre J. Walker, Hon-Wa Yew, and Andrés Riedemann. "Clapeyron.jl: An Extensible, Open-Source Fluid Thermodynamics Toolkit". In: *Ind. Eng. Chem. Res.* 61.20 (May 2022), pp. 7130–7153. ISSN: 0888-5885, 1520-5045. DOI: 10.1021/acs.iecr.2c00326.

[62] Michael Rubinstein and Ralph H. Colby. *Polymer Physics*. Oxford, New York: Oxford University Press, Aug. 2003. ISBN: 978-0-19-852059-7.

[85] Charles E. Sing, Jos W. Zwanikken, and Monica Olvera de la Cruz. "Electrostatic control of block copolymer morphology". In: *Nat. Mater.* 13.7 (July 2014), pp. 694–698. ISSN: 1476-4660. DOI: 10.1038/nmat4001.

[88] Pengfei Zhang et al. "Salting-Out and Salting-In of Polyelectrolyte Solutions: A Liquid-State Theory Study". In: *Macromolecules* 49.24 (Dec. 2016), pp. 9720–9730. ISSN: 0024-9297, 1520-5835. DOI: 10.1021/acs.macromol.6b02160.

[90] Andrew S. Ylitalo et al. "Electrostatic Correlations and Temperature-Dependent Dielectric Constant Can Model LCST in Polyelectrolyte Complex Coacervation". In: *Macromolecules* 54.24 (Dec. 2021), pp. 11326–11337. ISSN: 0024-9297, 1520-5835. DOI: 10.1021/acs.macromol.1c02000.

[98] L. Blum and J. S. Hoeye. "Mean spherical model for asymmetric electrolytes. 2. Thermodynamic properties and the pair correlation function". In: *J. Phys. Chem.* 81.13 (June 1977), pp. 1311–1316. ISSN: 0022-3654, 1541-5740. DOI: 10.1021/j100528a019.

[116] Charles E. Sing and Sarah L. Perry. “Recent progress in the science of complex coacervation”. In: *Soft Matter* 16.12 (Mar. 2020), pp. 2885–2914. ISSN: 1744-6848. DOI: 10.1039/D0SM00001A.

[117] Artem M. Rumyantsev, Nicholas E. Jackson, and Juan J. de Pablo. “Polyelectrolyte Complex Coacervates: Recent Developments and New Frontiers”. en. In: *Annu. Rev. Condens. Matter Phys.* 12.Volume 12, 2021 (Mar. 2021), pp. 155–176. ISSN: 1947-5454, 1947-5462. DOI: 10.1146/annurev-conmatphys-042020-113457.

[124] J. W. Jiang et al. “Thermodynamic properties and phase equilibria of charged hard sphere chain model for polyelectrolyte solutions”. In: *Mol. Phys.* 99.13 (July 2001), pp. 1121–1128. ISSN: 0026-8976. DOI: 10.1080/00268970110043414.

[129] Artem M. Rumyantsev et al. “Controlling Complex Coacervation via Random Polyelectrolyte Sequences”. In: *ACS Macro Lett.* (Sept. 2019). DOI: 10.1021/acsmacrolett.9b00494.

[130] Artem M. Rumyantsev, Alexey A. Gavrilov, and Albert Johner. “Complete Diagram of Conformational Regimes for Polyampholytic Disordered Proteins”. In: *Macromolecules* 57.11 (June 2024), pp. 5533–5544. ISSN: 0024-9297. DOI: 10.1021/acs.macromol.4c00429.

[135] Kevin Shen and Zhen-Gang Wang. “Electrostatic correlations and the polyelectrolyte self energy”. In: *J. Chem. Phys.* 146.8 (Feb. 2017), p. 084901. ISSN: 0021-9606. DOI: 10.1063/1.4975777.

[136] Pengfei Zhang et al. “Polyelectrolyte complex coacervation: Effects of concentration asymmetry”. In: *J. Chem. Phys.* 149.16 (July 2018), p. 163303. ISSN: 0021-9606. DOI: 10.1063/1.5028524.

[139] Scott P. O. Danielsen et al. “Small ion effects on self-coacervation phenomena in block polyampholytes”. In: *J. Chem. Phys.* 151.3 (July 2019), p. 034904. ISSN: 0021-9606. DOI: 10.1063/1.5109045.

[143] David Beyer, Christian Holm, and Zhen-Gang Wang. “A Sequence-Specific Theory for Charge-Regulating IDPs”. In: *ChemRxiv* 2026.0202 (). DOI: 10.26434/chemrxiv.10001808/v1.

[144] James McCarty et al. “Complete Phase Diagram for Liquid–Liquid Phase Separation of Intrinsically Disordered Proteins”. In: *J. Phys. Chem. Lett.* 10.8 (Apr. 2019), pp. 1644–1652. DOI: 10.1021/acs.jpclett.9b00099.

[145] Artem M. Rumyantsev and Albert Johner. “Salt-Added Solutions of Markov Polyampholytes: Diagram of States, Antipolyelectrolyte Effect, and Self-Coacervate Dynamics”. en. In: *Macromolecules* 56.13 (July 2023), pp. 5201–5216. ISSN: 0024-9297, 1520-5835. DOI: 10.1021/acs.macromol.3c00512.

[154] Charles E. Sing and Jian Qin. "Bridging Field Theory and Ion Pairing in the Modeling of Polyelectrolytes and Complex Coacervation". In: *Macromolecules* (July 2023). DOI: 10.1021/acs.macromol.3c01020.

[159] Shensheng Chen and Zhen-Gang Wang. "Driving force and pathway in polyelectrolyte complex coacervation". In: *Proc. Natl. Acad. Sci. U.S.A.* 119.36 (Sept. 2022), e2209975119. DOI: 10.1073/pnas.2209975119.

[162] Tomáš Boublík. "Hard-Sphere Equation of State". In: *J. Chem. Phys.* 53.1 (July 1970), pp. 471–472. ISSN: 0021-9606, 1089-7690. DOI: 10.1063/1.1673824.

[165] M. S. Wertheim. "Fluids with highly directional attractive forces. I. Statistical thermodynamics". In: *J. Stat. Phys.* 35.1-2 (Apr. 1984), pp. 19–34. ISSN: 0022-4715, 1572-9613. DOI: 10.1007/BF01017362.

[166] M. S. Wertheim. "Fluids with highly directional attractive forces. II. Thermodynamic perturbation theory and integral equations". In: *J. Stat. Phys.* 35.1-2 (Apr. 1984), pp. 35–47. ISSN: 0022-4715, 1572-9613. DOI: 10.1007/BF01017363.

[167] M. S. Wertheim. "Fluids with highly directional attractive forces. III. Multiple attraction sites". In: *J. Stat. Phys.* 42.3-4 (Feb. 1986), pp. 459–476. ISSN: 0022-4715, 1572-9613. DOI: 10.1007/BF01127721.

[168] M. S. Wertheim. "Fluids with highly directional attractive forces. IV. Equilibrium polymerization". In: *J. Stat. Phys.* 42.3-4 (Feb. 1986), pp. 477–492. ISSN: 0022-4715, 1572-9613. DOI: 10.1007/BF01127722.

[169] David Chandler and Hans C. Andersen. "Optimized Cluster Expansions for Classical Fluids. II. Theory of Molecular Liquids". In: *J. Chem. Phys.* 57.5 (Sept. 1972), pp. 1930–1937. ISSN: 0021-9606. DOI: 10.1063/1.1678513.

[170] Hans C. Andersen, David Chandler, and John D. Weeks. "Optimized Cluster Expansions for Classical Fluids. III. Applications to Ionic Solutions and Simple Liquids". In: *J. Chem. Phys.* 57.7 (Oct. 1972), pp. 2626–2631. ISSN: 0021-9606. DOI: 10.1063/1.1678641.

[172] Hans C. Andersen, David Chandler, and John D. Weeks. "Roles of Repulsive and Attractive Forces in Liquids : The Equilibrium Theory of Classical Fluids". en. In: *Advances in Chemical Physics*. _eprint: https://onlinelibrary.wiley.com/doi/pdf/10.1002 John Wiley & Sons, Ltd, 1976, pp. 105–156. ISBN: 978-0-470-14253-0. DOI: 10.1002/9780470142530.ch2.

[179] Aidan P. Thompson et al. "LAMMPS - a flexible simulation tool for particle-based materials modeling at the atomic, meso, and continuum scales". In: *Comput. Phys. Commun.* 271 (Feb. 2022), p. 108171. ISSN: 0010-4655. DOI: 10.1016/j.cpc.2021.108171.

[187] Naveen Michaud-Agrawal et al. “MDAnalysis: A toolkit for the analysis of molecular dynamics simulations”. In: *J. Comput. Chem.* 32.10 (July 2011), pp. 2319–2327. ISSN: 01928651. DOI: 10.1002/jcc.21787.

[188] Eric Darve, David Rodríguez-Gómez, and Andrew Pohorille. “Adaptive biasing force method for scalar and vector free energy calculations”. In: *J. Chem. Phys.* 128.14 (Apr. 2008), p. 144120. ISSN: 0021-9606. DOI: 10.1063/1.2829861.

[189] Jérome Hénin et al. “Exploring Multidimensional Free Energy Landscapes Using Time-Dependent Biases on Collective Variables”. In: *J. Chem. Theory Comput.* 6.1 (Jan. 2010), pp. 35–47. ISSN: 1549-9618. DOI: 10.1021/ct9004432.

[190] Giacomo Fiorin, Michael L. Klein, and Jérôme Hénin. “Using collective variables to drive molecular dynamics simulations”. In: *Mol. Phys.* 111.22-23 (Dec. 2013). _eprint: https://doi.org/10.1080/00268976.2013.813594, pp. 3345–3362. ISSN: 0026-8976. DOI: 10.1080/00268976.2013.813594.

[208] Sean Friedowitz et al. “Looping-in complexation and ion partitioning in nonstoichiometric polyelectrolyte mixtures”. In: *Sci. Adv.* 7.31 (July 2021), eabg8654. DOI: 10.1126/sciadv.abg8654.

[212] Clifford P. Brangwynne, Timothy J. Mitchison, and Anthony A. Hyman. “Active liquid-like behavior of nucleoli determines their size and shape in Xenopus laevis oocytes”. In: *Proc. Natl. Acad. Sci. U.S.A.* 108.11 (Mar. 2011), pp. 4334–4339. DOI: 10.1073/pnas.1017150108.

[213] Vladimir N. Uversky et al. “Intrinsically disordered proteins as crucial constituents of cellular aqueous two phase systems and coacervates”. In: *FEBS Lett.* 589.1 (Jan. 2015), pp. 15–22. ISSN: 0014-5793. DOI: 10.1016/j.febslet.2014.11.028.

[214] Simon Alberti et al. “Current practices in the study of biomolecular condensates: a community comment”. en. In: *Nat. Commun.* 16.1 (Aug. 2025), p. 7730. ISSN: 2041-1723. DOI: 10.1038/s41467-025-62055-8.

[215] Hasan Cinar et al. “Pressure-Induced Dissolution and Reentrant Formation of Condensed, Liquid–Liquid Phase-Separated Elastomeric α-Elastin”. en. In: *Chem. Eur. J.* 24.33 (2018). _eprint: https://chemistry-europe.onlinelibrary.wiley.com/doi/pdf/10
pp. 8286–8291. ISSN: 1521-3765. DOI: 10.1002/chem.201801643.

[216] Gregory L. Dignon et al. “Temperature-Controlled Liquid–Liquid Phase Separation of Disordered Proteins”. In: *ACS Cent. Sci.* 5.5 (May 2019), pp. 821–830. ISSN: 2374-7943. DOI: 10.1021/acscentsci.9b00102.

[217] Omar Adame-Arana et al. “Liquid Phase Separation Controlled by pH”. In: *Biophys. J.* 119.8 (Oct. 2020), pp. 1590–1605. ISSN: 0006-3495. DOI: 10.1016/j.bpj.2020.07.044.

[218] Georg Krainer et al. “Reentrant liquid condensate phase of proteins is stabilized by hydrophobic and non-ionic interactions”. en. In: *Nat. Commun.* 12.1 (Feb. 2021), p. 1085. ISSN: 2041-1723. DOI: 10.1038/s41467-021-21181-9.

[219] Rahul K. Das and Rohit V. Pappu. “Conformations of intrinsically disordered proteins are influenced by linear sequence distributions of oppositely charged residues”. In: *Proc. Natl. Acad. Sci. U.S.A.* 110.33 (Aug. 2013), pp. 13392–13397. DOI: 10.1073/pnas.1304749110.

[220] Rahul K Das, Kiersten M Ruff, and Rohit V Pappu. “Relating sequence encoded information to form and function of intrinsically disordered proteins”. In: *Curr. Opin. Struct. Biol.* New constructs and expression of proteins / Sequences and topology 32 (June 2015), pp. 102–112. ISSN: 0959-440X. DOI: 10.1016/j.sbi.2015.03.008.

[221] Yi-Hsuan Lin, Julie D. Forman-Kay, and Hue Sun Chan. “Sequence-Specific Polyampholyte Phase Separation in Membraneless Organelles”. In: *Phys. Rev. Lett.* 117.17 (Oct. 2016), p. 178101. DOI: 10.1103/PhysRevLett.117.178101.

[222] Chi W. Pak et al. “Sequence Determinants of Intracellular Phase Separation by Complex Coacervation of a Disordered Protein”. eng. In: *Mol. Cell* 63.1 (July 2016), pp. 72–85. ISSN: 1097-4164. DOI: 10.1016/j.molcel.2016.05.042.

[223] Timothy J. Nott et al. “Phase Transition of a Disordered Nuage Protein Generates Environmentally Responsive Membraneless Organelles”. English. In: *Mol. Cell* 57.5 (Mar. 2015), pp. 936–947. ISSN: 1097-2765. DOI: 10.1016/j.molcel.2015.01.013.

[224] Charles E. Sing. “Development of the modern theory of polymeric complex coacervation”. In: *Adv. Colloid Interface Sci.* Complex Coacervation: Principles and Applications 239 (Jan. 2017), pp. 2–16. ISSN: 0001-8686. DOI: 10.1016/j.cis.2016.04.004.

[225] Yi-Hsuan Lin, Julie D. Forman-Kay, and Hue Sun Chan. “Theories for Sequence-Dependent Phase Behaviors of Biomolecular Condensates”. In: *Biochemistry* 57.17 (May 2018), pp. 2499–2508. ISSN: 0006-2960. DOI: 10.1021/acs.biochem.8b00058.

[226] Scott P. O. Danielsen et al. “Molecular design of self-coacervation phenomena in block polyampholytes”. In: *Proc. Natl. Acad. Sci. U.S.A.* 116.17 (Apr. 2019), pp. 8224–8232. DOI: 10.1073/pnas.1900435116.

[227] Jonghoon Lee, Yuri O. Popov, and Glenn H. Fredrickson. “Complex coacervation: A field theoretic simulation study of polyelectrolyte complexation”. In: *J. Chem. Phys.* 128.22 (June 2008), p. 224908. ISSN: 0021-9606. DOI: 10.1063/1.2936834.

[228] Robert A. Riggleman, Rajeev Kumar, and Glenn H. Fredrickson. "Investigation of the interfacial tension of complex coacervates using field-theoretic simulations". In: *J. Chem. Phys.* 136.2 (Jan. 2012), p. 024903. ISSN: 0021-9606, 1089-7690. DOI: 10.1063/1.3674305.

[229] Sarah L. Perry and Charles E. Sing. "PRISM-Based Theory of Complex Coacervation: Excluded Volume versus Chain Correlation". In: *Macromolecules* 48.14 (July 2015), pp. 5040–5053. ISSN: 0024-9297. DOI: 10.1021/acs.macromol.5b01027.

[230] V. Yu. Borue and I. Ya. Erukhimovich. "A statistical theory of globular polyelectrolyte complexes". In: *Macromolecules* 23.15 (July 1990), pp. 3625–3632. ISSN: 0024-9297. DOI: 10.1021/ma00217a015.

[231] M. Castelnovo and J.-F. Joanny. "Complexation between oppositely charged polyelectrolytes: Beyond the Random Phase Approximation". en. In: *Eur. Phys. J. E* 6.1 (Dec. 2001), pp. 377–386. ISSN: 1292-8941. DOI: 10.1007/s10189-001-8051-7.

[232] Alexander Kudlay and Monica Olvera de la Cruz. "Precipitation of oppositely charged polyelectrolytes in salt solutions". In: *J. Chem. Phys.* (2004). DOI: 10.1063/1.1629271.

[233] Li-Wei Chang et al. "Sequence and entropy-based control of complex coacervates". en. In: *Nat. Commun.* 8.1 (Nov. 2017), p. 1273. ISSN: 2041-1723. DOI: 10.1038/s41467-017-01249-1.

[234] Shensheng Chen, Pengfei Zhang, and Zhen-Gang Wang. "Complexation between Oppositely Charged Polyelectrolytes in Dilute Solution: Effects of Charge Asymmetry". In: *Macromolecules* 55.10 (May 2022), pp. 3898–3909. ISSN: 0024-9297. DOI: 10.1021/acs.macromol.2c00339.

[235] Tae Hyun Kim et al. "Flexible biomimetic block copolymer composite for temperature and long-wave infrared sensing". In: *Sci. Adv.* 9.6 (Feb. 2023), eade0423. DOI: 10.1126/sciadv.ade0423.

[236] Kyosuke Adachi and Kyogo Kawaguchi. "Predicting Heteropolymer Interactions: Demixing and Hypermixing of Disordered Protein Sequences". In: *Phys. Rev. X* 14.3 (July 2024), p. 031011. DOI: 10.1103/PhysRevX.14.031011.

[237] Seowon Kim et al. "Droplets, Micelles, and More Complex Structures of Polyampholyte Aggregates". In: *Macromolecules* 58.13 (July 2025), pp. 6971–6980. ISSN: 0024-9297. DOI: 10.1021/acs.macromol.5c00786.

[238] Wesley W. Oliver, William M. Jacobs, and Michael A. Webb. "When B2 is Not Enough: Evaluating Simple Metrics for Predicting Phase Separation of Intrinsically Disordered Proteins". In: *J. Phys. Chem. B* 129.37 (Sept. 2025), pp. 9551–9565. ISSN: 1520-6106. DOI: 10.1021/acs.jpcb.5c04955.

[239] Seowon Kim et al. “Aggregation of polyampholytes: Influence of salt concentration”. In: *J. Chem. Phys.* 164.11 (Mar. 2026), p. 114906. ISSN: 0021-9606. DOI: 10.1063/5.0321613.

[240] Alex S. Holehouse et al. “CIDER: Resources to Analyze Sequence-Ensemble Relationships of Intrinsically Disordered Proteins”. In: *Biophys. J.* 112.1 (Jan. 2017), pp. 16–21. ISSN: 0006-3495. DOI: 10.1016/j.bpj.2016.11.3200.

[241] Lucas Sawle and Kingshuk Ghosh. “A theoretical method to compute sequence dependent configurational properties in charged polymers and proteins”. In: *J. Chem. Phys.* 143.8 (Aug. 2015), p. 085101. ISSN: 0021-9606. DOI: 10.1063/1.4929391.

[242] Dinesh Sundaravadivelu Devarajan and Jeetain Mittal. “Sequence-Encoded Spatiotemporal Dependence of Viscoelasticity of Protein Condensates Using Computational Microrheology”. In: *JACS Au* 4.11 (Nov. 2024), pp. 4394–4405. DOI: 10.1021/jacsau.4c00740.

[243] Dinesh Sundaravadivelu Devarajan et al. “Sequence-dependent material properties of biomolecular condensates and their relation to dilute phase conformations”. en. In: *Nat. Commun.* 15.1 (Mar. 2024), p. 1912. ISSN: 2041-1723. DOI: 10.1038/s41467-024-46223-w.

[244] Shensheng Chen and Zhen-Gang Wang. “Charge Asymmetry Suppresses Coarsening Dynamics in Polyelectrolyte Complex Coacervation”. In: *Phys. Rev. Lett.* 131.21 (Nov. 2023), p. 218201. DOI: 10.1103/PhysRevLett.131.218201.

[245] Xu Chen et al. “Multiphase Coacervates Driven by Electrostatic Correlations”. In: *ACS Macro Lett.* 10.8 (Aug. 2021), pp. 1041–1047. DOI: 10.1021/acsmacrolett.1c00282.

[246] Jie Wang et al. “Interfacial Tensions of Polyelectrolyte Multiphase Coacervation”. In: *Macromolecules* 57.20 (Oct. 2024), pp. 9698–9710. ISSN: 0024-9297. DOI: 10.1021/acs.macromol.4c02017.

[247] Artem M. Rumyantsev et al. “Unifying Weak and Strong Charge Correlations within the Random Phase Approximation: Polyampholytes of Various Sequences”. In: *Macromolecules* 55.14 (July 2022), pp. 6260–6274. ISSN: 0024-9297. DOI: 10.1021/acs.macromol.2c00569.

[248] Yi-Hsuan Lin et al. “Charge pattern matching as a ‘fuzzy’ mode of molecular recognition for the functional phase separations of intrinsically disordered proteins”. en. In: *New J. Phys.* 19.11 (Nov. 2017), p. 115003. ISSN: 1367-2630. DOI: 10.1088/1367-2630/aa9369.

[249] Keshawa P. Shukla and Walter G. Chapman. “TPT2 and SAFTD equations of state for mixtures of hard chain copolymers”. In: *Mol. Phys.* (2000). DOI: 10.1080/00268970009483407.

[250] Bennett D. Marshall and Walter G. Chapman. “Higher Order Classical Density Functional Theory for Branched Chains and Rings”. In: *J. Phys. Chem. B* 115.50 (Dec. 2011), pp. 15036–15047. ISSN: 1520-6106. DOI: 10.1021/jp2078677.

[251] Bennett D. Marshall and Walter G. Chapman. “Three new branched chain equations of state based on Wertheim’s perturbation theory”. In: *J. Chem. Phys.* 138.17 (May 2013), p. 174109. ISSN: 0021-9606. DOI: 10.1063/1.4803023.

[252] Leying Qing et al. “Thermodynamic Perturbation Theory for Charged Branched Polymers”. In: *J. Chem. Theory Comput.* 21.1 (Jan. 2025), pp. 333–346. ISSN: 1549-9618. DOI: 10.1021/acs.jctc.4c01187.

[253] Erich A. Müller and Keith E. Gubbins. “Simulation of hard triatomic and tetratomic molecules”. In: *Mol. Phys.* 80.4 (Nov. 1993), pp. 957–976. ISSN: 0026-8976. DOI: 10.1080/00268979300102791.

[254] Erich A. Müller and Keith E. Gubbins. “Triplet correlation function for hard sphere systems”. In: *Mol. Phys.* 80.1 (Sept. 1993), pp. 91–101. ISSN: 0026-8976. DOI: 10.1080/00268979300102081.

[255] Yi-Hsuan Lin and Hue Sun Chan. “Phase Separation and Single-Chain Compactness of Charged Disordered Proteins Are Strongly Correlated”. In: *Biophys. J.* 112.10 (May 2017), pp. 2043–2046. ISSN: 0006-3495. DOI: 10.1016/j.bpj.2017.04.021.

[256] Jian Zhang, Ran Kou, and Guangming Liu. “Effect of Salt Concentration on the pH Responses of Strong and Weak Polyelectrolyte Brushes”. In: *Langmuir* 33.27 (July 2017), pp. 6838–6845. ISSN: 0743-7463. DOI: 10.1021/acs.langmuir.7b01395.

[257] Maria Victoria Nugnes et al. “DisProt in 2026: enhancing intrinsically disordered proteins accessibility, deposition, and annotation”. In: *Nucleic Acids Res.* 54.D1 (Jan. 2026), pp. D383–D392. ISSN: 1362-4962. DOI: 10.1093/nar/gkaf1175.

[258] Yaxin An, Michael A. Webb, and William M. Jacobs. “Active learning of the thermodynamics-dynamics trade-off in protein condensates”. In: *Sci. Adv.* 10.1 (Jan. 2024), eadj2448. DOI: 10.1126/sciadv.adj2448.

Chapter 4

TOPOLOGY-DRIVEN PHASE SEPARATION IN CHARGED POLYMER SOLUTIONS

In this chapter, we develop a topology-specific theory of polyelectrolyte coacervation using the random phase approximation and apply it to both simple and complex coacervation. Our results for stars and dendrimers show that more compact chain topologies display a greater propensity for liquid-liquid phase separation, as a function of both Bjerrum length and salt concentration. For mixtures of different topologies, we demonstrate that differences in polymer topology alone are sufficient to drive multiphase coacervation of polyelectrolytes, which we rationalize in terms of an effective χ parameter. Analysis of a simplified global phase diagram reveals that the propensity for such topology-driven phase separation is largest at a finite molecular weight. Overall, our results establish polymer topology as a powerful design lever for tuning the phase diagram of charged macromolecules independently of molecular weight, net charge, and monomer chemistry, since changes in topology enable fine-tuning of the effective charge density without altering these molecular characteristics.

This chapter includes work from our previously published preprint: David Beyer, Pierre J. Walker, Lena Tarrach, Zhen-Gang Wang, and Christian Holm. *How Topology Shapes the Phase Behavior of Polyelectrolytes*. arXiv:2607.15703 [cond-mat.soft]. July 2026. DOI: 10.48550/arXiv.2607.15703

4.1 Introduction

The phase behavior of charged macromolecules plays an important role in cell biology [259, 260], soft matter science [44, 116, 117, 261], and various technological applications [262]. For example, charged biopolymers can spontaneously phase separate, leading to droplet-like structures known as biomolecular condensates [260, 263, 264, 265]. An analogous phenomenon occurs for synthetic polyelectrolytes [44, 116, 117]: as illustrated in Figure 4.1(a), aqueous solutions of polyelectrolytes can split into a dense coacervate phase and a dilute supernatant through liquid-liquid phase separation (LLPS). Depending on the composition of the system—either solely consisting of polyelectrolytes with the same sign of charge or containing both polyanions and polycations—the coacervate is called a simple coacervate or

a complex coacervate. Recent works have revealed that mixtures of different polyelectrolytes may even split into multiple distinct coacervate phases [266, 245, 267, 246, 268, 269, 270]—so-called "multiphase coacervation."

Together with the charge-sequence effects examined in Chapter 3, this establishes molecular architecture — sequence and topology alike — as a design variable for phase behavior that operates independently of net charge, chain length, and monomer chemistry.

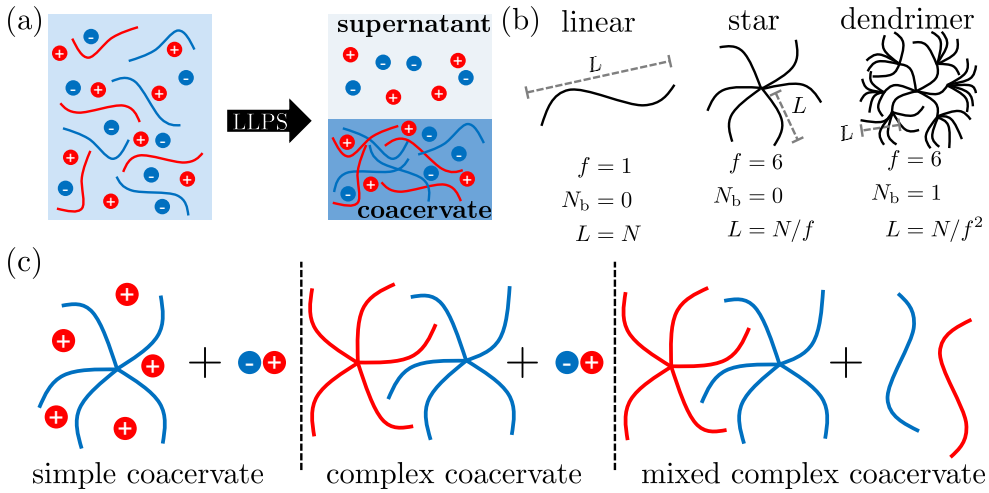


Figure 4.1: (a) Polyelectrolyte solutions can split into a supernatant with a low polyelectrolyte concentration and a coacervate with a high polyelectrolyte concentration through LLPS. Blue and red chains correspond to polyanions and polycations, respectively. (b) Schematic representation of the different polymer topologies investigated in this work: linear chains, stars, and dendrimers. Note that for visual clarity, the different topologies are not shown at the same scale. (c) Overview of the different mixtures of polyelectrolytes studied in this work: simple coacervates (left panel), complex coacervates (middle panel), and salt-free, mixed complex coacervates (right panel).

A key question in polyelectrolyte physics is identifying the parameters that govern the coacervate phase behavior. Previous studies have demonstrated that LLPS can be controlled by adjusting parameters such as temperature [90], salt concentration [271, 207], and pH [272, 273]. Furthermore, the phase behavior of charged macromolecules is also influenced by properties intrinsic to polymers, including charge density and net charge [209, 234, 274], chain stiffness [275], and architectural parameters such as the sequence of charged residues [221, 222, 225, 233, 226, 276, 277, 236]. Another architectural parameter that could influence the phase behavior of polyelectrolytes is the polymer topology. However, although there exist a small number of publications studying the coacervation of polyelectrolytes with non-linear

topologies [278, 279, 280, 281, 282, 283, 137, 284, 285, 286], the majority of studies focus on linear chains, presumably because of their prominence in biological systems and ease of synthesis. Previous works studying the effects of molecular architecture on polyelectrolyte coacervation invariably varied both chain topology and other parameters such as molecular weight simultaneously [278, 280], making it difficult to isolate the effects of chain topology. Moreover, we are not aware of any systematic theoretical investigation establishing the phase behavior of complex mixtures containing polyelectrolytes of different topologies. To address these open questions, we develop a minimal, topology-specific theory of polyelectrolyte coacervates and apply it to simple and complex coacervation, revealing several topology-driven effects, including topology-driven multiphase coacervation.

4.2 Theory

Because the space of polymer topologies is astronomically large, we use a class of simple model architectures that allow us to systematically vary the chain topology via a small number of easily interpretable parameters. The model architectures studied in the following are dendrimers, which have previously been studied, for example, in the context of binary polyelectrolyte complexation [287]. We consider dendrimers with f arms emerging from the central core (see Figure 4.1(b)). Each arm branches into $f-1$ branches (these branches then branch into $f-1$ sub-branches, etc); in total, there are N_b generations of branchings. For a given topology, the number of monomers between two branchings is always taken to be the same (L), resulting in three parameters that fully characterize our model topologies ($\mathcal{T} = (f, N_\mathrm{b}, N)$): the number of arms ($f$), the number of generations (N_b), and the overall molecular weight (N). To focus solely on the effect of topology, we set the degree of polymerization of the polymers to a constant value, $N = 200$, in the following. We represent the polymer chains using a continuous Gaussian chain model, which allows us to derive a simple closed-form expression for the single-chain structure factors and is justified given that $L \gg 1$ for all model architectures considered.

To construct phase diagrams of coacervates consisting of polyelectrolyte chains with different topologies, we need a topology-specific expression for the free energy. Approaches such as the Voorn-Overbeek theory [44] or liquid-state theory [253, 88, 138, 136, 90, 250, 251, 288] cannot account for differences in polymer topology. Therefore, we combine the Flory-Huggins free energy with a Coulomb correlation term derived within the random phase approximation (RPA) [289], which has been widely used to study the phase behavior of polyelectrolytes [290, 291, 227, 278,

292, 134, 129, 245]. The free energy, F, for a mixture of salt, polyelectrolytes of various topologies, and neutral solvent reads

$$\frac{\beta F b^3}{V} = \sum_i \frac{\phi_i}{N_i} \ln \phi_i + \frac{1}{2} \sum_{i,j} \chi_{ij} \phi_i \phi_j + \frac{b^3}{4\pi^2} \int_0^\infty \mathrm{d}k\, k^2 \left[\ln \left(1 + \frac{4\pi l_\mathrm{B}}{k^2 b^3} \sum_i \phi_i \sigma_i^2 g_i(k; \mathcal{T}_i) \right) - \frac{4\pi l_\mathrm{B}}{k^2 b^3} \sum_i \phi_i \sigma_i^2 \right. \tag{4.1}$$

with sums running over all species i. The first two terms are the Flory-Huggins free energy, where ϕ_i and N_i are the volume fraction and molecular weight of species i, respectively. b is the Kuhn length, which, for simplicity, is assumed to be the same for all polymers. Furthermore, we set the volume of small ions and solvent molecules to b^3. χ_{ij} is the interaction parameter of species i and j, which is set to $\chi_{ij} = 1/2$ for polymer-solvent interactions to emulate a θ-solvent and set to zero for all other interactions [129]. The final term accounts for electrostatic correlations of polyelectrolytes and small ions at the RPA level. Here, k is the wave number and $l_\mathrm{B} \equiv e^2/4\pi\epsilon_0\epsilon_\mathrm{r} k_\mathrm{B} T$ is the Bjerrum length of the system, with the elementary charge e, the vacuum permittivity ϵ_0, and the dielectric constant of the solvent ϵ_r. σ_i is the charge fraction of species i, i.e. the average fraction of elementary charges per monomer; we set $\sigma_i = 0.2$ for all polyelectrolyte species and $\sigma_i = 1$ for salt ions. $g_i(k; \mathcal{T}_i)$ is the single-chain structure factor of species i, which explicitly depends on the corresponding topology $\mathcal{T}_i$.

For salt ions, we have $g_i = 1$. For a continuous chain with a dendrimer-like topology, characterized by a degree of polymerization N, branching number f, and N_b generations, the single-chain structure factor is defined as

$$g(k; \mathcal{T}) = \frac{1}{N} \int_0^N \mathrm{d}s \int_0^N \mathrm{d}s' \left\langle e^{i\mathbf{k}\cdot[\mathbf{r}(s) - \mathbf{r}(s')]} \right\rangle, \tag{4.2}$$

where s and s' denote contour positions along the polymer backbone. Assuming Gaussian chain statistics, the characteristic function for monomers belonging to the same edge takes the form

$$\left\langle e^{i\mathbf{k}\cdot[\mathbf{r}(s) - \mathbf{r}(s')]} \right\rangle = \exp\left(-\frac{k^2 b^2 |s - s'|}{6} \right). \tag{4.3}$$

The correlations between points belonging to the same edge of the dendrimer, therefore, generate the standard Debye function $D(x)$,

$$\frac{1}{L^2} \int_0^L \mathrm{d}s \int_0^L \mathrm{d}s' \exp\left(-\frac{k^2 b^2 |s - s'|}{6} \right) = \frac{2}{x^2} \left(e^{-x} + x - 1 \right) = D(x), \tag{4.4}$$

where we introduced the abbreviation $x \equiv Lk^2b^2/6$ and L, which is the length of a single graph edge. Correlations between a branch point and the positions on an adjacent edge generate the auxiliary function $h(x)$,

$$\frac{1}{L}\int_0^L \mathrm{d}s \exp\left(-\frac{k^2b^2s}{6}\right) = \frac{1}{x}\left(1 - e^{-x}\right) = h(x). \tag{4.5}$$

The full dendrimer structure factor is obtained by combining same-edge and inter-edge correlations. The latter depend only on the graph distance between edges and can be collected into a generating function $G(z; f, N_\mathrm{b})$, where $z = e^{-x}$. The resulting single-chain structure factor is

$$g(k;\mathcal{T}) = \frac{N}{E(f,N_\mathrm{b})}\left[D(x) + \frac{G(z;f,N_\mathrm{b})}{E(f,N_\mathrm{b})}h^2(x)\right], \tag{4.6}$$

where

$$E = f\frac{(f-1)^{N_\mathrm{b}+1} - 1}{f-2} \tag{4.7}$$

is the total number of edges in the dendrimer, allowing us to calculate the length of a single edge,

$$L = \frac{N}{E(f,N_\mathrm{b})}. \tag{4.8}$$

For $N_\mathrm{b} = 0$, we have:

$$G(z) = f(f-1), \tag{4.9}$$

and for $N_\mathrm{b} = 1$, we have:

$$G(z) = (f-1)f(f+1) + 2f(f-1)^2z + f(f-1)^3z^2. \tag{4.10}$$

To find the composition of coexisting phases, we follow the same approach described in Chapter 2, subject to an incompressibility constraint $\sum_i \phi_i = 1$. In practice, we use an implementation of equation 4.1 in the Clapeyron.jl software package [20], which uses automatic differentiation to evaluate derivatives of the free energy and allows for efficient numerical computation of phase diagrams.

4.3 Results and discussion

We now apply our theory to model systems of increasing complexity (Figure 4.1(c)), progressing from simple coacervates (with added salt) to complex coacervates (with added salt) to mixtures of complex coacervates. Each system intends to identify the effects of polyelectrolyte topology on their phase behavior.

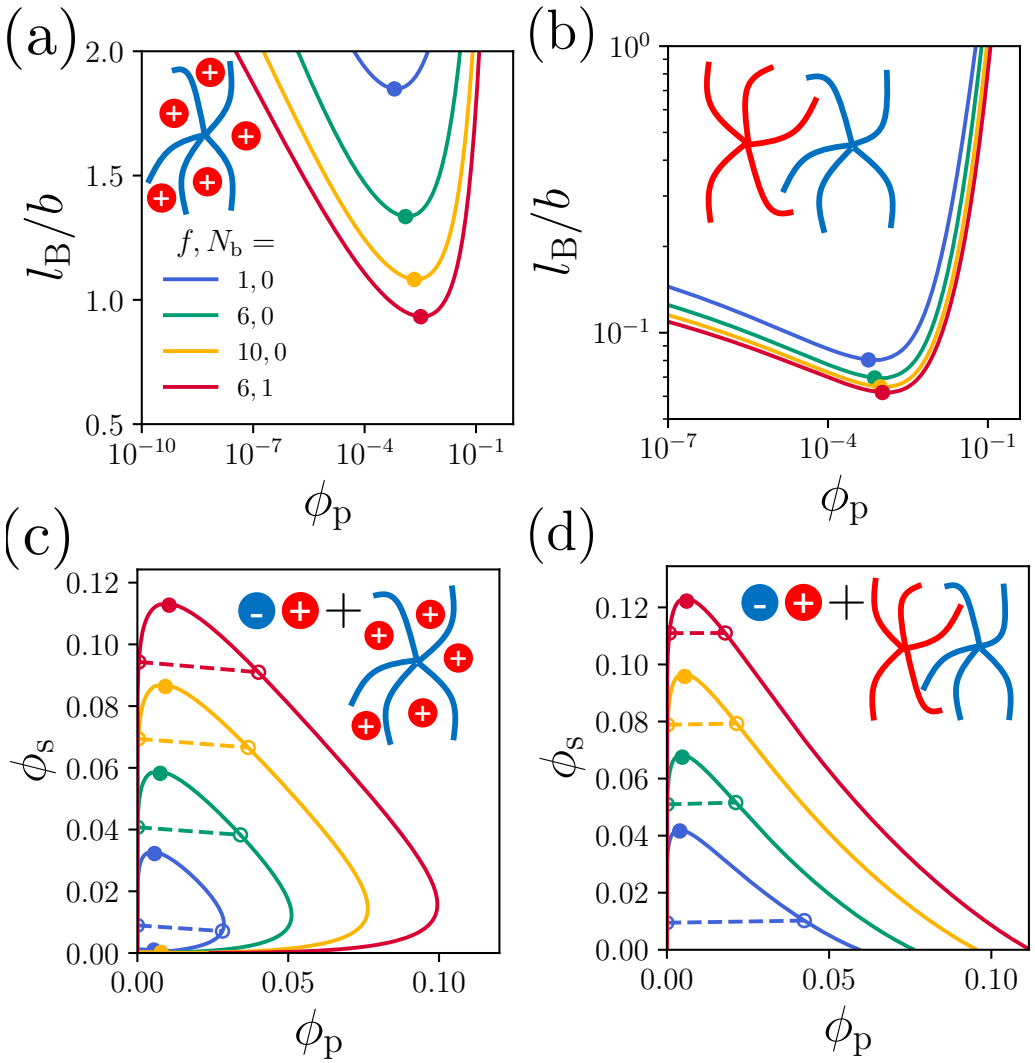


Figure 4.2: Phase diagrams of simple (subfigure (a) and (c)) and complex (subfigure (b) and (d)) coacervates of varying topology. Subfigures (a) and (b) show salt-free phase diagrams as a function of the polymer volume fraction and the Bjerrum length. Subfigures (c) and (d) show diagrams in the presence of salt as a function of the polymer volume fraction and the salt volume fraction (the Bjerrum length is set to $l_B = b$). Solid lines correspond to the co-existence boundary; dashed lines correspond to tie lines connecting coexisting phases (empty markers); solid markers denote the critical points.

Simple and complex coacervates

First, we consider a salt-free simple coacervate, i.e., a polyelectrolyte with counterions in the absence of salt. Figure 4.2(a) shows that this system undergoes LLPS for a sufficiently high Bjerrum length ("simple coacervation"). As the Bjerrum length is reduced, the electrostatic interactions, and thus the driving force for LLPS, weaken, causing the coacervate and supernatant branches to approach each other and finally

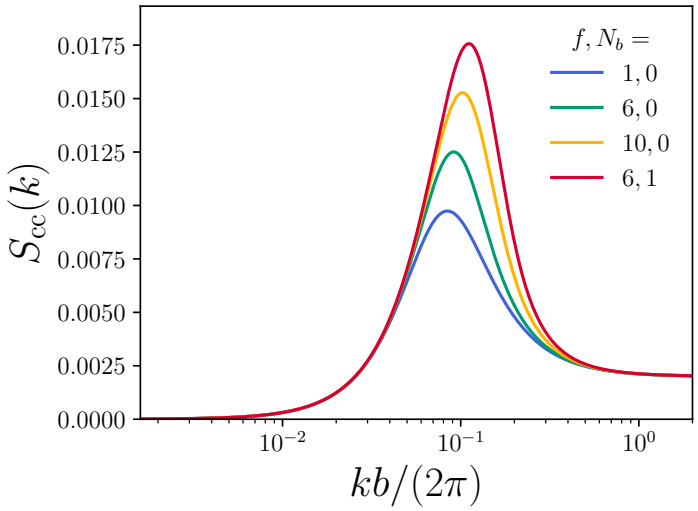


Figure 4.3: Charge–charge structure factor of a simple polyelectrolyte of varying topology with its counterion at $l_B = b$, $\sigma = 0.2$, $\phi_p = 0.01$ and $N = 200$.

merge at the critical point. Despite the fact that the total charge and molecular weight of each topology shown in the plot are identical, a comparison shows that the critical Bjerrum length decreases in the order $(1,0) \rightarrow (6,0) \rightarrow (10,0) \rightarrow (6,1)$ (using the notation introduced in the legend of Figure 4.2(a)). This increased tendency to phase separate is driven solely by changes in topology and stems from the more compact nature of branched architectures, which leads to a locally increased charge density and, therefore, to stronger electrostatic correlations driving LLPS. The increased compactness is evident from the RPA structure factors of the different topologies, obtained as:

$$S_{cc}(k) = \frac{\sum_i \phi_i \sigma_i^2 g_i(k;\mathcal{T}_i)}{1 + \frac{4\pi l_B}{k^2 b^3} \sum_i \phi_i \sigma_i^2 g_i(k;\mathcal{T}_i)} \,. \tag{4.11}$$

The resulting structure factor for a dilute simple polyelectrolyte with its counterion is shown in Figure 4.3. In all cases, a maximum appears at a finite k, implying compact conformations. These maximum becomes more pronounced and shifts to higher k as the polymer topology becomes more branched, implying further compactification of the single chain. This behavior demonstrates the higher local charge density of branched topologies.

Assuming that the location of the maximum of the single-chain charge-charge structure factor approximately represents the inverse volume taken up by a single chain, we can estimate (see appendix for derivation) the increase in charge density when

going from a linear chain to a topology $\mathcal{T}$, first for a star topology:

$$\frac{\rho_{\mathrm{c,eff}}(\mathrm{star})}{\rho_{\mathrm{c,eff}}(\mathrm{chain})} \sim \left(\frac{f^2}{3f-2}\right)^{3/4}, \tag{4.12}$$

and for a dendrimer

$$\frac{\rho_{\mathrm{c,eff}}(\mathrm{dendrimer})}{\rho_{\mathrm{c,eff}}(\mathrm{chain})} \sim \left(\frac{f^2}{3f-2}\right)^{3/2}. \tag{4.13}$$

An interesting but sensible result from these two equations is that, for the same branching number f, dendrimers achieve a greater effective charge density than stars, consistent with the results in Figure 4.2.

Notably, topology-induced changes in charge density are distinct from those reported for linear polyelectrolytes [245], where changes in linear charge density are invariably accompanied by variations in monomer size or polymer chemical composition. In contrast, changes in topology allow the monomer properties and charge density to be decoupled, enabling fine-tuning of the phase behavior while maintaining a fixed polyelectrolyte chemistry and molecular weight. For salt-free complex coacervates, we observe a largely analogous behavior (Figure 4.2(b)). However, the critical Bjerrum length for complex coacervates is more than an order of magnitude smaller than for simple coacervates. This higher propensity for LLPS is caused by strong electrostatic correlations between the polyelectrolytes driving the phase split, as opposed to weaker polyelectrolyte-counterion correlations in simple coacervates.

In the next step, we fix the Bjerrum length to $l_\mathrm{B} = b$ and study coacervation in the presence of added salt [1]. As shown in Figure 4.2(c), for simple coacervation, all topologies exhibit the same qualitative phase behavior. The most prominent feature of the phase diagrams is a reentrant coacervation: at low salt concentration, an increase in salt leads to a broadening of the two-phase region, i.e., the polymer concentration in the coacervate increases. For star topologies, where the salt-free critical l_B is greater than b, the addition of salt even induces phase separation, as indicated by the critical points at low salt concentrations. The observed reentrant behavior occurs due to initial increases in electrostatic correlations upon the addition of salt, strengthening the driving force for coacervation. Conversely, at sufficiently high salt concentration, electrostatic screening begins to dominate, weakening the

[1] For many polymers, $b \approx 0.4 - 0.6$ nm [293], meaning that this Bjerrum length would be slightly smaller than that of water.

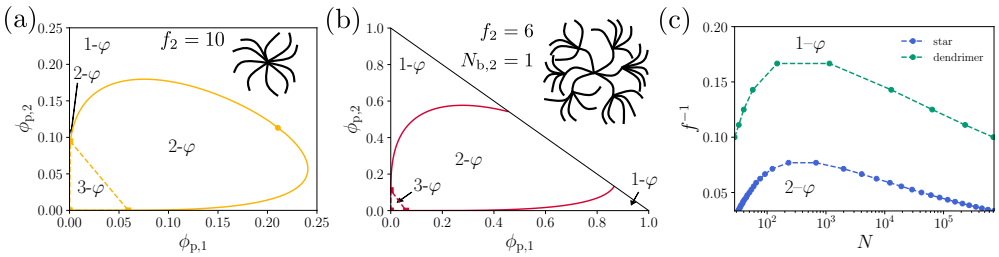


Figure 4.4: Phase behavior of mixed complex coacervates where symmetric pairs are considered for all topologies, i.e. the same number of polyanions and polycations is always added to the system for a particular topology. "1-φ", "2-φ" and "3-φ" denote regions where one, two or three phases coexist, respectively. (a) Phase diagram of a salt-free mixture of linear chains (volume fraction $\phi_{p,1}$) and stars ($f_2 = 10$, volume fraction $\phi_{p,2}$). (b) Phase diagram of a salt-free mixture of linear chains (volume fraction $\phi_{p,1}$) and dendrimers with one generation of branching ($f_2 = 6$, $N_{b,2} = 1$, volume fraction $\phi_{p,2}$). (c) Global phase diagram of a salt- and solvent-free blend of linear chains with stars (blue) and dendrimers ($N_b = 1$, green) with varying degree of polymerization (N) and degree of asymmetry (taken as f^{-1}). Points represent conditions at which the blend of polyelectrolytes will not phase separate at $l_B = b$. If a mixture lies below these curves, the addition of solvent will eventually result in three-phase separation.

driving force for coacervation and causing the two phase region to shrink and eventually close at the critical point. Changes in topology lead to a trend consistent with the salt-free case: more compact architectures exhibit a larger two-phase region and thus higher salt resistance, with the phase separation propensity increasing in exactly the same order as for the salt-free case. At the same time, the critical polymer concentration slightly increases, which also mirrors the behavior observed for the salt-free systems.

Consistent with other theories on simple coacervates [88, 136], negatively-sloped tie lines are observed due to differences in electrostatic screening between the supernatant and the coacervate. For complex coacervates (Figure 4.2(d)), the phase behavior is largely similar. However, we do not observe reentrant coacervation, i.e., the two-phase region monotonically shrinks with increasing salt concentration. This behavior originates from the stronger electrostatic correlations in complex coacervates: because the correlations between polyelectrolyte chains are already quite strong in the absence of salt, adding salt has only a minor effect that is overwhelmed by the increase in electrostatic screening. Moreover, we observe that in contrast to the simple coacervates and prior works, the tie lines are positively-sloped, due to the stronger electrostatic correlations in the complex coacervate.

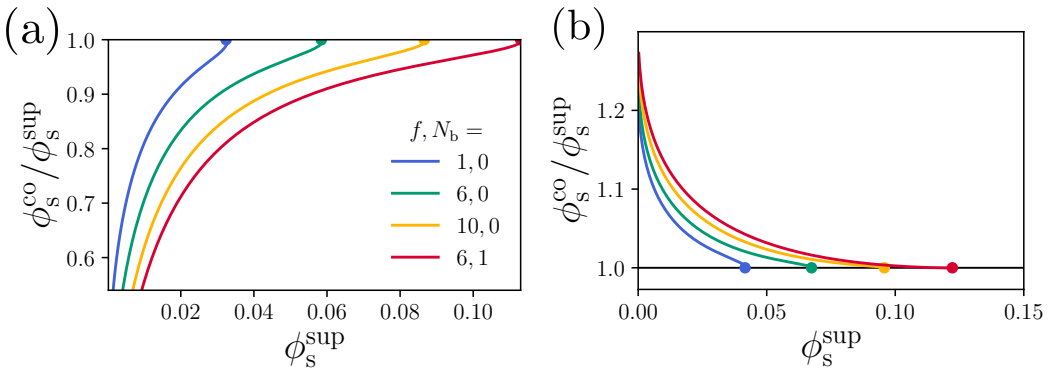


Figure 4.5: Salt partitioning in a simple (a) and complex (b) coacervate as a function of salt concentration in the supernatant with varying polyelectrolyte topology. For all systems, $l_B = b$.

While a few tie-lines are included within Figures 4.2(b) and 4.2(d), it is often of interest to examine how the partitioning of salt varies across the phase diagram. In Figure 4.5, we present the partition coefficient of salts within a simple (a) and complex (b) coacervate as a function of salt concentration in the supernatant with varying polyelectrolyte topology. Figure 4.5(a) demonstrates that for a simple coacervate, the partition coefficient is consistently smaller than unity; i.e., salt is rejected by the simple coacervate and the salt concentrations in the two phases only equalize at the critical point. Comparing different topologies, we observe that more compact molecular architectures reject salt more strongly, with the ability to reject salt increasing in exactly the same order as the phase separation propensity. This type of behavior is expected in simple coacervates, as the higher ion concentration in the supernatant results in greater electrostatic screening in this phase. Thus, with effectively weaker electrostatic interactions, the salt will preferentially partition into the supernatant. For the complex coacervate, we observe that ions preferentially partition into the coacervate rather than the supernatant (Figure 4.5(b)), which continues up to the critical point. The preferential partitioning into the coacervate is due to the stronger electrostatic correlations within this phase due to the presence of the oppositely charged polyelectrolytes, in contrast to the simple coacervate system containing a single polyelectrolyte with its small counterion.

Mixtures of complex coacervates

Having studied simple and complex coacervates in which only a single polymer topology is present in the system, we now turn to mixtures of different topologies. To avoid unnecessary complexity, we consider complex coacervates containing pairs of linear polyanions and polycations, mixed with pairs of polyanions and polycations

with a non-linear topology (see Figure 4.1(c)), and set $l_B = b$. For systems with minor topological asymmetries, e.g., linear chains and stars with $f = 6$ arms, almost ideal mixing occurs within the coacervate phase and the observed phase behavior is largely analogous to the results reported in the previous sections. In contrast, for systems with stronger asymmetries in polymer topology, such as linear chains mixed with 10-arm stars (Figure 4.4(a)), a more complex phase diagram emerges: in addition to single-phase behavior ("1-φ") and two-phase coexistence ("2-φ"), we also observe three-phase coexistence ("3-φ"). These three coexisting phases, corresponding to the vertices of the dashed triangle, are a supernatant with a low overall polymer concentration, a coacervate phase in which the linear chains are enriched, and *another* coacervate phase with a high concentration of stars. Notably, this three-phase coexistence only occurs in a regime where the concentrations of both polymer topologies are fairly low.

The driving force behind the observed three-phase separation (and, at higher concentrations, the two-phase separation between polyelectrolytes of different topologies) ultimately stems from differences in chain topology: the effect of topology on the electrostatic interactions between chains manifests itself as a change in the effective charge densities of the polyelectrolytes and, in fact, the whole single-chain structure factors. To elucidate the mechanism of topology-driven phase separation, we use an approach previously established by Chen et al. [245, 137]. Let us consider the free energy density of a general mixture,

$$\mathfrak{f} \equiv \frac{\beta F b^3}{V} \tag{4.14}$$

The thermodynamic stability of a bulk phase is governed by the curvature of this free energy density. The second-order variation of $\mathfrak{f}$ under infinitesimal density variations $\delta\phi_i$ can be written as

$$\delta^2\mathfrak{f} = \sum_i \frac{1}{N_i\phi_i}\delta\phi_i^2 + \frac{1}{2}\sum_{i,j}\left[\chi_{ij} + \frac{\partial^2\mathfrak{f}_{\mathrm{RPA}}}{\partial\phi_i\partial\phi_j}\right]\delta\phi_i\delta\phi_j. \tag{4.15}$$

The Hessian matrix of the RPA contribution, $\frac{\partial^2\mathfrak{f}_{\mathrm{RPA}}}{\partial\phi_i\partial\phi_j}$, reads

$$\frac{\partial^2\mathfrak{f}_{\mathrm{RPA}}}{\partial\phi_i\partial\phi_j} = -\frac{b^3}{4\pi^2}\int_0^\infty \mathrm{d}k\, k^2 \left(\frac{4\pi l_B}{k^2b^3}\right)^2 \frac{\sigma_i^2\sigma_j^2 g_i(k;\mathcal{T}_i)g_j(k;\mathcal{T}_j)}{\left(1 + \frac{4\pi l_B}{k^2b^3}\sum_l \phi_l\sigma_l^2 g_l(k;\mathcal{T}_l)\right)^2} \tag{4.16}$$

$$= -\int_0^\infty \mathrm{d}k\, \alpha(k)\sigma_i^2\sigma_j^2 g_i(k;\mathcal{T}_i)g_j(k;\mathcal{T}_j), \tag{4.17}$$

where we defined the abbreviation

$$\alpha(k) \equiv \frac{b^3 k^2}{4\pi^2} \left(\frac{4\pi l_\mathrm{B}}{k^2 b^3}\right)^2 \frac{1}{\left(1 + \frac{4\pi l_\mathrm{B}}{k^2 b^3} \sum_l \phi_l \sigma_l^2 g_l(k; \mathcal{T}_l)\right)^2}. \tag{4.18}$$

Following the approach of Chen et al. [245, 137], we can now rewrite the variation $\delta^2 \mathfrak{f}$ using the incompressibility condition $\sum_i \delta\phi_i = 0$:

$$\begin{aligned} \delta^2 \mathfrak{f} &= \sum_i \frac{1}{N_i \phi_i} \delta\phi_i^2 + \frac{1}{2} \sum_{i,j} \left[\chi_{ij} + \frac{\partial^2 \mathfrak{f}_\mathrm{RPA}}{\partial\phi_i \partial\phi_j}\right] \delta\phi_i \delta\phi_j \\ &= \sum_i \frac{1}{N_i \phi_i} \delta\phi_i^2 + \frac{1}{2} \sum_{i,j} \left[\chi_{ij} + \frac{\partial^2 \mathfrak{f}_\mathrm{RPA}}{\partial\phi_i \partial\phi_j} + A_i + A_j\right] \delta\phi_i \delta\phi_j. \end{aligned} \tag{4.19}$$

Note that this equation holds for *arbitrary* $A_i, A_j \in \mathbb{R}$. Setting

$$A_i = \frac{1}{2} \int_0^\infty \mathrm{d}k\, \alpha(k) \sigma_i^4 g_i^2(k; \mathcal{T}_i), \tag{4.20}$$

$\delta^2 \mathfrak{f}$ can be written as

$$\delta^2 \mathfrak{f} = \sum_i \frac{1}{N_i \phi_i} \delta\phi_i^2 + \frac{1}{2} \sum_{i,j} \chi_{ij}^\mathrm{eff} \delta\phi_i \delta\phi_j, \tag{4.21}$$

with the effective χ parameter,

$$\chi_{ij}^\mathrm{eff} \equiv \chi_{ij} + \frac{1}{2} \int_0^\infty \mathrm{d}k\, \alpha(k) \left[\sigma_i^2 g_i(k; \mathcal{T}_i) - \sigma_j^2 g_j(k; \mathcal{T}_j)\right]^2. \tag{4.22}$$

Let us now consider two polyelectrolyte species i and j that have the same charge densities, $\sigma_i = \sigma_j = \sigma$, but different topologies, $\mathcal{T}_i \neq \mathcal{T}_j$. In this case, the effective interaction between the species is governed by

$$\chi_{ij}^\mathrm{eff} \equiv \chi_{ij} + \frac{\sigma^4}{2} \int_0^\infty \mathrm{d}k\, \alpha(k) \left[g_i(k; \mathcal{T}_i) - g_j(k; \mathcal{T}_j)\right]^2. \tag{4.23}$$

Therefore, if the two topologies are sufficiently different, such that χ_{ij}^eff exceeds a critical value, differences in topology alone can drive liquid-liquid phase separation.

For a mixture of linear chains with dendrimers (Figure 4.4(b)), a slightly different phase behavior is observed: first, the concentration regime in which three-phase coexistence occurs is slightly larger. Second, the two-phase region no longer terminates at a critical point and instead intersects the solvent-free edge $\phi_{\mathrm{p},2} = 1 - \phi_{\mathrm{p},1}$. As in Figure 4.4(a), the driving force of multiphase coacervation is the difference in the intramolecular charge correlations, which are described by single-chain structure

factors. Due to weak electrostatic screening, the topology-driven LLPS is particularly pronounced at low polyelectrolyte concentrations. However, the differences in topology are so large that even in the solvent-free case, screening is insufficient to close the two-phase region. On the whole, the mixture of linear chains and dendrimers therefore exhibits a much larger concentration range where some form of topology-driven phase separation—either into two or three phases—occurs.

To characterize the effect of topological asymmetries on the global phase behavior, we consider a solvent- and salt-free blend comprised of linear polyelectrolytes and polyelectrolytes of arbitrary topology. For a given molecular weight, N, we then calculate the minimal degree of asymmetry (characterized by f) needed to drive LLPS between the different topologies. As shown in Figure 4.4(c), both for stars and dendrimers ($N_\mathrm{b} = 1$), we observe a non-monotonic dependence of the asymmetry f required to drive LLPS on the molecular weight N. Because dendrimers have an innately greater degree of topological asymmetry than stars, a lower degree of branching is needed for topology-induced LLPS, resulting in a larger two-phase region. The observed non-monotonicity can be understood as follows: on the left branch, where the molecular weight is low, electrostatic correlations are weak. Therefore, to induce LLPS, the charge density must be increased, resulting in a positive correlation between N and f^{-1}. Conversely, for large N, the RPA expression for the electrostatic correlation free energy decays as $N^{-3/2}$, which is faster than the entropy of mixing, N^{-1} (see appendix for more details). In order to induce LLPS, there must thus be a sufficiently high degree of topological asymmetry to overcome the entropy of mixing, resulting in a decrease of f^{-1} with N. These results are consistent with the scaling behavior of $\chi_{ij}^{\mathrm{eff}} - \chi_{ij}$ that we derive in the appendix: for small N we have $\chi_{ij}^{\mathrm{eff}} - \chi_{ij} \sim N^{5/2}$, and for large N we have $\chi_{ij}^{\mathrm{eff}} - \chi_{ij} \sim N^{-3/2}$. Taken together, our analytical results therefore suggest that topology-induced LLPS should be most pronounced for polyelectrolytes of finite molecular weight, which is in agreement with the numerically obtained phase diagrams.

4.4 Conclusion

In this chapter, we have theoretically studied the influence of polymer topology on the phase behavior of polyelectrolyte coacervates. The emerging picture is that more compact chain topologies show a greater propensity for LLPS, as a function of both Bjerrum length and salt concentration. Furthermore, we also investigated the phase behavior that results when polyelectrolytes of the same molecular weight but different topologies are mixed. These systems exhibited a more complex phase

behavior, including three-phase coexistence driven solely by differences in topology, which we could rationalize in terms of an effective χ parameter. Analysis of a simplified global phase diagram revealed that the propensity for such topology-driven LLPS has a non-monotonic functional dependence on the molecular weight, becoming increasingly suppressed for very small or large molecular weights. Overall, our results establish polymer topology as a powerful design lever for tuning the phase diagram of charged macromolecules independently of molecular weight, net charge, and monomer chemistry, since changes in topology enable fine-tuning of the effective charge density without altering these molecular characteristics. Looking ahead, it will be interesting to test our predictions using simulations that do not rely on the approximations of our RPA theory and ultimately through experiments. In particular, it would be worthwhile to investigate topology-modulated quantities and phenomena that are not accessible within our theory, including single-chain conformations, material properties, and polymer dynamics.

4.5 Appendix

Effective charge density

The increased charge compaction can also be demonstrated analytically by deriving the asymptotic scaling laws for the effective charge density. For simplicity, we focus on the single-chain charge–charge structure factor:

$$S_{\mathrm{p}}(k) = \frac{\sigma_{\mathrm{p}}^2 g_{\mathrm{p}}(k;\mathcal{T}_{\mathrm{p}})}{1 + \frac{4\pi l_{\mathrm{B}}}{k^2 b^3} \sum_i \phi_i \sigma_i^2 g_i(k;\mathcal{T}_i)}. \tag{4.24}$$

At infinite dilution, $\phi_{\mathrm{p}} \to 0$, keeping the ion concentration fixed, $\phi_i > 0$, we have:

$$S_{\mathrm{p}}(k) = \sigma_{\mathrm{p}}^2 g_{\mathrm{p}}(k;\mathcal{T}_{\mathrm{p}}) \frac{1}{1 + \frac{4\pi l_{\mathrm{B}}}{k^2 b^3} \sum_i \phi_i \sigma_i^2}\,. \tag{4.25}$$

Recognizing the second term in the denominator as the square of the inverse Debye screening length, $\kappa_{\mathrm{s}}^2 = \frac{4\pi l_{\mathrm{B}}}{b^3} \sum_i \phi_i \sigma_i^2$, we can write:

$$S_{\mathrm{p}}(k) = \sigma_{\mathrm{p}}^2 g_{\mathrm{p}}(k;\mathcal{T}_{\mathrm{p}}) \frac{k^2}{k^2 + \kappa_{\mathrm{s}}^2}\,. \tag{4.26}$$

$$\frac{S_{\mathrm{p}}(k)}{\sigma_{\mathrm{p}} L} = \left(\frac{2}{(Lb^2k^2/6)^2} \left[e^{-(Lb^2k^2/6)} + (Lb^2k^2/6) - 1 \right] \right. \tag{4.27}$$

$$\left. + \frac{G(z;f,N_{\mathrm{b}})}{E(f,N_{\mathrm{b}})} \left[\frac{1}{(Lb^2k^2/6)} \left(1 - e^{-(Lb^2k^2/6)} \right) \right]^2 \right) \frac{k^2}{k^2 + \kappa_{\mathrm{s}}^2}\,. \tag{4.28}$$

Using $x = Lb^2k^2/6$ and defining $B(x) \equiv G(e^{-x}; f, N_\mathrm{b})/E(f, N_\mathrm{b})$ and $\mathcal{K} \equiv Lb^2\kappa_\mathrm{s}^2/6$, we get

$$\frac{S_\mathrm{p}(x)}{\sigma_\mathrm{p} L} = \frac{F(x)}{x(x+\mathcal{K})}, \tag{4.29}$$

where

$$F(x) = 2\left(e^{-x} + x - 1\right) + B(z)\left(1 - e^{-x}\right)^2. \tag{4.30}$$

Differentiating w.r.t. x to find the maximum results in

$$\frac{d}{dx}\left(\frac{S_\mathrm{p}(x)}{\sigma_\mathrm{p} L}\right) = \frac{x(x+\mathcal{K})F'(x) - (2x+\mathcal{K})F(x)}{x^2(x+\mathcal{K})^2}, \tag{4.31}$$

with

$$F'(x) = 2(1 - e^{-x})(1 + B(x)e^{-x}) + B'(x)(1 - e^{-x})^2 \tag{4.32}$$

The root of equation 4.31 (which is the maximum of $S_\mathrm{p}(k)$) corresponds to the solution of the equation:

$$x(x+\mathcal{K})F'(x) - (2x+\mathcal{K})F(x) = 0. \tag{4.33}$$

At low salt concentration or large chain length, $\mathcal{K} \to 0$, the asymptotic behavior for small $\mathcal{K}$ can be obtained by expanding the equation in powers of x:

$$(1 + B_0)\mathcal{K}x^2 - \left(\frac{1}{3} + B_0 + B_1\right)x^4 + O(\mathcal{K}x^3, x^5) = 0. \tag{4.34}$$

For a star topology we have

$$B_0 = f - 1,\ B_1 = 0, \tag{4.35}$$

and for a dendrimer topology we have

$$B_0 = f^2 - 1,\ B_1 = 2(f-1)^2. \tag{4.36}$$

Solving equation 4.34 gives the solution:

$$x^* \approx \sqrt{\frac{3(1+B_0)}{1 + 3(B_0 + B_1)}}\sqrt{\mathcal{K}}. \tag{4.37}$$

In the case of a linear chain we thus obtain

$$(k^*)^2 \approx 3\sqrt{2}\frac{\kappa_\mathrm{s}}{N^{1/2}b}. \tag{4.38}$$

In the case of a star polymer, we get

$$(k^*)^2 \approx 3\sqrt{2}\frac{\kappa_\mathrm{s}}{N^{1/2}b}\sqrt{\frac{f^2}{3f-2}}. \tag{4.39}$$

For the dendrimer topology we get

$$(k^*)^2 \approx 3\sqrt{2}\frac{\kappa_s}{N^{1/2}b}\frac{f^2}{3f-2}\,. \tag{4.40}$$

Assuming that $(k^*)^3$ approximately represents the inverse volume taken up by a single chain, we can estimate the increase in charge density when going from a linear chain to a topology $\mathcal{T}$:

$$\frac{\rho_{c,\mathrm{eff}}(\mathcal{T})}{\rho_{c,\mathrm{eff}}(\mathrm{chain})} \sim \frac{(k^*_{\mathcal{T}})^3}{(k^*_{\mathrm{chain}})^3}. \tag{4.41}$$

Thus, for a star topology, we obtain

$$\frac{\rho_{c,\mathrm{eff}}(\mathrm{star})}{\rho_{c,\mathrm{eff}}(\mathrm{chain})} \sim \left(\frac{f^2}{3f-2}\right)^{3/4}, \tag{4.42}$$

and for a dendrimer

$$\frac{\rho_{c,\mathrm{eff}}(\mathrm{dendrimer})}{\rho_{c,\mathrm{eff}}(\mathrm{chain})} \sim \left(\frac{f^2}{3f-2}\right)^{3/2}. \tag{4.43}$$

Large-N asymptotics of the RPA free energy

To understand the large-N behavior of topology-driven phase separation, let us consider a four-component system containing pairs of oppositely charged polyelectrolytes with topology $\mathcal{T}_A$ and topology $\mathcal{T}_B$, all with the same degree of polymerization N and charge fraction σ. The RPA contribution to the free energy is

$$\frac{\beta F_{\mathrm{RPA}} b^3}{V} = \frac{b^3}{4\pi^2}\int_0^\infty \mathrm{d}k\, k^2\left[\ln\left(1+\frac{4\pi l_B\sigma^2}{k^2b^3}\left[\phi_A g_A(k;\mathcal{T}_A)+\phi_B g_B(k;\mathcal{T}_B)\right]\right)-\frac{4\pi l_B\sigma^2}{k^2b^3}\left[\phi_A+\phi_B\right]\right]. \tag{4.44}$$

The electrostatic contribution which governs topology-driven phase separation is the excess RPA contribution relative to the two pure-topology reference systems, which for a solvent-free system is given by

$$\begin{aligned}\frac{\beta\Delta F_{\mathrm{RPA}} b^3}{V} = \frac{b^3}{4\pi^2}\int_0^\infty \mathrm{d}k\, k^2\Bigg[&\ln\left(1+\frac{4\pi l_B\sigma^2}{k^2b^3}\left[\phi_A g_A(k;\mathcal{T}_A)+(1-\phi_A) g_B(k;\mathcal{T}_B)\right]\right)\\ &-\phi_A\ln\left(1+\frac{4\pi l_B\sigma^2}{k^2b^3}g_A(k;\mathcal{T}_A)\right)-(1-\phi_A)\ln\left(1+\frac{4\pi l_B\sigma^2}{k^2b^3}g_B(k;\mathcal{T}_B)\right)\Bigg].\end{aligned} \tag{4.45}$$

We now introduce the simplified notation

$$\zeta = \frac{4\pi l_B\sigma^2}{b^3}, \qquad g_i(k;\mathcal{T}_i) = N D_i(k^2N), \tag{4.46}$$

where D_i is the generalized Debye function of species i. Note that for economy of notation, we have suppressed the dependence of D_i on the other architectural parameters, since here we are only interested in the scaling with N. We also define the composition-weighted, generalized Debye function

$$\bar{D}(k^2N, \phi_A) = \phi_A D_A(k^2N) + (1 - \phi_A) D_B(k^2N). \tag{4.47}$$

Splitting the first logarithm in equation 4.45 into ϕ_A and $(1 - \phi_A)$ contributions gives

$$\frac{\beta \Delta F_{\mathrm{RPA}} b^3}{V} = \frac{b^3}{4\pi^2} \int_0^\infty \mathrm{d}k\, k^2 \left[\phi_A \ln \left(\frac{1 + \frac{N\zeta}{k^2} \bar{D}(k^2N, \phi_A)}{1 + \frac{N\zeta}{k^2} D_A(k^2N)} \right) + (1 - \phi_A) \ln \left(\frac{1 + \frac{N\zeta}{k^2} \bar{D}(k^2N, \phi_A)}{1 + \frac{N\zeta}{k^2} D_B(k^2N)} \right) \right]. \tag{4.48}$$

To extract the large-N dependence, we rescale the integration variable according to

$$q^2 = k^2 N, \qquad k^2\, \mathrm{d}k = N^{-3/2} q^2\, \mathrm{d}q. \tag{4.49}$$

This gives

$$\frac{\beta \Delta F_{\mathrm{RPA}} b^3}{V} = \frac{b^3}{4\pi^2 N^{3/2}} \int_0^\infty \mathrm{d}q\, q^2 \left[\phi_A \ln \left(\frac{1 + \frac{N^2\zeta}{q^2} \bar{D}(q^2, \phi_A)}{1 + \frac{N^2\zeta}{q^2} D_A(q^2)} \right) + (1 - \phi_A) \ln \left(\frac{1 + \frac{N^2\zeta}{q^2} \bar{D}(q^2, \phi_A)}{1 + \frac{N^2\zeta}{q^2} D_B(q^2)} \right) \right]. \tag{4.50}$$

In the large-N limit, the integrand admits an asymptotic expansion in powers of N^{-2}, with a leading order term that is independent of N. Asymptotically, the excess RPA contribution thus becomes

$$\frac{\beta \Delta F_{\mathrm{RPA}} b^3}{V} \approx \frac{b^3}{4\pi^2 N^{3/2}} \int_0^\infty \mathrm{d}q\, q^2 \left[\phi_A \ln \left(\frac{\bar{D}(q^2, \phi_A)}{D_A(q^2)} \right) + (1 - \phi_A) \ln \left(\frac{\bar{D}(q^2, \phi_A)}{D_B(q^2)} \right) \right], \tag{4.51}$$

which scales as

$$\frac{\beta \Delta F_{\mathrm{RPA}} b^3}{V} \sim N^{-3/2}. \tag{4.52}$$

This scaling is physically intuitive: in the melt phase, as N becomes sufficiently large, the influence of branching diminishes because monomers are increasingly "unable" to distinguish whether neighboring monomers belong to the same branch or to different branches.

Asymptotic scaling of the effective χ parameter

To examine the N-dependence of χ_{ij}^{eff}, we consider a salt-free mixture of polyelectrolytes with the same molecular weight and perform the same transformations as in the previous section. We find that $\alpha(k)$ exhibits the following N-dependence:

$$\alpha(k) \equiv \frac{b^3 q^2}{4\pi^2 N} \left(\frac{4\pi l_{\text{B}} N}{q^2 b^3}\right)^2 \frac{1}{\left(1 + \frac{4\pi l_{\text{B}} N}{q^2 b^3} \sum_l \phi_l \sigma_l^2 g_l(q; \mathcal{T}_l)\right)^2}. \tag{4.53}$$

Therefore, in the limit of large N, we obtain the scaling behavior

$$\alpha(k) \sim \frac{1}{N^3} \to \chi_{ij}^{\text{eff}} - \chi_{ij} \sim N^{-3/2}. \tag{4.54}$$

Conversely, for small N we get

$$\alpha(k) \sim N \to \chi_{ij}^{\text{eff}} - \chi_{ij} \sim N^{5/2} \tag{4.55}$$

References

[1] David Beyer et al. *How Topology Shapes the Phase Behavior of Polyelectrolytes*. arXiv:2607.15703 [cond-mat.soft]. July 2026. DOI: 10.48550/arXiv.2607.15703.

[20] Pierre J. Walker, Hon-Wa Yew, and Andrés Riedemann. "Clapeyron.jl: An Extensible, Open-Source Fluid Thermodynamics Toolkit". In: *Ind. Eng. Chem. Res.* 61.20 (May 2022), pp. 7130–7153. ISSN: 0888-5885, 1520-5045. DOI: 10.1021/acs.iecr.2c00326.

[44] J. T. G. Overbeek and M. J. Voorn. "Phase separation in polyelectrolyte solutions. Theory of complex coacervation". In: *J. Cell. Comp. Physiol.* 49.S1 (1957), pp. 7–26. ISSN: 1553-0809. DOI: 10.1002/jcp.1030490404.

[88] Pengfei Zhang et al. "Salting-Out and Salting-In of Polyelectrolyte Solutions: A Liquid-State Theory Study". In: *Macromolecules* 49.24 (Dec. 2016), pp. 9720–9730. ISSN: 0024-9297, 1520-5835. DOI: 10.1021/acs.macromol.6b02160.

[90] Andrew S. Ylitalo et al. "Electrostatic Correlations and Temperature-Dependent Dielectric Constant Can Model LCST in Polyelectrolyte Complex Coacervation". In: *Macromolecules* 54.24 (Dec. 2021), pp. 11326–11337. ISSN: 0024-9297, 1520-5835. DOI: 10.1021/acs.macromol.1c02000.

[116] Charles E. Sing and Sarah L. Perry. "Recent progress in the science of complex coacervation". In: *Soft Matter* 16.12 (Mar. 2020), pp. 2885–2914. ISSN: 1744-6848. DOI: 10.1039/D0SM00001A.

[117] Artem M. Rumyantsev, Nicholas E. Jackson, and Juan J. de Pablo. "Polyelectrolyte Complex Coacervates: Recent Developments and New Frontiers". en. In: *Annu. Rev. Condens. Matter Phys.* 12.Volume 12, 2021 (Mar. 2021), pp. 155–176. ISSN: 1947-5454, 1947-5462. DOI: 10.1146/annurev-conmatphys-042020-113457.

[129] Artem M. Rumyantsev et al. "Controlling Complex Coacervation via Random Polyelectrolyte Sequences". In: *ACS Macro Lett.* (Sept. 2019). DOI: 10.1021/acsmacrolett.9b00494.

[134] Kris T. Delaney and Glenn H. Fredrickson. "Theory of polyelectrolyte complexation—Complex coacervates are self-coacervates". In: *J. Chem. Phys.* 146.22 (June 2017), p. 224902. ISSN: 0021-9606. DOI: 10.1063/1.4985568.

[136] Pengfei Zhang et al. "Polyelectrolyte complex coacervation: Effects of concentration asymmetry". In: *J. Chem. Phys.* 149.16 (July 2018), p. 163303. ISSN: 0021-9606. DOI: 10.1063/1.5028524.

[137] Xu Chen, Er-Qiang Chen, and Shuang Yang. "Multiphase Coacervation of Polyelectrolytes Driven by Asymmetry of Charged Sequence". In: *Macromolecules* 56.1 (Jan. 2023), pp. 3–14. ISSN: 0024-9297. DOI: 10.1021/acs.macromol.2c01205.

[138] Pengfei Zhang et al. "Salt Partitioning in Complex Coacervation of Symmetric Polyelectrolytes". In: *Macromolecules* 51.15 (Aug. 2018), pp. 5586–5593. ISSN: 0024-9297. DOI: 10.1021/acs.macromol.8b00726.

[207] Lu Li et al. "Phase Behavior and Salt Partitioning in Polyelectrolyte Complex Coacervates". In: *Macromolecules* 51.8 (Apr. 2018), pp. 2988–2995. ISSN: 0024-9297, 1520-5835. DOI: 10.1021/acs.macromol.8b00238.

[209] Angelika E. Neitzel et al. "Polyelectrolyte Complex Coacervation across a Broad Range of Charge Densities". In: *Macromolecules* (July 2021). DOI: 10.1021/acs.macromol.1c00703.

[221] Yi-Hsuan Lin, Julie D. Forman-Kay, and Hue Sun Chan. "Sequence-Specific Polyampholyte Phase Separation in Membraneless Organelles". In: *Phys. Rev. Lett.* 117.17 (Oct. 2016), p. 178101. DOI: 10.1103/PhysRevLett.117.178101.

[222] Chi W. Pak et al. "Sequence Determinants of Intracellular Phase Separation by Complex Coacervation of a Disordered Protein". eng. In: *Mol. Cell* 63.1 (July 2016), pp. 72–85. ISSN: 1097-4164. DOI: 10.1016/j.molcel.2016.05.042.

[225] Yi-Hsuan Lin, Julie D. Forman-Kay, and Hue Sun Chan. "Theories for Sequence-Dependent Phase Behaviors of Biomolecular Condensates". In: *Biochemistry* 57.17 (May 2018), pp. 2499–2508. ISSN: 0006-2960. DOI: 10.1021/acs.biochem.8b00058.

[226] Scott P. O. Danielsen et al. “Molecular design of self-coacervation phenomena in block polyampholytes”. In: *Proc. Natl. Acad. Sci. U.S.A.* 116.17 (Apr. 2019), pp. 8224–8232. DOI: 10.1073/pnas.1900435116.

[227] Jonghoon Lee, Yuri O. Popov, and Glenn H. Fredrickson. “Complex coacervation: A field theoretic simulation study of polyelectrolyte complexation”. In: *J. Chem. Phys.* 128.22 (June 2008), p. 224908. ISSN: 0021-9606. DOI: 10.1063/1.2936834.

[233] Li-Wei Chang et al. “Sequence and entropy-based control of complex coacervates”. en. In: *Nat. Commun.* 8.1 (Nov. 2017), p. 1273. ISSN: 2041-1723. DOI: 10.1038/s41467-017-01249-1.

[234] Shensheng Chen, Pengfei Zhang, and Zhen-Gang Wang. “Complexation between Oppositely Charged Polyelectrolytes in Dilute Solution: Effects of Charge Asymmetry”. In: *Macromolecules* 55.10 (May 2022), pp. 3898–3909. ISSN: 0024-9297. DOI: 10.1021/acs.macromol.2c00339.

[236] Kyosuke Adachi and Kyogo Kawaguchi. “Predicting Heteropolymer Interactions: Demixing and Hypermixing of Disordered Protein Sequences”. In: *Phys. Rev. X* 14.3 (July 2024), p. 031011. DOI: 10.1103/PhysRevX.14.031011.

[245] Xu Chen et al. “Multiphase Coacervates Driven by Electrostatic Correlations”. In: *ACS Macro Lett.* 10.8 (Aug. 2021), pp. 1041–1047. DOI: 10.1021/acsmacrolett.1c00282.

[246] Jie Wang et al. “Interfacial Tensions of Polyelectrolyte Multiphase Coacervation”. In: *Macromolecules* 57.20 (Oct. 2024), pp. 9698–9710. ISSN: 0024-9297. DOI: 10.1021/acs.macromol.4c02017.

[250] Bennett D. Marshall and Walter G. Chapman. “Higher Order Classical Density Functional Theory for Branched Chains and Rings”. In: *J. Phys. Chem. B* 115.50 (Dec. 2011), pp. 15036–15047. ISSN: 1520-6106. DOI: 10.1021/jp2078677.

[251] Bennett D. Marshall and Walter G. Chapman. “Three new branched chain equations of state based on Wertheim’s perturbation theory”. In: *J. Chem. Phys.* 138.17 (May 2013), p. 174109. ISSN: 0021-9606. DOI: 10.1063/1.4803023.

[253] Erich A. Müller and Keith E. Gubbins. “Simulation of hard triatomic and tetratomic molecules”. In: *Mol. Phys.* 80.4 (Nov. 1993), pp. 957–976. ISSN: 0026-8976. DOI: 10.1080/00268979300102791.

[259] Anthony A. Hyman, Christoph A. Weber, and Frank Jülicher. “Liquid-Liquid Phase Separation in Biology”. In: *Annu. Rev. Cell Dev. Biol.* 30.Volume 30, 2014 (Oct. 2014), pp. 39–58. ISSN: 1081-0706, 1530-8995. DOI: 10.1146/annurev-cellbio-100913-013325.

[260] Salman F. Banani et al. “Biomolecular condensates: organizers of cellular biochemistry”. en. In: *Nat. Rev. Mol. Cell Biol.* 18.5 (May 2017), pp. 285–298. ISSN: 1471-0080. DOI: 10.1038/nrm.2017.7.

[261] Murugappan Muthukumar. *Physics of Charged Macromolecules: Synthetic and Biological Systems*. Cambridge: Cambridge University Press, 2023. ISBN: 978-0-521-86487-9. DOI: 10.1017/9781139046749.

[262] Isaac A. Ramírez Marrero and Sarah L. Perry. “Fundamentals and Design Rules of Polyelectrolyte Complex Materials: A Comprehensive Review”. en. In: *Chem. Rev.* (Apr. 2026), acs.chemrev.5c00971. ISSN: 0009-2665, 1520-6890. DOI: 10.1021/acs.chemrev.5c00971.

[263] Jeong-Mo Choi, Alex S. Holehouse, and Rohit V. Pappu. “Physical Principles Underlying the Complex Biology of Intracellular Phase Transitions”. In: *Annu. Rev. Biophys.* 49.Volume 49, 2020 (May 2020), pp. 107–133. ISSN: 1936-122X, 1936-1238. DOI: 10.1146/annurev-biophys-121219-081629.

[264] Nicola Galvanetto et al. “Extreme dynamics in a biomolecular condensate”. en. In: *Nature* 619.7971 (July 2023), pp. 876–883. ISSN: 1476-4687. DOI: 10.1038/s41586-023-06329-5.

[265] Yifan Dai, Zhen-Gang Wang, and Richard N. Zare. “Unlocking the electrochemical functions of biomolecular condensates”. In: *Nat. Chem. Biol.* 20.11 (Nov. 2024), pp. 1420–1433. ISSN: 1552-4469. DOI: 10.1038/s41589-024-01717-y.

[266] Tiemei Lu and Evan Spruijt. “Multiphase Complex Coacervate Droplets”. In: *J. Am. Chem. Soc.* 142.6 (Feb. 2020), pp. 2905–2914. ISSN: 0002-7863. DOI: 10.1021/jacs.9b11468.

[267] William M. Jacobs. “Theory and Simulation of Multiphase Coexistence in Biomolecular Mixtures”. In: *J. Chem. Theory Comput.* 19.12 (June 2023), pp. 3429–3445. ISSN: 1549-9618. DOI: 10.1021/acs.jctc.3c00198.

[268] Aman Agrawal et al. “Charge Density Mismatch Drives Demixing in Multicomponent Polyelectrolyte Complexes”. In: *Macromolecules* 58.15 (Aug. 2025), pp. 7776–7787. ISSN: 0024-9297. DOI: 10.1021/acs.macromol.5c00912.

[269] Evan Spruijt. “Chapter 6 - Multiphase complex droplets”. In: *Droplets of Life*. Ed. by Vladimir N. Uversky. Academic Press, Jan. 2023, pp. 173–204. ISBN: 978-0-12-823967-4. DOI: 10.1016/B978-0-12-823967-4.00015-4.

[270] Tiemei Lu et al. “Controlling Multiphase Coacervate Wetting and Self-Organization by Interfacial Proteins”. In: *J. Am. Chem. Soc.* 147.26 (July 2025), pp. 22622–22633. ISSN: 0002-7863. DOI: 10.1021/jacs.5c03870.

[271] Evan Spruijt et al. “Binodal Compositions of Polyelectrolyte Complexes”. In: *Macromolecules* 43.15 (Aug. 2010), pp. 6476–6484. ISSN: 0024-9297. DOI: 10.1021/ma101031t.

[272] F. Weinbreck et al. “Complex Coacervation of Whey Proteins and Gum Arabic”. In: *Biomacromolecules* 4.2 (Mar. 2003), pp. 293–303. ISSN: 1525-7797. DOI: 10.1021/bm025667n.

[273] Hannes Ausserwöger et al. “Biomolecular condensates sustain pH gradients at equilibrium through charge neutralization”. en. In: *Nat. Chem.* 18.2 (Feb. 2026), pp. 246–257. ISSN: 1755-4349. DOI: 10.1038/s41557-025-02039-9.

[274] Chengjie Luo et al. “Theory of Condensate Size Control by Molecular Charge Asymmetry”. In: *ACS Macro Lett.* 14.10 (Oct. 2025), pp. 1484–1491. DOI: 10.1021/acsmacrolett.5c00342.

[275] Anisha Shakya et al. “Role of Chain Flexibility in Asymmetric Polyelectrolyte Complexation in Salt Solutions”. In: *Macromolecules* 53.4 (Feb. 2020), pp. 1258–1269. ISSN: 0024-9297. DOI: 10.1021/acs.macromol.9b02355.

[276] Tyler K. Lytle et al. “Designing Electrostatic Interactions via Polyelectrolyte Monomer Sequence”. In: *ACS Cent. Sci.* 5.4 (Apr. 2019), pp. 709–718. ISSN: 2374-7943. DOI: 10.1021/acscentsci.9b00087.

[277] Boyuan Yu et al. “Complex coacervation of statistical polyelectrolytes: role of monomer sequences and formation of inhomogeneous coacervates”. In: *Mol. Syst. Des. Eng.* 6.10 (2021), pp. 790–804. DOI: 10.1039/D1ME00076D.

[278] Jian Qin and Juan J. de Pablo. “Criticality and Connectivity in Macromolecular Charge Complexation”. In: *Macromolecules* 49.22 (Nov. 2016), pp. 8789–8800. ISSN: 0024-9297. DOI: 10.1021/acs.macromol.6b02113.

[279] Brandon M. Johnston et al. “The effect of comb architecture on complex coacervation”. In: *Org. Biomol. Chem.* 15.36 (Sept. 2017), pp. 7630–7642. ISSN: 1477-0539. DOI: 10.1039/C7OB01314K.

[280] Tyler K. Lytle and Charles E. Sing. “Tuning chain interaction entropy in complex coacervation using polymer stiffness, architecture, and salt valency”. In: *Mol. Syst. Des. Eng.* 3.1 (Feb. 2018), pp. 183–196. ISSN: 2058-9689. DOI: 10.1039/c7me00108h.

[281] Andrea Tagliabue et al. “Can oppositely charged polyelectrolyte stars form a gel? A simulational study”. In: *Soft Matter* 17.6 (Feb. 2021), pp. 1574–1588. ISSN: 1744-6848. DOI: 10.1039/D0SM01617A.

[282] Roman Staňo et al. “Electrostatically Cross-Linked Reversible Gels—Effects of pH and Ionic Strength”. In: *Macromolecules* 54.10 (May 2021), pp. 4769–4781. ISSN: 0024-9297. DOI: 10.1021/acs.macromol.1c00470.

[283] Boyuan Yu et al. “Structure and Dynamics of Hybrid Colloid–Polyelectrolyte Coacervates: Insights from Molecular Simulations”. In: *Macromolecules* 56.18 (Sept. 2023), pp. 7256–7270. ISSN: 0024-9297. DOI: 10.1021/acs.macromol.3c01079.

[284] Jun-Jie Zhang and Bin Li. “Self-Assembly of Star-Polyelectrolytes in Various Solution Conditions”. In: *Macromolecules* 57.1 (Jan. 2024), pp. 396–408. ISSN: 0024-9297, 1520-5835. DOI: 10.1021/acs.macromol.3c01580.

[285] Kaden C. Stevens and Matthew V. Tirrell. “Impact of a Lightly Branched Star Polyelectrolyte Architecture on Polyelectrolyte Complexes”. In: *ACS Macro Lett.* 13.6 (June 2024), pp. 688–694. DOI: 10.1021/acsmacrolett.4c00167.

[286] Utku Gürel et al. “Characterizing the Structural Conformation of Highly Charged Star-Linear Polyelectrolyte Mixtures in Solution”. In: *Macromolecules* 58.19 (Oct. 2025), pp. 10464–10474. ISSN: 0024-9297. DOI: 10.1021/acs.macromol.5c01180.

[287] P. Welch and M. Muthukumar. “Dendrimer–Polyelectrolyte Complexation: A Model Guest–Host System”. In: *Macromolecules* 33.16 (Aug. 2000), pp. 6159–6167. ISSN: 0024-9297. DOI: 10.1021/ma000021d.

[288] Yuchong Zhang and Walter G. Chapman. “Modeling Thermodynamic Properties of Isomeric Alkanes with a New Branched Equation of State”. In: *Ind. Eng. Chem. Res.* 57.5 (Feb. 2018), pp. 1679–1688. ISSN: 0888-5885. DOI: 10.1021/acs.iecr.7b03951.

[289] Glenn Fredrickson. *The Equilibrium Theory of Inhomogeneous Polymers*. Oxford University Press, Dec. 2005. ISBN: 978-0-19-171795-6.

[290] V. Yu. Borue and I. Ya. Erukhimovich. “A statistical theory of weakly charged polyelectrolytes: fluctuations, equation of state and microphase separation”. en. In: *Macromolecules* 21.11 (Nov. 1988), pp. 3240–3249. ISSN: 0024-9297, 1520-5835. DOI: 10.1021/ma00189a019.

[291] Khaled A. Mahdi and Monica Olvera de la Cruz. “Phase Diagrams of Salt-Free Polyelectrolyte Semidilute Solutions”. In: *Macromolecules* 33.20 (Oct. 2000), pp. 7649–7654. ISSN: 0024-9297. DOI: 10.1021/ma000142d.

[292] Yi-Hsuan Lin et al. “Random-phase-approximation theory for sequence-dependent, biologically functional liquid-liquid phase separation of intrinsically disordered proteins”. In: *J. Mol. Liq.* From simple liquids to macromolecular solutions: recent experimental and theoretical developments. In Honor of the 70th birthday of Vojko Vlachy 228 (Feb. 2017), pp. 176–193. ISSN: 0167-7322. DOI: 10.1016/j.molliq.2016.09.090.

[293] Marina I. Giannotti and G. Julius Vancso. “Interrogation of Single Synthetic Polymer Chains and Polysaccharides by AFM-Based Force Spectroscopy”. In: *ChemPhysChem* 8.16 (2007), pp. 2290–2307. ISSN: 1439-7641. DOI: 10.1002/cphc.200700175.

P a r t II

DYNAMIC BEHAVIOR OF CHARGE-CONTAINING MACROMOLECULAR SYSTEMS

(FOCUS: CONDUCTIVITY, MECHANICAL RESPONSE AND ION PAIRING)

Introduction

The preceding part developed a thermodynamic map of charge-containing systems, identifying the regions of phase space in which different equilibrium states emerge. Such a map, however, describes only the available destinations. It does not reveal the routes by which a system moves between them, the rate at which matter and charge travel through a material, or how the material responds when displaced from equilibrium. Two systems occupying similar positions on a thermodynamic map may follow markedly different dynamical paths, just as two locations separated by the same distance may be connected by roads of very different length, resistance, and accessibility. The purpose of this part is therefore to complement the equilibrium maps developed previously by examining the molecular pathways that govern transport, relaxation, and mechanical response in charge-containing materials.

Whereas equilibrium phase behavior can be characterized through free energies and static correlation functions, dynamic properties depend on time-dependent correlations, kinetic pathways, and competition among processes occurring over different length and time scales. Foundational relations developed by Einstein[294], Sutherland[295], von Smoluchowski[296], Stokes[297], Onsager[30, 31], and others remain indispensable because they connect macroscopic transport coefficients to molecular motion, hydrodynamic resistance, and coupled thermodynamic forces. Their direct application to chemically complex charged materials, however, often relies on assumptions such as independent molecular motion, dilute conditions, or a clear separation between microscopic relaxation processes.

These assumptions become particularly restrictive in charge-containing soft materials. The long-ranged and many-body nature of electrostatic interactions correlates the motion of different species, while molecular association, chemical reactions, and network rearrangements introduce additional pathways through which charge, mass, and stress can relax. Consequently, equilibrium structure constrains dynamics but does not determine it uniquely. Systems with similar compositions, degrees of association, or average molecular structures may nevertheless exhibit substantially different conductivity, diffusivity, or mechanical response.

The central objective of this part is to determine how microscopic association and exchange processes give rise to macroscopic transport and response. Across the systems considered here, intuitive one-to-one relationships between molecular association and dynamic behavior frequently break down. Ion pairing does not uniquely determine conductivity, the equilibrium charge state of a polymer network

does not uniquely determine ionic mobility, and the number or strength of physical crosslinks does not alone determine mechanical relaxation. Instead, these properties emerge from collective motion, exchange kinetics, and competition among multiple dynamical pathways.

Chapter 5 begins at the molecular scale by examining the relationship between ion association and electrical conductivity in ionic-liquid–solvent mixtures. Conductivity is commonly interpreted in terms of the fraction of dissociated ions, suggesting a direct relationship between ion pairing and charge transport. Ion pairing, however, is a static structural measure, whereas conductivity is a collective dynamic property governed by correlations among ionic motions. By quantifying ion association and conductivity independently, we demonstrate that these properties need not vary together and that the degree of ion dissociation cannot, by itself, serve as a general measure of ionic transport. The results further show that, even when electrostatic interactions dominate the macroscopic behavior, chemically specific short-range interactions can control the molecular association equilibria from which that behavior emerges.

Chapter 6 introduces a further level of dynamical coupling by examining ion transport through charge-regulating polyelectrolyte hydrogels. In these materials, ionic motion cannot be separated from the local chemical state of the polymer network: protonation, electrostatic binding, and molecular diffusion alter one another as the system evolves. Charge regulation therefore introduces both an equilibrium response to the local electrostatic environment and a dynamic pathway through which ions can bind, unbind, and move through the material. By disentangling the competing processes governing transport, we identify the origins of the resulting nonmonotonic dependence of ionic mobility on network charge and establish design principles for controlling transport in responsive polymer networks.

Chapter 7 extends this perspective from the motion of molecular species through a network to the relaxation of the network itself. In physically crosslinked hydrogels, mechanical response is governed not only by the number and strength of the crosslinks, but also by their spatial organization, stoichiometry, and exchange dynamics. By combining quantum chemistry, liquid-state theory, and coarse-grained molecular simulations, we connect molecular-scale metal–ligand interactions to the collective mechanical response of the polymer network. This multiscale analysis identifies the ratio of dynamic crosslinkers to available binding sites as a central design variable governing the tunability of the material. Owing to the generality of

this balance between crosslink availability, occupancy, and exchange, the resulting principles extend beyond the specific chemical systems considered in this chapter.

Together, these three chapters trace a progression from molecular association and collective charge transport, through reaction-coupled diffusion within a polymer network, to the mechanical relaxation of the network itself. They demonstrate that the dynamic behavior of charge-containing materials cannot generally be inferred from static measures of association alone. Ionic conductivity, molecular diffusion, and mechanical response instead emerge from the collective motion and reorganization of ions, molecules, and polymer networks across multiple length and time scales. In this way, the chapters provide a dynamic counterpart to the thermodynamic map developed in the preceding part, revealing not only where charge-containing systems reside, but how they move, respond, and relax within that landscape.

References

[30] Lars Onsager. “Zur Theorie der Electrolyte. I”. In: *Phys. Z.* 27 (1926), pp. 388–392.

[31] Lars Onsager. “Zur Theorie der Electrolyte. II”. In: *Phys. Z.* 28 (1927), pp. 277–298.

[294] A. Einstein. “Über die von der molekularkinetischen Theorie der Wärme geforderte Bewegung von in ruhenden Flüssigkeiten suspendierten Teilchen”. en. In: *Ann. Phys. (Berlin, Ger.)* 322.8 (1905), pp. 549–560. ISSN: 1521-3889. DOI: 10.1002/andp.19053220806.

[295] William Sutherland. “LXXV. A dynamical theory of diffusion for non-electrolytes and the molecular mass of albumin”. In: *Philos. Mag.* 6th ser. 9.54 (June 1905), pp. 781–785. DOI: 10.1080/14786440509463331.

[296] M. von Smoluchowski. “Zur kinetischen Theorie der Brownschen Molekularbewegung und der Suspensionen”. In: *Ann. Phys. (Berlin, Ger.)* 326.14 (Jan. 1906), pp. 756–780. DOI: 10.1002/andp.19063261405.

[297] G. G. Stokes. “On the Effect of the Internal Friction of Fluids on the Motion of Pendulums”. In: *Trans. Cambridge Philos. Soc.* 9 (Jan. 1851). ADS Bibcode: 1851TCaPS...9....8S, p. 8.

Chapter 5

DECOUPLING ION ASSOCIATION FROM CONDUCTIVITY IN IONIC-LIQUID–SOLVENT MIXTURES

Ionic-liquid–solvent electrolytes are promising materials for electrochemical energy storage, yet the microscopic connection between ion association and macroscopic conductivity remains difficult to interpret. A common approach is to identify the ionicity, defined as the ratio of measured to Nernst–Einstein conductivity, with an apparent free ion fraction. However, this interpretation conflates local ion dissociation with collective ion-motion correlations. In this work, using all-atom molecular dynamics simulations of 1-butyl-3-methylimidazolium tetrafluoroborate ([BMIM][BF_4]) in water, acetonitrile, acetone, and dimethyl sulfoxide, we independently quantify ion association, ionicity, viscosity, and conductivity across the full composition range. We find that ion dissociation is not governed by bulk solvent dielectric constant alone. Instead, ion-pair formation is controlled by short-range, site-specific association interactions involving the imidazolium ring hydrogens, BF_4^- fluorines, and solvent donor sites, explaining why water is a comparatively weak dissociating solvent despite its high dielectric constant. To rationalize these trends, we combine Wertheim's first-order thermodynamic perturbation theory for local ion association with the mean-spherical approximation conductivity theory of Blum and Turq for correlated charge transport. This framework captures the simulated conductivity trends and separates the role of free ion population from relaxation, electrophoretic, viscosity, and ion-asymmetry effects. Because ionic liquids remain miscible with these molecular solvents across the entire composition range, unlike simple electrolytes or polyelectrolytes, we can trace this decoupling continuously from dilute electrolyte to neat ionic liquid, revealing a non-monotonic minimum in ionicity and apparent ionicities exceeding unity—behavior that is difficult to access in systems confined to dilute compositions by phase separation. We thus demonstrate through simulation and analytical theory the lack of direct dependence of ionicity on ion dissociation, and further highlight that the origin of the anomalous trends in ionicity are linked to dynamic properties, rather than static properties like ion dissociation.

This chapter includes work currently in preparation: Pierre Walker and Zhen-Gang Wang. "Decoupling Ion Association from Conductivity in Ionic-Liquid–Solvent

Mixtures". In: *In preparation* (2026)

5.1 Introduction

Ionic liquids (ILs) are organic salts that exist as liquids at or near room temperature. Their negligible vapor pressures, wide electrochemical stability windows[298, 299], and broadly tunable physicochemical properties make them attractive for applications including next-generation battery and polymer electrolytes,[46, 50, 300, 51] green solvents and CO_2 capture media,[301, 302] polymerized ionic-liquid membranes for gas separation,[52] and functional polymer–IL composite materials.[3, 303] When mixed with molecular solvents, ILs form electrolyte solutions whose conductivity, viscosity, and electrochemical stability can be tuned continuously with composition, making them promising candidates for battery and supercapacitor electrolytes.[304, 305, 306, 307] Although pure ILs often exhibit limited conductivity because of their high viscosity, dilution with low-viscosity molecular solvents can substantially increase ion mobility and produce broad conductivity maxima at intermediate compositions, as shown in Figure 5.1(d).

Despite these promising properties, a quantitative understanding of IL electrolytes remains challenging because their transport behavior reflects several coupled molecular effects. Coulombic interactions, hydrogen bonding, dispersion interactions, steric packing, and hydrophobic effects can all contribute to local ion association and the formation of ionic clusters, even at relatively high dilution.[308, 92, 309] As a result, the fraction of free or unpaired ions has often been invoked as an intuitive descriptor of conductivity, and numerous studies have explored the relationship between ion association and charge transport in IL-containing systems (see Figure 5.1(a)).[308, 305, 310] Ionic liquids offer a particularly stringent test of this idea. Unlike simple electrolytes or polyelectrolytes, which typically phase-separate or gel well before reaching high charge density, ILs remain miscible with molecular solvents across the entire composition range, from dilute electrolyte to neat molten salt. This makes it possible to track the relationship between ion association and conductivity continuously into a regime of very high charge concentration, where non-monotonic trends in ionicity and apparent ionicities exceeding unity have been reported.[311, 312] Both observations are unexpected under a naive picture in which ion pairing simply removes charge carriers from transport, and neither is easily explained without a more complete theoretical treatment. Although a number of studies have already shown, largely empirically, that the ion dissociation fraction is a poor proxy for ionicity, what has been missing is an analytical framework that

identifies the distinct physical origins of each quantity and thereby explains, rather than demonstrates, this apparent disconnect.

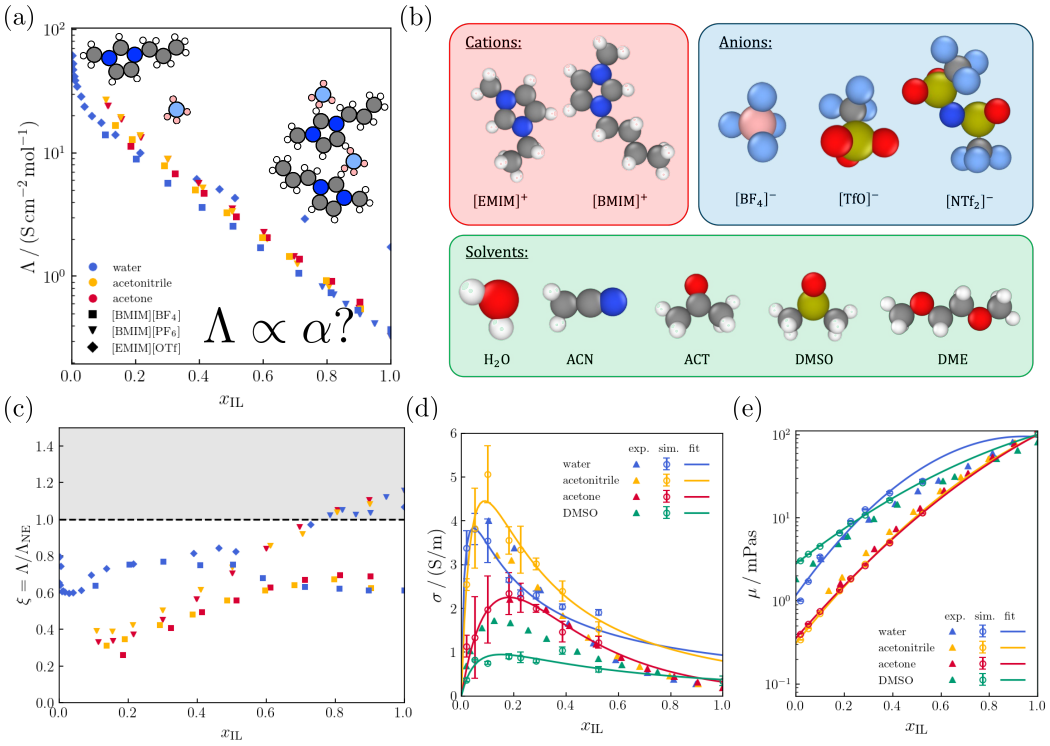


Figure 5.1: (a) Molar conductivity of ionic-liquid–solvent mixtures obtained from the ILThermo database. (b) Chemical structures of the ionic-liquid cation/anion pairs and solvents studied in this chapter. (c) Ionicity, $\Lambda/\Lambda_{\mathrm{NE}}$, as a function of ionic-liquid mole fraction x_{IL} for the systems shown in (a). Ionicity is estimated using the Walden–Stokes approximation, $\xi = \Lambda\eta/\Lambda_{\mathrm{NE}}^{\mathrm{Stokes}}$, where $\Lambda_{\mathrm{NE}}^{\mathrm{Stokes}}$ is computed using Stokes–Einstein–Sutherland ion radii; the gray region denotes systems with apparent ionicity ≥ 1. (d) Ionic conductivity σ and (e) dynamic viscosity η on a logarithmic scale as a function of x_{IL} for [BMIM][BF_4] in four solvents. Open symbols denote simulation results; filled symbols denote experimental data.[313] Lines in (d) and (e) are guides to the eye.

An influential operational formulation of this idea was proposed by Nordness et al.,[313, 304] who related an apparent dissociated ion fraction to conductivity measurements through

$$\alpha_{\mathrm{app}} = \frac{\Lambda}{\Lambda_{\mathrm{NE}}}, \tag{5.1}$$

where Λ is the measured molar conductivity and

$$\Lambda_{\mathrm{NE}} = \frac{e_{\mathrm{c}}^2 N_{\mathrm{A}}}{k_{\mathrm{B}} T}\,(D_+ + D_-) \tag{5.2}$$

is the Nernst–Einstein molar conductivity for a monovalent electrolyte. Here, e_{c} is the elementary charge, N_{A} is Avogadro's constant, k_{B} is the Boltzmann constant, T

is the temperature, and D_i is the self-diffusion coefficient of ion species i. In this approach, the self-diffusion coefficients are estimated using the Stokes–Einstein–Sutherland relation,

$$D_i = \frac{k_B T}{6\pi\eta r_i}, \tag{5.3}$$

where η is the dynamic viscosity and r_i is the hydrodynamic radius of species i. Combining these expressions gives

$$\alpha_{\mathrm{app}} = \frac{\Lambda}{\Lambda_{\mathrm{NE}}} = \frac{6\pi\Lambda\eta}{e_c^2 N_A \left(r_+^{-1} + r_-^{-1}\right)}, \tag{5.4}$$

suggesting that an apparent dissociated fraction can be obtained from conductivity and viscosity measurements, provided the ion radii are known. The physical motivation is clear: if the Nernst–Einstein expression represents the conductivity expected for fully mobile, uncorrelated ions, then the ratio $\Lambda/\Lambda_{\mathrm{NE}}$ provides a convenient measure of deviations from that ideal limit.

This interpretation has proven useful for organizing experimental trends, but it also raises important questions. In IL–solvent mixtures, the apparent dissociated fraction obtained in this way can exhibit a minimum with composition, such that the inferred degree of dissociation eventually increases as more ionic liquid is added, as shown in Figure 5.1(c). This behavior is not immediately obvious from a simple ion-pairing picture, in which increasing the concentration of oppositely charged ions might be expected to promote association. Consequently, several studies have sought to rationalize this non-monotonic behavior and its relationship to ion transport.[314, 315, 316]

At the same time, a number of authors have emphasized that $\Lambda/\Lambda_{\mathrm{NE}}$—conventionally known as the *ionicity*, ξ—is not generally equivalent to the fraction of free ions.[311, 312, 317, 318, 319, 308] Rather, ionicity compares collective charge transport with an uncorrelated self-diffusive reference. It therefore contains information about ion–ion correlations and collective motion. By this definition, values of $\xi > 1$ are not mathematically excluded, and have indeed been observed experimentally in ionic-liquid systems, as shown in Figure 5.1(c). Much of this discussion has focused on either pure ionic liquids or simple aqueous electrolytes, leaving the interpretation of ionicity in IL–solvent mixtures less clear. Moreover, local ion association can still be strongly linked to transport: even dilute charged systems, such as polyelectrolytes, may form neutral pairs or complexes to maximize electrostatic interactions,[320, 321, 45, 322] and ion-pair lifetimes have been directly connected to transport properties, including conductivity.[310, 78, 323] Thus, the key question

is not whether ion association matters, but how local ion dissociation and collective conductivity are quantitatively related.

To address this question, we combine molecular dynamics simulations with a theoretical framework that separately describes ion association and charge transport. We simulate [BMIM][BF_4] in four molecular solvents: water, acetonitrile, acetone, and dimethyl sulfoxide (DMSO). The ionic liquid is described using the OPLS Virtual-Site Ionic Liquid (VSIL) force field,[324] which has been shown to reproduce structural and transport properties of pure ILs,[324, 325] while the neutral solvents are described using the standard OPLS force field.[326] Although the main analysis focuses on [BMIM][BF_4], we also consider additional ionic-liquid and solvent combinations, including [EMIM][BF_4], [BMIM][NTf_2], [BMIM][TFO], and [EMIM][NTf_2], to assess the generality of the force-field and association framework; these systems are summarized in Figure 5.1(b).

Using the molecular dynamics results, we then develop a theoretical description that combines Wertheim's first-order thermodynamic perturbation theory (TPT1),[165, 166, 167, 168] used to model local ion association, with the MSA conductivity theory of Blum, Turq, and co-workers,[327, 328] used to describe collective charge transport. This approach allows us to distinguish the free ion fraction from the ionicity and to identify how solvent-specific association, electrostatic correlations, electrophoretic effects, viscosity, and ion-specific asymmetries jointly determine conductivity in IL–solvent mixtures. Further simulation and theoretical details are provided in the Methods section.

5.2 Methods

Molecular Dynamics

All simulations were performed with GROMACS 2021.[329] The [BMIM][BF_4] ionic liquid was described using the OPLS Virtual-Site Ionic Liquid (VSIL) force field,[324] which places partial charges on massless virtual sites on the imidazolium ring to reproduce the anisotropic charge distribution of the cation. All molecular solvents were described using the OPLS-AA force field;[326] water was modeled using SPC/E.[330] Initial configurations were generated with Packmol.[184]

Nine compositions were simulated for each solvent, spanning $x_{\mathrm{IL}} \approx 0.02$–$1.00$, using 40–440 [BMIM][$BF_4$] ion pairs combined with 0–2000 solvent molecules in cubic simulation boxes. Periodic boundary conditions were applied in all directions, and electrostatic interactions were treated using particle-mesh Ewald summation[331].

Van der Waals and short-range electrostatic interactions were truncated at 1.4 nm. All covalent bonds were constrained using LINCS[332]. The temperature was maintained at $T = 298.15$ K using the Nosé–Hoover thermostat[180, 181], while the pressure was maintained at $p = 1$ bar during equilibration using the Berendsen barostat[333]. Each system was energy-minimized, equilibrated for 100 ps in the NVT ensemble and 10 ns in the NpT ensemble, and then simulated for a further 40 ns in the NVT ensemble for production.

The ionic conductivity was calculated from the collective charge displacement using the Einstein relation,

$$\sigma = \lim_{t\to\infty} \frac{1}{6Vk_{\mathrm{B}}Tt} \sum_i \sum_j \left\langle q_i \Delta\mathbf{r}_i(t) \cdot q_j \Delta\mathbf{r}_j(t) \right\rangle , \tag{5.5}$$

where i and j run over molecular ions, q_i is the net ionic charge, and $\Delta\mathbf{r}_i(t) = \mathbf{r}_i(t) - \mathbf{r}_i(0)$ is the unwrapped center-of-mass displacement of ion i. Molar conductivities were obtained from $\Lambda = \sigma / c_{\mathrm{IL}}$, where c_{IL} is the molar concentration of ionic-liquid pairs. The conductivity was decomposed into self, distinct, and cation–anion cross contributions following McDaniel and Son [78] and Fong et al. [334, 335], using fast-Fourier-transform algorithms implemented in the MDCraft library.[187, 14]

Viscosities were obtained from non-equilibrium molecular dynamics simulations using the cosine-acceleration method of Hess [336]. Three field amplitudes, 0.01, 0.025, and 0.05 nm ps^{-2}, were simulated for 10 ns each, and the zero-field viscosity was obtained by extrapolation to vanishing field amplitude.

Ion association was characterized using the site–site radial distribution function between imidazolium ring hydrogens on BMIM^+ and fluorine atoms on BF_4^-. The cutoff distance was chosen as the first minimum of this radial distribution function, $r_c = 3.5$ Å. To avoid overcounting multiple fluorine contacts from the same BF_4^- ion, the bound fraction was evaluated directly from the trajectories by counting unique site associations. Specifically, the fraction of paired cation association sites was computed as

$$X_{\mathrm{pair}} = \frac{1}{N_i n_{i,a}} \sum_{\mu=1}^{N_i} \sum_{a=1}^{n_{i,a}} \Theta\left(r_c - \min_{\nu,b} r_{\mu a,\nu b} \right), \tag{5.6}$$

where N_i is the number of cations, $n_{i,a}$ is the number of cation association sites, $r_{\mu a,\nu b}$ is the distance between site a on cation μ and site b on anion ν, and Θ is the Heaviside step function. A similar method was used to obtain the number of ion–solvent pairs.

Association Theory

The free ion fraction was modeled using Wertheim's first-order thermodynamic perturbation theory (TPT1).[165, 166, 167, 168] The fraction of sites of type a on species i that remain unassociated, $X_{i,a}^{\text{free}}$, satisfies the mass-action equation

$$X_{i,a}^{\text{free}} = \frac{1}{1 + \sum_j \sum_b x_j n_{j,b} \Delta_{ij,ab} X_{j,b}^{\text{free}}}, \tag{5.7}$$

where x_j is the mole fraction of species j, $n_{j,b}$ is the number of sites of type b on species j, and $\Delta_{ij,ab}$ is the association strength between sites a and b on species i and j, respectively. This equation can be solved iteratively using the routines in Clapeyron.jl[20]. This equation is identical to the one derived in chapter 1.

For [BMIM][BF_4] in a molecular solvent, we used a reduced association model with effective association sites on each ion species: three sites on the imidazolium of $BMIM^+$ and four from the fluorines on BF_4^-. Each solvent was also assigned one electron donor site, while water was assigned an additional two hydrogen donor sites.

Conductivity Theory

The molar conductivity of an associating electrolyte was described using the MSA-based theory of Blum, Turq, and co-workers.[327, 328] In this formulation, the conductivity is evaluated as a sum over charged species,

$$\Lambda = \sum_i \alpha_i \lambda_i^0 \Bigg[1 + S_{\text{el.},i}(1 + S_{\text{rel.},i}) + S_{\text{rel.},i} \left(1 + \frac{2}{3} S_{\text{rel.},i} \right) \Bigg], \tag{5.8}$$

where the sum runs over charged species, λ_i^0 is the infinite-dilution molar conductivity contribution of species i, and α_i is the fraction of species i contributing to free-ion transport.

The MSA screening parameter was computed from the total concentration of charged species,

$$\kappa^2 = \frac{e^2}{\varepsilon_0 \varepsilon_r k_B T} \sum_i \rho_i Z_i^2, \tag{5.9}$$

where ρ_i is the number density of species i, Z_i is its valency, and ε_r is the composition-dependent dielectric constant. The MSA parameter Γ is then obtained

from

$$2\Gamma = \frac{\kappa}{1 + \Gamma d}, \tag{5.10}$$

or equivalently

$$\Gamma = \frac{\sqrt{1 + 2\kappa d} - 1}{2d}, \tag{5.11}$$

where $d = \sigma_{\mathrm{HS}}$ is the effective ion diameter.

The electrophoretic correction for species i is

$$S_{\mathrm{el.},i} = -\frac{k_{\mathrm{B}}T}{3\pi\eta D_i^0}\frac{\Gamma}{1 + \Gamma d}, \tag{5.12}$$

where η is the composition-dependent viscosity and D_i^0 is the infinite-dilution self-diffusion coefficient of species i, obtained from simulations. The relaxation correction is obtained by summing pairwise contributions,

$$S_{\mathrm{rel.},i} = \sum_{j \neq i} S_{\mathrm{rel.},ij}, \tag{5.13}$$

with

$$\kappa_{ij}^2 = \frac{e^2}{\varepsilon_0 \varepsilon_r k_{\mathrm{B}}T}\frac{\rho_i Z_i^2 D_i^0 + \rho_j Z_j^2 D_j^0}{D_i^0 + D_j^0}, \tag{5.14}$$

and

$$S_{\mathrm{rel.},ij} = -\frac{1}{24\pi\varepsilon_0\varepsilon_r k_{\mathrm{B}}T}\frac{\kappa_{ij}^2 e^2 |Z_i Z_j|}{d(1 + \Gamma d)^2} \times \frac{1 - \exp(-2\kappa_{ij}d)}{\kappa_{ij}^2 + 2\Gamma\kappa_{ij} + 2\Gamma^2\left[1 - \exp(-\kappa_{ij}d)\right]}. \tag{5.15}$$

The corresponding Nernst–Einstein contribution within the same approximation is

$$\Lambda_{\mathrm{NE}} = \sum_i \alpha_i \lambda_i^0 \left(1 + S_{\mathrm{rel.},i}\right). \tag{5.16}$$

The ionicity predicted by the theory was then computed as

$$\xi = \frac{\Lambda}{\Lambda_{\mathrm{NE}}}. \tag{5.17}$$

This formulation makes explicit that the free-ion fraction controls the absolute magnitude of both Λ and Λ_{NE}, while deviations of ξ from unity arise from the relaxation and electrophoretic corrections to correlated ion motion.

The composition-dependent dielectric constant, molar volume, and viscosity entering these expressions were obtained from the mixing rules and simulation results described above.

5.3 Results and Discussion

Before using the simulations to examine the relationship between ion dissociation and conductivity, we first establish the fidelity of the force-field description for the systems of interest. Figures 5.1(d) and 5.1(e) compare the simulated ionic conductivity and viscosity, respectively, with available experimental data for [BMIM][BF_4] systems. Other systems are examined within the appendix (Figures 5.4b and 5.4a). Without further adjustment of the force-field parameters, both properties are generally reproduced with good accuracy across the solvents considered. The main exception is DMSO, for which the conductivity is underestimated by approximately a factor of two. This discrepancy is consistent with the corresponding overestimation of the dynamic viscosity in Figure 5.1(e). Nevertheless, the simulations capture the qualitative differences in transport properties across the four solvent environments. We therefore use these simulations as a molecularly resolved basis for analysing how ion dissociation, local solvation, and collective transport are related in ionic-liquid–solvent mixtures.

Ion Dissociation

Defining an ion pair in ionic liquids is less straightforward than in simple electrolytes. For monoatomic ions, ion pairing is often described using a distance criterion between oppositely charged species. In ionic liquids, however, the molecular complexity of the ions introduces multiple possible contact geometries, making ion pairing more closely analogous to a site-specific association, such as a hydrogen bond, than to a purely distance-based Coulombic pair.

This site-specific character is illustrated in Figure 5.2(a) for $BMIM^+$ and BF_4^- (similar analysis is carried out in Figure 5.6a for other ionic liquids). Among the possible interatomic radial distribution functions, the most well-defined peaks are observed between the fluorine atoms of BF_4^- and the hydrogens on the imidazolium ring of $BMIM^+$. The additional features at larger distances arise from neighboring fluorine atoms associated with the same BF_4^- ion. The inset of Figure 5.2(a) further highlights this local structure through the spatial distribution function of BF_4^- around the imidazolium hydrogens, which reveals highly localized association regions. This picture is consistent with previous molecular simulation and quantum chemistry studies of hydrogen-bond-like interactions in imidazolium-based ionic liquids.[309, 337] We therefore define an IL association using the first minimum of the relevant site–site radial distribution function, located at $r_c = 3.5$ Å. The fraction of bound IL association sites, X_{IL}, is then obtained by normalizing the number of bound sites

by the total number of available sites.

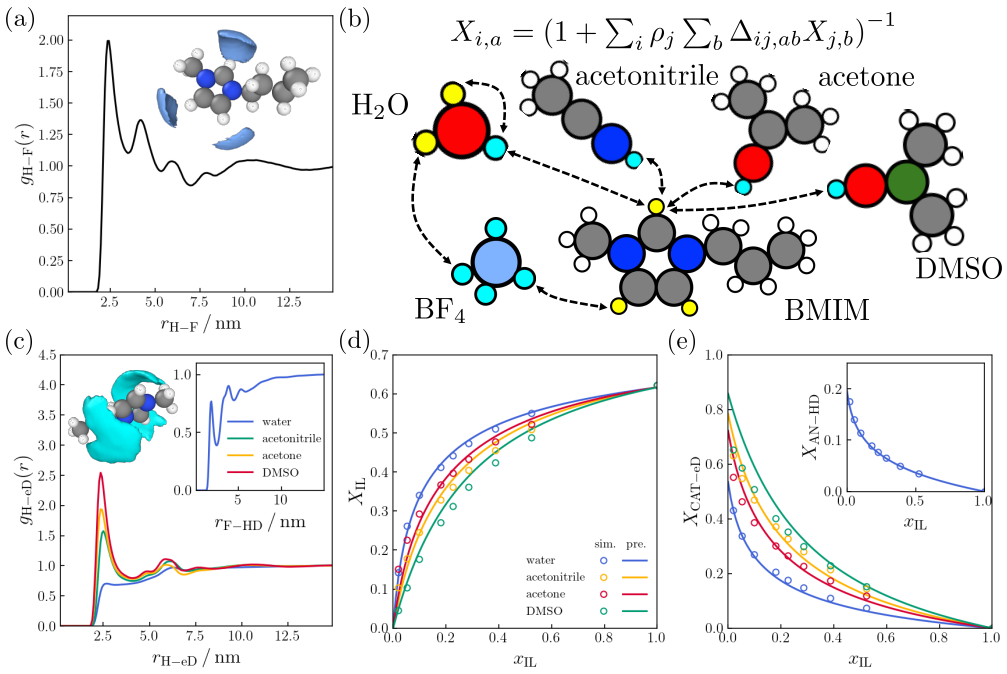


Figure 5.2: Ion dissociation in [BMIM][BF_4]–solvent mixtures. (a) Site–site radial distribution function $g(r)$ between BF_4^- fluorine atoms and $BMIM^+$ imidazolium hydrogens in the pure ionic liquid; inset: spatial distribution function of BF_4^- around $BMIM^+$. (b) Schematic of the association network illustrating competition between $BMIM^+$, BF_4^-, and solvent molecules. (c) Radial distribution functions between $BMIM^+$ and the electron-donor atom of each solvent in the dilute-IL limit, $x_{IL} \approx 0.02$; inset shows the corresponding radial distribution function between BF_4^- and water hydrogen atoms. (d) Bound IL-site fraction X_{IL} as a function of x_{IL} obtained from simulation, shown as open symbols, and Wertheim TPT1 theory, shown as lines. (e) Solvent electron-donor–cation association fraction $X_{CAT\text{-}eD}$; inset shows the solvent hydrogen-donor–anion association fraction.

Figure 5.2(d) shows X_{IL} as a function of the IL mole fraction x_{IL} for all four solvents. In every case, X_{IL} increases monotonically with increasing ionic-liquid concentration. Thus, as more ionic-liquid association sites become available, the probability of forming an ion-pair contact increases smoothly. Notably, no maximum in X_{IL} is observed over the composition range studied here. This monotonic increase is, in large part, an expected consequence of concentration alone: because the number of available IL–IL association sites grows with x_{IL}, a comparable qualitative trend would arise even for random mixing of non-interacting species, simply through mass action. The composition dependence of X_{IL} therefore does not, by itself, indicate a change in the strength of ion–ion interactions with x_{IL}; rather, it is the solvent-dependent differences in this trend that are informative. We also note that

X_{IL} does not reach unity even in the neat ionic liquid ($x_{IL} = 1$). This reflects the finite, rather than infinitely strong, association between $BMIM^+$ and BF_4^-: steric constraints on the imidazolium ring and the finite energetics of the fluorine–hydrogen contact limit full site saturation. This is consistent with simulation and experimental evidence that ionic liquids form finite-sized ionic clusters rather than an infinite, fully associated network, even in the pure liquid.[76, 77, 92]

The different solvents also vary substantially in their ability to disrupt IL–IL association beyond this baseline concentration-driven trend. As shown in Figure 5.2(d), the effectiveness of the solvents in reducing ion pairing follows the sequence DMSO > acetonitrile > acetone > water. A continuum electrostatic picture would suggest that solvents with larger dielectric constants should more effectively screen the Coulombic attraction between oppositely charged ions and therefore promote ion dissociation. Excluding water, the ordering in Figure 5.2(d) broadly follows this expectation. Water, however, has by far the largest dielectric constant among the solvents considered, yet it is the least effective at dissociating [BMIM][BF_4]. This observation suggests that bulk dielectric screening alone is insufficient to rationalize ion-pair formation in these mixtures. Instead, ion dissociation is strongly influenced by short-range, chemically specific association interactions at well-defined molecular sites.

To identify the relevant solvent–ion association sites, we examined radial distribution functions between the ions and the different solvent atoms. The most prominent solvent–cation interactions involve the electron-donor atoms of the solvents, namely oxygen or nitrogen atoms, coordinating with the imidazolium hydrogens of $BMIM^+$. Figure 5.2(c) compares these radial distribution functions in the dilute-IL limit (similar analysis is carried out in Figure 5.5b for other ionic liquids). Acetonitrile, acetone, and DMSO produce sharp and prominent first peaks, indicating strong coordination with the imidazolium ring. By contrast, water produces a weaker and broader feature. This broader distribution is consistent with the smaller size and reduced steric hindrance of water, which allows it to sample a wider range of configurations around the imidazolium ring, as also reflected in the spatial distribution shown in the inset of Figure 5.2(c).

Water is also distinct from the other solvents considered here because it can donate hydrogen bonds to the fluorine atoms of BF_4^-. This additional interaction is visible in the inset of Figure 5.2(c), where a well-defined peak appears between water hydrogens and BF_4^- fluorine atoms. Thus, water can interact with both ions: through

its oxygen atom with $BMIM^+$, and through its hydrogen atoms with BF_4^-.

Using analogous site-based criteria, we computed the fraction of cation and anion sites associated with solvent electron-donor and hydrogen-donor sites, respectively. These results are shown in Figure 5.2(e). The trends are consistent with those observed for the IL–IL association fraction in Figure 5.2(d): water binds most weakly to $BMIM^+$, while the other solvents follow the same general ordering observed in the ion-dissociation trends.

To rationalize these solvent-dependent differences in ion dissociation, we model the association network using Wertheim's first-order thermodynamic perturbation theory, TPT1.[165, 166, 167, 168] Related association-based approaches have previously been used to describe ionic-liquid interactions and phase behavior.[338, 79, 339] The association network considered here is summarized schematically in Figure 5.2(b). In this model, $BMIM^+$, BF_4^-, and the solvent molecules compete for a finite number of association sites. Unlike the other solvents, water is able to associate with both $BMIM^+$ and BF_4^-, while also forming solvent–solvent associations.

The generic TPT1 mass-action equations can be written as

$$X_{i,a}^{\mathrm{free}} = \frac{1}{1 + \sum_j \sum_b \phi_j n_{j,b} \Delta_{ij,ab} X_{j,b}^{\mathrm{free}}}, \tag{5.18}$$

where the indices i and j denote molecular species, a and b denote association-site types, ϕ_i is the volume fraction of species i, $X_{i,a}^{\mathrm{free}}$ is the fraction of sites of type a on species i that remain unassociated, $n_{i,a}$ is the number of such sites per molecule, and $\Delta_{ij,ab}$ characterizes the association strength between sites a and b on species i and j, respectively.

In principle, the association parameters $\Delta_{ij,ab}$ may be estimated from existing association models or from quantum chemistry calculations. Here, for simplicity, and to maintain consistency with the conductivity model developed below, we determine these parameters by fitting to the simulated IL–IL association fraction, X_{IL}. The resulting model is then compared against the independently measured ion–solvent association fractions. The fitted parameters are given in Table 5.1. As shown in Figures 5.2(d) and 5.2(e), this compact association model accurately reproduces both the IL–IL association fraction and the solvent–ion association trends, indicating that the dominant composition dependence of ion dissociation can be captured through a site-specific association framework. Similar agreement is also achieved for other ionic liquid systems in Figures 5.6a and Figures 5.6b.

Table 5.1: Association parameters ($\Delta_{ij,ab}$) used within the proposed theory (equation 5.7).

species i	site a	species j	site b	$\Delta_{ij,ab}$
$BMIM^+$	H	BF_4^-	F	6.0305
$BMIM^+$	H	TFO^-	O	1.8504
$BMIM^+$	H	H_2O	O	1.1109
$BMIM^+$	H	ACN	N	3.6384
$BMIM^+$	H	ACT	O	2.5959
$BMIM^+$	H	DMSO	O	6.0305
$EMIM^+$	H	BF_4^-	F	8.4417
$EMIM^+$	H	NTf_2^-	O	2.1920
$EMIM^+$	H	H_2O	O	1.8504
$EMIM^+$	H	DME	O	3.0735
BF_4^-	F	H_2O	H	0.1586
TFO^-	O	H_2O	H	0.1912
H_2O	H	H_2O	O	0.5581

The fitted association parameters also provide molecular insight into the solvent ordering. The cation–solvent association strength follows the same sequence observed in Figures 5.2(d) and 5.2(e). This trend is consistent with the solvent dipole moments, which provide a simple proxy for the strength of local IL–solvent association[340]: DMSO, 3.96 D; acetonitrile, 3.92 D; acetone, 2.88 D; and water, 1.85 D. This ordering also agrees with previous quantum chemistry calculations of solvent interactions with imidazolium-based ionic liquids.[309, 337]

The behavior of water highlights the importance of competition within the association network. Although water can interact with both $BMIM^+$ and BF_4^-, its cation association is relatively weak, and its ability to self-associate introduces an additional competing pathway. As the water content increases, water–water association becomes increasingly favorable and can reduce the availability of water molecules for disrupting IL–IL contacts. This provides a molecular explanation for why water, despite its large dielectric constant, is less effective at promoting ion dissociation than the other solvents considered here.

These results do not imply that electrostatic interactions are unimportant in ionic-liquid–solvent mixtures. Rather, they indicate that bulk dielectric screening is not, by itself, sufficient to describe local ion-pair formation. Short-range association specificity controls the local dissociation equilibrium, while the charged nature of the ions can still strongly influence collective and long-ranged properties.[85, 3] This distinction between local association and collective charge transport is central

to the conductivity behavior examined in the following section.

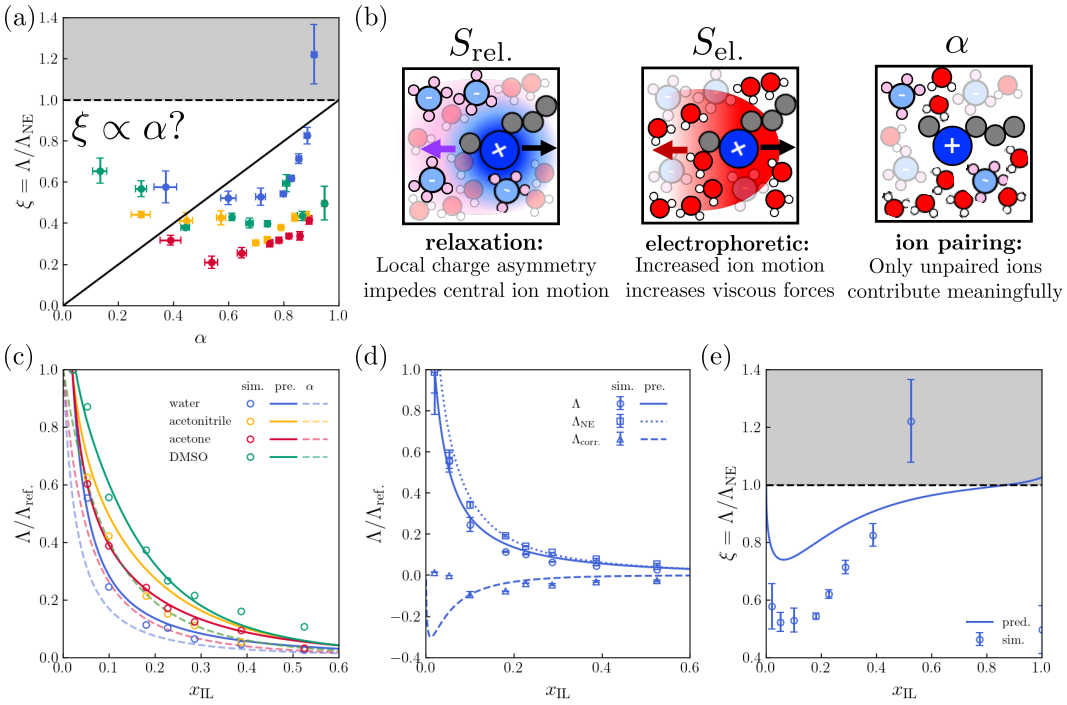


Figure 5.3: Relationship between ion dissociation, ionicity, and conductivity in [BMIM][BF_4]–solvent mixtures. (a) Ionicity, $\xi = \Lambda/\Lambda_{NE}$, plotted against the free ion fraction α for all simulated systems. The solid line denotes the simple proportionality $\xi = \alpha$, while the dashed line marks $\xi = 1$. (b) Schematic illustration of the conductivity decomposition. The conductivity depends on the free ion fraction α, relaxation corrections associated with distortion of the ionic atmosphere, and electrophoretic corrections associated with solvent back-flow and collective ion motion. (c) Normalized molar conductivity, $\Lambda/\Lambda_{ref.}$, and free ion fraction, α, as functions of ionic-liquid mole fraction x_{IL}, where the reference point is the lowest simulated IL mole fraction for each solvent. (d) Onsager decomposition of the molar conductivity for [BMIM][BF_4] in water into the self contribution, $\Lambda_{self} \equiv \Lambda_{NE}$, and the combined correlation contribution, $\Lambda_{corr} = \Lambda_{dist} + \Lambda_{cross}$. Symbols denote simulation results and lines denote the corresponding MSA predictions. (e) Ionicity ξ as a function of x_{IL} from simulation and theory, showing the emergence of a minimum at intermediate composition and apparent ionicities exceeding unity at high ionic-liquid content.

Conductivity

Having established that the simulations reproduce the qualitative trends in the experimental transport properties, Figures 5.1(d) and 5.1(e), and that the ion-dissociation fractions can be rationalized using a site-specific association model, we now examine how ion dissociation relates to ionic conductivity. A natural starting point is

the comparison between the ionicity, $\xi = \frac{\Lambda}{\Lambda_{\mathrm{NE}}}$, and the free ion fraction, α, shown in Figure 5.3(a). If ion pairing were the dominant origin of deviations from ideal Nernst–Einstein behavior, one might expect these two quantities to be closely related. However, the simulation results show that this relationship is not one-to-one. At relatively large values of α, there is a weak positive correlation between ξ and α, although with appreciable solvent-dependent scatter. At smaller values of α, this trend becomes less clear and can even appear inverted. In water-rich systems, apparent ionicities greater than unity are also observed, despite the fact that such values are difficult to interpret within a simple picture in which ion pairing only removes charge carriers from transport.

This apparent disconnect does not mean that ion dissociation is unimportant. Indeed, Figure 5.3(c) shows that both the molar conductivity and free ion fraction decrease monotonically with increasing x_{IL}. Moreover, when normalized by their respective values at the lowest simulated IL concentration, the solvent-dependent ordering of the conductivity decay broadly follows the ordering of ion dissociation discussed in the previous section. It is therefore understandable why ion pairing and conductivity are often discussed together. However, the comparison in Figure 5.3(a) indicates that ionicity cannot be interpreted as a direct measure of the free ion fraction alone. Instead, the conductivity reflects both the number of available charge carriers and the collective dynamical correlations between them.

To clarify this relationship, we use the conductivity theory developed by Blum, Turq, and co-workers,[327, 328] which extends Onsager's treatment of electrolyte conductance[341, 342, 32] using the mean-spherical approximation. For an associating electrolyte, the molar conductivity may be written as

$$\Lambda = \Lambda_0 \alpha \left[1 + S_{\mathrm{el.}}(1 + S_{\mathrm{rel.}}) + S_{\mathrm{rel.}} \left(1 + \frac{2}{3} S_{\mathrm{rel.}} \right) \right], \tag{5.19}$$

where Λ_0 is the infinite-dilution molar conductivity, α is the free ion fraction, $S_{\mathrm{rel.}}$ is the relaxation correction, and $S_{\mathrm{el.}}$ is the electrophoretic correction. The physical content of these contributions is illustrated schematically in Figure 5.3(b). In the absence of ion motion, the ionic atmosphere surrounding a central ion is, on average, symmetric and exerts no net force on that ion. When the ion moves, this atmosphere becomes distorted and its relaxation produces a retarding contribution to the ion motion. The electrophoretic correction instead accounts for hydrodynamic backflow: the motion of charged species drags solvent and surrounding ions, modifying

the effective friction experienced during charge transport. Finally, the prefactor α accounts for the reduction in mobile charge carriers due to ion association.

Combining this conductivity theory with the association model introduced above gives the theoretical curves shown in Figure 5.3(c) and Figure 5.7. Here, the free ion fraction is obtained from the Wertheim TPT1 model, while the dielectric constant and viscosity entering the transport corrections are described using composition-dependent mixing rules. Full expressions for $S_{\text{rel.}}$, $S_{\text{el.}}$, and the other terms entering Eq. 5.19 are given in the Methods. The resulting theory captures the main simulation trends, indicating that the conductivity can be rationalized by combining local association equilibria with collective electrostatic and hydrodynamic transport corrections. With this framework established, we can decompose the theory to determine why the ionicity does not simply track the free ion fraction.

Equation 5.19 contains the free ion fraction as an explicit prefactor, consistent with the intuitive expectation that ion association reduces the number of mobile charge carriers. However, this prefactor is not the only composition-dependent contribution to the conductivity. The relaxation and electrophoretic corrections also vary with composition through changes in screening, dielectric response, viscosity, and ion concentration. Thus, even if ion dissociation controls part of the conductivity, the ionicity depends on how the same physical effects enter both Λ and Λ_{NE}.

To make this point more transparent, we consider the Onsager decomposition of the molar conductivity,

$$\Lambda = \overbrace{\Lambda_{\text{self}}}^{\Lambda_{\text{NE}}} + \underbrace{\Lambda_{\text{dist}} + \Lambda_{\text{cross}}}_{\Lambda_{\text{corr.}}}, \tag{5.20}$$

where Λ_{self} is the self contribution, equivalent to the Nernst–Einstein conductivity, and $\Lambda_{\text{dist}} + \Lambda_{\text{cross}}$ represents the combined distinct and cation–anion cross-correlation contributions. We refer to this combined term as $\Lambda_{\text{corr.}}$. This decomposition is commonly used to analyse correlated ion transport in concentrated electrolytes and ionic liquids.[78, 334, 335]

Within the MSA framework, the corresponding Nernst–Einstein contribution can be written as[343, 344]

$$\Lambda_{\text{NE}} = \Lambda_0 \alpha (1 + S_{\text{rel.}}). \tag{5.21}$$

In this expression, the relaxation correction modifies the single-ion contribution because the motion of an individual ion is affected by the distortion of its surrounding

ionic atmosphere. By contrast, the electrophoretic correction arises from collective hydrodynamic back-flow between ions and therefore enters through the correlated contribution. Subtracting Eq. 5.21 from Eq. 5.19 gives the corresponding theoretical estimate of $\Lambda_{\text{corr.}}$.

Figure 5.3(d) compares this decomposition with the simulation results for [BMIM][BF_4] in water (decompositions for other ionic liquid + solvent systems are available in Figures 5.8 and 5.9). The theory captures the Nernst–Einstein contribution quantitatively and the correlation contribution qualitatively. The less precise agreement for $\Lambda_{\text{corr.}}$ is not unexpected: in molecular ionic liquids, many-body correlations include not only electrostatic relaxation and hydrodynamic effects, but also dispersion interactions, steric packing, and specific association interactions. Nevertheless, the decomposition is useful because it shows how changes in ion dissociation and changes in ion correlations contribute differently to the total conductivity.

One perhaps unexpected feature of Eq. 5.21 is the appearance of the free ion fraction, α, as a prefactor in the Nernst–Einstein contribution. This reflects an important distinction: the self-diffusion coefficient of ions is not necessarily equivalent to the diffusion coefficient of free ions alone. More generally, the Nernst–Einstein contribution should include a sum over all possible association states of each ion, including free ions, ion pairs, and higher-order clusters, each weighted by its charge, abundance, and mobility. In the simplified treatment used here, we assume that once an ion is part of a pair or larger cluster, its diffusion coefficient has dropped so substantially that it no longer contributes meaningfully to conductivity; free ions therefore provide the dominant contribution to the self-diffusive charge transport captured by Λ_{NE}. More elaborate cluster-based transport theories can relax this approximation by explicitly accounting for the mobilities and charges of different ionic aggregates.[345]

An important consequence follows from taking the ratio of Eq. 5.19 and Eq. 5.21. Because the cation–anion cross term contributing to $\Lambda_{\text{corr.}}$ in Eq. 5.19 is scaled by the same free-ion prefactor α as Λ_{NE}, rather than by the population of paired ions, there is no double counting or implicit cancellation between the self and correlated contributions: the two terms are separated by construction. This shared prefactor is precisely what cancels on taking the ratio, giving

$$\xi = \frac{\Lambda}{\Lambda_{\text{NE}}} = (1 + S_{\text{el.}}) + \frac{2}{3}\frac{S_{\text{rel.}}}{1 + S_{\text{rel.}}}. \tag{5.22}$$

Note that, for simplicity, this form of the theory assumes the ions are symmetric.

Thus, within this simplified form of the theory, ionicity is not directly proportional to the free ion fraction. Instead, it measures the relative importance of collective correlation effects compared with the self-diffusive contribution. The free ion fraction still affects the absolute conductivity through the prefactor in Eqs. 5.19 and 5.21. As such, the ratio $\Lambda/\Lambda_{\mathrm{NE}}$ is not, by itself, a direct measure of the number of dissociated ions.

This distinction helps explain the behavior shown in Figure 5.3(e). Both simulations and theory exhibit a minimum in ionicity at low-to-intermediate ionic-liquid composition, followed by an increase at larger x_{IL}. At low ionic-liquid content, increasing ion concentration strengthens electrostatic correlations. The relaxation contribution therefore becomes more important and suppresses collective charge transport relative to the ideal Nernst–Einstein limit, decreasing ξ. In a simple electrolyte with weak composition dependence of viscosity and dielectric constant, this trend would be expected to dominate over a broad concentration range.

Ionic-liquid–solvent mixtures differ from this simple limit because their transport properties change strongly with composition[346]. In particular, the viscosity increases substantially as the ionic-liquid content increases, as shown in Figure 5.1(e). This increase in viscosity reduces both the total conductivity and the Nernst–Einstein conductivity by slowing molecular motion. However, it also reduces the magnitude of the electrophoretic correction, because hydrodynamic back-flow becomes less effective when the medium is more viscous. As a result, the electrophoretic correction weakens at larger x_{IL}, causing the ionicity to increase again. The minimum in ionicity therefore arises from a competition between increasing electrostatic correlations at low IL concentration and the viscosity-mediated reduction of electrophoretic corrections at higher IL concentration. This mechanism is particularly relevant for ionic-liquid mixtures because they combine strong Coulombic correlations with large, composition-dependent changes in viscosity over a broad miscible composition range.

The occurrence of apparent ionicities greater than unity is more subtle. Equations 5.19–5.22 are written for a simplified symmetric electrolyte, which makes the cancellation of the explicit free-ion prefactor especially transparent. Real ionic liquids, however, are molecularly asymmetric: cations and anions differ in size, shape, charge distribution, and association interactions. When cation and anion are perfectly symmetric, their relative motion is maximally correlated and the cation–anion cross term is correspondingly strong and negative. As the size, mass, or mobility of

the two ions become increasingly asymmetric, the faster ion increasingly dominates the pair's relative motion, degrading this correlation and, beyond a certain point, reversing its sign so that the cross-correlation contribution becomes less negative or even positive, increasing the collective conductivity relative to the Nernst–Einstein estimate. In this case, values of $\xi > 1$ do not imply that more charge carriers exist than expected; rather, they indicate that the collective ion motions enhance charge transport relative to the uncorrelated self-diffusion reference.

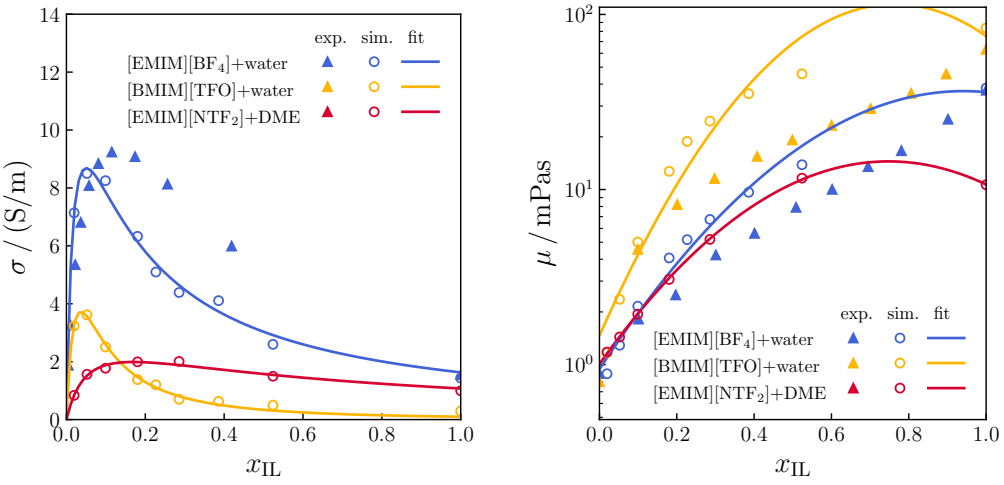
Finally, we note that this analysis also clarifies the limitations of using the Stokes–Einstein–Sutherland relation to infer ionicity across ionic-liquid compositions. One might argue that, in the dilute limit, the Stokes–Einstein–Sutherland estimate should approximate the diffusion coefficient of isolated free ions. However, even at relatively low ionic-liquid concentrations, electrostatic and hydrodynamic correlations can already contribute measurably to transport because of the long-ranged and many-body nature of Coulomb interactions. As a result, deviations from ideal Nernst–Einstein behavior need not require extensive ion pairing or clustering.

We also note that the association fraction X_{IL} used throughout this chapter is a static, structural measure: it does not distinguish between long-lived ion pairs and transient contacts that separate again on a timescale short compared with diffusive ion motion. A dynamic, lifetime-resolved definition of ion pairing would be expected to correlate more closely with ionicity, since only sufficiently long-lived contacts can meaningfully suppress dynamic cation–anion correlations[78, 310].

Taken together, these results show that ion dissociation and conductivity are related, but not interchangeable, descriptors of transport in ionic-liquid–solvent mixtures. Solvent-specific association controls the local population of free ions, while the measured conductivity and ionicity are further shaped by collective electrostatic correlations, electrophoretic effects, viscosity, and ion-specific asymmetries. Consequently, trends in ionicity should not be interpreted as direct measures of ion-pair populations. Instead, they provide a complementary measure of how correlated ion motion modifies charge transport relative to the ideal Nernst–Einstein limit. The same distinction between local association and collective dynamic response reappears in a very different context in Chapter 7, where the ratio of dynamic metal-ligand crosslinkers to available binding sites, rather than crosslink density alone, governs the mechanical response of a polymer network.

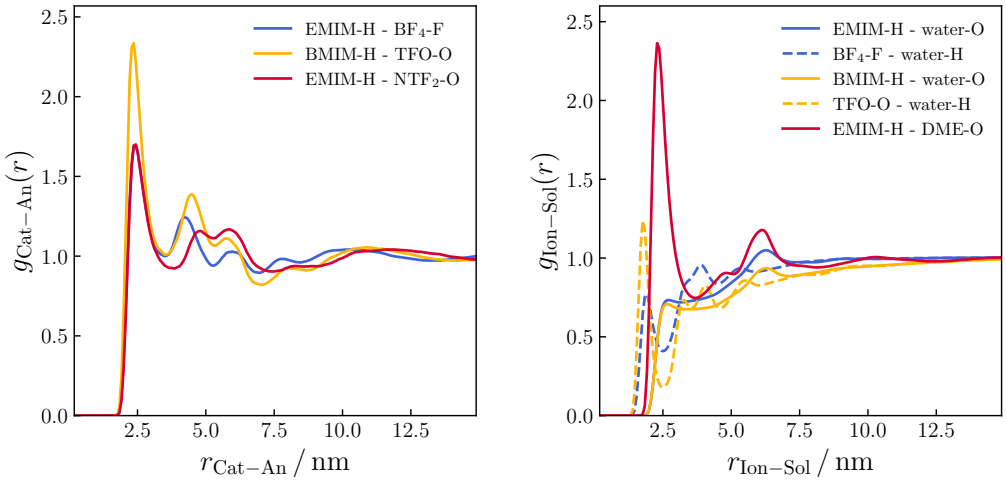
5.4 Appendix

Additional Figures



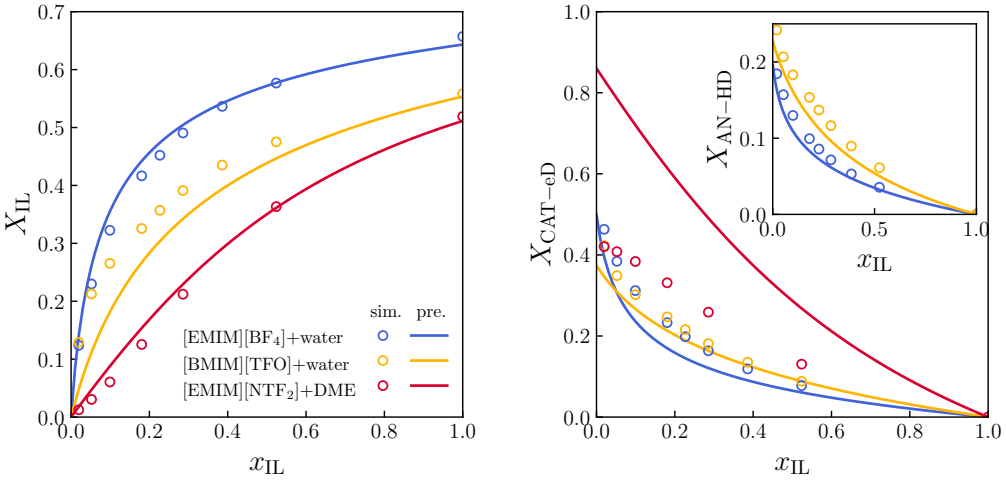
(a) (b)

Figure 5.4: (a) Ionic conductivity σ and (b) dynamic viscosity η on a logarithmic scale as a function of x_{IL} for various ionic liquid and solvent systems. Open symbols denote simulation results; filled symbols denote experimental data. Lines in (a) and (b) are guides to the eye.



(a) (b)

Figure 5.5: (a) Site–site radial distribution function $g(r)$ between anionic and cationic binding systems in the pure ionic liquid. (b) Radial distribution functions between cationic sites and the electron-donor atom of each solvent (solid lines) and between anionic binding sites and hydrogen-donor atoms of each solvent (dashed lines) in the dilute-IL limit, $x_{\mathrm{IL}} \approx 0.02$.



(a) (b)

Figure 5.6: For ionic liquid + solvent systems not considered in the main text: (a) Bound IL-site fraction X_{IL} as a function of x_{IL} obtained from simulation, shown as open symbols, and Wertheim TPT1 theory, shown as lines. (b) Solvent electron-donor–cation association fraction $X_{\mathrm{CAT\text{-}eD}}$; inset shows the solvent hydrogen-donor–anion association fraction.

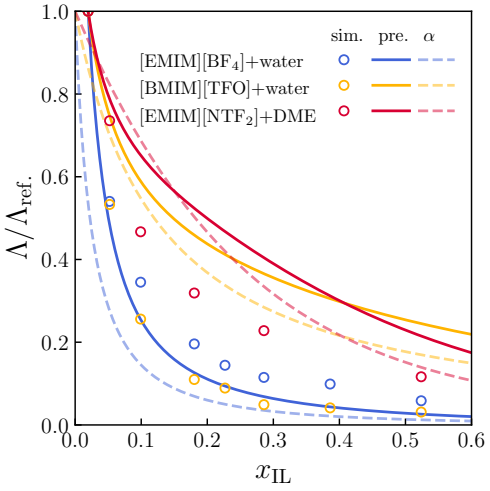
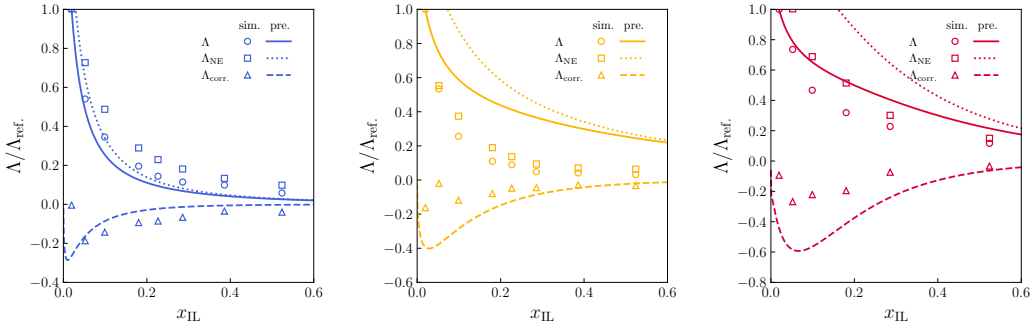


Figure 5.7: For ionic liquid + solvent systems not considered in the main text: Normalized molar conductivity, $\Lambda/\Lambda_{\text{ref.}}$, and free ion fraction, α, as functions of ionic-liquid mole fraction x_{IL}, where the reference point is the lowest simulated IL mole fraction for each system.



(a) (b) (c)

Figure 5.8: Onsager decomposition of the molar conductivity for (a) [EMIM][BF_4] in water, (b) [BMIM][TFO] in water and (c) [EMIM][NTf_2] in DME into the self contribution, $\Lambda_{\text{self}} \equiv \Lambda_{\text{NE}}$, and the combined correlation contribution, $\Lambda_{\text{corr}} = \Lambda_{\text{dist}} + \Lambda_{\text{cross}}$. Symbols denote simulation results and lines denote the corresponding MSA predictions.

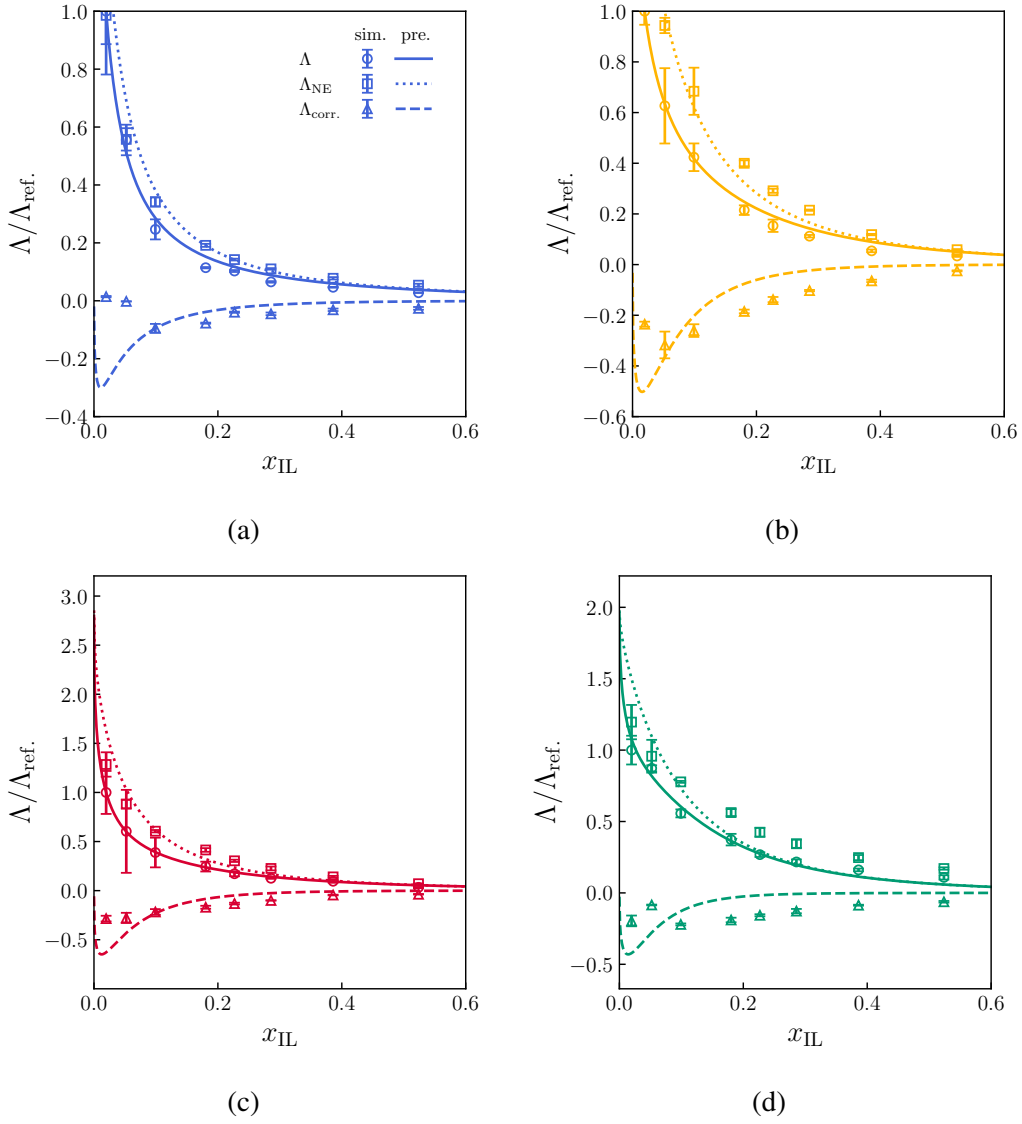


Figure 5.9: Onsager decomposition of the molar conductivity for [BMIM][BF_4] in (a) water, (b) acetonitrile, (c) acetone and (d) DMSO into the self contribution, $\Lambda_{\text{self}} \equiv \Lambda_{\text{NE}}$, and the combined correlation contribution, $\Lambda_{\text{corr}} = \Lambda_{\text{dist}} + \Lambda_{\text{cross}}$. Symbols denote simulation results and lines denote the corresponding MSA predictions.

References

[3] Pierre J. Walker and Zhen-Gang Wang. "Anomalous Phase Behavior of Polymer–Ionic Liquid Mixtures". In: *J. Phys. Chem. B* 129 (Nov. 2025). ISSN: 1520-6106. DOI: 10.1021/acs.jpcb.5c04858.

[9] Pierre Walker and Zhen-Gang Wang. "Decoupling Ion Association from Conductivity in Ionic-Liquid–Solvent Mixtures". In: *In preparation* (2026).

[14] Benjamin B. Ye, Pierre J. Walker, and Zhen-Gang Wang. "MDCraft: A Python assistant for performing and analyzing molecular dynamics simulations of soft matter systems". In: *J. Open Source Softw.* 9.100 (Aug. 2024), p. 7013. ISSN: 2475-9066. DOI: 10.21105/joss.07013.

[20] Pierre J. Walker, Hon-Wa Yew, and Andrés Riedemann. "Clapeyron.jl: An Extensible, Open-Source Fluid Thermodynamics Toolkit". In: *Ind. Eng. Chem. Res.* 61.20 (May 2022), pp. 7130–7153. ISSN: 0888-5885, 1520-5045. DOI: 10.1021/acs.iecr.2c00326.

[32] Raymond M. Fuoss and Lars Onsager. "Conductance of Unassociated Electrolytes." In: *J. Phys. Chem.* 61.5 (May 1957), pp. 668–682. ISSN: 0022-3654. DOI: 10.1021/j150551a038.

[45] Arthur Veis. "A review of the early development of the thermodynamics of the complex coacervation phase separation". In: *Adv. Colloid Interface Sci.* Polyelectrolyte-Macroion Coacervation 167.1 (Sept. 2011), pp. 2–11. ISSN: 0001-8686. DOI: 10.1016/j.cis.2011.01.007.

[46] Andrzej Lewandowski and Agnieszka Świderska-Mocek. "Ionic liquids as electrolytes for Li-ion batteries—An overview of electrochemical studies". In: *J. Power Sources* 194.2 (Dec. 2009), pp. 601–609. ISSN: 0378-7753. DOI: 10.1016/j.jpowsour.2009.06.089.

[50] Irene Osada et al. "Ionic-Liquid-Based Polymer Electrolytes for Battery Applications". In: *Angew. Chem., Int. Ed.* 55.2 (2016), pp. 500–513. ISSN: 1521-3773. DOI: 10.1002/anie.201504971.

[51] Sharmin Sultana et al. "Ionic Liquid-Based Gels for Applications in Electrochemical Energy Storage and Conversion Devices: A Review of Recent Progress and Future Prospects". In: *Gels* 8.1 (Jan. 2022), p. 2. ISSN: 2310-2861. DOI: 10.3390/gels8010002.

[52] Jason E. Bara et al. "Synthesis and Performance of Polymerizable Room-Temperature Ionic Liquids as Gas Separation Membranes". In: *Ind. Eng. Chem. Res.* 46.16 (Aug. 2007), pp. 5397–5404. ISSN: 0888-5885. DOI: 10.1021/ie0704492.

[76] B. L. Bhargava and Michael L. Klein. "Aqueous solutions of imidazolium ionic liquids: molecular dynamics studies". In: *Soft Matter* 5.18 (Sept. 2009), pp. 3475–3480. ISSN: 1744-6848. DOI: 10.1039/B908046E.

[77] Shimou Chen et al. “Ionic liquid clusters: structure, formation mechanism, and effect on the behavior of ionic liquids”. In: *Phys. Chem. Chem. Phys.* 16 (Mar. 2014), pp. 5893–5906. DOI: 10.1039/C3CP53116C.

[78] Jesse G. McDaniel and Chang Yun Son. “Ion Correlation and Collective Dynamics in BMIM/BF $_4$ -Based Organic Electrolytes: From Dilute Solutions to the Ionic Liquid Limit”. In: *J. Phys. Chem. B* 122.28 (July 2018), pp. 7154–7169. ISSN: 1520-6106, 1520-5207. DOI: 10.1021/acs.jpcb.8b04886.

[79] Xiaoyan Ji, Christoph Held, and Gabriele Sadowski. “Modeling imidazolium-based ionic liquids with ePC-SAFT”. In: *Fluid Phase Equilib.* 335 (Dec. 2012), pp. 64–73. ISSN: 03783812. DOI: 10.1016/j.fluid.2012.05.029.

[85] Charles E. Sing, Jos W. Zwanikken, and Monica Olvera de la Cruz. “Electrostatic control of block copolymer morphology”. In: *Nat. Mater.* 13.7 (July 2014), pp. 694–698. ISSN: 1476-4660. DOI: 10.1038/nmat4001.

[92] Michael McEldrew et al. “Ion Clusters and Networks in Water-in-Salt Electrolytes”. In: *J. Electrochem. Soc.* 168.5 (May 2021), p. 050514. ISSN: 0013-4651, 1945-7111. DOI: 10.1149/1945-7111/abf975.

[165] M. S. Wertheim. “Fluids with highly directional attractive forces. I. Statistical thermodynamics”. In: *J. Stat. Phys.* 35.1-2 (Apr. 1984), pp. 19–34. ISSN: 0022-4715, 1572-9613. DOI: 10.1007/BF01017362.

[166] M. S. Wertheim. “Fluids with highly directional attractive forces. II. Thermodynamic perturbation theory and integral equations”. In: *J. Stat. Phys.* 35.1-2 (Apr. 1984), pp. 35–47. ISSN: 0022-4715, 1572-9613. DOI: 10.1007/BF01017363.

[167] M. S. Wertheim. “Fluids with highly directional attractive forces. III. Multiple attraction sites”. In: *J. Stat. Phys.* 42.3-4 (Feb. 1986), pp. 459–476. ISSN: 0022-4715, 1572-9613. DOI: 10.1007/BF01127721.

[168] M. S. Wertheim. “Fluids with highly directional attractive forces. IV. Equilibrium polymerization”. In: *J. Stat. Phys.* 42.3-4 (Feb. 1986), pp. 477–492. ISSN: 0022-4715, 1572-9613. DOI: 10.1007/BF01127722.

[180] Shūichi Nosé. “A molecular dynamics method for simulations in the canonical ensemble”. In: *Mol. Phys.* 52.2 (June 1984), pp. 255–268. ISSN: 0026-8976. DOI: 10.1080/00268978400101201.

[181] William G. Hoover. “Canonical dynamics: Equilibrium phase-space distributions”. In: *Phys. Rev. A* 31.3 (Mar. 1985), pp. 1695–1697. DOI: 10.1103/PhysRevA.31.1695.

[184] L. Martínez et al. “PACKMOL: A package for building initial configurations for molecular dynamics simulations”. In: *J. Comput. Chem.* 30.13 (Oct. 2009), pp. 2157–2164. ISSN: 01928651, 1096987X. DOI: 10.1002/jcc.21224.

[187] Naveen Michaud-Agrawal et al. “MDAnalysis: A toolkit for the analysis of molecular dynamics simulations”. In: *J. Comput. Chem.* 32.10 (July 2011), pp. 2319–2327. ISSN: 01928651. DOI: 10.1002/jcc.21787.

[298] Shyue Ping Ong et al. “Electrochemical Windows of Room-Temperature Ionic Liquids from Molecular Dynamics and Density Functional Theory Calculations”. In: *Chem. Mater.* 23.11 (June 2011), pp. 2979–2986. ISSN: 0897-4756. DOI: 10.1021/cm200679y.

[299] Benjamin Bobin Ye and Zhen-Gang Wang. “A coarse-grained model of room-temperature ionic liquids between metal electrodes: a molecular dynamics study”. In: *Phys. Chem. Chem. Phys.* 24.19 (May 2022), pp. 11573–11584. ISSN: 1463-9084. DOI: 10.1039/D2CP00166G.

[300] Lars Olow Simon Colbin, Yunqi Shao, and Reza Younesi. “Ion-Pairing: A Bygone Treatment of Electrolyte Solutions?” en. In: *Batteries Supercaps* 8.1 (2025), e202400160. ISSN: 2566-6223. DOI: 10.1002/batt.202400160.

[301] B. Gurkan et al. “Molecular Design of High Capacity, Low Viscosity, Chemically Tunable Ionic Liquids for CO2 Capture”. In: *J. Phys. Chem. Lett.* 1.24 (Dec. 2010), pp. 3494–3499. DOI: 10.1021/jz101533k.

[302] Moumita Saha et al. “A Comprehensive Review of Novel Emerging Electrolytes for Supercapacitors: Aqueous and Organic Electrolytes Versus Ionic Liquid-Based Electrolytes”. In: *Energy Fuels* 38.10 (May 2024), pp. 8528–8552. ISSN: 0887-0624. DOI: 10.1021/acs.energyfuels.4c00685.

[303] Issei Nakamura. “Spinodal Decomposition of a Polymer and Ionic Liquid Mixture: Effects of Electrostatic Interactions and Hydrogen Bonds on Phase Instability”. In: *Macromolecules* 49.2 (Jan. 2016), pp. 690–699. ISSN: 0024-9297. DOI: 10.1021/acs.macromol.5b02189.

[304] Oscar Nordness and Joan F. Brennecke. “Ion Dissociation in Ionic Liquids and Ionic Liquid Solutions”. In: *Chem. Rev.* 120.23 (Dec. 2020), pp. 12873–12902. ISSN: 0009-2665, 1520-6890. DOI: 10.1021/acs.chemrev.0c00373.

[305] Marija Bešter-Rogač, Alexander Stoppa, and Richard Buchner. “Ion Association of Imidazolium Ionic Liquids in Acetonitrile”. In: *J. Phys. Chem. B* 118.5 (Feb. 2014), pp. 1426–1435. ISSN: 1520-6106, 1520-5207. DOI: 10.1021/jp412344a.

[306] Cheng Zhong et al. “A review of electrolyte materials and compositions for electrochemical supercapacitors”. In: *Chem. Soc. Rev.* 44.21 (Oct. 2015), pp. 7484–7539. ISSN: 1460-4744. DOI: 10.1039/C5CS00303B.

[307] Samuel Varner and Zhen-Gang Wang. “Effects of dilution in ionic liquid supercapacitors”. In: *Phys. Chem. Chem. Phys.* 24.44 (Nov. 2022), pp. 27362–27374. ISSN: 1463-9084. DOI: 10.1039/D2CP03398D.

[308] Oldamur Hollóczki et al. “On the origin of ionicity in ionic liquids. Ion pairing versus charge transfer”. In: *Phys. Chem. Chem. Phys.* 16.32 (July 2014), pp. 16880–16890. ISSN: 1463-9084. DOI: 10.1039/C4CP01177E.

[309] Kun Dong et al. “Hydrogen Bonds in Imidazolium Ionic Liquids”. In: *J. Phys. Chem. A* 110.31 (Aug. 2006), pp. 9775–9782. ISSN: 1089-5639, 1520-5215. DOI: 10.1021/jp054054c.

[310] Yong Zhang and Edward J. Maginn. “Direct Correlation between Ionic Liquid Transport Properties and Ion Pair Lifetimes: A Molecular Dynamics Study”. In: *J. Phys. Chem. Lett.* 6.4 (Feb. 2015), pp. 700–705. ISSN: 1948-7185, 1948-7185. DOI: 10.1021/acs.jpclett.5b00003.

[311] Douglas R. MacFarlane et al. “On the concept of ionicity in ionic liquids”. In: *Phys. Chem. Chem. Phys.* 11.25 (2009), p. 4962. ISSN: 1463-9076, 1463-9084. DOI: 10.1039/b900201d.

[312] Kazuhide Ueno, Hiroyuki Tokuda, and Masayoshi Watanabe. “Ionicity in ionic liquids: correlation with ionic structure and physicochemical properties”. In: *Phys. Chem. Chem. Phys.* 12.8 (Feb. 2010), pp. 1649–1658. ISSN: 1463-9084. DOI: 10.1039/B921462N.

[313] Oscar Nordness et al. “Characterization of Aqueous 1-Ethyl-3-Methylimidazolium Ionic Liquids for Calculation of Ion Dissociation”. In: *J. Phys. Chem. B* 123.6 (Feb. 2019), pp. 1348–1358. ISSN: 1520-6106, 1520-5207. DOI: 10.1021/acs.jpcb.8b11892.

[314] Yu-Jeng Lin, Nazir Hossain, and Chau-Chyun Chen. “Modeling dissociation of ionic liquids with electrolyte NRTL model”. In: *J. Mol. Liq.* 329 (May 2021), p. 115524. ISSN: 01677322. DOI: 10.1016/j.molliq.2021.115524.

[315] Bong-Seop Lee and Shiang-Tai Lin. “The Origin of Ion-Pairing and Redissociation of Ionic Liquid”. In: *J. Phys. Chem. B* 121.23 (June 2017), pp. 5818–5823. ISSN: 1520-6106, 1520-5207. DOI: 10.1021/acs.jpcb.7b01189.

[316] Bong-Seop Lee and Shiang-Tai Lin. “A Priori Prediction of Dissociation Phenomena and Phase Behaviors of Ionic Liquids”. In: *Ind. Eng. Chem. Res.* 54.36 (Sept. 2015), pp. 9005–9012. ISSN: 0888-5885, 1520-5045. DOI: 10.1021/acs.iecr.5b01762.

[317] Kenneth R. Harris. “Relations between the Fractional Stokes-Einstein and Nernst-Einstein Equations and Velocity Correlation Coefficients in Ionic Liquids and Molten Salts”. In: *J. Phys. Chem. B* 114.29 (July 2010), pp. 9572–9577. ISSN: 1520-6106, 1520-5207. DOI: 10.1021/jp102687r.

[318] Kenneth R. Harris. “Can the Transport Properties of Molten Salts and Ionic Liquids Be Used To Determine Ion Association?” In: *J. Phys. Chem. B* 120.47 (Dec. 2016), pp. 12135–12147. ISSN: 1520-6106, 1520-5207. DOI: 10.1021/acs.jpcb.6b08381.

[319] Kenneth R. Harris. "Comment on "Ionic Conductivity, Diffusion Coefficients, and Degree of Dissociation in Lithium Electrolytes, Ionic Liquids, and Hydrogel Polyelectrolytes"". In: *J. Phys. Chem. B* 122.48 (Dec. 2018), pp. 10964–10967. ISSN: 1520-6106, 1520-5207. DOI: 10.1021/acs.jpcb.8b08610.

[320] Arthur Veis and Catherine Aranyi. "PHASE SEPARATION IN POLYELECTROLYTE SYSTEMS. I. COMPLEX COACERVATES OF GELATIN". In: *J. Phys. Chem.* 64.9 (Sept. 1960), pp. 1203–1210. ISSN: 0022-3654. DOI: 10.1021/j100838a022.

[321] Xiao Xu et al. "Potential of mean force and transient states in polyelectrolyte pair complexation". In: *J. Chem. Phys.* 145.3 (July 2016), p. 034901. ISSN: 0021-9606. DOI: 10.1063/1.4958675.

[322] Pengfei Zhang and Zhen-Gang Wang. "Supernatant Phase in Polyelectrolyte Complex Coacervation: Cluster Formation, Binodal, and Nucleation". In: *Macromolecules* 55.10 (May 2022), pp. 3910–3923. ISSN: 0024-9297. DOI: 10.1021/acs.macromol.2c00340.

[323] Ray Matsumoto, Matthew W. Thompson, and Peter T. Cummings. "Ion Pairing Controls Physical Properties of Ionic Liquid-Solvent Mixtures". In: *J. Phys. Chem. B* 123.46 (Nov. 2019), pp. 9944–9955. ISSN: 1520-6106. DOI: 10.1021/acs.jpcb.9b08509.

[324] Brian Doherty, Xiang Zhong, and Orlando Acevedo. "Virtual Site OPLS Force Field for Imidazolium-Based Ionic Liquids". In: *J. Phys. Chem. B* 122.11 (Mar. 2018), pp. 2962–2974. ISSN: 1520-6106, 1520-5207. DOI: 10.1021/acs.jpcb.7b11996.

[325] Kun Yue, Brian Doherty, and Orlando Acevedo. "Comparison between ab initio molecular dynamics and opls-based force fields for ionic liquid solvent organization". In: *J. Phys. Chem. B* 126.21 (June 2022), pp. 3908–3919. ISSN: 1520-6106, 1520-5207. DOI: 10.1021/acs.jpcb.2c01636.

[326] William L. Jorgensen, David S. Maxwell, and Julian Tirado-Rives. "Development and Testing of the OPLS All-Atom Force Field on Conformational Energetics and Properties of Organic Liquids". In: *J. Am. Chem. Soc.* 118.45 (Nov. 1996), pp. 11225–11236. ISSN: 0002-7863, 1520-5126. DOI: 10.1021/ja9621760.

[327] Olivier Bernard et al. "Conductance in electrolyte solutions using the mean spherical approximation". In: *J. Phys. Chem.* 96.9 (Apr. 1992), pp. 3833–3840. ISSN: 0022-3654, 1541-5740. DOI: 10.1021/j100188a049.

[328] Pierre Turq et al. "Conductance in Associated Electrolytes Using the Mean Spherical Approximation". In: *J. Phys. Chem.* 99.2 (Jan. 1995), pp. 822–827. ISSN: 0022-3654, 1541-5740. DOI: 10.1021/j100002a053.

[329] Mark James Abraham et al. “GROMACS: High performance molecular simulations through multi-level parallelism from laptops to supercomputers”. In: *SoftwareX* 1-2 (Sept. 2015), pp. 19–25. ISSN: 2352-7110. DOI: 10.1016/j.softx.2015.06.001.

[330] H. J. C. Berendsen, J. R. Grigera, and T. P. Straatsma. “The missing term in effective pair potentials”. In: *J. Phys. Chem.* 91.24 (Nov. 1987), pp. 6269–6271. ISSN: 0022-3654, 1541-5740. DOI: 10.1021/j100308a038.

[331] Tom Darden, Darrin York, and Lee Pedersen. “Particle mesh Ewald: An N·log(N) method for Ewald sums in large systems”. In: *J. Chem. Phys.* 98.12 (June 1993), pp. 10089–10092. ISSN: 0021-9606. DOI: 10.1063/1.464397.

[332] Berk Hess et al. “LINCS: A linear constraint solver for molecular simulations”. en. In: *J. Comput. Chem.* 18.12 (1997), pp. 1463–1472. ISSN: 1096-987X. DOI: 10.1002/(SICI)1096-987X(199709)18:12<1463::AID-JCC4>3.0.CO;2-H.

[333] H. J. C. Berendsen et al. “Molecular dynamics with coupling to an external bath”. In: *J. Chem. Phys.* 81.8 (Oct. 1984), pp. 3684–3690. ISSN: 0021-9606. DOI: 10.1063/1.448118.

[334] Kara D. Fong et al. “Ion Correlations and Their Impact on Transport in Polymer-Based Electrolytes”. In: *Macromolecules* 54.6 (Mar. 2021), pp. 2575–2591. ISSN: 0024-9297, 1520-5835. DOI: 10.1021/acs.macromol.0c02545.

[335] Kara D. Fong et al. “Transport phenomena in electrolyte solutions: Nonequilibrium thermodynamics and statistical mechanics”. In: *AIChE J.* 66.12 (2020), e17091. ISSN: 1547-5905. DOI: 10.1002/aic.17091.

[336] Berk Hess. “Determining the shear viscosity of model liquids from molecular dynamics simulations”. In: *J. Chem. Phys.* 116.1 (2002), p. 209. ISSN: 00219606. DOI: 10.1063/1.1421362.

[337] Yan-Zhen Zheng et al. “Hydrogen-bonding interactions between [BMIM][BF4] and dimethyl sulfoxide”. In: *J. Mol. Struct.* 1069 (July 2014), pp. 140–146. ISSN: 00222860. DOI: 10.1016/j.molstruc.2014.01.013.

[338] Yushu Chen, Fabrice Mutelet, and Jean-Noël Jaubert. “Modeling the Solubility of Carbon Dioxide in Imidazolium-Based Ionic Liquids with the PC-SAFT Equation of State”. In: *J. Phys. Chem. B* 116.49 (Dec. 2012), pp. 14375–14388. ISSN: 1520-6106, 1520-5207. DOI: 10.1021/jp309944t.

[339] Zachary A. H. Goodwin et al. “Gelation, clustering, and crowding in the electrical double layer of ionic liquids”. In: *J. Chem. Phys.* 157.9 (Sept. 2022), p. 094106. ISSN: 0021-9606. DOI: 10.1063/5.0097055.

[340] Th. Dhileep N. Reddy and Bhabani S. Mallik. "Reciprocity between ion-dipole and hydrogen bond interactions in the binary mixtures of N,N-Dimethylformamide with ionic liquids". In: *J. Mol. Liq.* 301 (Mar. 2020), p. 112487. ISSN: 01677322. DOI: 10.1016/j.molliq.2020.112487.

[341] Lars Onsager. "Electric Moments of Molecules in Liquids". In: *J. Am. Chem. Soc.* 58.8 (Aug. 1936), pp. 1486–1493. ISSN: 0002-7863. DOI: 10.1021/ja01299a050.

[342] Raymond M. Fuoss. "Conductance of Dilute Solutions of 1-1 Electrolytes [1]". In: *J. Am. Chem. Soc.* 81.11 (June 1959), pp. 2659–2662. ISSN: 0002-7863, 1520-5126. DOI: 10.1021/ja01520a016.

[343] Olivier Bernard et al. "Self-diffusion in electrolyte solutions using the mean spherical approximation". In: *J. Phys. Chem.* 96.1 (Jan. 1992), pp. 398–403. ISSN: 0022-3654. DOI: 10.1021/j100180a074.

[344] Aziza Chhih et al. "Transport coefficients and apparent charges of concentrated electrolyte solutions – Equations for practical use". In: *Ber. Bunsenges. Phys. Chem.* 98.12 (1994), pp. 1516–1525. ISSN: 0005-9021. DOI: 10.1002/bbpc.19940981204.

[345] Michael McEldrew et al. "Correlated Ion Transport and the Gel Phase in Room Temperature Ionic Liquids". In: *J. Phys. Chem. B* 125.10 (Mar. 2021), pp. 2677–2689. ISSN: 1520-6106, 1520-5207. DOI: 10.1021/acs.jpcb.0c09050.

[346] Yunqi Shao et al. "Role of Viscosity in Deviations from the Nernst–Einstein Relation". In: *J. Phys. Chem. B* 124.23 (June 2020), pp. 4774–4780. ISSN: 1520-6106, 1520-5207. DOI: 10.1021/acs.jpcb.0c02544.

Chapter 6

DYNAMIC CHARGE REGULATION ENHANCES ION MOBILITY IN POLYELECTROLYTE NETWORKS

Weak polyelectrolyte hydrogels are emerging as a versatile platform for ion transport and separation, desalination, and energy applications. However, a predictive understanding of how dynamic charge regulation at the nanoscopic scale influences ionic mobility in these polymer networks remains elusive. In this chapter, using large-scale molecular simulations, we dissect the coupled mechanisms governing small-ion transport in weak polyelectrolyte hydrogels, and reveal how charge density, competitive binding, and dynamic charge regulation jointly control ion mobility. By systematically isolating these effects, we uncover a pronounced non-monotonic dependence of ion self-diffusion on hydrogel pK_a and salt concentration for multivalent ions. Strikingly, allowing the hydrogel backbone to dynamically regulate its charge eliminates this non-monotonicity and leads to dramatic enhancements in ion mobility, with diffusion coefficients increasing by up to an order of magnitude for trivalent ions. We attribute this effect to a protonation-assisted hopping mechanism that continuously remodels the local electrostatic landscape, providing an additional molecular-scale pathway for ion unbinding beyond translational escape and accelerating ion-pair kinetics without affecting the fraction of free ions. Our results demonstrate that dynamic nanoscale charge regulation can decouple ion mobility from equilibrium binding strength, offering a powerful design lever unavailable in fixed-charge materials. Building upon these insights, we propose simple molecular design principles for next-generation ion-conducting hydrogels and suggest new strategies for nanostructured membranes, energy materials, and biologically inspired charge-adaptive soft matter.

This chapter includes work from our previously published preprint: Pierre J. Walker, David Beyer, Christian Holm, and Zhen-Gang Wang. *Ion Transport Enhancement in Charge-Regulating Hydrogels*. 2026. DOI: 10.26434/chemrxiv.15004897/v2

6.1 Introduction

Polyelectrolyte hydrogels—soft solids consisting of chemically or physically crosslinked polyelectrolyte chains—have emerged as a promising class of tunable materials with remarkable physicochemical properties.[347, 348, 349, 4, 235, 350] An important

feature of these charged polymer networks is their exceptional swelling capacity in aqueous solutions, which is reactive to external stimuli, including salt,[351] temperature,[235] and light.[352] This responsiveness gives rise to numerous advanced applications of polyelectrolyte hydrogels, ranging from desalination[350] and electroadhesion[353] to targeted drug delivery[354] and nanomechanics.[355]

Although much of the experimental and theoretical focus has been on hydrogels composed of *strong* polyelectrolytes with a *fixed-charge* backbone, many hydrogels consist of *weak* polyelectrolytes, such as the commonly used poly(acrylic acid). In contrast to strong polyelectrolytes, weak polyelectrolytes contain weakly acidic or basic groups, whose degree of ionization depends on the pH value.[356] Naively, one might expect the behavior of weak polyelectrolytes to be equivalent to that of strong polyelectrolytes with a varying fraction of ionized monomers. However, because the ionization state of these weak monomers is determined by reversible acid-base equilibria, weak polyelectrolytes often dynamically adapt their ionization state in response to various physicochemical factors, including system pH, salt concentration and valency, and even electrostatic interactions with other polyelectrolytes. Such *charge regulation* effects are known to play an important role in numerous systems in soft matter science and biophysics, for example weak polyelectrolyte brushes[357, 358, 359, 360, 361, 362, 363] and complexes,[364, 365, 366] globular[367, 368, 369] and intrinsically disordered[370, 371, 143] proteins, and nanoparticles[372, 373, 374] and colloids.[375, 376] In weak polyelectrolyte hydrogels, charge regulation results in a pH-responsive swelling response,[377] non-trivial interactions with guest molecules[378, 379] and, in special cases, even a first-order swelling transition.[380, 381, 355]

The pH-responsive behavior of charge-regulating polyelectrolyte hydrogels has been studied in detail using experiments,[380, 382] (semi-)analytical theory[383, 384, 381], and coarse-grained simulations. [377, 385, 386, 387] However, virtually all theoretical studies on these systems so far have either focused on static equilibrium properties or large-scale conformational motions.[388, 389] In contrast, a mechanistic understanding regarding the transport of small (multivalent) ions and charged guest molecules through charge-regulating polyelectrolyte networks has not been attained yet, although it is highly relevant for applications ranging from hydrogel-based membranes and filters over targeted drug-delivery to biocondensates. This lack of understanding is unsurprising, since charge regulation is inherently entangled with numerous other factors contributing to transport properties, including the salt

concentration, ion binding, polymer density, and network architecture, all of which complicate the theoretical analysis. For example, while it is known that varying the charge fraction of a hydrogel can affect the transport properties of added salt, the very addition of salt (particularly with a high valency ion) to a charge-regulating hydrogel can shift the ionization equilibrium through favorable electrostatic interactions, changing the ionization fraction of the hydrogel in turn. This coupling between local charge state and the surrounding electrostatic environment echoes the solvent-polarization feedback identified in Chapter 2: just as dielectric response there fed back onto the effective electrostatic interaction, here protonation equilibrium feeds back onto ion mobility. Similarly, ionization equilibria, salt partitioning and hydrogel swelling are all tightly coupled,[377] which in turn influences the transport of small ions.

Despite the complexities described above, developing a molecular-level understanding of ion transport in charge-regulating hydrogels—linking nanoscopic phenomena with macroscopic bulk properties—is of paramount importance for the rational design of hydrogel-based materials across various applications and scientific disciplines. Gaining this understanding purely based on experimental observations is practically infeasible due to the challenges in disentangling the various factors explained above. It is therefore indispensable to leverage theory and computer simulations to understand the various effects influencing ion transport in charge-regulating polymer networks. While analytical approaches typically neglect many details that may be relevant for these complex systems and employ drastic approximations, molecular simulations at the all-atom level are computationally too expensive for studying large, charge-regulating hydrogels. The best compromise between these two extremes are coarse-grained, implicit solvent simulations, which neglect chemical specificity but maintain a particle-based description and fully account for electrostatic correlation effects, chain connectivity, etc. It is for this reason that we leverage coarse-grained molecular dynamics simulations in this publication: by reducing the system complexity to a few key design parameters, it is substantially easier to examine the contribution of isolated effects on macroscopic properties. To achieve this, we adopt a hierarchical strategy starting from a simple model system, adding complexity (salt, charge regulation) step-by-step. As we show below, this approach allows us to obtain simple molecular design principles for next-generation ion-conducting hydrogels. These insights are subsequently leveraged to suggest new strategies for membranes, energy materials, and biologically inspired charge-adaptive soft matter.

6.2 Methods

Model

Following the approach used in previous simulation studies [390, 391, 386, 387, 377], we represent our polyelectrolyte hydrogel as a unit cell of a diamond-like network, as shown in Figure 6.1(a). In this architecture, polymer strands consisting of $N = 60$ beads connect tetravalent crosslinking nodes. Each polymer bead is assumed to be a weak acid (HA), which can dissociate into an anionic bead (A^-) by releasing a free cation (H^+) into solution:

$$HA \rightleftharpoons A^- + H^+. \tag{6.1}$$

This chemical reaction is governed by the equilibrium constant $K_a = \frac{a_{A^-} a_{H^+}}{a_{AH}}$ ($pK_a = -\log_{10} K_a$), where a_i is the activity of species i.

In addition to polymer chains and counterions, a $Z:1$ electrolyte is added to the system at a concentration C_s. The cations X^Z, acting as counterions for the polyelectrolyte network, have valency Z (+1, +2, or +3). The anions X^- are always monovalent.

HA, A^-, H^+, and X^- beads all have the same effective diameter $\sigma = 0.355\,\text{nm}$; in a previous work, this value was shown to accurately reproduce the excess chemical potential of aqueous NaCl solutions [392]. The cations X^Z are half the size of the other beads ($\sigma = 0.1775\,\text{nm}$) to distinguish them from H^+ and to account for the smaller solvation diameter of higher-valency ions [393]. All particles have the same mass $m = 1.0$ in the system of reduced Lennard-Jones units. The solvent is taken to be water at $T = 298.15\,\text{K}$ and is treated implicitly, such that the Bjerrum length is $\lambda_B = 0.71\,\text{nm}$.

Our coarse-grained, implicit-solvent model for polyelectrolyte chains and ions is derived from the model of Kremer, Grest and Stevens.[183, 394] This model represents monomers and ions as spherical, bead-like particles that interact via (1) repulsive steric interactions, (2) electrostatic interactions and (3) FENE bonds. Steric interactions between types of particles are modeled using the Weeks-Chandler-Andersen (WCA) potential.[395] The WCA potential between particle types i and j is given by

$$U^{ij}_{\text{WCA}}(r) = \begin{cases} 4\epsilon\left(\left(\frac{\sigma_i+\sigma_j}{2r}\right)^{12} - \left(\frac{\sigma_i+\sigma_j}{2r}\right)^{6}\right) + \epsilon & \text{if } r \le 2^{\frac{1}{6}}\frac{\sigma_i+\sigma_j}{2} \\ 0 & \text{if } r > 2^{\frac{1}{6}}\frac{\sigma_i+\sigma_j}{2}, \end{cases} \tag{6.2}$$

where $\epsilon = k_\mathrm{B}T$, with $T = 298.15\,\mathrm{K}$, is the energy scale of the interaction. σ_i is a measure for the bead diameter of particle type i which we set to $\sigma = 0.355\,\mathrm{nm}$ for all species except the cations X^+, which have a smaller diameter of $\sigma_{\mathrm{X}^+} = \sigma/2 = 0.1775\,\mathrm{nm}$.

In addition to steric interactions, all charged particles also interact through the Coulomb potential[23]

$$U^{ij}_{\mathrm{Coulomb}}(r) = \frac{\lambda_\mathrm{B} k_\mathrm{B} T z_i z_j}{r}, \tag{6.3}$$

where z_i is the charge number of particle type i. Here, the solvent of the system is taken to be water at $T = 298.15\,\mathrm{K}$ and is treated implicitly such that the Bjerrum length of the system is $\lambda_\mathrm{B} = 0.71\,\mathrm{nm}$. The Coulomb interactions in periodic boundary conditions are summed up using the PPPM method with a relative error of 10^{-4}.[396, 397, 398]

To connect monomers into polymer chains, we use FENE bonds,[183] which are described by the interaction potential

$$U_{\mathrm{FENE}}(r) = \begin{cases} -\frac{k\Delta r_{\max}^2}{2} \ln\left(1 - \left(\frac{r}{\Delta r_{\max}}\right)^2\right) & \text{if } r \leq \Delta r_{\max} \\ \infty & \text{if } r > \Delta r_{\max}. \end{cases} \tag{6.4}$$

Throughout this chapter, we set the spring constant to $k = 30\,k_\mathrm{B}T/\sigma^2$ and use a value of $\Delta r_{\max} = 1.5\,\sigma$ for the maximum bond extension.

To characterize the effects of charge regulation on small-ion transport, we vary three parameters: the valency of the added salt cation ($Z = +1, +2, +3$), the salt concentration ($C_\mathrm{s} \in \{0.001, 0.05\}$ M), and the equilibrium constant of the acid–base reaction ($\mathrm{p}K_\mathrm{a} \in \{-3, 3\}$). As most hydrogels are primarily comprised of water, we assume a high swelling ratio such that the polymer volume fraction is low ($\phi \approx 0.05$, corresponding to $C_\mathrm{m} \approx 0.16$ M). This monomer concentration lies in the lower regime of typical hydrogels and was chosen to minimize screening contributions from ions originating within the network itself, thereby amplifying changes induced by the addition of multivalent salts, which are the focus of this chapter.

In general, the equilibrium volume of a charge-regulating polyelectrolyte hydrogel is determined by a complex balance of acid–base equilibria, ion partitioning, electrostatic interactions, and network elasticity [377]. As we will show in the following, even at fixed volume, ion transport in charge-regulating hydrogels involves a convolution of multiple factors that are difficult to isolate. Allowing the network to swell

or contract would only further complicate this analysis. Therefore, in the present chapter, we fix the monomer concentration across all simulations in order to focus specifically on transport mechanisms. An extension of this work to account for gel swelling and volume changes represents a natural direction for future research.

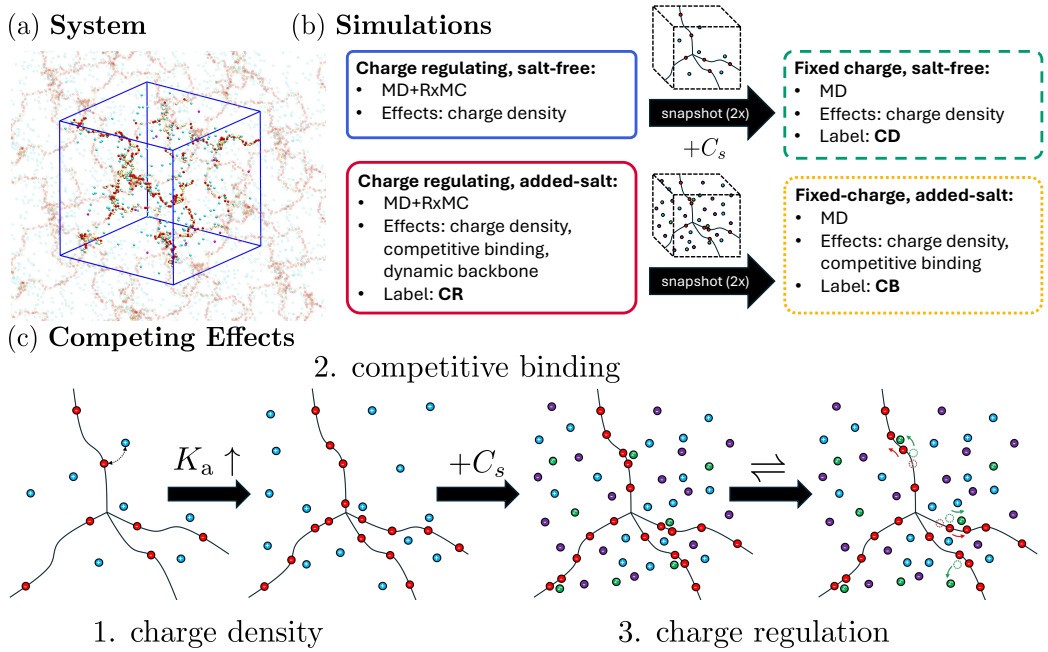


Figure 6.1: Overview of the methodology used in this chapter. (a) Simulated hydrogel architecture using a diamond-like unit cell. (b) Summary of the types of simulations performed in this chapter, the approach used and their labels. (c) Different competing effects investigated in this chapter: 1. variation in hydrogel charge density, 2. added-salt induced competitive binding and 3. dynamical charge regulation of the hydrogel backbone.

Simulation Methods

In this chapter, we identify three key effects that influence ion transport in charge-regulating hydrogels (cf. Figure 6.1(c)): (1) the influence of hydrogel charge density on ion transport, (2) competitive binding of cations to the hydrogel backbone, and (3) the role of *dynamical* charge regulation. Performing simulations that account for all three effects simultaneously would make it difficult to disentangle their individual contributions. We therefore perform three types of simulation that progressively add complexity, allowing the role of each effect to be isolated. The setup of these different types of simulation is summarized in Figure 6.1(b) and will be explained in detail in the following paragraphs.

To simulate the molecular motions of our system as well as the acid-base reactions,

we use a hybrid scheme combining Molecular Dynamics (MD) with Monte Carlo (MC) . At a fixed particle number, the positions of all particles (small ions and monomers) are propagated using Langevin dynamics with Gaussian white noise. In the simulations, we solve the Langevin equations for all particle positions numerically using the Velocity-Verlet integrator with a time step of $\Delta t = 0.01\,\tau$, where τ is the Lennard-Jones time scale. We set the bare friction coefficient to $\gamma = 1.0\,\tau^{-1}$, corresponding to a diffusion coefficient of $D = 1.0\,\sigma^2\tau^{-1}$ for non-interacting beads. While Langevin dynamics capture the effects of hydrodynamics to some extent, we have chosen not to explicitly account for the effects of long-range hydrodynamic interactions using methods such as DPD[399] or Lattice-Boltzmann[400] in order to fully isolate the effects of charge regulation. The simulations are conducted using version 4.2.4 of the open source simulation suite ESPResSo[401, 402].

The monomers of our hydrogel are weakly acidic groups participating in the acid-base reaction

$$\mathrm{HA} \rightleftharpoons \mathrm{A}^- + \mathrm{H}^+, \tag{6.5}$$

which is governed by the equilibrium constant $K_\mathrm{a} = 10^{-\mathrm{p}K_\mathrm{a}}$. To model this reaction, we use the Reaction Ensemble Monte Carlo method[403, 404] (RxMC). In this method, elementary reaction steps are represented by Monte Carlo moves that are probabilistically accepted. A single MC move proceeds as follows. First, the *extent of reaction* ξ is randomly selected ($\xi = +1$ for the forward reaction in Equation 6.5, $\xi = -1$ for the reverse reaction in Equation 6.5). Next reactant particles are randomly selected, i.e. a monomer HA if $\xi = +1$ or a monomer A^- and counterion H^+ if $\xi = -1$. Then, a new state is proposed by changing the identity of the selected monomer according to Equation 6.5 and either deleting the selected counterion H^+ (if $\xi = -1$) or inserting an additional counterion H^+ at a random position into the simulation box (if $\xi = +1$). Subsequently, the proposed new state (n) is accepted with a probability given by

$$P_\mathrm{n,o}^\mathrm{RxMC} = \min\left\{1, \frac{N_\mathrm{HA}^\mathrm{o}!N_\mathrm{A^-}^\mathrm{o}!N_\mathrm{H^+}^\mathrm{o}!(K_\mathrm{A}n^\ominus V)^\xi}{\left(N_\mathrm{HA}^\mathrm{o}-\xi\right)!\left(N_\mathrm{A^-}^\mathrm{o}+\xi\right)!\left(N_\mathrm{H^+}^\mathrm{o}+\xi\right)!}\exp\left(-\beta\Delta\mathcal{U}_\mathrm{n,o}\right)\right\}. \tag{6.6}$$

In this equation, N_i^o denotes the particle number of species i in the old state (o), $n^\ominus$ is the number density corresponding to the reference concentration $c^\ominus = 1\,\mathrm{M}$, V is the volume of the simulation box and $\Delta\mathcal{U}_\mathrm{n,o}$ is the change in potential energy between the old state and the proposed new state. If the proposed new state is rejected, the old state is retained.

In the simulations, the MD integration steps are combined with MC moves by performing alternating cycles consisting of 10^3 MD and 10^3 MC steps respectively. To test the influence of the ratio of MD and MC steps, we also perform simulations where the number of MC steps per cycle is either reduced or enhanced by a factor of 10.

Salt-free simulations: We first perform simulations of the hydrogel in the absence of added salt. To emulate changes in the hydrogel charge density with decreasing pK_a (Figure 6.1(c)), we combine MD with the Reaction Ensemble Monte Carlo method[403, 404] (RxMC). The RxMC method is one of several Monte Carlo schemes that allow simulating acid-base equilibria in weak polyelectrolytes.[405, 403, 404, 406, 356] In this chapter, we choose RxMC rather than the Grand-Reaction method [356], as the latter would additionally capture effects such as gel swelling [377] and ion partitioning [392], which are intentionally excluded here to simplify the physical picture.

To reach the desired polymer volume fraction, we use a simulation protocol similar to previous works:[377, 385] after initializing the gel network in a fully extended state, the simulation box is compressed isotropically at a rate of $0.1\,\sigma/\tau$ until the target monomer concentration is reached. The system is then equilibrated for 10^5 MD steps, during which 10^3 RxMC moves are attempted every 10^3 MD steps. This procedure allows the network to relax and the backbone charges to reach equilibrium. Subsequent production runs are performed for 2×10^7 MD steps, maintaining the same ratio of the MD steps to the MC moves. This ratio is consistent with previous simulations studying the effects of dynamical charge regulation [355] and is intended to emulate the rapid kinetics of typical acid–base reactions [407, 408, 409], assisted by Grotthuss proton hopping [410].

Although the salt-free simulations do not provide information on the transport of multivalent ions, they characterize the ionization equilibrium and charge distribution within the gel network. Because the simulations are performed in the absence of multivalent salt, they allow the influence of hydrogel charge density to be examined independently of competitive binding. To study ion dynamics in a hydrogel with a given charge density, we randomly select equilibrated charge configurations from the RxMC trajectories (including monovalent counterions), freeze the backbone charges, and add multivalent salt at varying concentrations. These systems are then simulated for an additional 2×10^7 MD steps without RxMC. In this way, we isolate

the effect of hydrogel charge density on ion transport. The described procedure is repeated for two independent charge realizations in order to average over charge fluctuations of the gel network. We refer to these quenched-charge simulations as charge-density (CD) simulations, after the effect being probed in these simulations (see Figure 6.1(b)).

Added salt simulations: Having isolated the effect of charge density, we next examine the combined influence of competitive binding and charge regulation. These effects are captured in simulations performed with MD+RxMC in the presence of added salt. We therefore initialize the gel network with multivalent salt and repeat the protocol described above: isotropic compression at a rate of $0.1\,\sigma/\tau$, equilibration for 10^5 MD steps, and production runs consisting of 2×10^7 MD steps, with 10^3 RxMC moves attempted every 10^3 MD steps. These simulations are referred to as charge-regulating (CR) simulations. From the production trajectories, we extract self-diffusion coefficients of the added salt ions; the validity of this procedure is discussed later. We also examine the effect of varying the ratio of MD steps to MC moves in the Discussion and Supplementary Information.

In the CR simulations, the effects of charge regulation and competitive binding are intrinsically coupled. To separate these contributions, we again select two equilibrated gel charge configurations from the CR trajectories, freeze the backbone charges, and perform additional simulations for 2×10^7 MD steps without RxMC. Because the mean degree of ionization and charge distribution are preserved, these simulations remove dynamical charge regulation while retaining competitive binding. These systems are referred to as competitive-binding (CB) simulations (see Figure 6.1(b)).

Analysis

All analysis in this chapter is performed using the programs MDAnalysis [187] and MDCraft [14].

Self-diffusion coefficients: The primary quantity of interest is the self-diffusion coefficient of the added ions, defined as

$$D_i = \lim_{t\to\infty} \frac{1}{6tN_i} \sum_{j=1}^{N_i} \langle |\mathbf{R}_j(t) - \mathbf{R}_j(0)|^2 \rangle, \tag{6.7}$$

where t is time, N_i is the number of particles of species i, and $\mathbf{R}_j(t)$ is the position of particle j at time t.

For simulations that include Monte Carlo steps (CR simulations), the validity of measured dynamical properties such as self-diffusion coefficients warrants careful consideration. In this chapter, transport properties are extracted exclusively for species that do not participate directly in Monte Carlo moves, such that their microscopic motion is governed solely by molecular dynamics. Consequently, we do not report the total ionic conductivity of the system, which would additionally require tracking the dynamics of the charged polymer backbone and protons, both of which are involved in RxMC moves.

Because particle motion is correlated, unphysical displacements associated with RxMC moves could in principle indirectly affect the dynamics of all species. Under the dilute conditions considered here, however, the influence of low-valency particles undergoing RxMC moves is expected to enter primarily through their collective contribution to electrostatic screening. When averaged over long trajectories, their effect is therefore anticipated to be comparable to that of physically diffusing particles. To validate this assumption, we explicitly examined the effect of varying the ratio of RxMC moves to MD steps over two orders of magnitude. These tests, reported in the Supplementary Information, indicate that while small deviations arise in low-salt, low-pK_a regimes, for most conditions the measured dynamical properties are not significantly affected by this ratio.

Ion pairing: To assess how charge regulation influences the transport of multivalent ions, we quantify the fraction of cations not bound to the anionic sites on the hydrogel backbone. An ion is defined as unbound when no anions are present within a distance 1.5σ of the cation center (corresponding approximately to the location of the first minimum in the radial distribution function). Because the fraction of bound cations is an equilibrium quantity, its averaged value is independent of the ratio of MD to RxMC steps; a small ensemble-dependent finite-size effect may in principle exist, but is not expected to be significant here.

Although equilibrium properties are expected to be identical between CR and CB simulations up to finite-size effects, their relaxation dynamics may differ. Of particular relevance is the ion-pair relaxation time [411, 310, 78], which has been shown to correlate strongly with ionic self-diffusion. Following previous work [310], we define the ion-pair relaxation time τ_{IP} as the time at which the survival probability $P(t)$ decays to $1/e$. This quantity is obtained from the autocorrelation function of

$h_{ij}(t)$:

$$P(t) = \langle h_{ij}(t) h_{ij}(0) \rangle_{ij} - \langle h_{ij}(t) \rangle_{ij}^2 \,, \tag{6.8}$$

where $\langle \cdot \rangle_{ij}$ denotes averages over all added cations and anionic hydrogel beads, and:

$$h_{ij}(t) = \begin{cases} 1 \,, & \|\mathbf{R}_i(t) - \mathbf{R}_j(t)\| \leq 1.5\,\sigma_{ij} \,, \\ 0 \,, & \|\mathbf{R}_i(t) - \mathbf{R}_j(t)\| > 1.5\,\sigma_{ij} \,. \end{cases} \tag{6.9}$$

Because the ion-pair relaxation time is a dynamical property, its validity in the presence of Monte Carlo steps has to be justified using arguments analogous to those applied to the self-diffusion coefficients. Across simulations in which the ratio of RxMC moves to MD steps was varied by two orders of magnitude, τ_{IP} was found to change at most by a factor of two.

Charge profile autocorrelation function: The addition of high-valency ions through competitive binding is expected to modify the charge distribution along the hydrogel backbone. To quantify these changes, we define the autocorrelation function of the charge profile [412], averaged along the polymer strands of the hydrogel (disregarding crosslinkers):

$$\rho_q(\Delta\ell) = \langle q_\ell q_{\ell+\Delta\ell} \rangle_{\mathrm{chain}} - \langle q \rangle_{\mathrm{chain}}^2 . \tag{6.10}$$

Here, q_ℓ is the (dimensionless) charge of bead ℓ and $\langle \cdot \rangle_{\mathrm{chain}}$ denotes averages along the polymer strands. The quantity $\langle q \rangle_{\mathrm{chain}}$ is equivalent to the degree of ionization α. $\rho_q(\Delta\ell)$ is positive when beads separated by $\Delta\ell$ along the chain are, on average, more highly charged than the bulk average, and negative in the opposite case.

6.3 Results

In total, more than 700 distinct systems were examined in the course of this chapter. Presenting results for every case in the main text would be impractical; all data are therefore provided in the Appendix, while the results shown here are selected to illustrate and elucidate the physical mechanisms of interest. The conclusions drawn are supported not only by the specific examples discussed below, but by the full ensemble of systems considered.

The remainder of this section is organized around systems of increasing complexity, designed to isolate the individual effects highlighted in Figure 6.1(c).

Charge Density

From ideal-solution theory it can be derived that increasing the pK_a of the deprotonation reaction reduces the equilibrium degree of ionization α of the hydrogel according to

$$10^{-\mathrm{p}K_a} = \left(\frac{C_m}{C_0}\right)\frac{\alpha^2}{1-\alpha}. \tag{6.11}$$

Here, $C_0 = 1\,\mathrm{M}$ is the reference concentration and C_m is the concentration of ionizable monomers. In polymer networks, connectivity between neighboring beads renders adjacent ionized beads energetically unfavorable due to strong electrostatic repulsion. As shown in Figure 6.2(a) for charge-regulating hydrogels in the absence of salt, this repulsion suppresses ionization of the hydrogel backbone and gives rise to an apparent shift in the pK_a. This well-known phenomenon in weak polyelectrolytes has been observed in a large number of studies and is termed the "polyelectrolyte effect." [377, 142, 413]

To capture realistic charge states of hydrogels at a given pK_a while isolating transport mechanisms, we first perform calculations by extracting equilibrated charge configurations from the charge-density simulations and quenching the backbone charges. Multivalent salts of varying concentration are then introduced, producing systems in which the hydrogel charge profile is fixed while the particle positions of monomers and mobile ions evolve dynamically. This process is illustrated visually in Figure 6.1(b). These simulations allow the effect of the hydrogel charge density (labeled as CD) on cation transport to be examined independently of competitive binding and dynamical charge regulation.

The resulting self-diffusion coefficients as functions of cation valency, salt concentration, and pK_a are shown in Figure 6.2(b). Overall, the self-diffusion coefficient decreases with increasing cation valency and increasing degree of ionization (decreasing pK_a), while higher salt concentrations partially restore mobility. For high-valency cations at low salt and low pK_a, a pronounced minimum in the diffusion coefficient is visible. In general, the effects of varying charge density are not surprising: if we consider small ions bound to the polymer backbone as practically motionless, only the fraction of unbound ions contributes to the self-diffusion coefficients. Increasing the degree of ionization (lowering the pK_a) provides more sites to which the added cations can bind, thus reducing the self-diffusion coefficient. A similar effect occurs when increasing the ion valency, because with stronger electrostatic interactions the fraction of bound cations will increase, leading to a decreasing self-diffusion coefficient. Adding more salt (and thus cations) simply

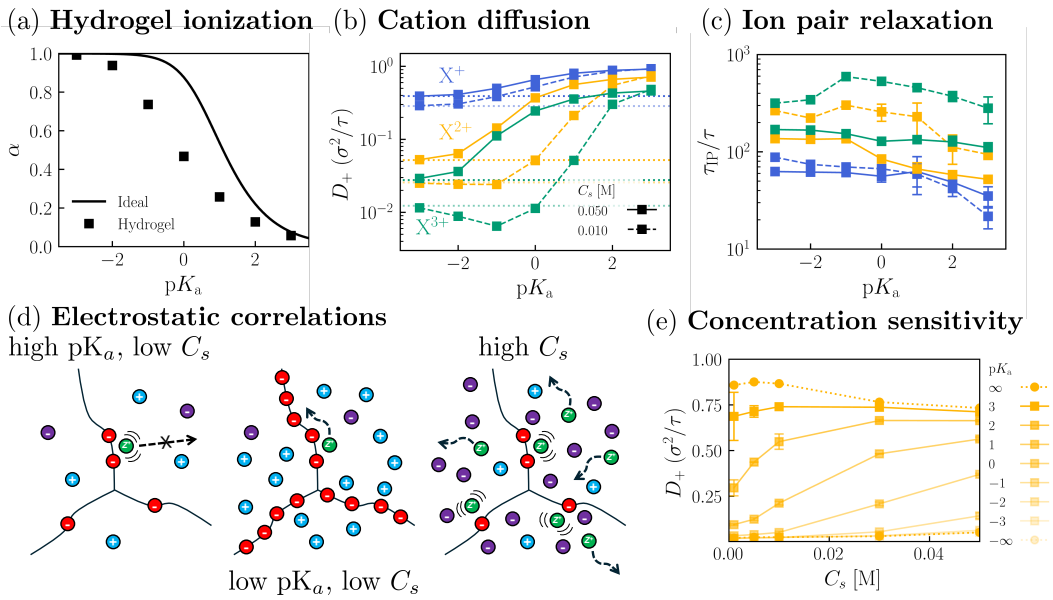


Figure 6.2: Effect of hydrogel charge density on ion transport. (a) Variation in the hydrogel degree of ionization with varying pK_a in the absence of salt. Predictions from the ideal limit have been included. (b) Cation self-diffusion coefficient obtained using the CD simulations with varying pK_a, cation valency and salt concentration. Colors denote valency (blue: monovalent, yellow: divalent, green: trivalent) and lines denote concentration (solid: 0.05 M, dashed: 0.01 M). Dotted lines denote the limited diffusion coefficient for a fully ionized hydrogels. (c) Ion pair relaxation times between the added cation and hydrogel backbone for the same conditions as (b), using the same colors and lines. (d) Visual illustration of the effects of electrostatic correlations on the binding between the cation and the hydrogel backbone. (e) Variations in the salt-concentration dependency of D_+ with varying pK_a for a divalent cation.

increases the amount of free ions, resulting in a larger self-diffusion coefficient. At sufficiently high ion concentrations, where electrostatic correlations and packing effects dominate, the self-diffusion coefficient would be expected to eventually decrease again.

Generally speaking, we find a good correlation between the fraction of free cations and the self-diffusion coefficient (see Figure 6.13). However, for high valency cations, we observe a minimum in the self-diffusion coefficient at low salt concentrations and low pK_a, which is not present in the unbound fraction. To explain this unexpected result, consider that in these regimes the fraction of free ions is extremely small. Therefore, the ions are bound most of the time and their effective diffusion coefficient is primarily governed by the rate of unbinding from the backbone rather than the diffusion coefficient of a free ion. Thus, the self-diffusion coefficient is

determined by the lifetime of ion–polymer associations and should (approximately) be inversely related to the ion-pair relaxation time [411, 78]. This relationship is borne out in Figure 6.2(c): divalent and trivalent systems exhibit relaxation times that decrease strongly with increasing salt concentration, consistent with enhanced electrostatic screening that weakens ion–polymer correlations and facilitates transport. At salt concentrations below 0.01 M, the ion-pair relaxation time for both multivalent ions displays a pronounced maximum at intermediate pK_a, coinciding with the minimum in the self-diffusion coefficient. We attribute this non-monotonic behavior to the change in binding environment for the added cations at low salt concentrations: as shown in Figure 6.2(d), at high pK_a and low salt concentrations, the cation is strongly bound to the backbone, with its motion being coupled to the much slower hydrogel backbone. With decreasing pK_a, more charged sites become available, such that it is favorable for the cation to translate along the backbone, increasing its diffusion coefficient. Distributing the charge uniformly along the hydrogel backbone eliminates the minima by providing easier mobility along the backbone (see Figure 6.14). At very high salt concentrations, when the amount of cations exceeds the amount of available sites at all pK_a, this minimum no longer appears as there are always free cations even when the hydrogel is fully charged. Although previous studies have explored the influence of charge fraction on ionic transport in hydrogels [414, 415, 235, 351], to our knowledge such pronounced non-monotonic behavior has not been reported.

Ion concentration provides an additional means of tuning transport, as shown in Figure 6.2(e). We include the limiting cases of neutral ($pK_a \to \infty$) and fully charged ($pK_a \to -\infty$) hydrogels. In the neutral limit, self-diffusion decreases monotonically with concentration, as expected from crowding and electrostatic correlations in bulk electrolytes. Once the hydrogel carries charge, however, electrostatic binding strongly suppresses mobility at low salt concentrations. Increasing salt initially enhances diffusion by saturating polymer binding sites; at still higher concentrations, diffusion is expected to decrease again as ion–ion correlations and packing effects become dominant.

At intermediate pK_a, where the hydrogel is only partially ionized, particularly for divalent and trivalent ions, the concentration dependence becomes highly sensitive to salt concentration. The strongest sensitivity to salt concentration occurs near $pK_a \approx 0$, while either increasing or decreasing pK_a diminishes this effect. This regime coincides with the inflection points in the pK_a-dependent trends of Figure 6.2(b),

corresponding to the maximum of the "charge regulation capacitance,"[367] where the system is particularly sensitive to changes in pK_a. Previous studies such as Yin *et al.* [351] would likely have observed similar features had a broader range of charge fractions been examined.

Taken together, the results presented in this section underscore the delicate interplay between hydrogel charge density and salt content in controlling ion transport. As we will see in the following sections, the inclusion of additional physical effects causes these two seemingly independent parameters to become coupled.

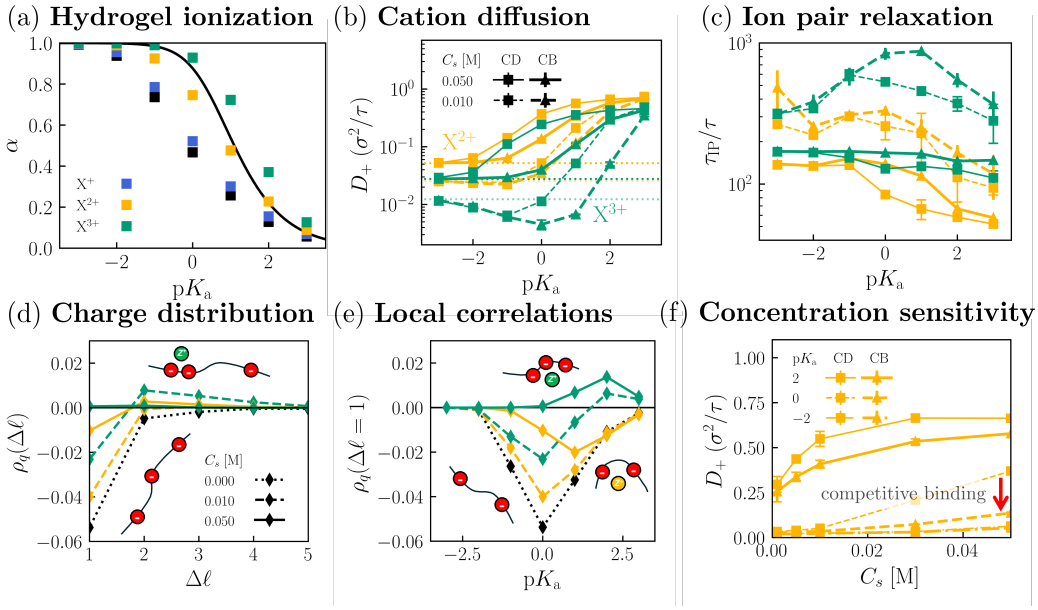


Figure 6.3: Effect of competitive binding on ion transport. (a) Variation in the hydrogel degree of ionization with varying pK_a in the presence of added salt. Predictions from the ideal limit have been included. (b) Cation self-diffusion coefficient obtained using the CD (lighter) and CB (darker) simulations with varying pK_a, cation valency and salt concentration. Colors denote valency (yellow: divalent, green: trivalent) and lines denote concentration (solid: 0.05 M, dashed: 0.01 M). Dotted lines denote the diffusion coefficient for fully ionized hydrogels. (c) Ion pair relaxation times between the added cation and hydrogel backbone for the same conditions as (b), using the same formatting scheme. (d) Charge profile autocorrelation with varying monomer separation $\Delta\ell$ using the same scheme as (b) for p$K_a = -1$ (e) Charge profile autocorrelation evaluated at a monomer separation $\Delta\ell = 1$ using the same scheme as (b) for p$K_a = -1$ (f) Variations in the salt-concentration dependency of D_+ with varying pK_a for a divalent cation between CD and CB simulations.

Competitive Binding

The results discussed in the previous section are directly relevant to hydrogels synthesized from mixtures of fixed-charged and uncharged monomers. Examples of such fixed-charged groups include sulfonates, quaternary ammonium groups, and certain ionic-liquid-based monomers [351], which all have very small pK_a. However, many commonly used monomers like carboxylic acids and phosphates exhibit more moderate pK_a values [235, 4]. In such systems, the deprotonation equilibrium can be strongly influenced by changes in solution conditions, for example by the addition of multivalent salts [356]. As shown in Figure 6.3(a), added salt shifts the equilibrium toward the deprotonated state due to favorable electrostatic interactions between cations and the polymer backbone, resulting in increased ionization fractions. While monovalent salts induce only minor changes, divalent and especially trivalent ions drive substantial shifts, with the latter pushing the degree of ionization beyond the ideal-solution limit at high concentrations, effectively reversing the polyelectrolyte effect.

To isolate the consequences of this salt-induced shift in ionization—without introducing dynamical charge regulation—we sample equilibrated charge profiles from charge-regulating simulations in the presence of added salt, quench the backbone charges, and perform additional competitive-binding (CB) simulations. This process is illustrated in Figure 6.1(b). Because monovalent salts produce negligible changes in the ionization state, they do not lead to appreciable differences relative to the CD results discussed earlier. Accordingly, the remainder of this section focuses on divalent and trivalent ions.

The resulting self-diffusion coefficients are shown in Figure 6.3(b). Qualitatively, the dependence on pK_a is identical to that observed in the CD simulations, reflecting the same competition between electrostatic binding and screening. There are, however, two quantitative differences. First, the inflection points in the self-diffusion curves shift between the two cases. This behavior mirrors the corresponding changes in ionization fraction shown in Figure 6.3(a) and in the fraction of unbound ions reported in Figure 6.9, becoming more pronounced at higher salt concentrations, consistent with the stronger forward shift of the deprotonation equilibrium. A second, more unexpected difference is the appearance of deeper minima in the self-diffusion coefficient at low salt concentrations. Because the fraction of unbound ions is nearly identical between the CD and CB simulations (see Figure 6.9), one might anticipate only a horizontal shift in the diffusion curves with pK_a. The

additional suppression of mobility therefore points to a structural reorganization of the backbone charge profile that enhances the ion-pair lifetimes, suppressing cation diffusion. This interpretation is supported by the ion-pair relaxation times shown in Figure 6.3(c), which exhibit correspondingly larger maxima at low salt concentrations. To probe the origin of this effect, we examine the correlation function of the charge profile along the polymer backbone (Eq. 6.10).

Representative results are shown in Figure 6.3(d). In the absence of salt, the nearest-neighbor value of ρ_q is negative. This indicates that if a bead i is charged, its immediate neighbors preferentially remain neutral in order to minimize electrostatic repulsion, a direct manifestation of the polyelectrolyte effect. Upon the addition of multivalent salt, binding of the cations to the backbone locally reduces the effective negative charge density, making it more favorable for neighboring beads to deprotonate and thus increasing ρ_q at short separations. Notably, the largest increase occurs for next-nearest neighbors ($\Delta\ell = 2$). Such an alternating ionization pattern allows beads i and $i+2$ to both carry charge while avoiding nearest-neighbor repulsion with bead $i+1$. Furthermore, this pattern enables both sites to be bridged by a single multivalent cation[416, 417]. The described phenomenon becomes clearer when examining $\rho_q(\Delta\ell = 1)$ as a function of valency and salt concentration in Figure 6.3(e). Increasing salt concentration and cation valency progressively raises $\rho_q(\Delta\ell = 1)$ from its salt-free value, ultimately rendering it positive for trivalent ions at $C_s = 0.05\,\mathrm{M}$. These results demonstrate that multivalent salts not only shift the overall degree of ionization, but also reorganize the spatial pattern of charges along the polymer backbone to maximize favorable ion–polymer interactions. The resulting binding environment makes it harder for the cations to move along the backbone, increasing ion-pair lifetimes and consequently further suppresses cation mobility relative to the CD case.

A practical consequence of salt-induced shifts in the deprotonation equilibrium is their impact on the concentration-dependence of ion transport. As discussed earlier, this effect is most pronounced at high salt concentrations, where forward shifts in ionization reduce the self-diffusion coefficient. Compared to systems with quenched charge profiles, this leads to a transport behavior that is more robust with respect to changes in salt concentration, as shown in Figure 6.3(f). While such behavior may be unfavorable for applications requiring highly responsive conductivity, it underscores the effect of charge sequence in tuning both thermodynamic and transport properties: even for a fixed average charge fraction, the local chemical environment can still be

engineered to balance ion solubility and diffusion coefficient.

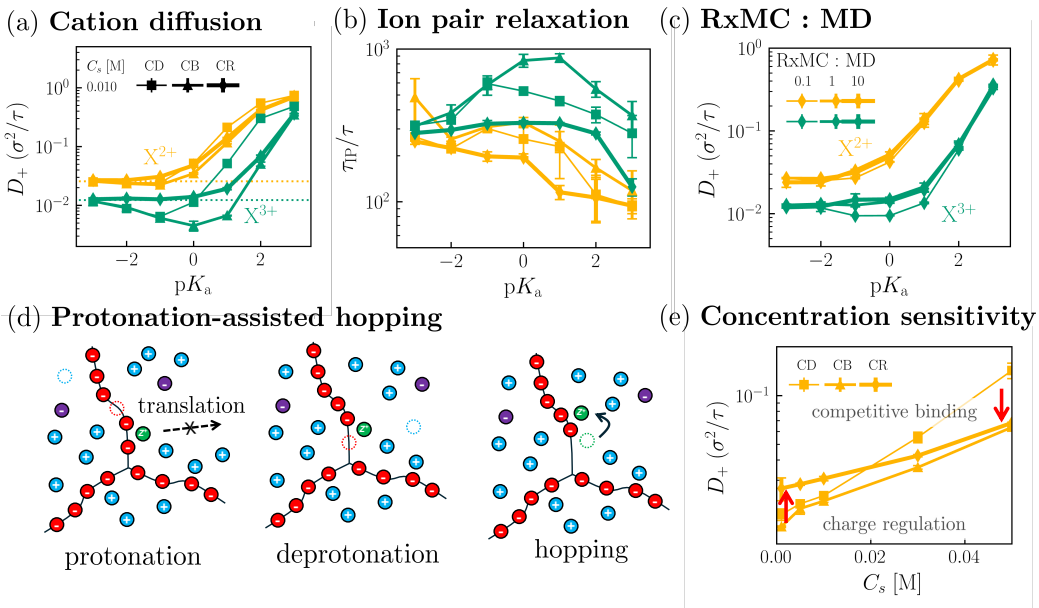


Figure 6.4: Effect of dynamical charge regulation on ion transport. (a) Cation self-diffusion coefficient obtained using the CR (light), CB (dark) and CD simulations with varying pK_a, cation valency and salt concentration. Colors denote valency (blue: monovalent, yellow: divalent, green: trivalent). Dotted lines denote the limited diffusion coefficient for a fully ionized hydrogels. (b) Ion pair relaxation times between the added cation and hydrogel backbone for the same conditions as (b), using the same colors. (c) Effect of varying the ratio of MC moves to MD steps on D_+ obtained from CR simulations. (d) Visual illustration of the protonation-assisted hopping mechanism to enhance ion transport. (e) Variations in the salt-concentration dependency of D_+ with varying pK_a for a divalent cation between the three simulation types.

Dynamical Charge Regulation

While charge regulation shifts the deprotonation equilibrium and induces structural changes in the hydrogel, allowing backbone sites to dynamically regulate their charge state during the simulation is expected to further influence cation transport. The validity of extracting dynamical properties from simulations involving both RxMC moves and MD steps is addressed in Section 6.2. The results of charge-regulating (CR) simulations are shown in Figure 6.4(a) and compared with those of the charge-density (CD) and competitive-binding (CB) cases. We focus on a single salt concentration (0.01 M), both for clarity and because these effects are most pronounced at low concentrations where the fraction of unbound ions is small. Across all conditions examined, CR simulations consistently yield higher self-

diffusion coefficients than CB systems with the same mean ionization fraction. At low pK_a, the mobility of the cation can even exceed that observed in CD simulations with a lower charge density. The magnitude of this enhancement depends strongly on cation valency: divalent ions display a nearly two-fold increase, whereas trivalent ions exhibit an order-of-magnitude speed-up. This behavior is striking, given that CR simulations possess fractions of unbound ions that are comparable to those of the corresponding CB and CD systems. Moreover, for both valencies, the non-monotonic minima observed previously in the self-diffusion coefficients disappear, demonstrating that dynamical charge regulation can overcome both electrostatic binding and the more favorable binding environments created by salt-induced charge reorganization.

The origin of the observed enhancement in diffusion can again be traced to the ion-pair relaxation times, shown in Figure 6.4(b), which are systematically shorter in CR simulations than in their CB counterparts. As illustrated in Figure 6.4(d), in CR systems, ion pairs can dissociate through two distinct mechanisms. The first mechanism is translational escape, whereby an ion diffuses away from the polymer backbone. As discussed earlier, this pathway strongly depends on the cation valency and the local binding environment. The second mechanism is unique to systems with dynamical charge regulation: the backbone site coordinating the ion may become protonated during an RxMC move. In general, the probability of such an event is governed by the pK_a value and the strength of the ion–polymer electrostatic interaction. Although protonation of a site is suppressed when a multivalent ion is bound to it, when protonation does occur, it is expected to be faster than translational escape. This additional pathway therefore shortens the ion-pair lifetime and increases the self-diffusion coefficient. Because binding is reversible, the equilibrium between bound and free ions satisfies

$$K_{\text{bind}} = \frac{1 - f_{\text{free}}}{f_{\text{free}}} \propto \frac{\tau_{\text{IP}}}{\tau_{\text{free}}}, \tag{6.12}$$

where f_{free} is the fraction of unbound cations and τ_{free} denotes the lifetime of a free ion. This expression assumes mass-action kinetics and therefore neglects higher-order ion–ion correlations. Although τ_{free} is difficult to extract directly because free states are typically short-lived, f_{free} is identical in the CR and CB simulations. Equation 6.12 therefore implies that the reduced ion-pair relaxation times in CR systems must be accompanied by correspondingly shorter free-state lifetimes.

In CR simulations, this concomitant shortening of both τ_{IP} and τ_{free} can be attributed to the constraints imposed by protonation moves: for a charged site to protonate with

appreciable probability, a nearby monomer must be charged and unoccupied. Once protonation occurs, a multivalent cation can rapidly migrate to this neighboring site and rebind. This correlated, protonation-assisted hopping process circumvents the otherwise large energetic penalty associated with protonating a site directly coordinating a multivalent ion, thereby accelerating both binding and unbinding kinetics and enabling faster ion motion. The described mechanism is most effective at low pK_a, where the binding of cations is substantial, yet a sufficient number of charged sites remain available. This behavior is almost similar to the hydrogel being uniformly charged (on average), shown in Figure 6.14. It is also loosely analogous to Grotthuss proton hopping in water[410, 351].

The rate of protonation events is controlled in part by the ratio of RxMC moves to MD steps. One would therefore expect that, in the limit of very infrequent RxMC moves, CR simulations should approach CB behavior. To test this expectation, we varied this ratio by two orders of magnitude (see Figure 6.4(c) and Figure 6.15). With increasing RxMC frequency, the ion-pair relaxation time decreases while the self-diffusion coefficient increases; however, these changes are far smaller than would be anticipated from the magnitude of the rate variation itself. This observation indicates that the protonation-assisted hopping mechanism is not strongly limited by the intrinsic protonation rate.

As noted earlier, dynamical charge regulation enhances cation mobility primarily at low salt concentrations, whereas competitive binding suppresses transport at higher concentrations. The combined effect is therefore a reduced sensitivity of the self-diffusion coefficient to salt concentration, as shown in Figure 6.4(e). This impact is most pronounced near the pK_a values at which the minima previously occurred: for $pK_a \leq 0$, the self-diffusion coefficient no longer increases monotonically with concentration and even exhibits weak non-monotonicity for trivalent ions at low salt concentrations.

6.4 Conclusion and Outlook

In this chapter, we have deconstructed the physical mechanisms that govern ion transport in charge-regulating hydrogels. At a fundamental level, the self-diffusion coefficient of small ions is determined by a competition between three factors: (1) electrostatic binding, which impedes ion motion; (2) electrostatic screening, which facilitates transport; and (3) charge regulation itself, which can either suppress or enhance mobility depending on conditions. These effects are strongly coupled,

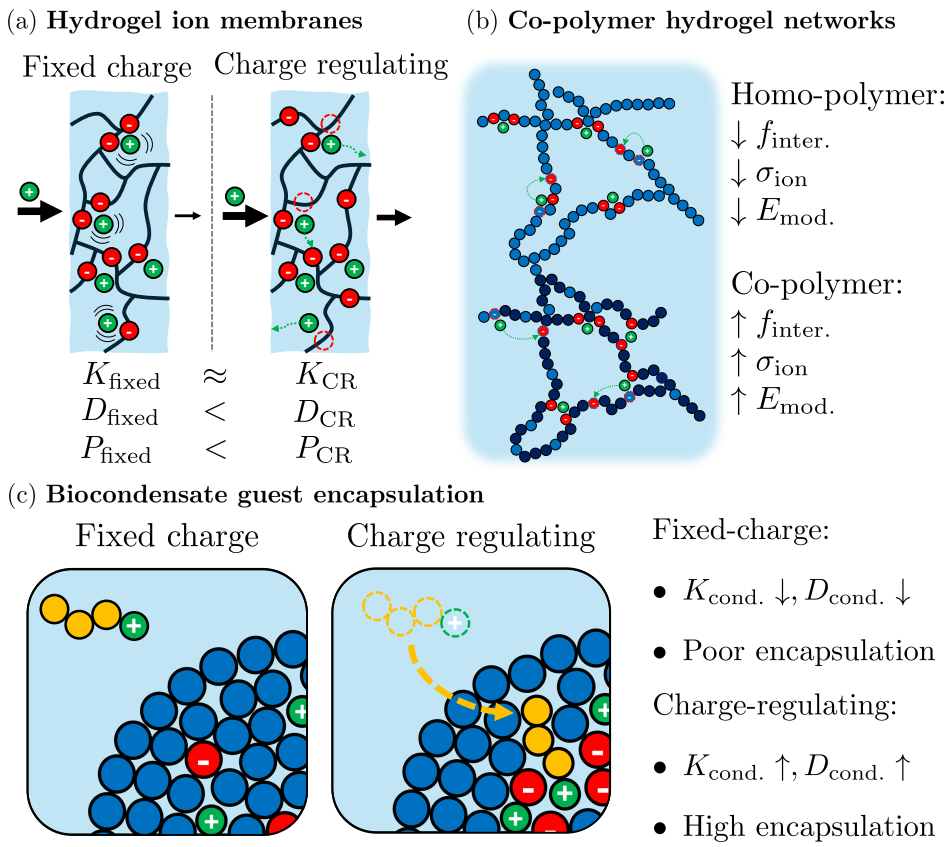


Figure 6.5: Implications of charge regulation for ion transport. (a) Hydrogel ion membranes: for the same charge profile, a charge regulating hydrogel will have the same ion partitioning as the fixed charge equivalent, but with enhanced diffusion and, therefore, permeability. (b) Co-polymer hydrogels: introducing neutral spacer monomers into a weak polyelectrolyte hydrogel will reduce the effects of competitive binding, increasing interchain crosslinks and improving the transport and mechanical properties of the gel. (c) Biocondensate guest encapsulation: the adaptive environment of a charge-regulating biocondensate may improve the uptake of guest molecules and enhance their diffusion coefficient.

making it challenging to rationally design charge-regulating materials. Building upon the insights gained through our coarse-grained simulations, we can formulate simple design heuristics for such systems, anticipating future developments in both experiments and simulations. We therefore conclude by outlining several promising directions for future experimental and theoretical investigations.

One important application of polyelectrolyte hydrogels is in ion-selective membranes, illustrated schematically in Figure 6.5(a). In this context, the relevant performance metric is the relative permeability,

$$P_{\text{gel}} = D_{\text{gel}} K_{\text{gel}}, \tag{6.13}$$

where P_i, D_i, and K_i denote the permeability, diffusion coefficient, and partition coefficient in medium i, respectively. Charge-regulating hydrogels offer a distinct advantage over fixed-charge systems: for a given mean charge fraction, ion solubilities are expected to be comparable. In contrast, the enhanced diffusion coefficients in charge-regulating networks translate directly into higher permeability. As shown above, this enhancement is most pronounced for multivalent ions and can reach nearly an order of magnitude depending on the hydrogel pK_a. This feature is particularly relevant for heavy-metal separations, where target ions often possess a high valency. Going beyond point-like small ions, it could potentially also be relevant for charged oligomers such as peptides in various biochemical and pharmaceutical processes. We emphasize that the present model treats ions in a simplified manner and neglects the polarizability and specific complexation effects that are known to be important for many heavy metals. Although it is not straightforward to predict how such chemical specificity would modify transport under charge regulation, we anticipate that protonation-assisted hopping would still provide a substantial kinetic advantage. Developing a more detailed understanding of specific systems will require either chemically specific coarse-grained models[418, 419] or even atomistic simulations in the future, in which charge regulation can be included using a range of different algorithms.[420, 421, 422, 423, 424, 425]

A central limitation of charge regulation identified in this work arises from competitive binding: the hydrogel adapts its charge profile to maximize favorable ion–polymer interactions, thereby reducing mobility at high concentrations. In applications such as sensors or battery electrolytes, where maximizing ionic transport is essential, mitigating this effect is crucial. One possible strategy is to employ co-polymer networks in which charge-regulating monomers are interspersed with neutral units, as illustrated in Figure 6.5(b). Neutral spacers would increase the average separation between charges, suppressing local overcharging and the associated long ion-pair lifetimes. In this regime, ion-mediated crosslinks between polymer chains are preferable to ions being locally sequestered along a single backbone. Separating charge-regulating sites entropically favors interchain bridges [93], while the increased ionic mobility associated with charge regulation should further benefit mechanical response relative to fixed-charge networks. Determining the optimal spacing between ionizable groups, such that protonation-assisted hopping remains effective while local overcharging is avoided, represents an intriguing direction for future work.

Another important avenue concerns the temperature dependence of ion transport. Temperature affects thermal motion, electrostatic interactions through the Bjerrum length, and the acid–base equilibrium itself. Because pK_a values typically decrease with increasing temperature[426, 427, 428, 429], our results suggest that heating could suppress ion mobility by increasing the degree of ionization, even as thermal agitation and reduced electrostatic coupling act in the opposite direction. Exploring this interplay may shed light on the unusual temperature sensitivity observed in some charge-regulating hydrogels, particularly when neutral spacers are incorporated [235].

Beyond synthetic materials, the concepts developed in this work have potential relevance in biological contexts. Charge-regulating hydrogels have qualitative similarities to biomolecular condensates,[260] in which many amino-acid residues titrate with pH. For charged guest molecules entering such chemically distinct environments,[265, 430, 273] charge regulation may simultaneously enhance solubility, by producing a more favorable local environment for the guest, and accelerate transport, improving encapsulation efficiency (Figure 6.5(c)). In the present work, we considered only a charge-regulating background matrix, but many guest molecules—such as small-molecule pharmaceutical compounds, flexible polypeptides, and globular proteins—also undergo protonation equilibria.[431] When both matrix and solute can adapt their charge, interactions may become more favorable than in fixed-charge systems,[367, 432, 378, 433] and protonation-assisted hopping could be further amplified because charge fluctuations of either component may trigger unbinding events. These effects have clear implications for drug delivery and nucleic-acid-based therapeutics.

Overall, by disentangling the coupled phenomena underlying charge regulation and ion transport, this work opens multiple avenues for future exploration across membrane science, energy materials, soft-matter mechanics, and biological physics. We anticipate that combining charge regulation with architectural control of polymer networks will provide a powerful framework for designing next-generation ion-conducting materials.

6.5 Appendix

Additional Figures

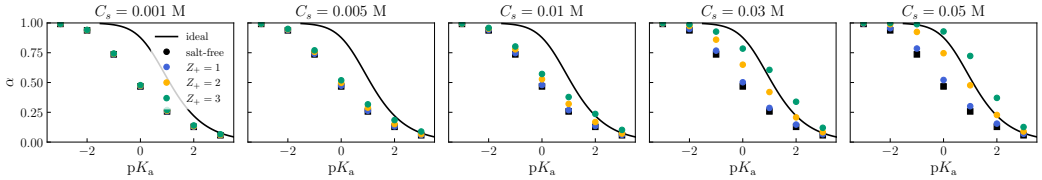


Figure 6.6: Variation in the hydrogel degree of ionization as a function of the pK_a value and for different salt concentrations and valencies. The black curves correspond to the theoretical prediction in the ideal limit.

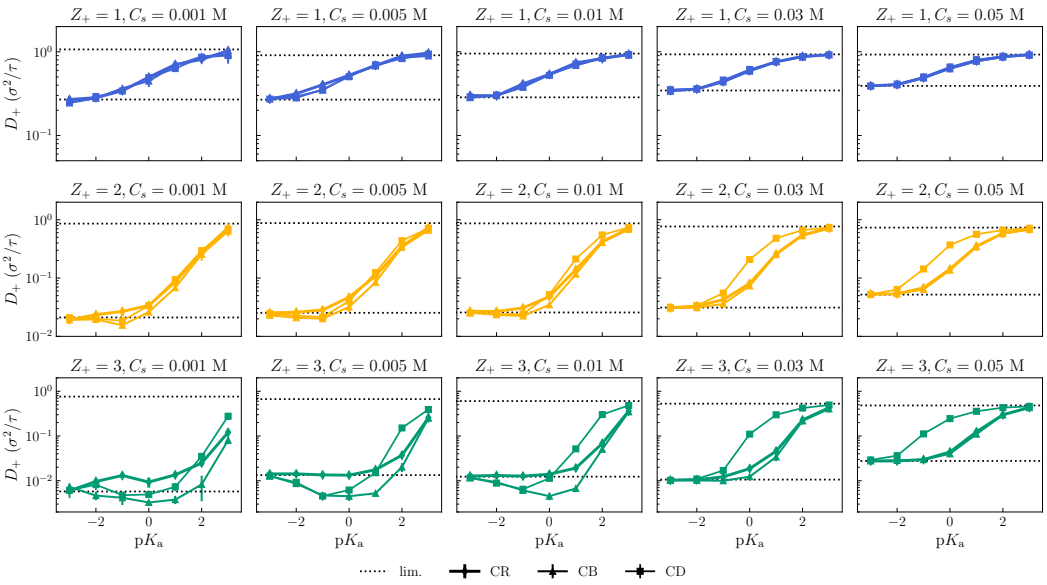


Figure 6.7: pK_a-dependence of diffusion coefficients obtained for mono-, di- and trivalent cations at different salt concentrations. The plots compare results obtained from simulations accounting for variations in the charge density (CD), competitive binding (CB) and dynamical charge regulation (CR). Dotted horizontal lines denote the diffusion coefficients obtained in the limits of fully ionized and neutral hydrogels.

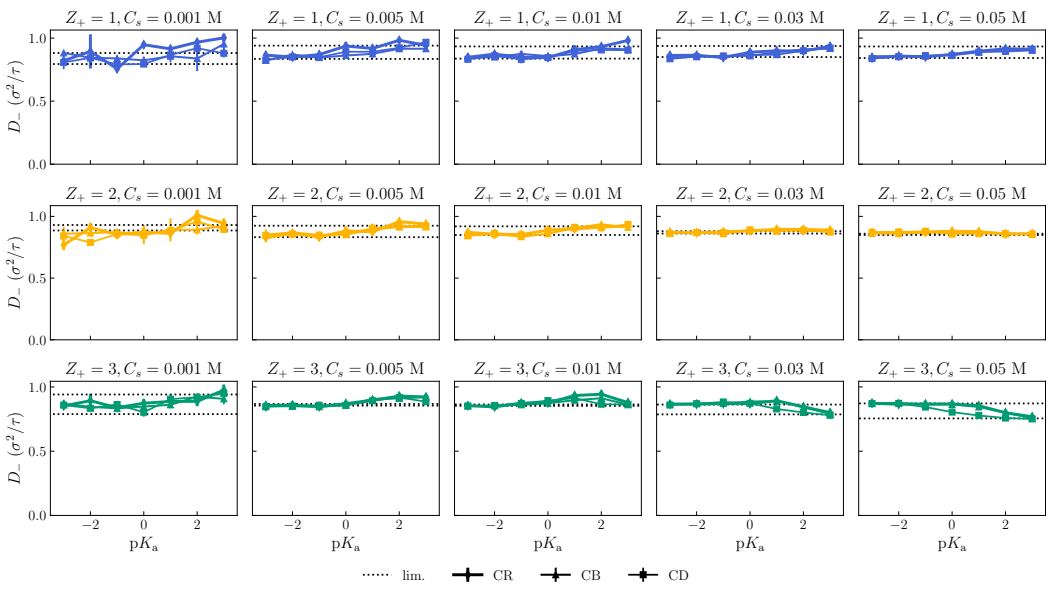


Figure 6.8: pK_a-dependence of monovalent anion diffusion coefficients obtained in the presence of mono-, di- and trivalent cations at different salt concentrations. The plots compare results obtained from simulations accounting for variations in the charge density (CD), competitive binding (CB) and dynamical charge regulation (CR). Dotted horizontal lines denote the diffusion coefficients obtained in the limits of fully ionized and neutral hydrogels.

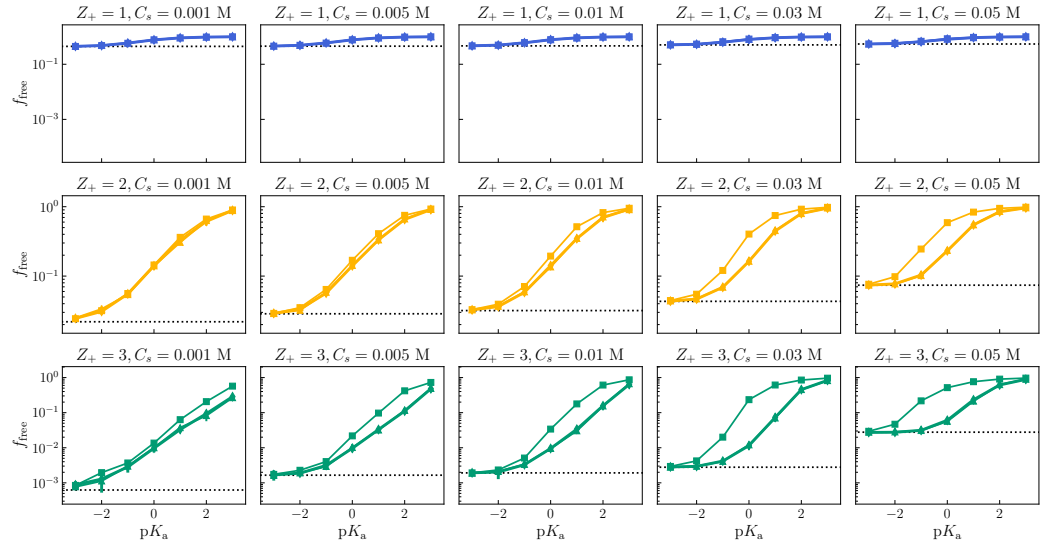


Figure 6.9: pK_a-dependence of the fraction of unbound cations obtained for mono-, di- and trivalent cations at different salt concentrations. The plots compare results obtained from simulations accounting for variations in the charge density (CD), competitive binding (CB) and dynamical charge regulation (CR). Dotted horizontal lines correspond to the fraction of unbound cations obtained in the limit of a fully ionized hydrogel.

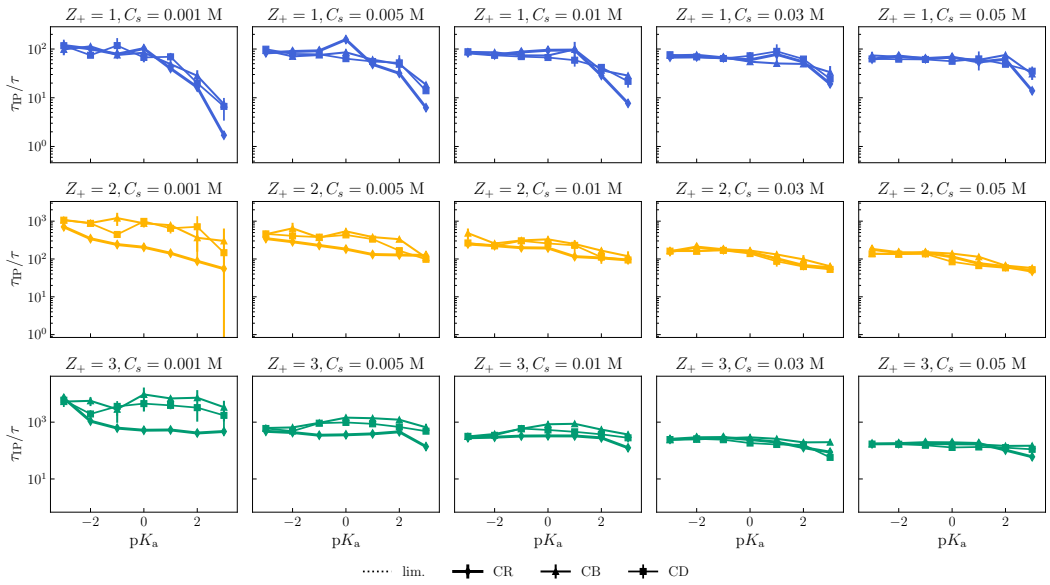


Figure 6.10: pK_a-dependence of the ion pair relaxation time obtained in the presence of mono-, di- and trivalent salts at different concentrations. The plots compare results obtained from simulations accounting for variations in the charge density (CD), competitive binding (CB) and dynamical charge regulation (CR).

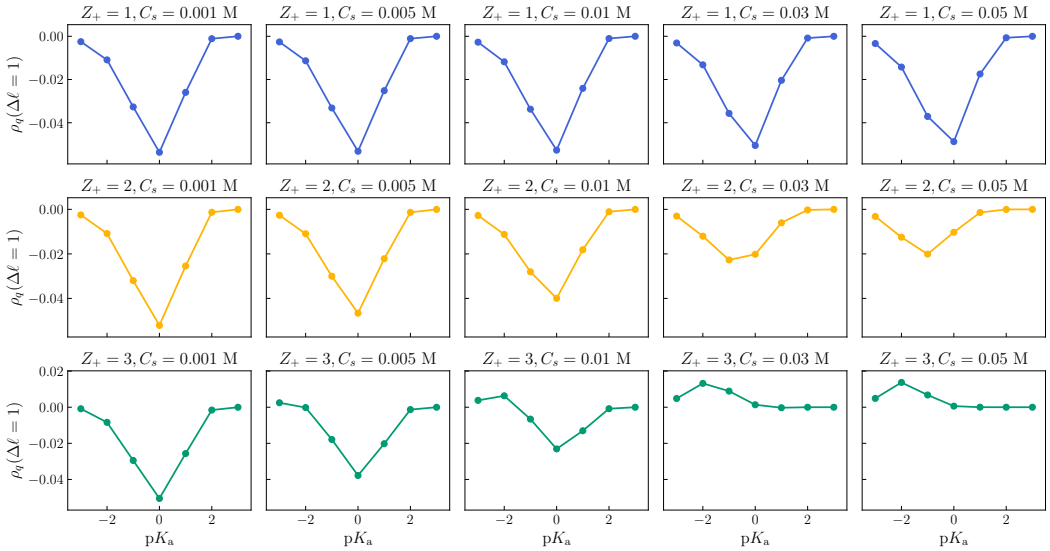


Figure 6.11: Nearest-neighbor polymer backbone charge autocorrelation function $\rho_q(l = 1)$ as a function of pK_a and obtained for different salt valencies and concentrations.

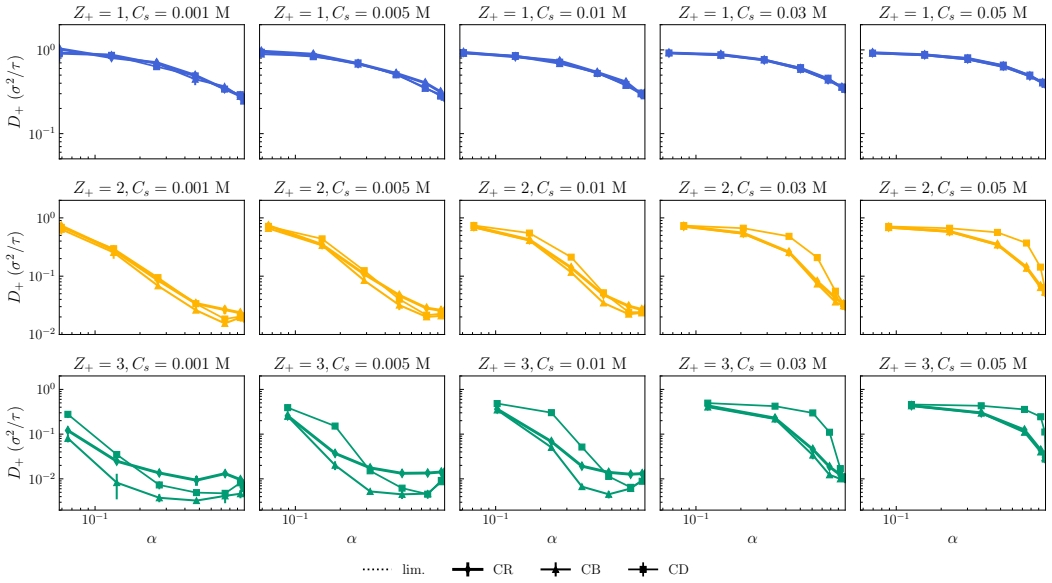


Figure 6.12: Diffusion coefficients obtained for mono-, di- and trivalent cations at different salt concentrations, plotted as a function of the hydrogel backbone degree of ionization α. The plots compare results obtained from simulations accounting for variations in the charge density (CD), competitive binding (CB) and dynamical charge regulation (CR).

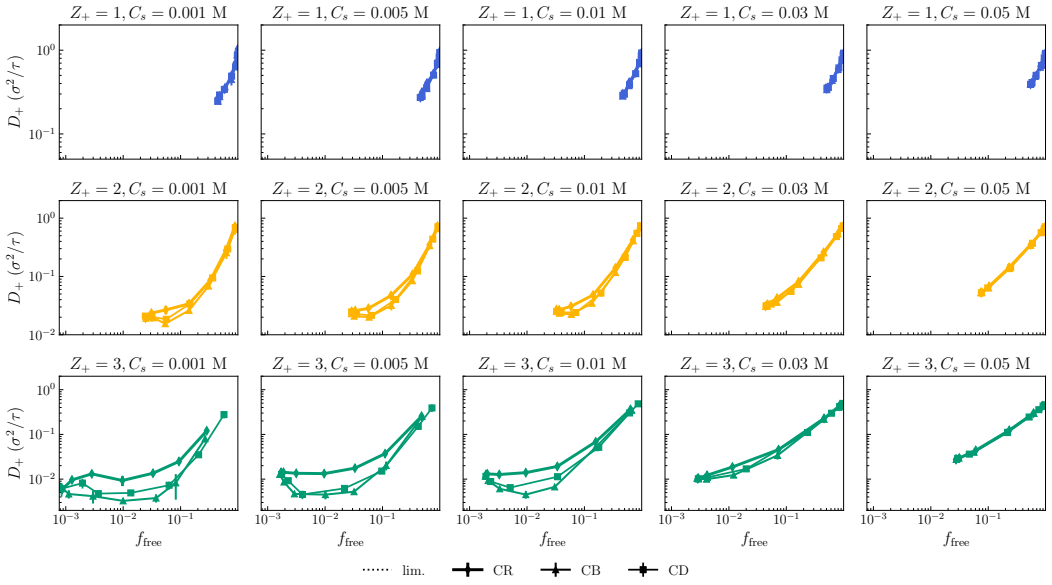


Figure 6.13: Diffusion coefficients obtained for mono-, di- and trivalent cations at different salt concentrations, plotted as a function of the fraction of unbound cations. The plots compare results obtained from simulations accounting for variations in the charge density (CD), competitive binding (CB) and dynamical charge regulation (CR).

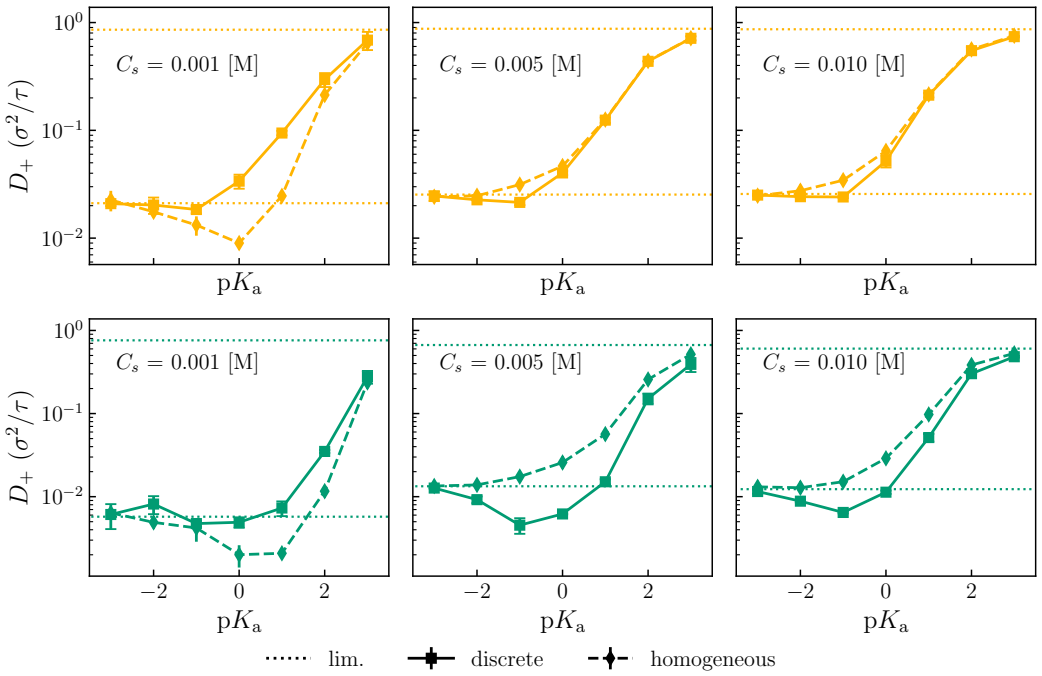


Figure 6.14: Diffusion coefficients obtained for divalent cations (upper row) and trivalent cations (lower row) at different salt concentrations, plotted as a function of the pK_a value. The plots compare results obtained from charge density simulations utilizing charge profiles obtained from prior RxMC simulations ("discrete") and profiles for which the same charge was distributed homogeneously across all monomers comprising hydrogel network ("homogeneous"). Dotted horizontal lines denote the diffusion coefficients obtained in the limits of fully ionized and neutral hydrogels.

References

[2] Pierre J. Walker et al. *Ion Transport Enhancement in Charge-Regulating Hydrogels*. 2026. DOI: 10.26434/chemrxiv.15004897/v2.

[4] Seola Lee et al. "Molecular control via dynamic bonding enables material responsiveness in additively manufactured metallo-polyelectrolytes". In: *Nat. Commun.* 15.1 (Aug. 2024), p. 6850. ISSN: 2041-1723. DOI: 10.1038/s41467-024-50860-6.

[14] Benjamin B. Ye, Pierre J. Walker, and Zhen-Gang Wang. "MDCraft: A Python assistant for performing and analyzing molecular dynamics simulations of soft matter systems". In: *J. Open Source Softw.* 9.100 (Aug. 2024), p. 7013. ISSN: 2475-9066. DOI: 10.21105/joss.07013.

[23] C. A. (Charles Augustin) Coulomb et al. *Mémoires sur l'électricité et la magnétisme*. Paris : Chez Bachelier, libraire ..., 1789.

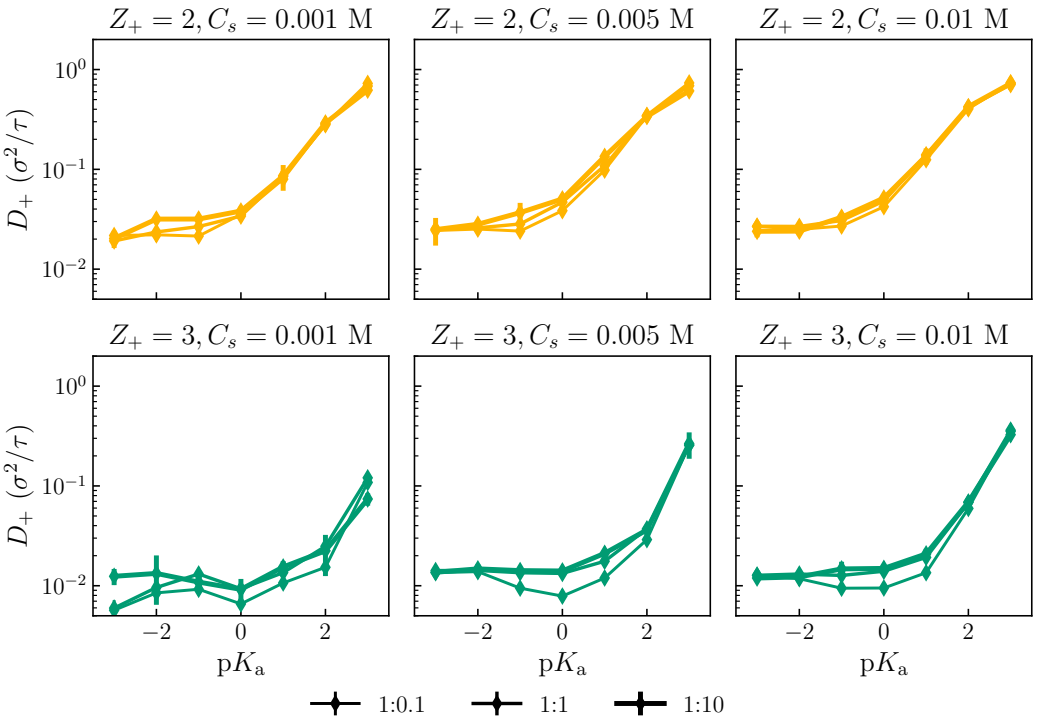


Figure 6.15: Diffusion coefficients obtained for divalent cations (upper row) and trivalent cations (lower row) at different salt concentrations, plotted as a function of the pK_a value. The plots compare results obtained from varying the ratio of MD to MC steps within the RxMC + MD simulations.

[78] Jesse G. McDaniel and Chang Yun Son. "Ion Correlation and Collective Dynamics in BMIM/BF $_4$ -Based Organic Electrolytes: From Dilute Solutions to the Ionic Liquid Limit". In: *J. Phys. Chem. B* 122.28 (July 2018), pp. 7154–7169. ISSN: 1520-6106, 1520-5207. DOI: 10.1021/acs.jpcb.8b04886.

[93] Alexander N. Semenov and Michael Rubinstein. "Thermoreversible Gelation in Solutions of Associative Polymers. 1. Statics". In: *Macromolecules* 31.4 (Feb. 1998), pp. 1373–1385. ISSN: 0024-9297, 1520-5835. DOI: 10.1021/ma970616h.

[142] Alejandro Gallegos and Jianzhong Wu. "Hierarchical Model of Weak Polyelectrolytes with Ionization and Conformation Consistency". In: *Macromolecules* 56.12 (June 2023), pp. 4760–4772. ISSN: 0024-9297, 1520-5835. DOI: 10.1021/acs.macromol.2c01910.

[143] David Beyer, Christian Holm, and Zhen-Gang Wang. "A Sequence-Specific Theory for Charge-Regulating IDPs". In: *ChemRxiv* 2026.0202 (). DOI: 10.26434/chemrxiv.10001808/v1.

[183] Kurt Kremer and Gary S. Grest. "Dynamics of entangled linear polymer melts: A molecular-dynamics simulation". In: *J. Chem. Phys.* 92.8 (Apr.

1990), pp. 5057–5086. ISSN: 0021-9606, 1089-7690. DOI: 10.1063/1.458541.

[187] Naveen Michaud-Agrawal et al. “MDAnalysis: A toolkit for the analysis of molecular dynamics simulations”. In: *J. Comput. Chem.* 32.10 (July 2011), pp. 2319–2327. ISSN: 01928651. DOI: 10.1002/jcc.21787.

[235] Tae Hyun Kim et al. “Flexible biomimetic block copolymer composite for temperature and long-wave infrared sensing”. In: *Sci. Adv.* 9.6 (Feb. 2023), eade0423. DOI: 10.1126/sciadv.ade0423.

[260] Salman F. Banani et al. “Biomolecular condensates: organizers of cellular biochemistry”. en. In: *Nat. Rev. Mol. Cell Biol.* 18.5 (May 2017), pp. 285–298. ISSN: 1471-0080. DOI: 10.1038/nrm.2017.7.

[265] Yifan Dai, Zhen-Gang Wang, and Richard N. Zare. “Unlocking the electrochemical functions of biomolecular condensates”. In: *Nat. Chem. Biol.* 20.11 (Nov. 2024), pp. 1420–1433. ISSN: 1552-4469. DOI: 10.1038/s41589-024-01717-y.

[273] Hannes Ausserwöger et al. “Biomolecular condensates sustain pH gradients at equilibrium through charge neutralization”. en. In: *Nat. Chem.* 18.2 (Feb. 2026), pp. 246–257. ISSN: 1755-4349. DOI: 10.1038/s41557-025-02039-9.

[310] Yong Zhang and Edward J. Maginn. “Direct Correlation between Ionic Liquid Transport Properties and Ion Pair Lifetimes: A Molecular Dynamics Study”. In: *J. Phys. Chem. Lett.* 6.4 (Feb. 2015), pp. 700–705. ISSN: 1948-7185, 1948-7185. DOI: 10.1021/acs.jpclett.5b00003.

[347] A. Katchalsky and I. Michaeli. “Polyelectrolyte gels in salt solutions”. fr. In: *J. Polym. Sci.* 15.79 (1955), pp. 69–86. ISSN: 1542-6238. DOI: 10.1002/pol.1955.120157906.

[348] Toyoichi Tanaka. “Gels”. In: *Sci. Am.* 244.1 (1981), 124–S–17. ISSN: 0036-8733.

[349] Mohammad A. Alkhadra et al. “Electrochemical Methods for Water Purification, Ion Separations, and Energy Conversion”. In: *Chem. Rev.* 122.16 (Aug. 2022), pp. 13547–13635. ISSN: 0009-2665. DOI: 10.1021/acs.chemrev.1c00396.

[350] Johannes Höpfner, Christopher Klein, and Manfred Wilhelm. “A Novel Approach for the Desalination of Seawater by Means of Reusable Poly(acrylic acid) Hydrogels and Mechanical Force”. en. In: *Macromol. Rapid Commun.* 31.15 (2010), pp. 1337–1342. ISSN: 1521-3927. DOI: 10.1002/marc.201000058.

[351] Junjie Yin et al. “Ion Conductivity of Polyelectrolyte Hydrogels with Varying Compositions”. In: *ACS Nano* 19.39 (Oct. 2025), pp. 34797–34806. ISSN: 1936-0851. DOI: 10.1021/acsnano.5c10246.

[352] Akira Mamada et al. “Photoinduced phase transition of gels”. In: *Macromolecules* 23.5 (Mar. 1990), pp. 1517–1519. ISSN: 0024-9297. DOI: 10.1021/ma00207a046.

[353] Leah K. Borden, Ankit Gargava, and Srinivasa R. Raghavan. “Reversible electroadhesion of hydrogels to animal tissues for suture-less repair of cuts or tears”. en. In: *Nat. Commun.* 12.1 (July 2021), p. 4419. ISSN: 2041-1723. DOI: 10.1038/s41467-021-24022-x.

[354] Jung Kwon Oh et al. “The development of microgels/nanogels for drug delivery applications”. In: *Prog. Polym. Sci.* 33.4 (Apr. 2008), pp. 448–477. ISSN: 0079-6700. DOI: 10.1016/j.progpolymsci.2008.01.002.

[355] Jiaxing Yuan and Tine Curk. “Designing Actuation in pH-Responsive Hydrogels”. In: *Macromolecules* 59.2 (Jan. 2026), pp. 939–949. ISSN: 0024-9297. DOI: 10.1021/acs.macromol.5c03370.

[356] Jonas Landsgesell et al. “Simulations of ionization equilibria in weak polyelectrolyte solutions and gels”. In: *Soft Matter* 15.6 (2019), pp. 1155–1185. DOI: 10.1039/C8SM02085J.

[357] E. B. Zhulina, T. M. Birshtein, and O. V. Borisov. “Theory of Ionizable Polymer Brushes”. en. In: *Macromolecules* 28.5 (Feb. 1995), pp. 1491–1499. ISSN: 0024-9297, 1520-5835. DOI: 10.1021/ma00109a021.

[358] Mario Tagliazucchi, Mónica Olvera de la Cruz, and Igal Szleifer. “Self-organization of grafted polyelectrolyte layers via the coupling of chemical equilibrium and physical interactions”. In: *Proc. Natl. Acad. Sci. U.S.A.* 107.12 (Mar. 2010), pp. 5300–5305. DOI: 10.1073/pnas.0913340107.

[359] F. Léonforte, U. Welling, and M. Müller. “Single-chain-in-mean-field simulations of weak polyelectrolyte brushes”. In: *J. Chem. Phys.* 145.22 (Dec. 2016), p. 224902. ISSN: 0021-9606. DOI: 10.1063/1.4971212.

[360] Gustav Ferrand-Drake del Castillo, Rebekah L. N. Hailes, and Andreas Dahlin. “Large Changes in Protonation of Weak Polyelectrolyte Brushes with Salt Concentration—Implications for Protein Immobilization”. In: *J. Phys. Chem. Lett.* 11.13 (July 2020), pp. 5212–5218. DOI: 10.1021/acs.jpclett.0c01289.

[361] Jiaxing Yuan and Yanwei Wang. “Conformation and Ionization Behavior of Charge-Regulating Polyelectrolyte Brushes in a Poor Solvent”. In: *J. Phys. Chem. B* 125.37 (Sept. 2021), pp. 10589–10596. ISSN: 1520-6106. DOI: 10.1021/acs.jpcb.1c04451.

[362] David Beyer, Peter Košovan, and Christian Holm. “Explaining Giant Apparent $\mathrm{p}{K}_{a}$ Shifts in Weak Polyelectrolyte Brushes”. In: *Phys. Rev. Lett.* 131.16 (Oct. 2023), p. 168101. DOI: 10.1103/PhysRevLett.131.168101.

[363] Xin Yuan et al. “pH response of sequence-controlled polyampholyte brushes”. In: *Soft Matter* 19.23 (2023), pp. 4333–4344. DOI: 10.1039/D3SM00447C.

[364] Vikramjit S. Rathee et al. “Role of Associative Charging in the Entropy–Energy Balance of Polyelectrolyte Complexes”. In: *J. Am. Chem. Soc.* 140.45 (Nov. 2018), pp. 15319–15328. ISSN: 0002-7863. DOI: 10.1021/jacs.8b08649.

[365] Bin Zheng et al. “Phase Separation of Polyelectrolytes: The Effect of Charge Regulation”. In: *J. Phys. Chem. B* 125.28 (July 2021), pp. 7863–7870. ISSN: 1520-6106. DOI: 10.1021/acs.jpcb.1c01986.

[366] Sebastian P. Pineda et al. “Charge Regulation Triggers Condensation of Short Oligopeptides to Polyelectrolytes”. In: *JACS Au* 4.5 (May 2024), pp. 1775–1785. DOI: 10.1021/jacsau.3c00668.

[367] Mikael Lund and Bo Jönsson. “On the Charge Regulation of Proteins”. In: *Biochemistry* 44.15 (Apr. 2005), pp. 5722–5727. ISSN: 0006-2960. DOI: 10.1021/bi047630o.

[368] Mikael Lund and Bo Jönsson. “Charge regulation in biomolecular solution”. en. In: *Q. Rev. Biophys.* 46.3 (Aug. 2013), pp. 265–281. ISSN: 0033-5835, 1469-8994. DOI: 10.1017/S003358351300005X.

[369] Paola B. Torres et al. “The electrostatic potential inside and around α-lactalbumin: Fluctuations and mean-field models”. In: *J. Chem. Phys.* 157.20 (Nov. 2022), p. 205101. ISSN: 0021-9606. DOI: 10.1063/5.0122275.

[370] Rivka Calinsky and Yaakov Levy. “A pH-Dependent Coarse-Grained Model for Disordered Proteins: Histidine Interactions Modulate Conformational Ensembles”. In: *J. Phys. Chem. Lett.* 15.37 (Sept. 2024), pp. 9419–9430. DOI: 10.1021/acs.jpclett.4c02314.

[371] Souradeep Ghosh et al. “Interplay of distinct modes of charge regulation on poly-acid ionization and conformation”. In: *J. Chem. Phys.* 163.19 (Nov. 2025), p. 194908. ISSN: 0021-9606. DOI: 10.1063/5.0297651.

[372] Jiaxing Yuan, Kyohei Takae, and Hajime Tanaka. “Impact of Charge Regulation on Self-Assembly of Zwitterionic Nanoparticles”. In: *Phys. Rev. Lett.* 128.15 (Apr. 2022), p. 158001. DOI: 10.1103/PhysRevLett.128.158001.

[373] Tine Curk and Erik Luijten. “Charge Regulation Effects in Nanoparticle Self-Assembly”. In: *Phys. Rev. Lett.* 126.13 (Mar. 2021), p. 138003. DOI: 10.1103/PhysRevLett.126.138003.

[374] Sebastian P. Pineda et al. “Patchy Charge Distribution Affects the pH in Protein Solutions during Dialysis”. In: *Langmuir* 41.8 (Mar. 2025), pp. 5387–5398. ISSN: 0743-7463. DOI: 10.1021/acs.langmuir.4c04942.

[375] Barry W. Ninham and V. Adrian Parsegian. “Electrostatic potential between surfaces bearing ionizable groups in ionic equilibrium with physiologic saline solution”. In: *J. Theor. Biol.* 31.3 (June 1971), pp. 405–428. ISSN: 0022-5193. DOI: 10.1016/0022-5193(71)90019-1.

[376] Amin Bakhshandeh et al. “Charge Regulation of Colloidal Particles: Theory and Simulations”. In: *Phys. Rev. Lett.* 123.20 (Nov. 2019), p. 208004. DOI: 10.1103/PhysRevLett.123.208004.

[377] Jonas Landsgesell et al. “The pH-Dependent Swelling of Weak Polyelectrolyte Hydrogels Modeled at Different Levels of Resolution”. In: *Macromolecules* 55.8 (Apr. 2022), pp. 3176–3188. ISSN: 0024-9297. DOI: 10.1021/acs.macromol.1c02489.

[378] Christian Strauch and Stefanie Schneider. “Monte Carlo simulation of the ionization and uptake behavior of cationic oligomers into pH-responsive polyelectrolyte microgels of opposite charge – a model for oligopeptide uptake and release”. en. In: *Soft Matter* 20.6 (2024), pp. 1263–1274. DOI: 10.1039/D3SM01426F.

[379] Christian Strauch, Lars Roß, and Stefanie Schneider. “Exploring guest molecule uptake in pH-responsive polyelectrolyte microgels via Monte Carlo simulations”. en. In: *Soft Matter* 20.48 (2024), pp. 9664–9672. DOI: 10.1039/D4SM00950A.

[380] Toyoichi Tanaka et al. “Phase Transitions in Ionic Gels”. In: *Phys. Rev. Lett.* 45.20 (Nov. 1980), pp. 1636–1639. DOI: 10.1103/PhysRevLett.45.1636.

[381] Bin Zheng et al. “Charge Regulation of Polyelectrolyte Gels: Swelling Transition”. In: *Macromolecules* 56.13 (July 2023), pp. 5217–5224. ISSN: 0024-9297. DOI: 10.1021/acs.macromol.3c00609.

[382] Jian Tang et al. “Swelling Behaviors of Hydrogels with Alternating Neutral/Highly Charged Sequences”. In: *Macromolecules* 53.19 (Oct. 2020), pp. 8244–8254. ISSN: 0024-9297. DOI: 10.1021/acs.macromol.0c01221.

[383] Gabriel S. Longo, Monica Olvera de la Cruz, and I. Szleifer. “Non-monotonic swelling of surface grafted hydrogels induced by pH and/or salt concentration”. In: *J. Chem. Phys.* 141.12 (Sept. 2014), p. 124909. ISSN: 0021-9606. DOI: 10.1063/1.4896562.

[384] Gabriel S. Longo, Monica Olvera de la Cruz, and Igal Szleifer. “pH-Controlled Nanoaggregation in Amphiphilic Polymer Co-networks”. In: *ACS Nano* 7.3 (Mar. 2013), pp. 2693–2704. ISSN: 1936-0851. DOI: 10.1021/nn400130c.

[385] David Beyer, Peter Košovan, and Christian Holm. “Simulations Explain the Swelling Behavior of Hydrogels with Alternating Neutral and Weakly Acidic Blocks”. In: *Macromolecules* 55.23 (Dec. 2022), pp. 10751–10760. ISSN: 0024-9297. DOI: 10.1021/acs.macromol.2c01916.

[386] Oleg V. Rud et al. “Polyelectrolyte Hydrogels as Draw Agents for Desalination of Solutions with Multivalent Ions”. In: *Macromolecules* 55.5 (Mar. 2022), pp. 1763–1770. ISSN: 0024-9297. DOI: 10.1021/acs.macromol.1c02266.

[387] Oleg V. Rud et al. “Modeling of weak polyelectrolyte hydrogels under compression – Implications for water desalination”. In: *Desalination* 506 (June 2021), p. 114995. ISSN: 0011-9164. DOI: 10.1016/j.desal.2021.114995.

[388] Jiaxing Yuan and Hajime Tanaka. “Switchable nanochannel flow control through weak polyelectrolyte brushes”. In: *Phys. Fluids* 37.2 (Feb. 2025), p. 022019. ISSN: 1070-6631. DOI: 10.1063/5.0249555.

[389] David Sean, Jonas Landsgesell, and Christian Holm. “Computer Simulations of Static and Dynamical Properties of Weak Polyelectrolyte Nanogels in Salty Solutions”. en. In: *Gels* 4.1 (Mar. 2018), p. 2. ISSN: 2310-2861. DOI: 10.3390/gels4010002.

[390] John G. Lieu et al. “Vapor-Liquid Equilibria for Dendritic-Polymer Solutions”. en. In: *J. Chem. Eng. Data* 44.3 (May 1999), pp. 613–620. ISSN: 0021-9568, 1520-5134. DOI: 10.1021/je980214k.

[391] Stefanie Schneider and Per Linse. “Monte Carlo Simulation of Defect-Free Cross-Linked Polyelectrolyte Gels”. In: *J. Phys. Chem. B* 107.32 (Aug. 2003), pp. 8030–8040. ISSN: 1520-6106. DOI: 10.1021/jp022336w.

[392] Jonas Landsgesell et al. “Grand-Reaction Method for Simulations of Ionization Equilibria Coupled to Ion Partitioning”. In: *Macromolecules* 53.8 (Apr. 2020), pp. 3007–3020. ISSN: 0024-9297. DOI: 10.1021/acs.macromol.0c00260.

[393] R. D. Shannon. “Revised effective ionic radii and systematic studies of interatomic distances in halides and chalcogenides”. In: (). DOI: 10.1107/S0567739476001551.

[394] Mark J. Stevens and Kurt Kremer. “Structure of salt-free linear polyelectrolytes”. en. In: *Phys. Rev. Lett.* 71.14 (Oct. 1993), pp. 2228–2231. ISSN: 0031-9007. DOI: 10.1103/PhysRevLett.71.2228.

[395] John D. Weeks, David Chandler, and Hans C. Andersen. “Role of Repulsive Forces in Determining the Equilibrium Structure of Simple Liquids”. In: *J. Chem. Phys.* 54.12 (Sept. 2003), pp. 5237–5247. ISSN: 0021-9606. DOI: 10.1063/1.1674820.

[396] R. W. Hockney and J. W. Eastwood. *Computer Simulation Using Particles*. Boca Raton: CRC Press, Mar. 2021. ISBN: 978-0-367-80693-4. DOI: 10.1201/9780367806934.

[397] Markus Deserno and Christian Holm. "How to mesh up Ewald sums. I. A theoretical and numerical comparison of various particle mesh routines". In: *J. Chem. Phys.* 109.18 (Nov. 1998), pp. 7678–7693. ISSN: 0021-9606. DOI: 10.1063/1.477414.

[398] Markus Deserno and Christian Holm. "How to mesh up Ewald sums. II. An accurate error estimate for the particle–particle–particle-mesh algorithm". In: *J. Chem. Phys.* 109.18 (Nov. 1998), pp. 7694–7701. ISSN: 0021-9606. DOI: 10.1063/1.477415.

[399] Robert D. Groot and Patrick B. Warren. "Dissipative particle dynamics: Bridging the gap between atomistic and mesoscopic simulation". In: *J. Chem. Phys.* 107.11 (Sept. 1997), pp. 4423–4435. ISSN: 0021-9606. DOI: 10.1063/1.474784.

[400] Timm Krüger et al. *The Lattice Boltzmann Method: Principles and Practice*. en. Springer, Nov. 2016. ISBN: 978-3-319-44649-3.

[401] Florian Weik et al. "ESPResSo 4.0 – an extensible software package for simulating soft matter systems". en. In: *Eur. Phys. J. Spec. Top.* 227.14 (Mar. 2019), pp. 1789–1816. ISSN: 1951-6401. DOI: 10.1140/epjst/e2019-800186-9.

[402] Rudolf Weeber et al. "ESPResSo, a Versatile Open-Source Software Package for Simulating Soft Matter Systems". In: *Comprehensive Computational Chemistry (First Edition)*. Ed. by Manuel Yáñez and Russell J. Boyd. Oxford: Elsevier, Jan. 2024, pp. 578–601. ISBN: 978-0-12-823256-9.

[403] J. Karl Johnson, Athanassios Z. Panagiotopoulos, and Keith E. Gubbins. "Reactive canonical Monte Carlo: A new simulation technique for reacting or associating fluids". In: *Mol. Phys.* 81.3 (Feb. 1994), pp. 717–733. ISSN: 0026-8976, 1362-3028. DOI: 10.1080/00268979400100481.

[404] W. R. Smith and B. Triska. "The reaction ensemble method for the computer simulation of chemical and phase equilibria. I. Theory and basic examples". In: *J. Chem. Phys.* 100.4 (Feb. 1994), pp. 3019–3027. ISSN: 0021-9606. DOI: 10.1063/1.466443.

[405] Christopher E. Reed and Wayne F. Reed. "Monte Carlo study of titration of linear polyelectrolytes". In: *J. Chem. Phys.* 96.2 (Jan. 1992), pp. 1609–1620. ISSN: 0021-9606. DOI: 10.1063/1.462145.

[406] Jonas Landsgesell, Christian Holm, and Jens Smiatek. "Wang–Landau Reaction Ensemble Method: Simulation of Weak Polyelectrolytes and General Acid–Base Reactions". In: *J. Chem. Theory Comput.* 13.2 (Feb. 2017), pp. 852–862. ISSN: 1549-9618. DOI: 10.1021/acs.jctc.6b00791.

[407] Louis P. Hammett. "Some Relations between Reaction Rates and Equilibrium Constants." en. In: *Chem. Rev.* 17.1 (Aug. 1935), pp. 125–136. ISSN: 0009-2665, 1520-6890. DOI: 10.1021/cr60056a010.

[408] R. P. Bell. “The rates of simple acid–base reactions”. en. In: *Q. Rev., Chem. Soc.* 13.3 (Jan. 1959), pp. 169–182. ISSN: 0009-2681. DOI: 10.1039/QR9591300169.

[409] Matteo Rini et al. “Bimodal proton transfer in acid-base reactions in water”. In: *J. Chem. Phys.* 121.19 (Nov. 2004), pp. 9593–9610. ISSN: 0021-9606. DOI: 10.1063/1.1804172.

[410] C. J. T. de Grotthuss. *Mémoire sur la décomposition de l’eau: et des corps qu’ elle tient en dissolution à l’aide de l’électricité galvanique*. fr. 1805.

[411] Christopher J. Fennell et al. “Ion Pairing in Molecular Simulations of Aqueous Alkali Halide Solutions”. In: *J. Phys. Chem. B* 113.19 (May 2009), pp. 6782–6791. ISSN: 1520-6106. DOI: 10.1021/jp809782z.

[412] Loris Burth, David Beyer, and Christian Holm. “A Comparison of Bead-Spring and Site-Binding Models for Weak Polyelectrolytes”. en. In: *Macromol. Theory Simul.* 34.4 (2025), e00020. ISSN: 1521-3919. DOI: 10.1002/mats.202500020.

[413] Yongha Kim et al. “Determination of Carboxyl Dissociation Degree and pKa in Weak Polyelectrolyte Membranes via POT Titration and FTIR Analysis for Clean Technologies in Sustainability”. In: *Macromolecules* 57.22 (Nov. 2024), pp. 10844–10860. ISSN: 0024-9297. DOI: 10.1021/acs.macromol.4c02139.

[414] Artem M. Rumyantsev et al. “Polyelectrolyte Gel Swelling and Conductivity vs Counterion Type, Cross-Linking Density, and Solvent Polarity”. In: *Macromolecules* 49.17 (Sept. 2016), pp. 6630–6643. ISSN: 0024-9297. DOI: 10.1021/acs.macromol.6b00911.

[415] Manping Jia, Le Luo, and Marco Rolandi. “Correlating Ionic Conductivity and Microstructure in Polyelectrolyte Hydrogels for Bioelectronic Devices”. en. In: *Macromol. Rapid Commun.* 43.6 (2022), p. 2100687. ISSN: 1521-3927. DOI: 10.1002/marc.202100687.

[416] Alec Glisman et al. “Binding Modes and Water-Mediation of Polyelectrolyte Adsorption to a Neutral CaCO3 Surface”. In: *Langmuir* 40.49 (Dec. 2024), pp. 25931–25939. ISSN: 0743-7463. DOI: 10.1021/acs.langmuir.4c03301.

[417] Alec Glisman et al. “Multivalent Ion-Mediated Polyelectrolyte Association and Structure”. In: *Macromolecules* 57.5 (Mar. 2024), pp. 1941–1949. ISSN: 0024-9297. DOI: 10.1021/acs.macromol.3c02437.

[418] Paulo C. T. Souza et al. “Martini 3: a general purpose force field for coarse-grained molecular dynamics”. In: *Nat. Methods* 18.4 (Apr. 2021), pp. 382–388. ISSN: 1548-7105. DOI: 10.1038/s41592-021-01098-3.

[419] Fabian Grünewald et al. “Titratable Martini model for constant pH simulations”. In: *J. Chem. Phys.* 153.2 (July 2020), p. 024118. ISSN: 0021-9606. DOI: 10.1063/5.0014258.

[420] Vinicius Martins de Oliveira, Ruibin Liu, and Jana Shen. “Constant pH molecular dynamics simulations: Current status and recent applications”. In: *Curr. Opin. Struct. Biol.* 77 (Dec. 2022), p. 102498. ISSN: 0959-440X. DOI: 10.1016/j.sbi.2022.102498.

[421] António M. Baptista, Paulo J. Martel, and Steffen B. Petersen. “Simulation of protein conformational freedom as a function of pH: constant-pH molecular dynamics using implicit titration”. en. In: *Proteins: Struct., Funct., Bioinf.* 27.4 (1997). _eprint: https://onlinelibrary.wiley.com/doi/pdf/10.1002/%28SICI%291097-0134%28199704%2927%3A4%3C523%3A%3AAID-PROT6%3E3.0.CO%3B2-B, pp. 523–544. ISSN: 1097-0134. DOI: 10.1002/(SICI)1097-0134(199704)27:4<523::AID-PROT6>3.0.CO;2-B.

[422] Michael S. Lee, Freddie R. Salsbury Jr., and Charles L. Brooks III. “Constant-pH molecular dynamics using continuous titration coordinates”. en. In: *Proteins: Struct., Funct., Bioinf.* 56.4 (2004). _eprint: https://onlinelibrary.wiley.com/doi/pdf/10.1002/p pp. 738–752. ISSN: 1097-0134. DOI: 10.1002/prot.20128.

[423] Noora Aho et al. “Scalable Constant pH Molecular Dynamics in GROMACS”. In: *J. Chem. Theory Comput.* 18.10 (Oct. 2022), pp. 6148–6160. ISSN: 1549-9618. DOI: 10.1021/acs.jctc.2c00516.

[424] Eliane Briand et al. “Constant pH Simulation with FMM Electrostatics in GROMACS. (A) Design and Applications”. In: *J. Chem. Theory Comput.* 21.4 (Feb. 2025), pp. 1762–1786. ISSN: 1549-9618. DOI: 10.1021/acs.jctc.4c01318.

[425] Bartosz Kohnke et al. “Constant pH Simulation with FMM Electrostatics in GROMACS. (B) GPU Accelerated Hamiltonian Interpolation”. In: *J. Chem. Theory Comput.* 21.4 (Feb. 2025), pp. 1787–1804. ISSN: 1549-9618. DOI: 10.1021/acs.jctc.4c01319.

[426] Bruce Monzyk and Alvin L. Crumbliss. “Acid dissociation constants (Ka) and their temperature dependencies (.DELTA.Ha, .DELTA.Sa) for a series of carbon- and nitrogen-substituted hydroxamic acids in aqueous solution”. en. In: *J. Org. Chem.* 45.23 (Nov. 1980), pp. 4670–4675. ISSN: 0022-3263, 1520-6904. DOI: 10.1021/jo01311a024.

[427] Hidetada Nagai, Ko Kuwabara, and Giorgio Carta. “Temperature Dependence of the Dissociation Constants of Several Amino Acids”. In: *J. Chem. Eng. Data* 53.3 (Mar. 2008), pp. 619–627. ISSN: 0021-9568. DOI: 10.1021/je700067a.

[428] Jetse C. Reijenga, Leonardo G. Gagliardi, and Ernst Kenndler. “Temperature dependence of acidity constants, a tool to affect separation selectivity in capillary electrophoresis”. In: *J. Chromatogr. A*. 15th International Symposium

on Capillary Electroseparation Techniques 1155.2 (July 2007), pp. 142–145. ISSN: 0021-9673. DOI: 10.1016/j.chroma.2006.09.084.

[429] Rajan Vijisha K. and Muraleedharan K. "The pKa values of amine based solvents for CO2 capture and its temperature dependence—An analysis by density functional theory". In: *Int. J. Greenhouse Gas Control* 58 (Mar. 2017), pp. 62–70. ISSN: 1750-5836. DOI: 10.1016/j.ijggc.2017.01.009.

[430] Shiv Rekhi and Jeetain Mittal. *Biomolecular Condensates Act as Distinct Solvation Environments that Reshape Amino Acid pKa Values*. en. Jan. 2026. DOI: 10.64898/2026.01.11.698869.

[431] Saehyun Choi et al. "Effect of Polypeptide Complex Coacervate Microenvironment on Protonation of a Guest Molecule". In: *J. Phys. Chem. B* 127.26 (July 2023), pp. 5978–5991. ISSN: 1520-6106. DOI: 10.1021/acs.jpcb.3c02098.

[432] Roman Staňo et al. "Sequestration of Small Ions and Weak Acids and Bases by a Polyelectrolyte Complex Studied by Simulation and Experiment". In: *Macromolecules* 57.3 (Feb. 2024), pp. 1383–1398. ISSN: 0024-9297. DOI: 10.1021/acs.macromol.3c01209.

[433] David Beyer, Christian Holm, and Zhen-Gang Wang. "Charge Regulation Effects in Weak Polyelectrolyte Complexation". In: *J. Phys. Chem. Lett.* 16.32 (Aug. 2025), pp. 8245–8251. DOI: 10.1021/acs.jpclett.5c01877.

Chapter 7

FROM METAL–LIGAND COORDINATION TO THE MECHANICS OF METALLO-POLYELECTROLYTE COMPLEXES

Metallo-polyelectrolyte complexes derive their mechanical response from the coupling between metal–ligand coordination, polymer ionization, and network topology. In this chapter, we develop a multiscale computational framework combining quantum-chemical calculations, thermodynamic theory, and coarse-grained molecular dynamics simulations to relate these molecular interactions to phase behavior, gelation, relaxation, and deformation. Electronic-structure calculations show that metal–acrylate binding is governed primarily by metal valency and contact separation, with additional ion-specific orbital contributions for some transition metals. The thermodynamic model predicts that increasing metal valency or polymer charge density promotes phase separation and gelation, while explicit coupling between protonation and metal binding produces an intermediate composition range favorable for network formation. Molecular dynamics simulations further show that trivalent ions form stronger, more persistent, and more highly connected networks than divalent ions, producing stiffer but less readily reorganized gels. Overall, the results demonstrate that MPEC mechanics are controlled not only by binding strength, but also by the competition between interchain bridges, intrachain loops, and network relaxation.

This chapter includes work from our previously published article: Seola Lee, Pierre J. Walker, Seneca J. Velling, Amylynn Chen, Zane W. Taylor, Cyrus J. B. M. Fiori, Vatsa Gandhi, Zhen-Gang Wang, and Julia R. Greer. "Molecular control via dynamic bonding enables material responsiveness in additively manufactured metallo-polyelectrolytes". In: *Nat. Commun.* 15.1 (Aug. 2024), p. 6850. ISSN: 2041-1723. DOI: 10.1038/s41467-024-50860-6

7.1 Introduction

Metallo-polyelectrolyte complexes (MPECs) are a class of dynamic soft materials formed through reversible interactions between multivalent metal ions and charged polymer chains. In these systems, metal cations electrostatically associate with polyanionic backbones while also forming secondary metal–ligand coordination

interactions, thereby acting as labile crosslinkers whose coordination states can reorganize in response to changes in their environment [434, 435, 436]. The coupling between local metal coordination, polymer charge state, and chain conformation gives rise to distinctive macroscopic properties. For example, variations in the local coordination environment can produce markedly different mechanical responses [437, 438], while the identity and oxidation state of the metal ion can influence ionic transport [235]. This molecular-level tunability makes MPECs promising candidates for applications including ion-exchange filtration, responsive adhesion, biomedical devices, sensors, soft robotics, and recyclable or reprocessable materials [439, 440, 441, 442].

The properties of MPECs emerge across a broad hierarchy of length and time scales. At the molecular scale, the chemical nature and coordination geometry of the metal–polymer interaction determine the strength and lifetime of individual associations [434, 443, 444]. At larger scales, these associations alter the charge state, conformation, aggregation, and connectivity of the polymer chains, ultimately controlling the structure, mechanics, transport properties, and responsiveness of the material. These coupled processes are strongly affected by metal valency, solution pH, and solvent quality [445, 446]. In particular, pH does not merely change the number of charged groups on a weak polyelectrolyte; it also modifies the competition between protonation and metal binding. Consequently, the polymer ionization fraction, metal association, and phase behavior must generally be determined self-consistently rather than prescribed independently.

Developing a molecular understanding of this coupling remains challenging. Much of the theoretical literature on charged polymers has focused on complex coacervation between fully ionized polyelectrolytes in the presence of monovalent ions [122, 202, 90, 447, 322]. Comparatively fewer studies have considered weak polyelectrolytes interacting with multivalent counterions, for which ion binding can produce bridging, aggregation, precipitation, or gelation [448, 449, 450, 451]. Furthermore, many models specify the polymer charge fraction *a priori*, whereas experimental control is typically exerted through solution pH. Simulations and experiments have demonstrated that charge regulation can produce substantial and non-trivial changes in polyelectrolyte structure and material properties [452, 4]. A predictive description of MPECs must therefore account simultaneously for acid–base equilibria, multivalent metal association, and collective polymer behavior.

Direct molecular simulation provides a route to resolving some of these mechanisms

but introduces its own difficulties. All-atom simulations can describe local coordination chemistry in detail, yet the slow relaxation of polymer conformations and metal-mediated aggregates makes it difficult to access the length and time scales relevant to gel formation and mechanical response [453, 416]. Coarse-grained models, including those based on the Kremer–Grest representation, extend the accessible scales and have been widely used to investigate ionic aggregation and dynamics in charged polymers [183, 454, 455, 456]. However, computational cost still increases substantially with ion valency because of the strong electrostatic correlations and long-lived associations that must be sampled. Moreover, coarse-graining requires decisions about how chemically specific metal–ligand interactions should be represented. Models that neglect these interactions may miss important coordination effects, whereas overly detailed models can sacrifice the computational efficiency needed to investigate mesoscale organization.

The broader collaborative study motivating this chapter combined the fabrication and experimental characterization of homogeneous poly(acrylic acid)-based MPEC gels with theory and simulation across multiple scales. The experimental measurements establish how changes in pH, metal valency, and composition affect the structure and macroscopic response of the gels. The focus of the present chapter is the computational framework developed to interpret these observations and identify the molecular mechanisms underlying them. Rather than attempting to reproduce every aspect of the material within a single model, we employ a hierarchy of complementary theoretical and computational approaches, each designed to resolve a different level of the MPEC behavior.

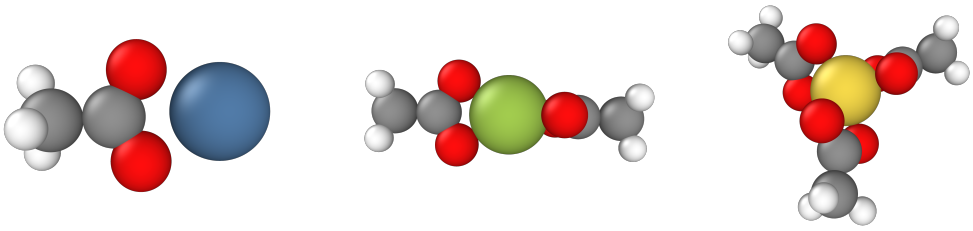
First, quantum-chemical calculations are used to examine the local interactions underlying metal–carboxylate association and to assess the physical assumptions employed in the reduced models (section 7.2). We next develop an association theory that couples protonation equilibria with multivalent metal binding, allowing the polymer charge state, extent of metal complexation, and phase behavior to be determined self-consistently (section 7.3). This theory provides a computationally efficient means of mapping broad changes in composition, pH, and ion valency and is used to guide the construction and interpretation of coarse-grained molecular dynamics simulations. These simulations then resolve the effects of metal-mediated association on polymer organization and dynamics at mesoscopic scales (section 7.4). Together, these methods connect local coordination chemistry to collective polymer behavior and provide a mechanistic basis for understanding

how chemical composition controls the structure and response of MPEC gels.

7.2 Metal–Ligand Binding

Before examining the mesoscale organization and macroscopic properties of MPEC gels, we first characterize the local interactions between metal ions and charged sites on the polymer backbone. In a purely electrostatic description, the behavior of a metal ion would be determined primarily by its valency and ionic radius. These are therefore the natural descriptors for constructing a chemically transferable coarse-grained model. However, such a description neglects ion-specific coordination effects and possible covalent contributions to metal–ligand binding, neither of which can be assessed directly within the coarse-grained framework. We therefore use electronic-structure calculations to determine whether valency and size provide an adequate first-order description of the metal–carboxylate interaction and to identify ions for which additional chemical specificity may be required.

Based on the benchmarks reported by Blaško, Pašteka, and Urban [457], the calculations were performed using the B3LYP density functional [458], together with the D3(BJ) dispersion correction [459] and the def2-TZVPP basis set [460, 461], as implemented in the ORCA quantum-chemistry package.



(a) Monovalent system (b) Divalent system (c) Trivalent system

Figure 7.1: Initial configurations used in all quantum chemistry calculations to obtain binding energies between acrylate and metal ions.

Binding energy

We first consider the binding of isolated acrylate ions to a series of metal cations. Poly(acrylic acid) is the primary polymer considered in the experimental MPEC system [4], making acrylate the simplest molecular representation of a charged site on the polymer backbone. Although this model neglects the connectivity and local environment of the polymer chain, it provides a computationally tractable means of comparing the intrinsic interactions of different metal ions with the carboxylate group.

For each metal ion, the number of acrylate ligands was chosen to balance its formal charge, as illustrated in Figure 7.3. This construction produces neutral complexes containing one, two, or three acrylate ions for monovalent, divalent, and trivalent metals, respectively. Solvation by water was represented implicitly using the conductor-like polarizable continuum model (CPCM) [462]. The resulting calculations should therefore be interpreted as a simplified comparison of metal–acrylate interactions rather than a complete description of the aqueous coordination environment, which may also contain explicitly coordinated water molecules and competing counterions.

The geometry of each metal–acrylate complex was first optimized, and its final electronic energy, E_{complex}, was calculated. The corresponding energy of the isolated metal ion, (E_m), was then obtained using the same level of theory and solvation model. Finally, the metal ion was removed from the optimized complex, after which the remaining acrylate ligands were re-optimized to obtain E_{acrylate}. The resulting binding energy was calculated as

$$\Delta E_{\text{bind}} = E_{\text{complex}} - E_m - E_{\text{acrylate}}, . \tag{7.1}$$

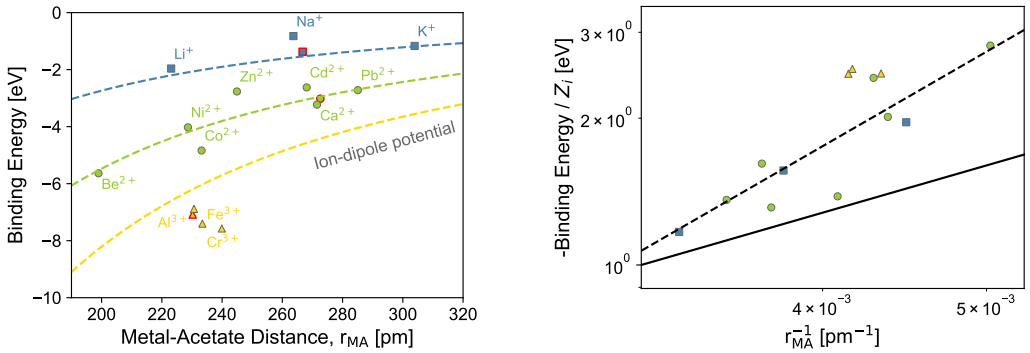
With this convention, a more negative value of ΔE_{bind} corresponds to stronger binding. Because both the complex and separated acrylate configurations are independently optimized, this quantity includes the energetic cost associated with reorganizing the ligands upon complex formation. The calculation procedure is illustrated in Figure 7.2. A characteristic contact separation was defined as the mean distance between the metal ion and the centers of mass of the acrylate ligands.



Figure 7.2: Visual representation of the process used to obtain binding energies from quantum chemistry calculations in the case of a divalent cation.

The calculated binding energies are shown in Figure 7.3. To assess their sensitivity to the choice of density functional, calculations for sodium, calcium, and aluminum were repeated using the long-range-corrected ωB97X-D3 functional [463, 464].

The two functionals produce similar binding energies for these representative ions, indicating that the qualitative trends are not strongly dependent on the selected functional.



(a) (b)

Figure 7.3: Binding energies obtained from quantum chemistry calculations. Symbols with a gray edge were calculated using the B3LYP-D3(BJ) functional and symbols with a red edge were calculated using the ωB97X-D3 functional. Dashed lines represent the predictions from the ion-dipole potential and the solid line represents predictions from the Coulombic potential.

The overall trends are consistent with a predominantly electrostatic picture: trivalent ions exhibit the strongest binding, whereas monovalent ions exhibit the weakest. When the binding-energy magnitude is normalized by the metal valency, the results approximately collapse onto a common curve, suggesting that the ionic charge provides the leading contribution to the variation in binding strength.

The binding-energy magnitude also decreases systematically with increasing metal–acrylate separation. Over the range of contact distances sampled here, the dependence is more closely described by an inverse-square scaling than by the inverse-distance scaling expected for a simple interaction between two point charges. An ion–dipole model, parameterized using the acrylate dipole moments obtained from the optimized structures, provides a particularly good description of the calculated values, as shown by the dashed curves in Figure 7.3b. This result suggests that the spatial distribution and orientation of charge within the carboxylate group are important even when the overall trends are dominated by metal valency.

This apparent inverse-square dependence should be regarded as an effective description of the short-range binding configurations rather than an asymptotic interaction law. At these separations, the metal ions interact with the distributed charge density of the carboxylate group, and the calculated energies also contain contributions

from ligand reorganization, continuum solvation, and ion-specific coordination. Nevertheless, the approximate collapse of the results demonstrates that a model based primarily on valency and an effective contact distance captures much of the variation among the metal ions considered.

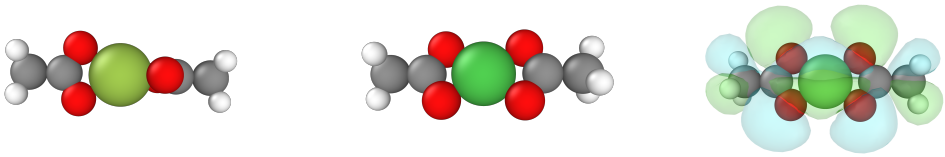
Electronic structure of the complexes

Although the binding energies are largely organized by metal valency and separation, several transition-metal ions exhibit additional electronic-structure effects. During optimization, the preferred spin multiplicities of the nickel, cobalt, iron, and chromium complexes differed from those of the corresponding isolated ions. This change indicates that coordination by the acrylate ligands alters the ligand-field environment and electronic structure of the metal center. It is therefore consistent with appreciable metal–ligand orbital mixing, although a change in spin state alone does not establish the formation of a particular covalent bond.

The distinction is particularly apparent for the divalent nickel and zinc complexes shown in Figure 7.4. Despite beginning from similar configurations in which the two carboxylate groups are approximately perpendicular, the optimized nickel complex adopts a more nearly coplanar arrangement. By contrast, the zinc complex retains a geometry that more effectively separates the negatively charged oxygen atoms. The planar geometry of the nickel complex is not favored by electrostatic interactions alone, because bringing the carboxylate groups into the same plane increases the proximity of their oxygen atoms.

Inspection of the molecular orbitals provides a possible explanation for this difference. As shown in Figure 7.4, the nickel complex contains an orbital with electron density delocalized across the metal center and the coordinating oxygen atoms. This metal–ligand orbital mixing provides a stabilizing contribution that is absent, or substantially weaker, for the closed-shell zinc ion. The additional stabilization can offset some of the electrostatic repulsion between the carboxylate groups and is also consistent with the moderately stronger binding calculated for nickel relative to other divalent ions of comparable size.

The corresponding differences are less pronounced among the trivalent complexes. In each case, the optimized geometry remains relatively similar to the initial configuration shown in Figure 7.1c, with the three acrylate ligands arranged around the central metal ion. For these complexes, the strong electrostatic repulsion among the negatively charged ligands places a substantial geometric constraint on the co-



(a) Zinc (b) Nickel (c) Nickel Molecular Orbital

Figure 7.4: Optimized complexes for zinc (7.4a) and nickel (7.4b) obtain from quantum chemistry calculations. Nickel molecular orbitals are shown in Figure 7.4c.

ordination environment, favoring configurations that maintain separation between the carboxylate groups. Consequently, metal-specific orbital interactions produce comparatively small changes in the optimized geometry.

The remaining differences in binding energy among trivalent ions may nevertheless contain contributions from ligand-field effects and metal–ligand orbital mixing. Overall, the calculations indicate that metal valency and contact separation capture the dominant variation in metal–acrylate binding, supporting their use as the principal descriptors in the coarse-grained model. Transition-metal complexes can exhibit additional coordination-specific interactions, however, and these effects represent a limitation of a purely electrostatic parametrization.

7.3 Phase Behavior and Gelation

In this section, we develop a theoretical framework for describing the phase behavior and gelation of MPECs as functions of metal valency, polymer charge density, and solution pH. We begin by reviewing the thermoreversible association model of Semenov and Rubinstein [93], which provides a useful conceptual description of gelation in polymers containing reversible "sticker" sites. We then extend this framework to MPECs by incorporating excluded-volume interactions, long-range electrostatic correlations, and association between multivalent metal ions and charged sites on the polymer backbone. Finally, we introduce charge regulation explicitly, allowing the polymer ionization state and metal coordination to be determined self-consistently from the pH and metal concentration. All calculations presented in this section were implemented in the open-source thermodynamic modelling package Clapeyron.jl [20]. This association-based approach parallels the ion-pairing framework used in Chapter 5: there, Wertheim theory separated local ion association from collective conductivity; here, an analogous separation of local metal–ligand binding from collective network mechanics is the key to isolating the crosslinker-to-binding-

site ratio as the relevant design variable.

Thermo-reversible gelation in associating polymers

We first review the theory of thermoreversible gelation developed by Semenov and Rubinstein [93]. In this model, each polymer contains N monomers and f reversible association sites, or stickers. The mean number of monomers separating neighboring stickers is

$$\ell = \frac{N}{f},, \tag{7.2}$$

and is assumed to satisfy $\ell \gg 1$. Each sticker can form a reversible bond with another sticker, with an association energy ϵ. A schematic representation of this model is shown in Figure 7.5.

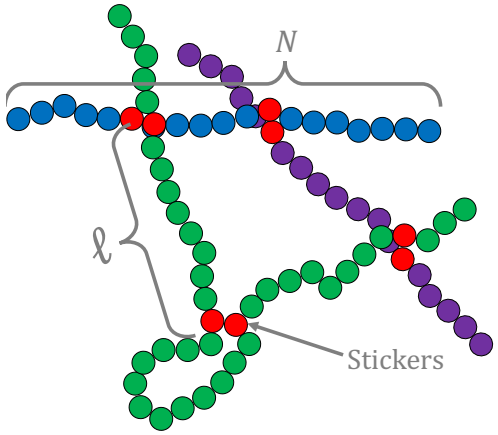


Figure 7.5: Visual representation of associating polymers of length N with sticker spacing ℓ. Colors have been used to distinguish between chains.

The Helmholtz free-energy density is decomposed into three contributions:

$$F = F_{\text{ref.}} + F_{\text{int.}} + F_{\text{st.}},, \tag{7.3}$$

where $F_{\text{ref.}}$ is the ideal-chain reference contribution, $F_{\text{int.}}$ describes non-specific monomer interactions, and $F_{\text{st.}}$ accounts for reversible sticker association. The ideal-chain reference is written as:

$$\frac{F_{\text{ref.}}}{k_{\text{B}}T} = -\frac{1}{V}\ln Z_{\text{ref.}} = \frac{c}{N}\ln\left(\frac{c}{eN}\right) \tag{7.4}$$

where k_{B}, T, V and c are the Boltzman constant, temperature, volume and monomer concentration, respectively. Non-specific monomer interactions are represented through a virial expansion,

$$\frac{F_{\text{int.}}}{k_{\text{B}}T} = \frac{v}{2}c^2 + \frac{w}{6}c^3\,, \tag{7.5}$$

where v and w are the excluded volume and three-body interaction parameters, respectively. To construct the sticker contribution, consider a system in which N_p sticker pairs are formed from a total of $N_{\text{st.}}$ stickers. Relative to the non-associating reference system, the partition function is

$$Z_{\text{st.}} = Z_{\text{ref.}} P_{\text{comb.}} W \exp\left(\beta\epsilon N_p\right), \tag{7.6}$$

where $\beta = 1/(k_{\text{B}}T)$. The number of distinct ways of selecting N_p sticker pairs is:

$$P_{\text{comb.}} = \frac{N_{\text{st.}}!}{(N_{\text{st.}} - 2N_p)!N_p!2^{N_p}}, \tag{7.7}$$

and W is the probability of all paired stickers being found close enough to one another, neglecting the presence of the association interaction:

$$W = \left(\frac{v_{\text{b}}}{V}\right)^{N_p}, \tag{7.8}$$

where v_b is the so-called bond volume. Using Stirling's approximation and minimizing the total free energy with respect to the number of pairs N_p, it is possible to obtain a simplified expression for the total free energy:

$$\frac{F}{k_{\text{B}}T} = \frac{c}{N}\ln\left(\frac{c}{eN}\right) + \frac{v}{2}c^2 + \frac{w}{6}c^3 + \frac{c}{\ell}\left(\frac{p}{2} + \ln(1-p)\right), \tag{7.9}$$

where p is the fraction of stickers paired, given by:

$$p = 1 - \frac{\sqrt{4(c\lambda)/\ell + 1} - 1}{2(c\lambda)/\ell}, \tag{7.10}$$

and λ can be thought of as the association strength, given by:

$$\lambda = v_b \exp\left(\beta\epsilon\right). \tag{7.11}$$

Using equation 7.9, it is possible to apply the conditions for phase equilibria (in this case, equality of chemical potential and osmotic pressure) to trace the phase boundary, as shown in Figure 7.6 (assuming we have a θ-solvent). The gel boundary can be estimated using the Stockmayer percolation criterionStockmayer [465]:

$$c_{\text{gel}} = \frac{\ell}{\lambda}\frac{(f-1)}{(f-2)^2}, \tag{7.12}$$

where c_{gel} is the concentration at the gel point. As discussed more rigorously in Semenov and Rubinstein [93]'s work, the above expression is only valid in the θ-solvent limit.

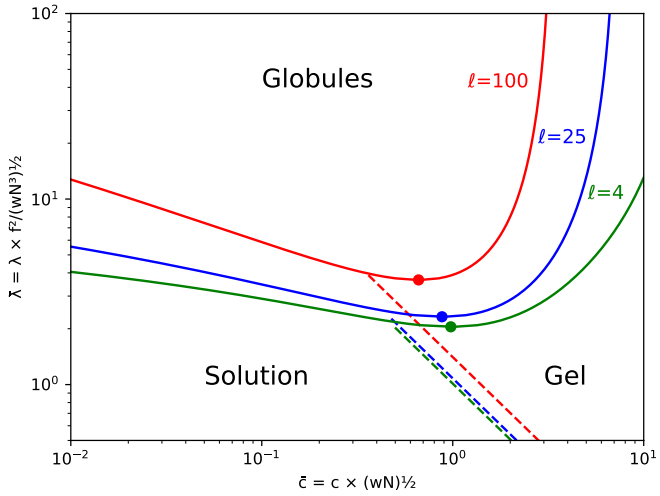


Figure 7.6: Phase diagram obtained from equation 7.9 where colors represent different sticker spacings, solid lines refer to the two-phase boundary and the dashed lines refer to the gel curve.

The model provides several useful qualitative insights into reversible crosslinking. At large λ, strong association drives separation into a polymer-rich phase and an extremely dilute supernatant. In the strong-association limit, Semenov and Rubinstein [93] interpreted the polymer-rich phase as a population of dense globules. Weakening the association narrows the coexistence region until the critical point is reached. At sufficiently high polymer concentration, a homogeneous percolated gel can then be obtained. Further reduction of λ eventually suppresses gelation and produces a homogeneous polymer solution. In the context of MPECs, changes in λ may represent changes in metal–ligand affinity, temperature, solvent dielectric response, or other environmental variables that modify the effective crosslink strength.

Decreasing ℓ, and therefore increasing the density of stickers along the chain, broadens the two-phase region and shifts the gel boundary towards lower polymer concentrations. The shift in the gel boundary follows directly from the increased number of possible intermolecular bonds. The enhanced phase separation reflects the larger associative contribution to the free energy when more stickers are available.

The simple theory nevertheless has important limitations when applied to MPECs. Its dimensionless association parameter cannot be mapped uniquely onto metal valency, ionic radius, or solvent dielectric properties. The model also treats each sticker bond as a one-to-one association. It therefore naturally represents a divalent crosslinker that bridges two polymer sites but does not distinguish the additional

coordination states available to trivalent ions. Moreover, excluded-volume and electrostatic interactions are represented only through phenomenological virial coefficients. While Danielsen and others[466, 467, 468, 469, 470, 471] have developed extensions of the Semenov and Rubinstein approach to improve upon these approximations, we directly address these limitations below by introducing an explicit molecular description of the polymer segments, mobile ions, and metal-mediated associations.

Multivalent, cation-mediated crosslinks in polyelectrolyte gels

Free-energy model

We retain ideal, non-interacting chains as the reference system but introduce three additional physical contributions (as done in prior chapters): excluded-volume interactions, long-range electrostatic correlations, and short-range association between charged polymer sites and multivalent metal ions. The resulting free energy is

$$F = F_{\text{id.}} + F_{\text{exc.}} + F_{\text{ele.}} + F_{\text{assoc.}} \,. \tag{7.13}$$

A schematic representation of the model is shown in Figure 7.7.

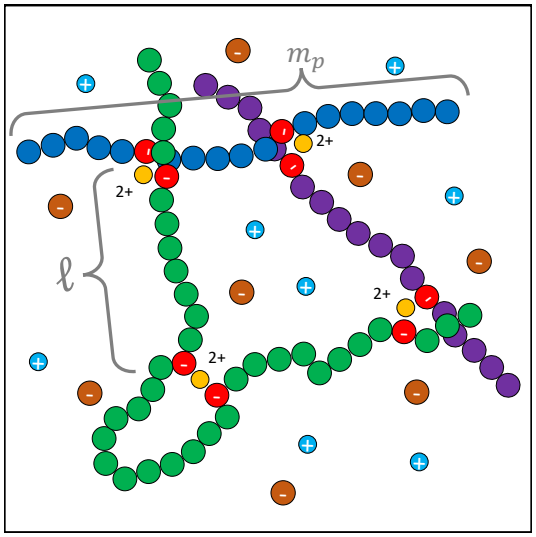


Figure 7.7: Visual representation of the proposed theory. Colors have been used to distinguish between chains. Charged sites on the polymer backbone have been highlighted in red. The metal crosslinker, polyelectrolyte counter-ion and metal co-ion have been highlighted in yellow, light blue and brown, respectively.

To describe excluded-volume interactions and polymer connectivity, we adopt a hard-chain reference inspired by Statistical Associating Fluid Theory [472]. Each

species is represented as a chain of m_i tangent hard-sphere segments of diameter σ_i. The hard-chain contribution is

$$\frac{F_{\text{exc.}}}{Nk_{\text{B}}T} = \bar{m}\frac{F_{\text{HS}}}{Nk_{\text{B}}T} - \sum_i x_i(m_i - 1)\ln\left[g_{\text{HS}}(\sigma_i)\right], \tag{7.14}$$

where x_i, m_i, and σ_i are the mole fraction, number of segments, and segment diameter of species i, respectively. The mean number of segments per molecule is

$$\bar{m} = \sum_i x_i m_i. \tag{7.15}$$

From this point onwards, N denotes the total number of molecular species in the system rather than the polymer chain length.

The hard-sphere contribution, F_{HS}, is represented using the Boublík–Mansoori–Carnahan–Starling–Leland equation of state [473, 162]:

$$\frac{F_{\text{HS}}}{Nk_{\text{B}}T} = \frac{1}{\zeta_0}\left[\frac{3\zeta_1\zeta_2}{1-\zeta_3} + \frac{\zeta_2^3}{\zeta_3(1-\zeta_3)^2} + \left(\frac{\zeta_2^3}{\zeta_3^2} - \zeta_0\right)\ln(1-\zeta_3)\right], \tag{7.16}$$

where the moment densities are

$$\zeta_n = \frac{\pi}{6}\rho\sum_i x_i m_i \sigma_i^n, \qquad n \in 0, 1, 2, 3, \tag{7.17}$$

and $\rho = N/V$ is the total molecular number density. The corresponding hard-sphere contact distribution function is approximated as

$$g_{\text{HS}}(\sigma_i) = \frac{1}{1-\zeta_3} + \frac{\sigma_i}{2}\frac{3\zeta_2}{(1-\zeta_3)^2} + \frac{\sigma_i^2}{4}\frac{2\zeta_2^2}{(1-\zeta_3)^3}. \tag{7.18}$$

Unlike the treatment of Zhang et al. [88], we use the hard-sphere contact function in Equation 7.14 only to describe covalent chain formation. In their model, every segment in the polymer chain is charged. In the present work, charged sites are separated by ℓ nominally neutral segments. Directly bonded segments therefore interact through the hard-chain reference, while electrostatic interactions between more distant charged sites are accounted for separately.

This separation becomes less accurate when the charged sites are sufficiently close that strong electrostatic correlations occur over only a few backbone segments. We therefore avoid applying the model in the limit where the charge spacing is smaller than, or comparable to, the electrostatic screening length.

The electrostatic contribution, $F_{\mathrm{ele.}}$, is represented using a finite-size Debye–Hückel expression:

$$\frac{F_{\mathrm{ele.}}}{N k_{\mathrm{B}} T} = -\frac{\rho}{3} l_{\mathrm{B}} \kappa \sum_i x_i f_i Z_i^2 \chi(\kappa \sigma_i), \tag{7.19}$$

where f_i is the number of charged sites on species i, and Z_i is the valency of each charged site. The Bjerrum length is

$$l_{\mathrm{B}} = \frac{\beta e_c^2}{4\pi \epsilon_0 \epsilon_{\mathrm{r}}}, \tag{7.20}$$

where e_c is the elementary charge, ϵ_0 is the vacuum permittivity, and ϵ_{r} is the relative dielectric constant of the medium. The inverse Debye screening length is

$$\kappa^2 = 4\pi l_{\mathrm{B}} \rho \sum_i x_i f_i Z_i^2. \tag{7.21}$$

The finite-size correction is

$$\chi(y) = \frac{3}{y^3}\left[\frac{3}{2} + \ln(1+y) - 2(1+y) + \frac{1}{2}(1+y)^2\right]. \tag{7.22}$$

Several approximations accompany the Debye–Hückel treatment. Most importantly, the electrostatic potential is linearized, and detailed ion-pair and chain-connectivity correlations are neglected. For sparsely charged polymers, intramolecular correlations between neighboring charged sites are expected to be weak when their separation substantially exceeds the electrostatic screening length. In a freely jointed-chain picture, this corresponds approximately to the condition $\kappa \ell \sigma \gg 1$. The approximation becomes progressively less reliable as the charge spacing decreases or the electrostatic coupling increases.

The solvent is also treated as a uniform dielectric continuum. Because the present calculations focus on a single temperature and do not attempt to predict solvent or

salt partitioning quantitatively, the dielectric inhomogeneity discussed in Chapter 2 is not included.

An implicit-solvent mean-spherical approximation could alternatively be used to describe the electrostatic contribution, as in Zhang et al. [88] and Ylitalo et al. [90]. Based on the analysis of Maribo-Mogensen, Kontogeorgis, and Thomsen [474], some of the differences between the MSA and Debye–Hückel expressions can be represented through an effective rescaling of the ion diameters. Because the present objective is to identify qualitative trends, and because the Debye–Hückel expression is less computationally demanding, we retain the latter.

For the association contribution, we assume that a metal ion contains $f_m = Z_m$ equivalent association sites. This imposes the condition that the ion cannot coordinate more monovalent polymer charges than are required to compensate its formal valency. Once the local complex is neutral, coordination by an additional negatively charged site is assumed to be energetically unfavorable. Each charged site on the polymer acts as a monovalent association site, giving f_p association sites per polymer chain.

The sticker free energy of Semenov and Rubinstein [93] can be recovered from first-order Wertheim thermodynamic perturbation theory in the ideal-reference and strong-association limits, where $g(r) \approx 1$, as discussed in Chapter 1. In the present model, however, association occurs in a reference fluid containing both excluded-volume and electrostatic correlations. We therefore retain the reference pair distribution function explicitly.

Let $\rho_i(\mathbf{r}_i)$ denote the local density of association sites of type i:

$$\rho_i(\mathbf{r}_i) = \frac{N_i(\mathbf{r}_i) f_i}{V}, \tag{7.23}$$

where $N_i(\mathbf{r}_i)$ denotes the local population of species i. If a fraction of the sites are associated, the local density of unassociated sites is

$$\rho_{i0}(\mathbf{r}_i) = \frac{N_i(\mathbf{r}_i) f_i}{V} X_i(\mathbf{r}_i), \tag{7.24}$$

where $X_i(\mathbf{r}_i)$ is the local fraction of sites of type i that remain unbound.

The free-energy change associated with polymer–metal bonding is then

$$\frac{F_{\text{assoc.}}}{k_{\text{B}}T} = \sum_i \int \rho_i(\mathbf{r}_i) \ln\left(\frac{\rho_{i0}(\mathbf{r}_i)}{\rho_i(\mathbf{r}_i)}\right) + \rho_i(\mathbf{r}_i) - \rho_{i0}(\mathbf{r}_i) d\mathbf{r}_i \tag{7.25}$$
$$- \int\int \rho_{p0}(\mathbf{r}_p)\rho_{m0}(\mathbf{r}_m) g(r_{pm}) f(r_{pm}) d\mathbf{r}_p d\mathbf{r}_m \,,$$

where the indices p and m denote polymer and metal association sites, respectively, and r_{pm} is their separation. The reference pair distribution function is $g(r)$, while the Mayer function is

$$f(r) = [\exp -\beta\phi(r) - 1] \,, \tag{7.26}$$

where $\phi(r)$ is the potential characterizing the association interaction. For a homogeneous system, the association free energy simplifies to:

$$\frac{F_{\text{assoc.}}}{k_{\text{B}}T} = \sum_i \left[\rho_i \ln\left(\frac{\rho_{i0}}{\rho_i}\right) + \rho_i - \rho_{i0}\right] \int d\mathbf{r}_i \tag{7.27}$$
$$- \rho_{p0}\rho_{m0} \int\int g(r_{pm}) f(r_{pm}) d\mathbf{r}_p d\mathbf{r}_m \,,$$

$$\frac{F_{\text{assoc.}}}{k_{\text{B}}T} = \sum_i N_i f_i \left[\ln X_i + 1 - X_i\right] \tag{7.28}$$
$$- 4\pi\rho_{p0}\rho_{m0} V \int g(r_{pm}) f(r_{pm}) r_{pm}^2 dr_{pm} \,,$$

$$\frac{F_{\text{assoc.}}}{N k_{\text{B}}T} = \sum_i x_i f_i \left[\ln X_i + 1 - X_i\right] - \rho x_p x_m f_p f_m X_p X_m \Delta_{pm} \,. \tag{7.29}$$

For clarity, the association strength is defined as

$$\Delta_{pm} = 4\pi \int g(r_{pm}) f(r_{pm}) r_{pm}^2 dr_{pm} \,. \tag{7.30}$$

Minimizing equation 7.29 with respect to all X_i, we obtain:

$$\frac{\partial}{\partial X_p}\left(\frac{F_{\text{assoc.}}}{N k_{\text{B}}T}\right) = x_p f_p \left[\frac{1}{X_p} - 1\right] - \rho x_p x_m f_p f_m X_m \Delta_{pm} = 0 \,, \tag{7.31}$$

$$\frac{\partial}{\partial X_m}\left(\frac{F_{\text{assoc.}}}{N k_{\text{B}}T}\right) = x_m f_m \left[\frac{1}{X_m} - 1\right] - \rho x_p x_m f_p f_m X_p \Delta_{pm} = 0 \,. \tag{7.32}$$

These relations can be rearranged to give the mass-action equations

$$X_p = \frac{1}{1 + \rho x_m f_m \Delta_{pm} X_m} \,, \tag{7.33}$$

$$X_m = \frac{1}{1 + \rho x_p f_p \Delta_{pm} X_p} \,. \tag{7.34}$$

Substituting these expressions to equation 7.29 will give:

$$\frac{F_{\text{assoc.}}}{Nk_{\text{B}}T} = \sum_i x_i f_i \left[\ln X_i + \frac{1 - X_i}{2} \right] . \tag{7.35}$$

At this stage, we note the similarities between equation 7.35 and the sticker contri-

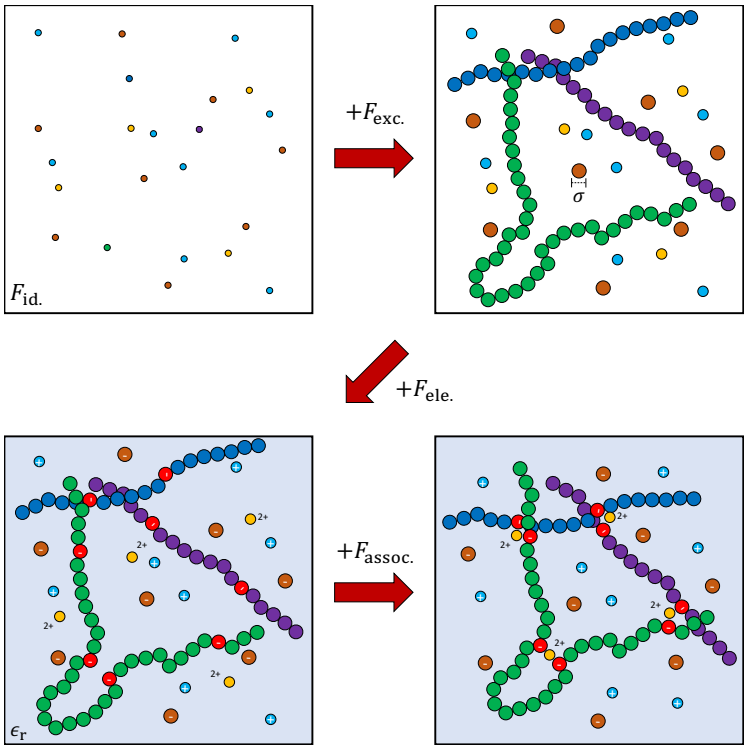


Figure 7.8: Summary of the impact of each term in the proposed theory. The dielectric medium is represented with a change in the background color. Color scheme is identical to that in Figure 7.7.

bution in equation 7.9. If the polymer sites were allowed to associate directly and $p = 1 - X_p$, the expression of Semenov and Rubinstein [93] would be recovered. The principal distinction is that Δ_{pm} now depends on the structure of a charged hard-sphere reference fluid.

For the attractive interaction between a metal ion of valency Z_m and a monovalent, negatively charged polymer site, we use

$$\phi(r_{pm}) = \frac{l_{\text{B}} Z_m}{r_{pm}} . \tag{7.36}$$

The corresponding Mayer function is

$$f(r_{pm}) = \exp\left(\frac{l_{\text{B}} Z_m}{r_{pm}} \right) - 1. \tag{7.37}$$

Analytical approximations for the pair distribution function of charged hard spheres can be obtained from the MSA [98], including the exponential approximation introduced by Jiang et al. [124]. Direct numerical evaluation of Equation 7.30, however, would be inconvenient during repeated phase-equilibrium calculations.

Following common SAFT practice, we therefore evaluate the pair distribution function and Mayer function at contact and absorb the remaining configurational integral into an effective bonding volume:

$$\Delta_{pm} = \kappa_{pm}\sigma_{pm}^3 g^{\mathrm{EXP}}(\sigma_{pm}) \left[\exp\left(\frac{l_{\mathrm{B}} Z_m}{\sigma_{pm}}\right) - 1\right]. \tag{7.38}$$

Here, $\kappa_{pm}\sigma_{pm}^3$ represents the effective volume over which a polymer site and metal ion are considered bonded. The complete hierarchy of free-energy contributions is summarized in Figure 7.8.

Definition of phase equilibrium

Consider a system with overall species densities ρ_{i0} that separates into phases α and β. The total Helmholtz free-energy density, $\Psi = F/V$, is

$$\Psi = \varphi\Psi_\alpha(\boldsymbol{\rho}_\alpha, T) + (1-\varphi)\Psi_\beta(\boldsymbol{\rho}_\beta, T)\,, \tag{7.39}$$

where φ is the volume fraction of phase α and $\boldsymbol{\rho}_j$ is the vector containing the density of each species in phase j. In order to conserve the total density of each species, we must introduce the Lagrangian multiplier, μ_i, for each species. Furthermore, as we are now including charged species, we must ensure electroneutrality in all phases. Given the input densities must satisfy electroneutrality, then we only require one more Lagrangian multiplier, ψ, to ensure this will be satisfied. As a result, the total Lagrangian for this system is:

$$\begin{aligned}\mathcal{L} = {} & \varphi\Psi_\alpha(\boldsymbol{\rho}_\alpha, T) + (1-\varphi)\Psi_\beta(\boldsymbol{\rho}_\beta, T) \\ & + \sum_i \mu_i(\varphi\rho_{i\alpha} + (1-\varphi)\rho_{i\beta} - \rho_{i0}) \\ & + \psi\varphi\sum_i \rho_{i\alpha} f_i Z_i\,.\end{aligned} \tag{7.40}$$

To determine the composition of each phase, we must minimize equation 7.40 with respect to all densities (ρ_{ij}), volume fraction (φ), and all Lagrangian multipliers. In

doing so, we find the following system of equations:

$$\mu_i = \frac{\partial \Psi_\alpha}{\partial \rho_{i\alpha}} + \psi f_i Z_i = \frac{\partial \Psi_\beta}{\partial \rho_{i\beta}}\,, \qquad \forall i \tag{7.41}$$

$$0 = \Psi_\alpha - \Psi_\beta + \sum_i \mu_i(\rho_{i\alpha} - \rho_{i\beta}) + \psi \sum_i \rho_{i\alpha} f_i Z_i\,, \tag{7.42}$$

$$0 = \varphi\rho_{i\alpha} + (1-\varphi)\rho_{i\beta} - \rho_{i0}\,, \qquad \forall i \tag{7.43}$$

$$0 = \sum_i \rho_{i\alpha} f_i Z_i\,. \tag{7.44}$$

The multipliers μ_i are related to the species chemical potentials, while ψ represents the electrostatic potential difference required to maintain electrochemical equilibrium between phases with different ionic compositions.

Phase behavior of polyelectrolytes with multivalent counter-ions

We first consider an idealized system in which the multivalent metal ion is itself the polymer counterion. No monovalent polymer counterions or metal-salt co-ions are present. We additionally assume that all species have the same segment diameter:

$$\sigma_p = \sigma_m = \sigma. \tag{7.45}$$

The system can then be described using the total reduced density

$$\bar{\rho} = \sigma^3 \sum_i \rho_i \tag{7.46}$$

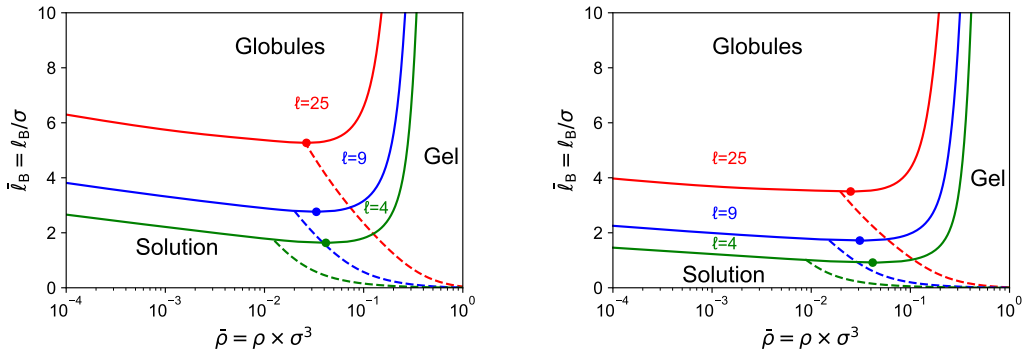
and the reduced Bjerrum length:

$$\bar{l}_\mathrm{B} = l_\mathrm{B}/\sigma \tag{7.47}$$

The calculated phase diagrams for divalent and trivalent counterions are shown in Figure 7.9.

The gel curve is also included in Figure 7.9. Following the reasoning of Stockmayer [465], we define the gel point through

$$(1-X_m)\sum_{i=2}^{Z_m}\binom{Z_m}{i}\frac{N-(i-1)\ell}{\ell}(1-X_p)^{i-1}X_p^{(Z_m-i)} = 1\,. \tag{7.48}$$



(a) Divalent system

(b) Trivalent system

Figure 7.9: Phase diagram for polyelectrolytes with divalent (7.9a) and trivalent (7.9b) counter-ions. Curve colors and styles are identical to Figure 7.6. In all cases, the bonding volume has been set to 10 and the chain length is set to 1000.

This equation is applicable to both divalent and trivalent systems. It assumes that the association sites on a metal ion are equivalent and that successive polymer–metal bonds form independently. In reality, each additional bond modifies the local electrostatic and steric environment. The association energies of the first, second, and third bonds are therefore unlikely to be identical. This limitation is addressed more explicitly in Section 7.3.

The phase diagrams retain the qualitative structure of the reversible-sticker model, with $\bar{l}$B playing a role analogous to $\ln\lambda$. Phase separation occurs above a critical electrostatic coupling strength, and the critical $\bar{l}$B decreases as the separation between charged sites is reduced. Increasing the linear charge density strengthens both electrostatic correlations and metal-mediated association, thereby stabilizing the polymer-rich phase.

These trends are consistent with the calculations of Zhang et al. [88], who predicted somewhat lower critical Bjerrum lengths for fully charged polymer chains. Because every segment in their model was charged, the electrostatic correlations were stronger than in the sparsely charged systems considered here.

The excluded-volume contribution prevents indefinite collapse of the polymer-rich phase. Numerically, the dense branch approaches the hard-sphere free-energy singularity at $\zeta_3 \to 1$, corresponding to $\bar{\rho} \to 6/\pi$ for equal-sized segments. This value should not be interpreted as the physical close-packing density of hard spheres. Rather, it reflects the divergence built into the hard-sphere equation of state.

The predicted dilute-phase densities can become extremely small, in some cases

reaching values of order 10^{-60}. Such values expose a limitation of the monomeric description of the dilute phase. Small, approximately neutral polymer–ion clusters would contribute substantially to the supernatant concentration but are not treated as distinct species in the present theory. Cluster formation has previously been shown to increase predicted supernatant concentrations substantially [322].

Excluded volume also changes the low-$\bar{l}_B$ behavior of the gel boundary. Unlike the corresponding result from the ideal sticker model in Figure 7.6, the gel curves bend towards the hard-sphere divergence as the electrostatic attraction is removed. In this weak-association limit, network formation can occur only at extremely high polymer concentrations, where the chains are forced into close proximity.

Increasing the counterion valency from two to three substantially lowers the critical Bjerrum length. Trivalent ions produce stronger electrostatic correlations and can connect a larger number of polymer sites, both of which favor condensation. The dense-phase density changes comparatively little because it is constrained by excluded volume, whereas the predicted supernatant density decreases strongly.

The trivalent system also gels at lower polymer concentrations. This shift arises from both the stronger polymer–metal association and the larger number of configurations through which a trivalent ion can connect multiple polymer sites. These qualitative trends are consistent with the greater propensity of trivalent ions to form strongly crosslinked gels and dense aggregates experimentally.

The reduced variables can be mapped approximately onto experimentally relevant conditions. Taking $\sigma \approx 0.4$ nm, consistent with common coarse-grained mappings [456], gives $\bar{l}_B \approx 1.8$ for water near ambient conditions. Within the assumptions of the model, this coupling is insufficient to produce phase separation for many of the divalent systems in Figure 7.9a, whereas several trivalent systems in Figure 7.9b lie inside the predicted coexistence region.

This observation is consistent with the experimental difficulty of preparing homogeneous trivalent MPEC gels through conventional solution casting, where rapid association can instead produce dense aggregates or globules. Furthermore, forming gels with large charge spacings requires relatively high polymer concentrations at these conditions.

Adding glycerol reduces the dielectric constant of the medium and therefore increases the Bjerrum length. For the chosen segment size, a reduced Bjerrum length of approximately 3–4 is representative of a glycerol-rich environment. The theory

consequently predicts that glycerol can reduce the polymer concentration required for gelation. This interpretation is qualitative because glycerol may also modify solvent quality, ion solvation, viscosity, and metal coordination. Nevertheless, Figure 7.9 motivates the range $\bar{l}_B \approx 1.8$–4 explored in the coarse-grained simulations described in Section 7.4.

Phase behavior of polyelectrolytes with multivalent salts

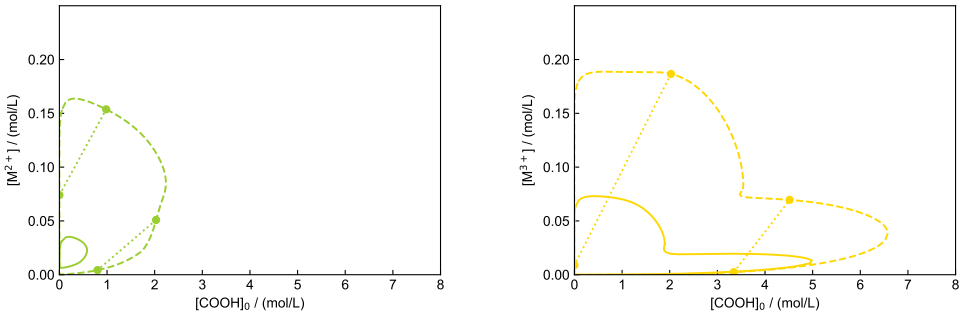
A more experimentally representative system contains a weak polyelectrolyte with monovalent counterions together with an added multivalent salt. The salt contributes both multivalent metal cations and monovalent co-ions. Even this case has not been studied in much depth experimentally or theoretically[448, 451, 4]. The definition for phase equilibria in this system remain identical to that in equation 7.40 and we can re-use our definition for the gel point from equation 7.48. As such, we are able to produce Figure 7.10.

For monovalent polyelectrolyte solutions without specific metal association, the coexistence region is generally approximately parabolic or elliptical, with tie lines lying primarily along the polymer-density direction [310, 88]. The metal-associating systems in Figure 7.10 exhibit qualitatively different behavior. Their tie lines are strongly diagonal, indicating coupled partitioning of polymer and metal ions.

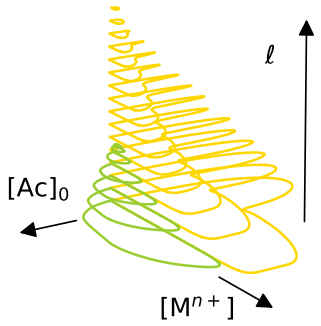
At the large Bjerrum length used here, most multivalent ions that enter the polymer-rich phase are strongly associated with charged polymer sites. The polymer and metal ions therefore partition together, while the unassociated monovalent counterions and salt co-ions preferentially remain in the dilute phase. Trivalent ions produce a larger coexistence region because their association is stronger and their higher functionality provides a greater free-energy gain from forming a polymer-rich network.

The trivalent system in Figure 7.10b additionally exhibits a narrow indentation in the coexistence envelope at high polymer density and low metal concentration. In this region, coexistence occurs between two polymer-rich phases with similar overall polymer concentrations but different metal contents. The behavior reflects competition between the energetic gain obtained through metal coordination and the translational and configurational entropy favored by a less-associated polymer phase.

One of these coexisting phases can lie above the estimated gel boundary while



(a) (b)



(c)

Figure 7.10: Phase diagram for polyelectrolytes + divalent (a) and trivalent (b) salts. Solid and dashed lines represent the phase envelope at high and low pH, respectively, while dotted lines dotted curves represent tie-lines. The bonding volume has been set to 10, the dimensionless Bjerrum length is set to 10 and the chain length is set to 1000. A 3D projection with varying charge spacing is shown in (c).

the other lies below it, as shown in Figure 7.10b. The theory therefore admits coexistence between a percolated and a non-percolated polymer-rich phase. In a sufficiently concentrated and entangled material, this could manifest as a gel-in-gel morphology. This interpretation remains a structural hypothesis because the equilibrium free-energy model does not explicitly describe rheology, network elasticity, or kinetic arrest. Figure 7.11 summarizes the combined phase and gelation behavior for both divalent and trivalent systems, highlighting the correspondingly larger coexistence and gelation regions obtained for trivalent ions.

Within the present model, pH is represented indirectly through the prescribed separation between charged polymer sites. Decreasing ℓ, corresponding to increasing the polymer ionization fraction, substantially enlarges the coexistence region while

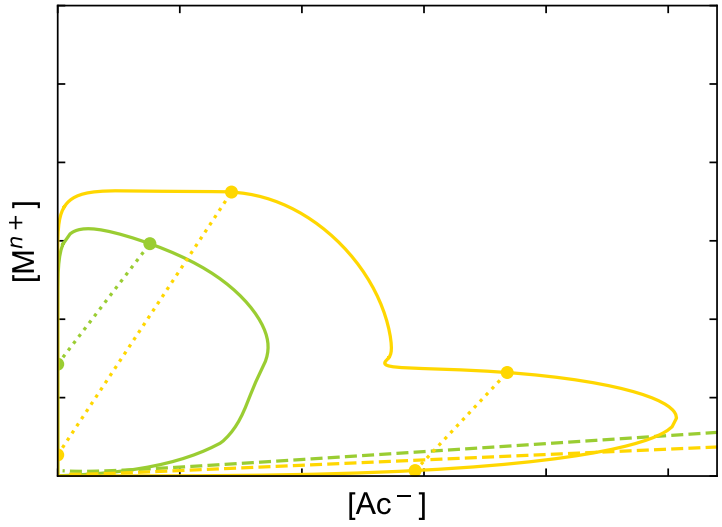


Figure 7.11: Phase diagram for polyelectrolytes + divalent and trivalent salts. Solid lines represent the phase envelope, dashed lines represent the gelation curve and dotted lines dotted curves represent tie-lines. The bonding volume has been set to 10, the dimensionless Bjerrum length is set to 10 and the chain length is set to 1000.

retaining its overall shape. At sufficiently large ℓ, corresponding to low polymer ionization, the electrostatic and associative driving forces become too weak to produce phase separation.

Effect of pH in polyelectrolytes

The preceding calculations prescribe the charge spacing ℓ independently of the metal concentration. For a weak polyelectrolyte, however, the ionization fraction is controlled by the solution pH and responds to the local electrostatic and chemical environment.

For an isolated monoprotic acid site, the Henderson–Hasselbalch relation is

$$\mathrm{pH} - \mathrm{p}K_\mathrm{a} = \log_{10}\left(\frac{\alpha}{1-\alpha}\right), \tag{7.49}$$

where α is the fraction of ionized sites. If every polymer segment can ionize and the mean charge spacing is defined as $\ell = 1/\alpha$, then

$$\ell = 1 + 10^{\mathrm{p}K_\mathrm{a} - \mathrm{pH}}. \tag{7.50}$$

In the low-ionization limit, $\ell \gg 1$, this reduces to

$$\mathrm{pH} - \mathrm{p}K_\mathrm{a} \simeq -\log_{10}\ell. \tag{7.51}$$

Metal binding couples directly to this acid–base equilibrium. Association stabilizes the deprotonated state and thereby shifts the ionization equilibrium towards additional deprotonation [356, 392]. Consequently, the polymer charge fraction cannot generally be specified independently of the metal concentration or valency.

In this section, we therefore extend the preceding model to describe the coupled effects of solution pH, metal concentration, and metal valency on polymer ionization and gel formation.

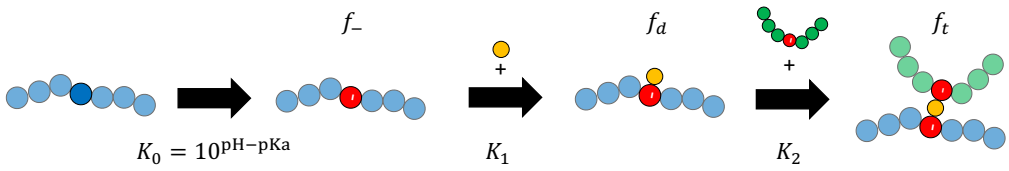


Figure 7.12: Visual representation of the possible associations of a weak polyelectrolyte in the presence of multivalent cations. Association constants are denoted by K_i and the fraction of polymers existing in state i are denoted by f_i. Color scheme is identical to Figure 7.8.

Theory

We consider the association states illustrated in Figure 7.12. A divalent ion can bind one or two polymer sites, whereas a trivalent ion can additionally bind a third site. These reactions are treated as sequential and reversible.

Consider a polymer containing m_p ionisable sites, of which m_- are deprotonated. The partition function associated with protonation is

$$Z_- = Z_{\mathrm{ref.}} P_{-,\mathrm{comb.}} K_0^{m_-} , \tag{7.52}$$

where $Z_{\mathrm{ref.}}$ is our reference partition function. The combinatorial term, $P_{-,\mathrm{comb.}}$ is given by:

$$P_{-,\mathrm{comb.}} = \frac{m_p!}{(m_p - m_-)! m_-!} . \tag{7.53}$$

The intrinsic acid–base equilibrium constant is represented as

$$K_0 = \rho_p 10^{(\mathrm{pH\text{-}pKa})} . \tag{7.54}$$

If we were to minimize equation 7.52 with respect to m_- and define a new variable, $f_- = m_-/m_p$, we would recover the Henderson–Hasselbach equation:

$$\mathrm{pH\text{-}pKa} = -\log\left(\frac{f_-}{1 - f_-}\right) . \tag{7.55}$$

We next suppose that m_d metal ions each form an initial bond with one of the m_- deprotonated polymer sites. Taking Z_- as the reference, the corresponding partition function is

$$Z_d = Z_- P_{d,\mathrm{comb.}} K_1^{m_d}\,, \tag{7.56}$$

where the combinatorial term is given by:

$$P_{d,\mathrm{comb.}} = \frac{m_-!}{(m_- - m_d)!m_d!}\frac{m_m!}{(m_m - m_d)!m_d!}m_d!\,. \tag{7.57}$$

The factor $m_d!$ counts the number of ways of pairing the selected metal ions with the selected polymer sites. Following from equation 7.38, the equilibrium constant for the first polymer–metal association is

$$K_1 = \rho_p \kappa_d \sigma_{pm}^3 g^{\mathrm{EXP}}(\sigma_{pm}) \left[\exp\left(\frac{l_\mathrm{B} Z_m}{\sigma_{pm}}\right) - 1\right], \tag{7.58}$$

where κ_d is the bonding-volume parameter for the first association.

The same construction can be applied to a second polymer site binding to a metal–polymer dimer and, for a trivalent ion, to a third site binding to the resulting three-body complex. The combined partition function is

$$Z_q = Z_{\mathrm{ref.}} K_0^{m_-} K_1^{m_d} K_2^{m_t} K_3^{m_q} \frac{m_p! m_m!}{(m_p - m_-)!(m_m - m_d)!(m_t - m_q)!(m_- - m_d - m_t - m_q)!m_q!}\,. \tag{7.59}$$

The association strengths for the second and third coordination events are approximated as

$$K_2 = \rho_p \kappa_t \sigma_{pm}^3 g^{\mathrm{EXP}}(\sigma_{pm}) \left[\exp\left(\frac{l_\mathrm{B}}{\sigma_{pm}}\left[Z_m - \frac{1}{2}\right]\right) - 1\right], \tag{7.60}$$

$$K_3 = \rho_p \kappa_q \sigma_{pm}^3 g^{\mathrm{EXP}}(\sigma_{pm}) \left[\exp\left(\frac{l_\mathrm{B}}{\sigma_{pm}}\left[Z_m - \frac{2}{\sqrt{3}}\right]\right) - 1\right]. \tag{7.61}$$

Here, κ_t and κ_q are the bonding-volume parameters for the second and third associations, respectively. The energetic corrections estimate the Coulomb repulsion generated by polymer sites that are already coordinated to the same metal ion. A linear arrangement is assumed for two coordinated polymer sites, while an equilateral planar arrangement is assumed for three. These approximations give

$$K_3 < K_2 < K_1, \tag{7.62}$$

consistent with the increasing electrostatic and steric penalty associated with successive coordination events. Defining

$$f_i = \frac{m_i}{m_p}, \tag{7.63}$$

and minimizing the partition function with respect to m_-, m_d, m_t, and m_q gives

$$K_0 = \frac{f_- - f_d - f_t - f_q}{1 - f_-}\,, \tag{7.64}$$

$$K_1 = \frac{f_d - f_t}{(f_m - f_d)(f_- - f_d - f_t - f_q)}\,, \tag{7.65}$$

$$K_2 = \frac{f_t - f_q}{(f_d - f_t)(f_- - f_d - f_t - f_q)}\,,$$

$$K_3 = \frac{f_q}{(f_t - f_q)(f_- - f_d - f_t - f_q)}\,,$$

The cumulative populations f_d, f_t, and f_q count metal ions that have formed at least one, two, or three polymer bonds, respectively. It is more intuitive to introduce populations that count polymer sites in each state exclusively:

$$X_- = f_- - f_d - f_t - f_q\,, \tag{7.66}$$

$$X_d = f_d - f_t - f_q\,, \tag{7.67}$$

$$X_t = 2(f_t - f_q)\,,$$

$$X_q = 3f_q\,.$$

Here, X_- is the fraction of free deprotonated sites, X_d is the fraction of sites in singly coordinated metal–polymer complexes, X_t is the fraction in doubly coordinated complexes, and X_q is the fraction in triply coordinated complexes.

The fraction of unassociated metal ions is

$$X_{m,\mathrm{free}} = f_m - X_d - X_t/2 - X_q/3\,. \tag{7.68}$$

Substituting into equations 7.64 gives:

$$K_0 = \frac{X_-}{1 - X_- - X_d - X_t - X_q}\,, \tag{7.69}$$

$$K_1 = \frac{X_d}{X_{m,\mathrm{free}} X_-}\,, \tag{7.70}$$

$$2K_2 = \frac{X_t}{X_d X_-}\,,$$

$$\frac{3}{2}K_3 = \frac{X_q}{X_t X_-}\,.$$

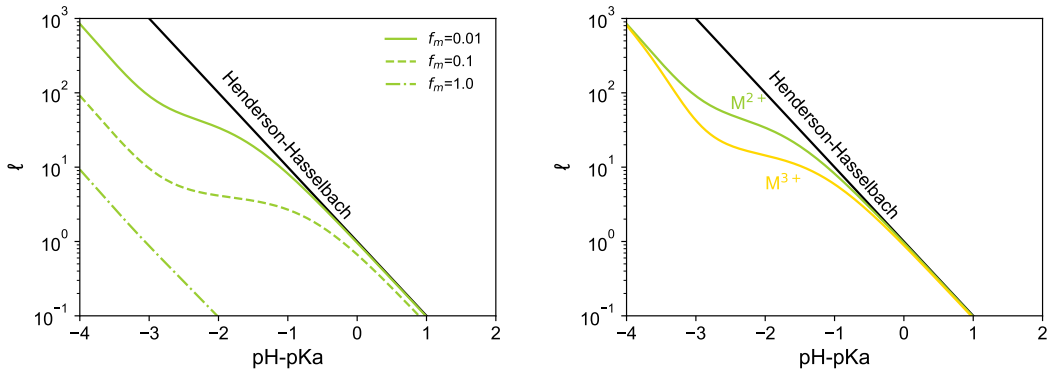
These equations represent the states in Figure 7.12 as a sequence of reversible reactions. They also make the coupling between ionization and metal coordination explicit. Metal association consumes free deprotonated sites and thereby shifts the acid–base equilibrium towards additional ionization. The effect is strongest when metal binding is favorable and the solution pH lies below the intrinsic polymer pK_a.

Interplay between pH and metal valency

We use the association theory developed above to examine the interplay between pH and metal valency. To isolate the influence of successive coordination events, we first set

$$K_1 = K_2 = K_3 = 1000 \tag{7.71}$$

and calculate the mean polymer charge spacing as a function of pH. The results are shown in Figure 7.13.



(a) (b)

Figure 7.13: Charge sparsity of a polyelectrolyte chain at different divalent metal concentrations (7.13a) and different valency metals at the same concentration (7.13b), $f_m = 0.01$.

Introducing divalent ions decreases the charge spacing at low pH, corresponding to an increase in the polymer ionization fraction. Strong metal binding consumes deprotonated sites and drives further deprotonation until either the available metal ions or the available polymer sites are saturated.

At sufficiently high pH, the number of ionized sites greatly exceeds the number of metal ions, and the intrinsic acid–base equilibrium again dominates. The curves therefore converge towards the metal-free Henderson–Hasselbalch result. As the metal concentration approaches the concentration of ionisable polymer sites, sufficient metal is present to bind a substantial fraction of the deprotonated sites over the full pH range. The metal-induced shift from the isolated-polymer ionization curve then persists to higher pH.

Trivalent ions produce a larger shift in the ionization equilibrium than divalent ions at intermediate pH because each ion can stabilize an additional deprotonated polymer site. At very low pH, however, ionized sites are sufficiently rare that most

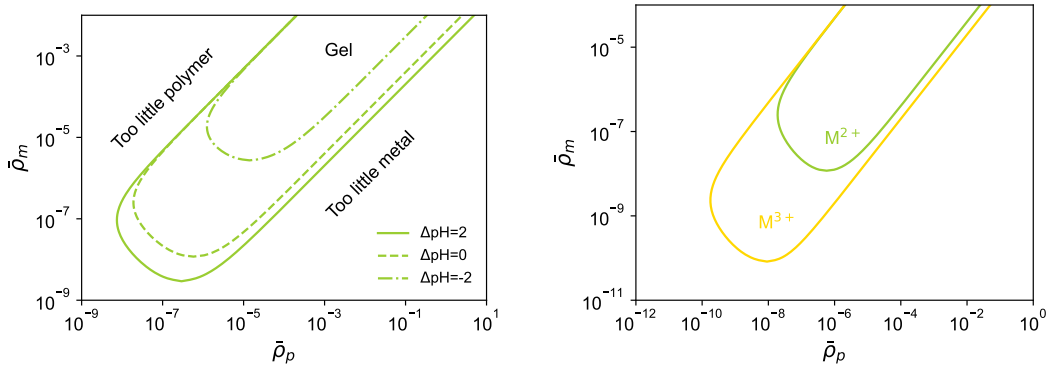
metal ions form only their first polymer bond. The behavior is therefore controlled primarily by K_1, which is taken to be identical for the two valencies.

At high pH, the polymer is nearly fully ionized even in the absence of metal binding, and the difference between divalent and trivalent ions again diminishes. These trends are consistent with previous reaction-ensemble simulations of weak polyelectrolytes in the presence of multivalent ions [356, 392].

Within the simplified population model, a percolation condition can be estimated from

$$f_t(m_p f_- - 1) = 2. \tag{7.72}$$

This relation approximates the onset of a system-spanning network from the number of multiply coordinated metal ions and the number of available charged polymer sites.



(a) (b)

Figure 7.14: Gel regions of a polyelectrolyte chain at different pH (7.14a) with a divalent metal ion and different valency metals at the same pH (7.14b), Δ pH=0.

The lower boundary of the gel region in Figure 7.14a corresponds to insufficient metal being available to produce a percolating population of bridges. In this regime, the metal concentration is also too small to perturb the polymer ionization equilibrium appreciably. The lower boundary therefore agrees qualitatively with the corresponding gel boundary in Figure 7.10.

Trivalent ions can form a network at slightly lower concentrations than divalent ions, as shown in Figure 7.14b. Their additional coordination state both increases their effective network functionality and promotes further polymer deprotonation.

The upper boundary has a different origin. At high metal concentration, metal binding drives the polymer towards extensive deprotonation. When the number of metal ions becomes sufficiently large relative to the number of charged sites, most metal ions form only a single polymer contact rather than bridging two or more sites. The fraction of elastically active crosslinks therefore decreases, and the system leaves the gel region.

Because this loss of bridging is controlled primarily by the excess number of metal ions, the upper boundary is comparatively insensitive to metal valency. Thus, adding more metal does not necessarily strengthen the gel indefinitely. Beyond an intermediate concentration, excess metal can saturate individual charged sites and suppress the formation of network-spanning bridges.

At low polymer and metal concentrations, neither component is sufficiently abundant to generate a percolated network. This regime is predicted to overlap partly with the two-phase region obtained from the free-energy model, although the coupling between phase separation, charge regulation, and gelation has not been solved self-consistently here.

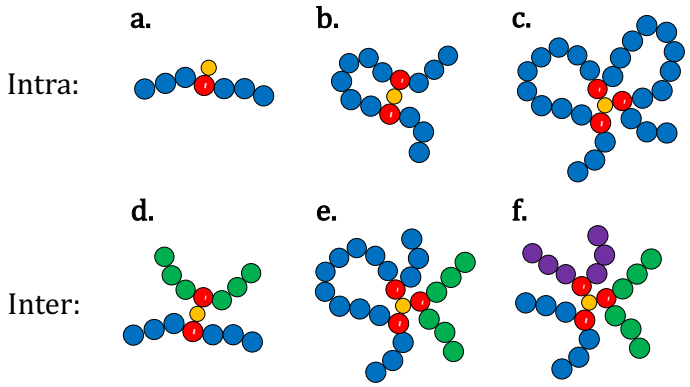


Figure 7.15: Different possible configurations for intra- (a-c) and inter- (d-f) crosslinks. Different colors represent different chains.

Competition between inter- and intra-crosslinking

Percolation requires metal ions to connect different polymer chains. Associations that connect two sites on the same chain instead form intrachain loops and do not contribute directly to the macroscopic network elasticity. Representative intrachain and interchain coordination states are illustrated in Figure 7.15.

Following Semenov and Rubinstein [93], we assume that all available metal ions are multiply coordinated and that intrachain bonds form only between neighboring charged sites along the backbone. For a Gaussian chain, the probability that two sites separated by ℓ segments meet scales as $\ell^{-3/2}$. The corresponding conformational entropy penalty is

$$\Delta S_{\text{intra.}} = -m_{\text{intra.}} k_{\text{B}} \ln\left(\ell^{3/2}\right), \tag{7.73}$$

where $m_{\text{intra.}}$ is the number of intrachain pairs. Taking the fully associated state as the reference, the partition function is

$$Z_{\text{intra.}} = Z_{\text{assoc.}} P_{\text{comb.}} W \exp\left(\frac{\Delta S_{\text{intra.}}}{k_{\text{B}}}\right). \tag{7.74}$$

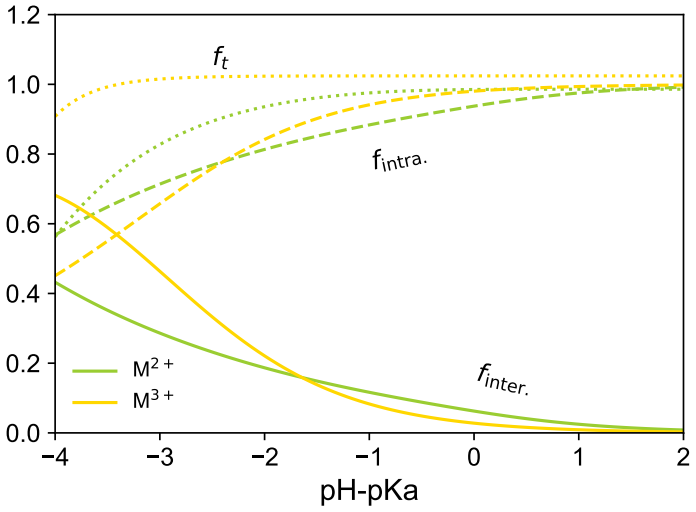


Figure 7.16: Inter-crosslink (solid), intra-crosslink (dashed) and trimer (dotted) fraction in divalent (green) and trivalent (yellow) systems at different pH where the metal ion concentration is sufficient to saturate all charged sites. All equilibrium constants have been set to 10^4 to ensure all trimers associate.

Here, $P_{\text{comb.}}$ and W are defined analogously to those in Section 7.3, with $m_{\text{intra.}}$ pairs selected from the multiply coordinated metal complexes.

Minimizing Equation 7.74 with respect to $m_{\text{intra.}}$ and defining $f_{\text{intra.}} = m_{\text{intra.}}/m_p$ gives

$$f_{\text{intra.}} = \frac{-1 + \sqrt{1 + 4\ell^{1/2}\rho_p\sigma_p^3}}{2\ell^{1/2}\rho_p\sigma_p^3}, \tag{7.75}$$

where ℓ is determined by the coupled protonation and metal-binding equilibria.

For divalent ions, each doubly coordinated metal is classified as either an intrachain or an interchain bridge. Trivalent ions permit additional mixed configurations in which two sites lie on one chain and the third lies on another, as illustrated in Figure 7.15. Accounting for these possibilities gives

$$f_{\text{intra.,tri}} = \frac{1}{f_t}\left(\frac{f_{\text{intra.}}X_t}{2} + \frac{f_{\text{intra.}}^2 X_q}{3}\right) \tag{7.76}$$

and

$$f_{\text{inter.,tri}} = \frac{1}{f_t}\left[\frac{(1-f_{\text{intra.}})X_t}{2} + \frac{3f_{\text{intra.}}(1-f_{\text{intra.}}) + (1-f_{\text{intra.}})^2}{3}X_q\right]. \tag{7.77}$$

These expressions apply in the strongly associated limit, $f_t \approx 1$.

As shown in Figure 7.16, the strongly associated approximation is well satisfied for the trivalent system across the pH range considered, whereas the divalent system approaches complete multiple coordination only at somewhat higher pH.

At low pH, charged sites are sparse along the polymer backbone. Intrachain loop formation then carries a large conformational penalty, and interchain bridging is favored. Trivalent ions form a larger interchain-crosslink fraction than divalent ions because their additional coordination site provides more ways of connecting distinct chains.

Increasing the pH increases the polymer ionization fraction and reduces the contour separation between neighboring charged sites. Intrachain coordination consequently becomes less entropically costly, leading to a larger loop fraction and fewer elastically active interchain crosslinks.

As shown in Figure 7.16, trivalent ions promote deprotonation more strongly than divalent ions. The crossover towards intrachain association therefore occurs more rapidly in the trivalent system. Above approximately

$$\text{pH} - \text{p}K_\text{a} \approx -1.8, \tag{7.78}$$

the model predicts a larger interchain-crosslink fraction for the divalent system, despite the greater maximum functionality of the trivalent ions.

These results provide a molecular interpretation of the experimentally observed weakening of MPEC gels at high pH [4]. Increasing the polymer charge fraction does not necessarily strengthen the macroscopic network. Instead, it can favor local

intrachain coordination at the expense of load-bearing bridges between different chains.

At lower and intermediate pH, trivalent ions retain an advantage because their larger coordination capacity produces a greater population of interchain connections. The mechanical response is therefore controlled not only by the total number and strength of metal–polymer bonds, but also by how those bonds are distributed between intrachain loops and network-forming interchain crosslinks.

7.4 Mechanical Properties

Although the framework developed by Rubinstein and Semenov [475] can, in principle, be extended to describe the linear dynamics of reversibly associating polymers, the collective relaxation and mechanical response of MPEC gels depend on spatially heterogeneous network structures that are difficult to resolve using the equilibrium theory alone. We therefore use coarse-grained molecular dynamics simulations to investigate how metal valency, polymer charge density, ion size, and solvent-mediated confinement influence the structure and dynamics of the MPEC network. The simulations are designed to connect the equilibrium trends developed in the previous section to the relaxation and deformation behavior of the resulting materials.

Kremer–Grest model for polyelectrolytes

Following previous simulations of ion-containing polymers [454, 455, 456, 476, 114], we represent the polyelectrolytes using the coarse-grained Kremer–Grest model [183]. An atomistic representation would provide a more chemically detailed description of the metal coordination environment, but the large energetic barriers and long polymer-relaxation times associated with multivalent ions make simulations at the relevant length and time scales computationally demanding [453, 477]. This remains the case even though suitable atomistic force-field parameters are available for many of the constituent species [478, 479].

The phenomena of primary interest here—network formation, polymer relaxation, cluster reorganization, and mechanical deformation—occur on length scales substantially larger than the local metal coordination environment. The Kremer–Grest model therefore provides an appropriate compromise between molecular resolution and computational accessibility. It also permits a relatively direct mapping between the simulation parameters and the reduced variables used in the phase diagrams developed in Section 7.3.

Covalent bonds between adjacent polymer beads are represented using the finitely extensible nonlinear elastic potential together with the repulsive part of the Lennard–Jones potential:

$$U_{\mathrm{FENE}}(r) = \begin{cases} -\dfrac{1}{2}kR_0^2 \ln\left[1 - \left(\dfrac{r}{R_0}\right)^2\right] + 4\epsilon\left[\left(\dfrac{\sigma}{r}\right)^{12} - \left(\dfrac{\sigma}{r}\right)^{6}\right] + \epsilon, & r \le 2^{1/6}\sigma, \\ -\dfrac{1}{2}kR_0^2 \ln\left[1 - \left(\dfrac{r}{R_0}\right)^2\right], & 2^{1/6}\sigma < r < R_0, \\ \infty, & r \ge R_0, \end{cases} \tag{7.79}$$

where $k = 30\epsilon/\sigma^2$ is the spring constant and $R_0 = 1.5\sigma$ is the maximum bond extension, following the original parametrization of Kremer and Grest [183]. Here, σ is the polymer-bead diameter and ϵ sets the energy scale.

Non-bonded excluded-volume interactions are represented using the Weeks–Chandler–Andersen potential [395]:

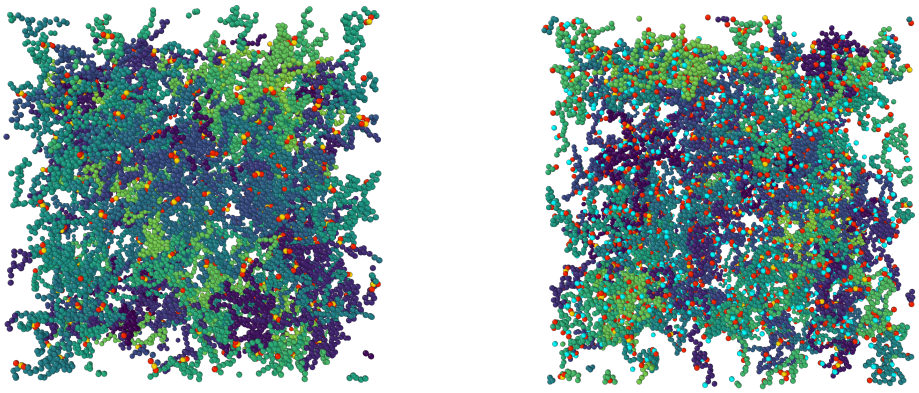
$$U_{\mathrm{WCA}}(r) = \begin{cases} 4\epsilon\left[\left(\dfrac{\sigma}{r}\right)^{12} - \left(\dfrac{\sigma}{r}\right)^{6}\right] + \epsilon, & r \le 2^{1/6}\sigma, \\ 0, & r > 2^{1/6}\sigma. \end{cases} \tag{7.80}$$

This choice produces an athermal polymer reference in which cohesion arises primarily from electrostatic interactions and metal-mediated crosslinking rather than from non-specific dispersion between polymer beads.

Explicit constant-pH simulation of a coarse-grained polyelectrolyte would require protonation and deprotonation moves to be coupled to both the local electrostatic environment and the metal-binding state [480, 481]. Rather than introduce this additional sampling issues, we construct fixed-charge models representing two limiting pH regimes, guided by Figures 7.10 and 7.13. Chapter 6 showed that dynamic charge regulation can substantially reshape both the local ion-binding environment and macroscopic ion transport; the fixed-charge treatment adopted here therefore neglects a coupling that may be significant for MPEC networks specifically.

At relatively low pH, the polymer ionization fraction is small and the charged sites are widely separated. We represent this regime using a charge spacing of $\ell = 27$. The number of multivalent metal ions is selected to compensate the polymer charge, such that most charged polymer sites can participate in metal-mediated complexes.

At higher pH, the polymer is more extensively deprotonated. This regime is represented using a smaller charge spacing of $\ell = 7$. The metal concentration is held fixed, so the additional polymer charge must be compensated by monovalent counterions. These two models do not describe pH continuously, but they capture the change from a sparsely charged, metal-dominated network to a more highly charged system containing a substantial population of monovalent counterions. Representative simulation configurations are shown in Figure 7.17.



(a) Low pH (b) High pH

Figure 7.17: Simulation snapshots of a polyelectrolyte chain in the presence of divalent metal ions at different low (left) and high (right) pH values.

Electrostatic interactions are represented using the Coulomb potential:

$$U_{\text{Coul.}}(r) = \frac{q_1 q_2}{4\pi\epsilon_0\epsilon_r r}, \tag{7.81}$$

where q_1 and q_2 are the charges of the interacting beads. The simulations are performed in reduced units with $\epsilon = \sigma = 1$. In these units, the strength of the electrostatic interaction is most directly characterized by the reduced Bjerrum length,

$$\bar{l}_B = \frac{l_B}{\sigma} = \frac{e_c^2}{4\pi\epsilon_0\epsilon_r\sigma k_B T}. \tag{7.82}$$

Consequently, assigning $\epsilon_r = 1$ in the simulation input should not be interpreted as directly representing a material with a physical relative permittivity of unity. The physical mapping also depends on the selected values of σ, ϵ, and T [456].

The electrostatic coupling was chosen to lie within the range motivated by Figure 7.9. This produces interactions stronger than those expected for a dilute aqueous solution

and is intended to represent the polymer-rich, glycerol-containing experimental material rather than pure water. Because solvent molecules are not represented explicitly, this parameter should be interpreted as an effective electrostatic coupling that incorporates both dielectric screening and coarse-graining.

The mobile ions are assigned a diameter smaller than that of the polymer backbone beads, with $\sigma_{\mathrm{ion}} = 0.5\sigma_p$ in the reference simulations. This choice reflects the smaller physical size of the ions and allows them to access the charged pendant groups. The charged sites are represented as pendant beads rather than charges placed directly on the polymer backbone. This introduces local conformational freedom and a degree of directionality into the polymer–metal association.

Each polymer contains approximately 336 backbone beads. This chain length places the unassociated Kremer–Grest chains well within the entangled regime [183], allowing the simulations to capture the coupling between physical entanglement and reversible metal-mediated crosslinking.

All initial configurations are first energy minimized. The systems are then equilibrated under NVT conditions, followed by NpT equilibration at a reduced temperature of

$$\bar{T} = \frac{k_{\mathrm{B}}T}{\epsilon} = 1. \tag{7.83}$$

The experimental gels coexist with an external solvent-rich environment and are therefore subject to a finite osmotic pressure rather than the zero-pressure condition commonly used for polymer melts. We apply a reduced pressure of approximately

$$\bar{P} = \frac{P\sigma^3}{\epsilon} = 10^{-3}. \tag{7.84}$$

This value is sufficiently small to represent weak external confinement while maintaining polymer-rich densities comparable to those predicted in Figure 7.9. It should be regarded as an effective pressure used to control the free volume of the implicit-solvent model, rather than a direct quantitative mapping of the experimental osmotic pressure.

Relaxation modes of polyelectrolytes

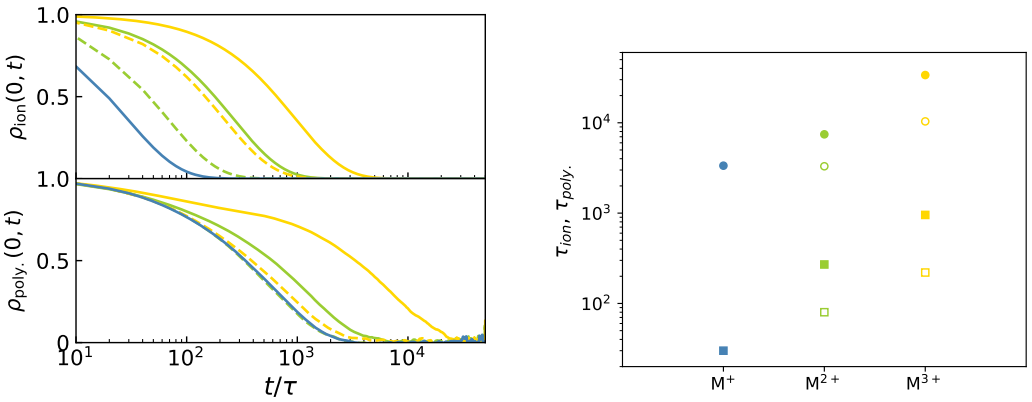
Following equilibration, longer production simulations are performed in the NVE ensemble to characterize the intrinsic relaxation of the systems without direct ther-

mostat or barostat perturbations. We focus on two complementary dynamical quantities: the lifetime of polymer–ion contacts and the relaxation of the polymer end-to-end vector. These quantities probe the local dynamics of the reversible crosslinks and the collective reorganization of the polymer network, respectively.

For a dynamical variable $A(t)$, we define the normalized autocorrelation function as

$$C_A(t) = \frac{\langle A(t_0 + t)A(t_0)\rangle_{t_0}}{\langle A(t_0)^2\rangle_{t_0}}. \tag{7.85}$$

The ion-pair correlation function is constructed from an indicator variable that records whether a metal ion and charged polymer site remain associated. The polymer relaxation is characterized using the autocorrelation of the chain end-to-end vector. Characteristic relaxation times are extracted from the decay of these correlation functions. The resulting autocorrelation functions and relaxation times are summarized in Figure 7.18.



(a) (b)

Figure 7.18: (a) Autocorrelation functions and (b) relaxation times of different modes of motion for different ion valencies (denoted by the different colors) and different pH regimes (solid lines correspond to low pH and dashed lines correspond to high pH).

The ion-pair relaxation time increases systematically with ion valency. Trivalent ions exhibit longer-lived contacts than divalent ions, which in turn exhibit longer-lived contacts than monovalent ions. This trend is consistent with the stronger electrostatic attraction of higher-valency ions and their ability to coordinate multiple charged sites simultaneously. Dissociation of a multivalent ion can require the disruption of several correlated contacts rather than the breaking of a single isolated ion pair.

The ion-pair lifetime also depends on polymer charge spacing. At high charge density, a metal ion is surrounded by a larger number of potential binding sites. This can stabilize multiply coordinated states, but it can also facilitate exchange between nearby sites. The measured relaxation therefore reflects both the energetic stability of an individual contact and the competition among neighboring charged groups.

The polymer end-to-end relaxation time reveals how these local associations influence the collective network. Taking the monovalent system as a reference, increasing the ion valency substantially slows the polymer relaxation. Monovalent counterions can condense around the polymer but cannot directly bridge two negatively charged sites. Their influence on the long-time chain dynamics therefore arises primarily from electrostatic screening and counterion condensation.

Divalent ions form both intrachain and interchain bridges. These reversible crosslinks increase the effective connectivity of the polymer network and restrict large-scale chain motion. Trivalent ions generate still slower relaxation because their contacts are longer lived and each ion can coordinate as many as three charged sites. The higher functionality favors compact, highly connected local structures, consistent with previous simulations of multivalent-ion-mediated polymer association [455].

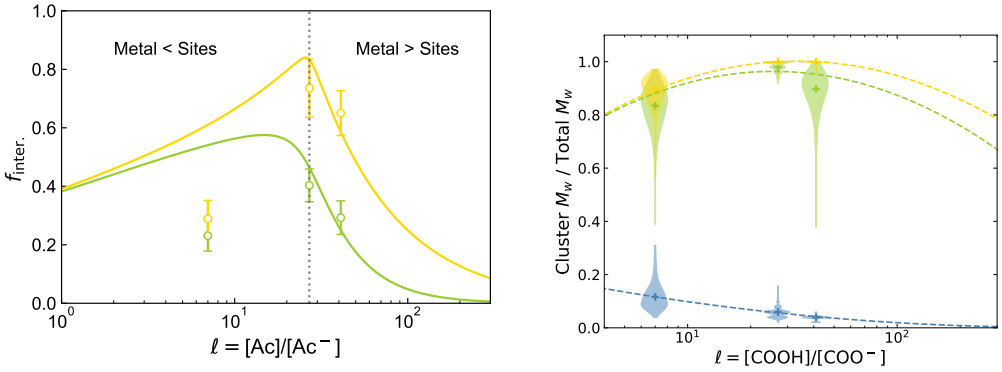
The end-to-end autocorrelation function of the low-pH trivalent system appears to contain two characteristic decay regimes. A possible interpretation is that the initial decay reflects local conformational fluctuations within a persistent network, while the slower decay corresponds to the collective rearrangement of the multiply connected polymer structure. The present analysis does not uniquely assign these modes, however, and a more detailed decomposition into local segmental, chain, and cluster relaxation would be required to establish their microscopic origin.

At high pH, the polymer relaxation times move towards the monovalent reference. As discussed in Section 7.3, increasing the charge density reduces the contour separation between charged sites and can favor intrachain coordination over network-forming interchain bridges. The resulting intrachain loops constrain local segments but contribute less strongly to macroscopic connectivity.

Smaller loops also require less large-scale chain reorganization than bridges connecting distant sites or separate chains. Consequently, the polymer can relax more rapidly even though metal–polymer contacts remain present. This convergence is incomplete for the trivalent system because the additional coordination site still permits highly connected local structures and longer-lived associations.

Cluster formation

The mechanical response of an MPEC gel depends not only on the number of metal–polymer contacts but also on whether those contacts join different chains into a system-spanning network. Following the approach of Semenov and Rubinstein [93] discussed in Section 7.3, we estimate the fraction of multivalent ions participating in interchain crosslinks as a function of polymer charge spacing. The theoretical predictions are compared with the molecular dynamics results in Figure 7.19.



(a) (b)

Figure 7.19: (a) Theoretically- (lines) and computationally- (markers with 95% confidence interval) predicted fraction of inter-crosslinked ions for divalent (green) and trivalent (yellow) systems at different charge sparsity. Dotted line corresponds to the sparsity where the metal ions perfectly neutralize the polyanion. (b) Violin plot of simulated cluster distribution in MPECs. Wider distributions represent larger fluctuations of the cluster size.

As shown in Figure 7.19a, trivalent ions generally exhibit a larger interchain-crosslink fraction than divalent ions. A single trivalent ion can connect three charged sites and therefore possesses more possible configurations that involve multiple polymer chains. The agreement between the theoretical trends and simulation results indicates that the competition between intra- and interchain association developed in Section 7.3 captures an important component of the simulated network topology.

The interchain-crosslink fraction is non-monotonic with charge spacing. When charged sites are very sparse, the probability of locating two or more suitable polymer sites near the same metal ion is small. Increasing the charge density initially promotes network formation by increasing the number of accessible binding sites. At still higher charge density, however, nearby sites on the same chain become increasingly accessible, and intrachain loops compete more effectively with interchain

bridges. The largest interchain fraction therefore occurs at an intermediate charge spacing where the availability of charged sites is balanced against the conformational preference for local intrachain association.

Figure 7.19b shows the distribution of the largest connected cluster, normalized by the total polymer population represented in the cluster analysis. Divalent and trivalent systems form clusters that span nearly all polymer chains under most of the conditions considered. The trivalent gels exhibit the narrowest cluster-size distributions, consistent with their stronger binding, greater connectivity, and slower structural relaxation.

No direct metal-mediated pathway exists for a monovalent ion to bridge two negatively charged polymer sites. Connectivity in the monovalent system must therefore arise from physical chain entanglements and transient spatial contacts rather than ion-mediated crosslinks. The resulting largest clusters are smaller and fluctuate more strongly than those in the multivalent systems.

The variation of cluster size with charge spacing broadly follows the interchain-crosslink fraction in Figure 7.19. This correspondence indicates that interchain coordination is a primary driver of the evolving polymer topology. The cluster-size distributions broaden as the charge spacing decreases beyond the optimum for interchain association. This greater structural variability is consistent with a network containing more competing local coordination states and may contribute to the faster polymer relaxation observed in Figure 7.18.

Mechanical response of polyelectrolytes

To probe the deformation response of the simulated gels, we apply uniaxial extension along the x direction. Following Sampath and Hall [456], the box length is increased at a constant engineering strain rate, $\dot{\epsilon}$:

$$dL_x = \dot{\epsilon} L_{0x}, dt, \tag{7.86}$$

where L_{0x} is the initial box length in the deformation direction. The corresponding engineering strain is

$$\epsilon_{\text{eng.}} = \frac{L_x - L_{0x}}{L_{0x}}. \tag{7.87}$$

A barostat is applied in the transverse directions to maintain a reduced pressure of 10^{-3}. This allows the simulation box to contract laterally as the material is stretched and approximates deformation under weak external osmotic confinement.

A strain rate of

$$\dot{\epsilon} = 6.52 \times 10^{-3} \tau^{-1} \tag{7.88}$$

is used, where τ is the reduced time unit. This relatively rapid rate is required to access large deformations within computationally feasible trajectories. The resulting curves should therefore be interpreted as finite-rate deformation responses rather than quasistatic equilibrium stress–strain relations. The initial portion of each curve can be used to compare apparent stiffnesses under the common imposed rate, while the response at large strain also contains substantial viscoelastic and structural-reorganization contributions.

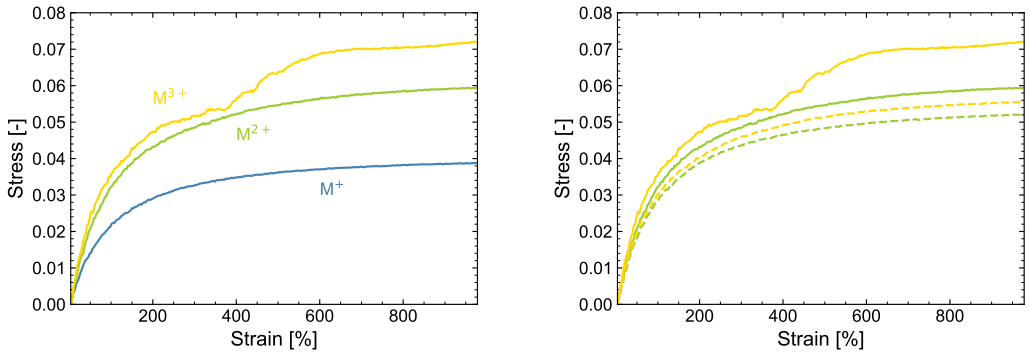
The virial stress tensor is calculated as

$$\sigma_{\alpha\beta} = \frac{1}{V} \left[\sum_i m_i v_{i\alpha} v_{i\beta} + \sum_i r_{i\alpha} f_{i\beta} \right], \tag{7.89}$$

where m_i is the particle mass, $r_{i\alpha}$ is the α component of its position, $v_{i\alpha}$ is the corresponding velocity component, and $f_{i\beta}$ is the β component of the force acting on it. The first term is the kinetic contribution, while the second contains the bonded and non-bonded virial contributions. The deformation response is characterized using the xx component of the stress tensor. The resulting curves are shown in Figure 7.20.

Figure 7.20 shows that the apparent stiffness increases strongly with metal valency. The trivalent systems generally sustain the largest stresses at a given deformation, followed by the divalent and monovalent systems. This ordering is consistent with the relaxation times shown in Figure 7.18. A network cannot relax an imposed deformation efficiently when its crosslinks are long lived relative to the deformation timescale. The larger functionality of trivalent ions also produces a more highly connected network, further increasing its resistance to deformation.

A step-like feature appears near 500% strain in the trivalent response. Similar non-monotonic features have been reported in simulations of ion-containing polymers [456], where they can arise from abrupt network rearrangements, strain-induced

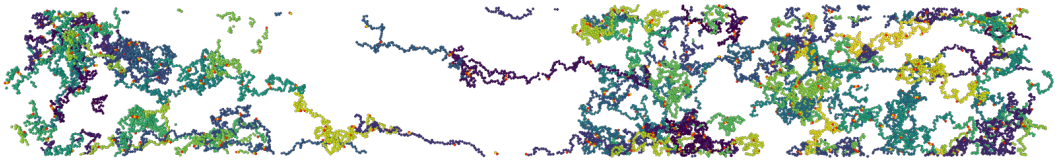


(a) (b)

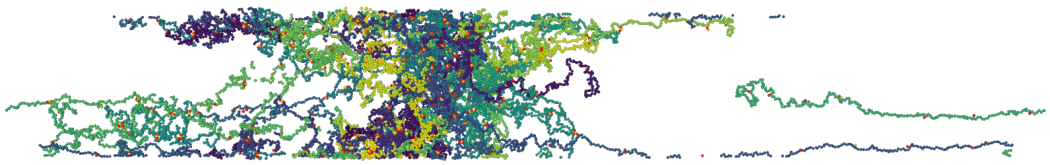
Figure 7.20: Stress-strain curves of different valencies (denoted by the different colors) and different pH regimes (solid lines correspond to low pH and dashed lines correspond to high pH). All systems used a constant strain rate of $\dot{\epsilon} = 6.52\times10^{-3}\tau^{-1}$.

alignment, or the failure of a subset of load-bearing connections. The present trajectories do not establish a unique origin, and the feature may also be sensitive to finite system size and strain rate.

The simulations do not provide a sharply defined macroscopic fracture point. Nevertheless, the configurations in Figure 7.21 provide insight into the contrasting deformation mechanisms of the divalent and trivalent networks.



(a) Divalent system



(b) Trivalent system

Figure 7.21: Simulation snapshot of divalent (7.21a) and trivalent (7.21b) systems at approximately 500% strain, close to the point at which both systems form two separate clusters.

In the divalent system, multiple chains become strongly extended and continue

to bridge the developing polymer-rich clusters. The comparatively short crosslink lifetime permits metal ions and polymer segments to reorganize during deformation, redistributing the imposed load across the network.

The trivalent system forms more compact and highly coordinated clusters. Fewer chains span the gap between these clusters, and the slower structural relaxation limits the ability of the network to generate new load-bearing pathways as it is stretched. The material can therefore sustain a large stress initially but undergoes more localized network separation at large deformation. This behavior is consistent with the experimentally observed contrast between the stiffer, more brittle trivalent gels and the more extensible divalent gels [4].

The greater ability of the divalent network to exchange and reform crosslinks also suggests a microscopic origin for its greater capacity for structural recovery and self-healing [482]. The simulations do not directly model a complete healing protocol, but they demonstrate that the divalent network can reorganize more readily on the deformation timescale.

The effect of pH is shown in Figure 7.20b. The high-pH systems generally exhibit a smaller initial stress response, consistent with their faster polymer relaxation in Figure 7.18 and with the experimental trends reported by Lee et al. [4]. Increased polymer charge density favors shorter intrachain loops and reduces the fraction of load-bearing interchain bridges, thereby decreasing the effective network stiffness.

The high-pH multivalent systems do not, however, become mechanically identical to the monovalent system. Although the polymer conformations relax more rapidly, the multivalent ion pairs remain longer lived than the monovalent contacts. At the imposed strain rate, these local associations cannot fully equilibrate during deformation and therefore continue to resist chain motion.

This competition is illustrated by the evolution of the interchain-crosslink fraction in Figure 7.22. The divalent gels lose interchain connections progressively during extension, indicating that their crosslinks exchange or dissociate as the network reorganizes. The interchain fraction in the trivalent gels changes much less over the same strain range. The persistent trivalent network resists deformation strongly but is less able to redistribute its binding sites to accommodate the applied strain.

Effect of ion size

The electronic-structure calculations in Figure 7.3 indicate that the leading variations in metal–acrylate binding can be associated with metal valency and an effective

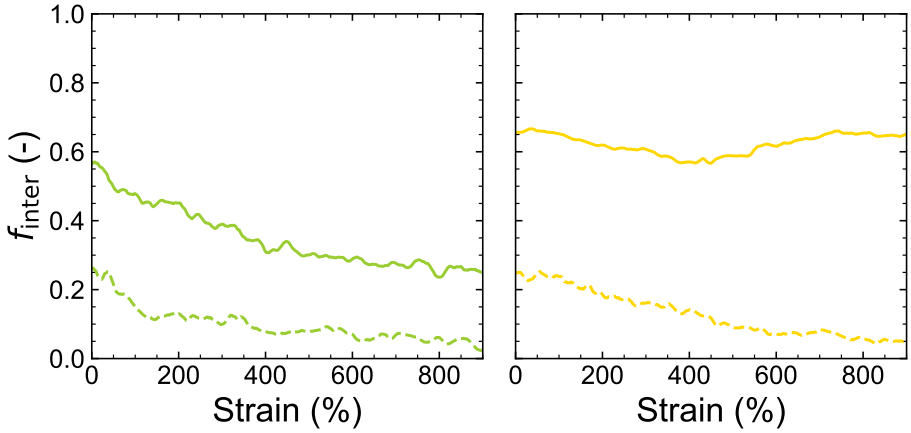


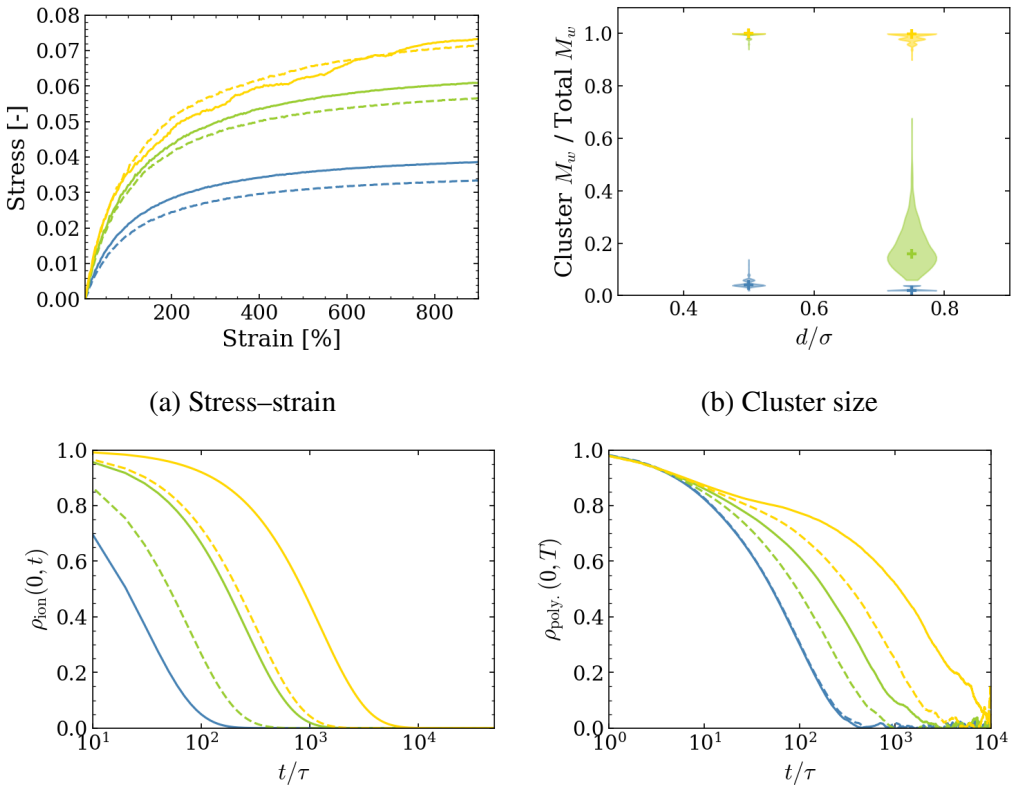
Figure 7.22: Fraction of inter-crosslinked ions during deformation. The change in fraction of inter-crosslinked divalent (left) and trivalent (right) ions during elastic deformations obtained using molecular dynamics simulations. Solid lines correspond to low pH regime and dashed lines correspond to high pH regime.

contact separation. The simulations discussed above isolate the effect of valency while holding the ion diameter fixed. We next vary the metal-ion diameter to determine how the effective contact separation influences network dynamics and mechanical response.

Two ion diameters are considered: $\sigma_{\text{ion}} = 0.5\sigma$ and $\sigma_{\text{ion}} = \sigma$. This deliberately broad range is intended to reveal the maximum qualitative sensitivity of the coarse-grained model to ion size. It should not be interpreted as a direct quantitative mapping onto the bare crystallographic radii of particular metal ions, because experimentally relevant sizes also depend on solvation and coordination state. The results are summarized in Figure 7.23.

Increasing the ion diameter decreases the stress sustained by the divalent gels at a given strain, as shown in Figure 7.23a. Increasing the contact separation weakens the Coulomb attraction between the ion and charged pendant groups. The resulting polymer–ion contacts relax more rapidly, as shown in Figure 7.23c, and the polymer end-to-end vector also decorrelates more quickly, as shown in Figure 7.23d. The more mobile network can reorganize during deformation and therefore sustains a smaller stress at the imposed strain rate.

The end-to-end relaxation of the monovalent system is nearly insensitive to ion diameter. Because monovalent ions cannot directly bridge two negatively charged sites, the lifetime of an individual polymer–ion contact does not control the connectivity



(a) Stress–strain

(b) Cluster size

(c) Ion-pair relaxation

(d) End-to-end vector relaxation

Figure 7.23: Results obtained from molecular dynamics simulations of MPEC gels with varying ion diameters: **a,** Stress-strain curves from uniaxial stretching. **b,** Cluster size distribution over different ion diameters. **c,** Ion-pair relaxation and **d,** end-to-end vector relaxation. Solid curves correspond to diameters of 0.5σ and dashed curves correspond to diameters of σ. The color scheme used in this figure follow the scheme used in the main text (blue: monovalent, green: divalent and yellow: trivalent ions).

of the polymer network. Changes in ion diameter therefore have a weaker influence on the large-scale chain dynamics than in the divalent and trivalent systems.

The monovalent stress response is nevertheless altered slightly. Increasing the ion diameter weakens counterion condensation and changes the effective electrostatic repulsion between polymer chains. The mechanical change in this case arises primarily from modified screening and packing rather than from a change in dynamic crosslink density.

The trivalent stress–strain curve is less sensitive to ion diameter than the divalent curve. Increasing the diameter accelerates both the ion-pair and polymer relaxation, but the trivalent system remains more slowly relaxing than the reference divalent

system. Moreover, each trivalent ion can still form three polymer contacts. As shown in Figure 7.23b, the largest-cluster distribution is consequently less affected than in the divalent system.

These results indicate that ion size provides a secondary control parameter that acts primarily through the polymer–metal contact strength. Valency determines the maximum functionality of the crosslinker, while ion diameter modifies the lifetime and spatial compactness of the resulting coordination structures.

Effect of solvent

Because the solvent is represented implicitly, its influence cannot be varied through an explicit change in molecular composition. Instead, two effective parameters can be modified: the dielectric screening, which controls the strength of the electrostatic interactions, and the applied pressure, which controls the free volume of the polymer-rich phase.

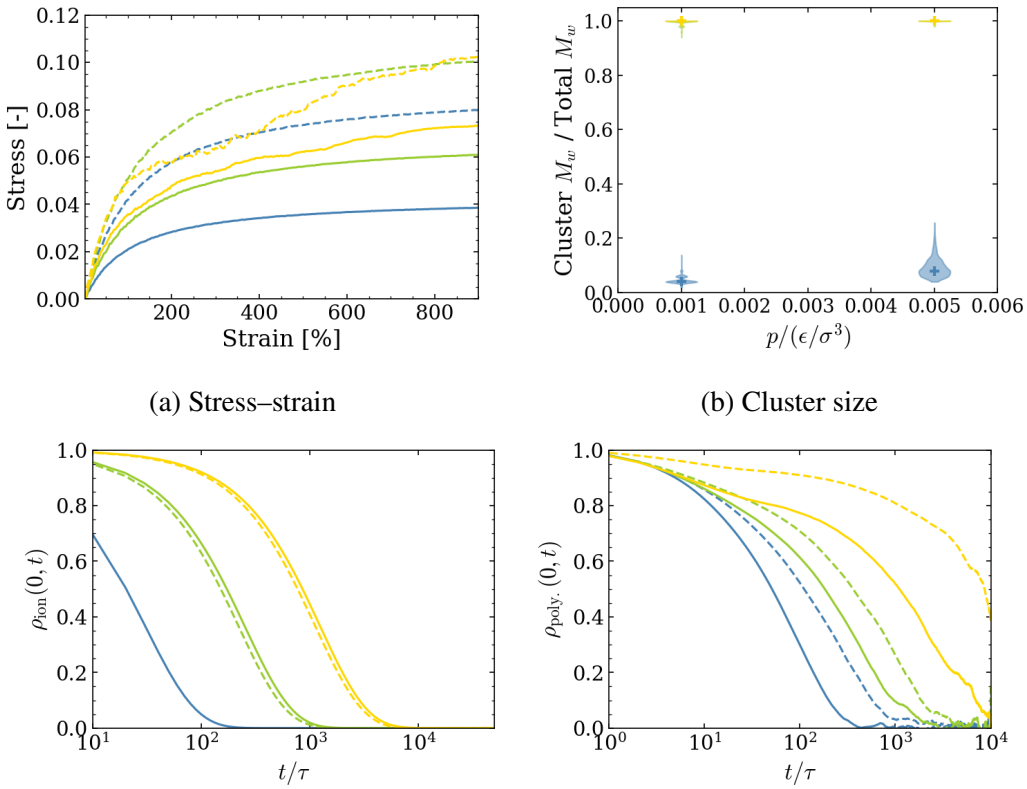
Changes in solvent composition can affect both quantities experimentally. Replacing glycerol with water increases the dielectric constant and weakens electrostatic association, but it can also change the swelling pressure, solvent quality, and polymer volume fraction. Because the simulated systems contain a high polymer concentration, we focus here on the free-volume contribution and vary the applied reduced pressure while keeping the electrostatic coupling fixed.

The pressure variation should therefore be interpreted as a simplified probe of solvent-mediated confinement rather than as a one-to-one mapping between pressure and water content. The results are shown in Figure 7.24.

Increasing the applied pressure increases the stress sustained at a given deformation for all three ion valencies, as shown in Figure 7.24a. This trend is qualitatively consistent with the stronger mechanical response observed experimentally upon changing the solvent composition [4].

Figures 7.24d and 7.24c show that the increased pressure reduces the available free volume and substantially slows the large-scale polymer motion. The chains are packed more closely and have less space in which to reorganize. Their end-to-end vectors therefore remain correlated for longer times, increasing the resistance of the network to deformation.

The divalent and trivalent systems also exhibit narrower cluster-size distributions at the higher pressure. Confinement suppresses large fluctuations in the connected



(a) Stress–strain

(b) Cluster size

(c) Ion-pair relaxation

(d) End-to-end vector relaxation

Figure 7.24: Results obtained from molecular dynamics simulations of MPEC gels with varying applied pressure: **a,** Stress-strain curves from uniaxial stretching. **b,** Cluster size distribution under different system pressure. **c,** Ion-pair relaxation and **d,** end-to-end vector relaxation. Solid curves correspond to pressures of $0.001\epsilon/\sigma^3$ and dashed curves correspond to pressures of $0.005\epsilon/\sigma^3$. The color scheme used in this figure follow the scheme used in the main text (blue: monovalent, green: divalent and yellow: trivalent ions).

network and stabilizes a more persistent cluster topology. This effect is particularly strong for the trivalent system, in which the combination of high connectivity and reduced free volume produces relaxation times beyond the duration of the production trajectory.

The trivalent end-to-end correlation function does not fully decay within the available simulation time. Its characteristic relaxation time therefore cannot be determined reliably from these trajectories. The increased mechanical response can still be interpreted qualitatively, but quantitative comparison with the other systems would require substantially longer simulations. Based on the observed decay, trajectories approximately two orders of magnitude longer may be required to sample

complete relaxation, which was not computationally feasible with the resources available for this work.

The monovalent system exhibits a broader rather than narrower cluster-size distribution at increased pressure. Because its clusters are not connected by metal-mediated bridges, closer packing brings independently moving chains into contact and increases the mean instantaneous cluster size. The membership of these clusters can fluctuate as individual chains diffuse and disentangle. Since the monovalent polymer relaxation remains faster than that of the divalent reference system, these fluctuations remain observable over the simulation timescale.

In contrast to the polymer relaxation, the ion-pair relaxation functions in Figure 7.24c change only weakly with pressure. A small acceleration is observed in some cases, possibly because closer packing increases the number of alternative charged sites available for ion exchange. The direct binding strength remains fixed because the electrostatic parameters are unchanged.

The pressure variation therefore influences the mechanical response primarily through polymer packing and collective chain mobility rather than through a substantial change in the lifetime of an individual polymer–ion contact. Within the implicit-solvent model, solvent-mediated free volume consequently provides a control parameter that is distinct from metal valency, ion size, and polymer charge density.

7.5 Conclusions

In this chapter, we developed a multiscale computational framework to understand how metal-ion chemistry, polymer ionization, and network topology govern the behavior of metallo-polyelectrolyte complexes. Rather than attempting to represent every relevant length scale within a single model, we combined electronic-structure calculations, thermodynamic theory, and coarse-grained molecular dynamics simulations. Together, these approaches connect the local interaction between a metal ion and a carboxylate group to the phase behavior, gelation, relaxation, and mechanical response of the resulting polymer network.

The electronic-structure calculations in Section 7.2 showed that the metal–acrylate binding energies are governed primarily by metal valency and the characteristic metal–ligand separation. Trivalent ions bind more strongly than divalent ions, which in turn bind more strongly than monovalent ions. Normalizing the binding energies by the metal valency produced an approximate collapse onto a common relationship with separation, supporting a predominantly electrostatic description

of the interaction. The observed distance dependence was more consistent with an effective ion–dipole interaction than with a simple point-charge Coulomb potential, demonstrating that the spatial charge distribution of the carboxylate group remains important at contact. Transition-metal ions also exhibited metal–ligand orbital mixing and changes in their preferred coordination geometries, indicating that ion-specific electronic effects can provide additional stabilization beyond the leading electrostatic contribution. Valency and effective ion size therefore provide useful first-order descriptors for coarse-grained modelling, although they do not capture all coordination-specific chemistry.

Building on these observations, Section 7.3 introduced a thermodynamic description of multivalent-ion-mediated phase separation and gelation. The reversible-sticker theory of Semenov and Rubinstein provided the conceptual starting point, showing how strong association can produce polymer-rich globules, homogeneous gels, or dissolved polymer solutions depending on the association strength and sticker density. We extended this framework by incorporating hard-chain excluded volume, long-range electrostatic correlations, and explicit association between charged polymer sites and multivalent metal ions. The resulting theory maps the phenomenological association strength onto physically interpretable quantities such as the Bjerrum length, metal valency, ion diameter, polymer charge spacing, and bonding volume.

The theory predicts that increasing the polymer charge density or metal valency strengthens association, lowers the electrostatic coupling required for phase separation, and permits gelation at lower polymer concentrations. Trivalent ions consequently produce substantially larger coexistence regions and lower gelation thresholds than divalent ions. The multivalent ions partition strongly with the polymer into the dense phase, producing diagonal tie lines that differ qualitatively from those expected for polyelectrolytes containing only monovalent ions. Under some conditions, the theory also predicts coexistence between polymer-rich phases with different metal contents, one of which may be percolated while the other remains fluid-like. This raises the possibility of gel–fluid or gel-in-gel phase separation, although the equilibrium theory alone cannot determine whether these states remain accessible or become kinetically arrested.

An important extension in Section 7.3 was the explicit coupling of acid–base equilibria to sequential metal coordination. Metal binding stabilizes deprotonated polymer sites and therefore shifts the ionization equilibrium beyond the isolated-polymer Henderson–Hasselbalch prediction. This coupling is strongest at intermediate pH,

where the intrinsic ionization fraction remains incomplete but sufficiently many charged sites are present to support multidentate metal coordination. Trivalent ions drive a larger increase in polymer ionization than divalent ions because they can stabilize an additional charged site.

The same theory predicts a bounded region of gel formation with respect to metal concentration. At low metal concentration, too few bridges are present to generate a percolating network. At very high metal concentration, the available polymer sites become individually saturated, causing many ions to form only a single polymer contact rather than bridging multiple sites. Gelation is therefore favored at an intermediate metal-to-polymer ratio. The theory also reveals a competition between network-forming interchain bridges and intrachain loops. Increasing the polymer charge density initially promotes crosslinking by providing more binding sites, but eventually favors local intrachain association because neighboring charged sites become easier to connect. Consequently, the fraction of elastically active interchain crosslinks is maximized at an intermediate charge spacing rather than increasing monotonically with the polymer ionization fraction.

The molecular dynamics simulations in Section 7.4 provided a direct description of how these equilibrium trends influence network structure and dynamics. Higher-valency ions formed longer-lived polymer contacts and produced slower polymer relaxation. Divalent ions generated reversible bridges that increased the effective connectivity of the entangled polymer network, while trivalent ions produced more compact, highly connected structures with substantially longer relaxation times. The simulations also reproduced the non-monotonic dependence of interchain crosslinking on polymer charge spacing predicted by the theoretical model. Divalent and trivalent systems formed system-spanning clusters, whereas monovalent ions could not directly bridge negatively charged polymer sites and therefore produced smaller, more weakly connected structures.

The simulated mechanical response followed directly from these differences in network topology and relaxation. Trivalent systems sustained the largest stresses because their highly connected networks could not relax appreciably on the deformation timescale. However, their compact structure and slow crosslink exchange limited their ability to redistribute stress, producing a comparatively stiff and brittle response. Divalent networks relaxed more readily, allowing chains and metal-mediated crosslinks to reorganize during deformation. These systems were consequently less stiff but more extensible and displayed a greater capacity to maintain

bridging chains between separating clusters. This dynamic reorganization also provides a molecular basis for the greater potential of divalent MPEC networks to recover and self-heal following deformation.

Increasing the polymer ionization fraction generally accelerated large-scale polymer relaxation and reduced the mechanical stiffness, despite increasing the total number of charged sites. This result can be understood through the increasing prevalence of short intrachain loops at high charge density, which reduces the fraction of load-bearing interchain connections. Nevertheless, the high-pH multivalent systems did not become mechanically equivalent to the monovalent reference because their individual polymer–metal contacts remained long lived. Their deformation response therefore reflects a competition between relatively rapid polymer conformational relaxation and slower ion-pair exchange.

The ion-size and pressure calculations further demonstrated that metal valency is not the only control parameter available for tuning MPEC mechanics. Increasing the effective ion diameter weakened the polymer–metal attraction, accelerated ion-pair and polymer relaxation, and reduced the stress response, particularly for divalent systems. Trivalent networks were less sensitive because their larger functionality preserved a highly connected cluster even when individual contacts were weakened. Increasing the applied pressure reduced the available free volume and slowed collective polymer motion without substantially changing the lifetime of individual ion pairs. The resulting gels sustained larger stresses and exhibited more persistent cluster structures. Solvent-mediated packing and metal coordination can therefore influence the material response through distinct microscopic mechanisms.

Overall, the results establish that the macroscopic behavior of MPEC gels cannot be predicted from the metal–ligand binding strength alone. Their properties emerge from the coupled effects of metal valency, ion size, polymer ionization, metal concentration, solvent-mediated packing, and the distribution of associations between intra- and interchain configurations. Stronger binding and higher crosslinker functionality generally increase stiffness, but they can also suppress network relaxation and promote brittle failure. Likewise, increasing the polymer charge density creates additional binding sites but can weaken the macroscopic network by favoring local loops over interchain bridges. The optimal material therefore lies between the limits of weak, rapidly exchanging association and strong, kinetically trapped coordination.

The multiscale framework developed here provides a computational basis for navi-

gating these competing effects. Electronic-structure calculations identify the molecular descriptors required to distinguish metal ions, thermodynamic theory maps how these descriptors influence phase separation and gelation, and molecular dynamics simulations reveal how the resulting network topology controls relaxation and mechanics. Together, these methods provide a route for rationally selecting metal ions, pH, composition, and solvent conditions to design MPEC gels with targeted combinations of stiffness, extensibility, stability, and dynamic responsiveness.

References

[4] Seola Lee et al. "Molecular control via dynamic bonding enables material responsiveness in additively manufactured metallo-polyelectrolytes". In: *Nat. Commun.* 15.1 (Aug. 2024), p. 6850. ISSN: 2041-1723. DOI: 10.1038/s41467-024-50860-6.

[20] Pierre J. Walker, Hon-Wa Yew, and Andrés Riedemann. "Clapeyron.jl: An Extensible, Open-Source Fluid Thermodynamics Toolkit". In: *Ind. Eng. Chem. Res.* 61.20 (May 2022), pp. 7130–7153. ISSN: 0888-5885, 1520-5045. DOI: 10.1021/acs.iecr.2c00326.

[88] Pengfei Zhang et al. "Salting-Out and Salting-In of Polyelectrolyte Solutions: A Liquid-State Theory Study". In: *Macromolecules* 49.24 (Dec. 2016), pp. 9720–9730. ISSN: 0024-9297, 1520-5835. DOI: 10.1021/acs.macromol.6b02160.

[90] Andrew S. Ylitalo et al. "Electrostatic Correlations and Temperature-Dependent Dielectric Constant Can Model LCST in Polyelectrolyte Complex Coacervation". In: *Macromolecules* 54.24 (Dec. 2021), pp. 11326–11337. ISSN: 0024-9297, 1520-5835. DOI: 10.1021/acs.macromol.1c02000.

[93] Alexander N. Semenov and Michael Rubinstein. "Thermoreversible Gelation in Solutions of Associative Polymers. 1. Statics". In: *Macromolecules* 31.4 (Feb. 1998), pp. 1373–1385. ISSN: 0024-9297, 1520-5835. DOI: 10.1021/ma970616h.

[98] L. Blum and J. S. Hoeye. "Mean spherical model for asymmetric electrolytes. 2. Thermodynamic properties and the pair correlation function". In: *J. Phys. Chem.* 81.13 (June 1977), pp. 1311–1316. ISSN: 0022-3654, 1541-5740. DOI: 10.1021/j100528a019.

[114] Ralf Everaers et al. "Kremer–Grest Models for Commodity Polymer Melts: Linking Theory, Experiment, and Simulation at the Kuhn Scale". In: *Macromolecules* 53.6 (Mar. 2020), pp. 1901–1916. ISSN: 0024-9297, 1520-5835. DOI: 10.1021/acs.macromol.9b02428.

[122] Allie C. Obermeyer et al. “Complex coacervation of supercharged proteins with polyelectrolytes”. In: *Soft Matter* 12.15 (Apr. 2016), pp. 3570–3581. ISSN: 1744-6848. DOI: 10.1039/C6SM00002A.

[124] J. W. Jiang et al. “Thermodynamic properties and phase equilibria of charged hard sphere chain model for polyelectrolyte solutions”. In: *Mol. Phys.* 99.13 (July 2001), pp. 1121–1128. ISSN: 0026-8976. DOI: 10.1080/00268970110043414.

[162] Tomáš Boublík. “Hard-Sphere Equation of State”. In: *J. Chem. Phys.* 53.1 (July 1970), pp. 471–472. ISSN: 0021-9606, 1089-7690. DOI: 10.1063/1.1673824.

[183] Kurt Kremer and Gary S. Grest. “Dynamics of entangled linear polymer melts: A molecular-dynamics simulation”. In: *J. Chem. Phys.* 92.8 (Apr. 1990), pp. 5057–5086. ISSN: 0021-9606, 1089-7690. DOI: 10.1063/1.458541.

[202] Minjung Lee, Sarah L. Perry, and Ryan C. Hayward. “Complex Coacervation of Polymerized Ionic Liquids in Non-aqueous Solvents”. In: *ACS Polym. Au* 1.2 (Oct. 2021), pp. 100–106. ISSN: 2694-2453, 2694-2453. DOI: 10.1021/acspolymersau.1c00017.

[235] Tae Hyun Kim et al. “Flexible biomimetic block copolymer composite for temperature and long-wave infrared sensing”. In: *Sci. Adv.* 9.6 (Feb. 2023), eade0423. DOI: 10.1126/sciadv.ade0423.

[310] Yong Zhang and Edward J. Maginn. “Direct Correlation between Ionic Liquid Transport Properties and Ion Pair Lifetimes: A Molecular Dynamics Study”. In: *J. Phys. Chem. Lett.* 6.4 (Feb. 2015), pp. 700–705. ISSN: 1948-7185, 1948-7185. DOI: 10.1021/acs.jpclett.5b00003.

[322] Pengfei Zhang and Zhen-Gang Wang. “Supernatant Phase in Polyelectrolyte Complex Coacervation: Cluster Formation, Binodal, and Nucleation”. In: *Macromolecules* 55.10 (May 2022), pp. 3910–3923. ISSN: 0024-9297. DOI: 10.1021/acs.macromol.2c00340.

[356] Jonas Landsgesell et al. “Simulations of ionization equilibria in weak polyelectrolyte solutions and gels”. In: *Soft Matter* 15.6 (2019), pp. 1155–1185. DOI: 10.1039/C8SM02085J.

[392] Jonas Landsgesell et al. “Grand-Reaction Method for Simulations of Ionization Equilibria Coupled to Ion Partitioning”. In: *Macromolecules* 53.8 (Apr. 2020), pp. 3007–3020. ISSN: 0024-9297. DOI: 10.1021/acs.macromol.0c00260.

[395] John D. Weeks, David Chandler, and Hans C. Andersen. “Role of Repulsive Forces in Determining the Equilibrium Structure of Simple Liquids”. In: *J. Chem. Phys.* 54.12 (Sept. 2003), pp. 5237–5247. ISSN: 0021-9606. DOI: 10.1063/1.1674820.

[416] Alec Glisman et al. “Binding Modes and Water-Mediation of Polyelectrolyte Adsorption to a Neutral CaCO3 Surface”. In: *Langmuir* 40.49 (Dec. 2024), pp. 25931–25939. ISSN: 0743-7463. DOI: 10.1021/acs.langmuir.4c03301.

[434] Hong Dong et al. “Cation-Induced Hydrogels of Cellulose Nanofibrils with Tunable Moduli”. In: *Biomacromolecules* 14.9 (Sept. 2013), pp. 3338–3345. ISSN: 1525-7797. DOI: 10.1021/bm400993f.

[435] Tianyu Zhu et al. “Metallo-polyelectrolytes as a class of ionic macromolecules for functional materials”. In: *Nat. Commun.* 9.1 (Oct. 2018), p. 4329. ISSN: 2041-1723. DOI: 10.1038/s41467-018-06475-9.

[436] Laura N. Neumann et al. “Dynamics and healing behavior of metallosupramolecular polymers”. In: *Sci. Adv.* 7.18 (Apr. 2021), eabe4154. DOI: 10.1126/sciadv.abe4154.

[437] Ming Zhong et al. “Dually cross-linked single network poly(acrylic acid) hydrogels with superior mechanical properties and water absorbency”. In: *Soft Matter* 12.24 (June 2016), pp. 5420–5428. ISSN: 1744-6848. DOI: 10.1039/C6SM00242K.

[438] Yuval Vidavsky et al. “Tuning the Mechanical Properties of Metallopolymers via Ligand Interactions: A Combined Experimental and Theoretical Study”. en. In: *Macromolecules* 53.6 (Mar. 2020), pp. 2021–2030. ISSN: 0024-9297. DOI: 10.1021/acs.macromol.9b02756.

[439] Yang Gao, Kangling Wu, and Zhigang Suo. “Photodetachable Adhesion”. In: *Adv. Mater.* 31.6 (2019), p. 1806948. ISSN: 1521-4095. DOI: 10.1002/adma.201806948.

[440] Elif Nur Durmaz et al. “Polyelectrolytes as Building Blocks for Next-Generation Membranes with Advanced Functionalities”. In: *ACS Appl. Polym. Mater.* 3.9 (Aug. 2021), pp. 4347–4374. ISSN: 2637-6105. DOI: 10.1021/acsapm.1c00654.

[441] Tianyu Zhu et al. “Rational Synthesis of Metallo-Cations Toward Redox- and Alkaline-Stable Metallo-Polyelectrolytes”. en. In: *J. Am. Chem. Soc.* 142.2 (Jan. 2020), pp. 1083–1089. ISSN: 0002-7863. DOI: 10.1021/jacs.9b12051.

[442] Sihan Tang et al. “Spontaneous water-on-water spreading of polyelectrolyte membranes inspired by skin formation”. en. In: *Nat. Commun.* 13.1 (June 2022), p. 3227. ISSN: 2041-1723. DOI: 10.1038/s41467-022-30973-6.

[443] Qian Zhu, Christopher W. Barney, and Kendra A. Erk. “Effect of ionic crosslinking on the swelling and mechanical response of model superabsorbent polymer hydrogels for internally cured concrete”. In: *Mater. Struct.* 48.7 (July 2015), pp. 2261–2276. ISSN: 1871-6873. DOI: 10.1617/s11527-014-0308-5.

[444] Eesha Khare, Niels Holten-Andersen, and Markus J. Buehler. “Transition-metal coordinate bonds for bioinspired macromolecules with tunable mechanical properties”. en. In: *Nat. Rev. Mater.* 6.5 (May 2021), pp. 421–436. ISSN: 2058-8437. DOI: 10.1038/s41578-020-00270-z.

[445] Jeri’Ann Hiller, Jonas D. Mendelsohn, and Michael F. Rubner. “Reversibly erasable nanoporous anti-reflection coatings from polyelectrolyte multilayers”. en. In: *Nat. Mater.* 1.1 (Sept. 2002), pp. 59–63. ISSN: 1476-4660. DOI: 10.1038/nmat719.

[446] Alan S. Michaels. “POLYELECTROLYTE COMPLEXES”. en. In: *Ind. Eng. Chem.* 57.10 (Oct. 1965), pp. 32–40. ISSN: 0019-7866. DOI: 10.1021/ie50670a007.

[447] Pengfei Zhang and Zhen-Gang Wang. “Interfacial Structure and Tension of Polyelectrolyte Complex Coacervates”. In: *Macromolecules* 54.23 (Dec. 2021), pp. 10994–11007. ISSN: 0024-9297, 1520-5835. DOI: 10.1021/acs.macromol.1c01809.

[448] M. Olvera de la Cruz et al. “Precipitation of highly charged polyelectrolyte solutions in the presence of multivalent salts”. In: *J. Chem. Phys.* 103.13 (Oct. 1995), pp. 5781–5791. ISSN: 0021-9606. DOI: 10.1063/1.470459.

[449] A. V. Ermoshkin and M. Olvera de la Cruz. “Polyelectrolytes in the Presence of Multivalent Ions: Gelation Versus Segregation”. In: *Phys. Rev. Lett.* 90.12 (Mar. 2003), p. 125504. DOI: 10.1103/PhysRevLett.90.125504.

[450] A. V. Ermoshkin and M. Olvera De La Cruz. “Gelation in strongly charged polyelectrolytes”. In: *J. Polym. Sci., Part B: Polym. Phys.* 42.5 (2004), pp. 766–776. ISSN: 1099-0488. DOI: 10.1002/polb.10752.

[451] Santiago E. Herrera et al. “Polyelectrolyte-multivalent molecule complexes: physicochemical properties and applications”. In: *Soft Matter* 19.11 (2023), pp. 2013–2041. DOI: 10.1039/D2SM01507B.

[452] C. Hofzumahaus, P. Hebbeker, and S. Schneider. “Monte Carlo simulations of weak polyelectrolyte microgels: pH-dependence of conformation and ionization”. In: *Soft Matter* 14.20 (2018), pp. 4087–4100. DOI: 10.1039/C7SM02528A.

[453] Sriteja Mantha et al. “Adsorption isotherm and mechanism of Ca2+ binding to polyelectrolyte”. In: *In preparation* (2023).

[454] Lisa M. Hall et al. “Ionic Aggregate Structure in Ionomer Melts: Effect of Molecular Architecture on Aggregates and the Ionomer Peak”. In: *J. Am. Chem. Soc.* 134.1 (Jan. 2012), pp. 574–587. ISSN: 0002-7863, 1520-5126. DOI: 10.1021/ja209142b.

[455] Alexandros Chremos and Jack F. Douglas. “Influence of higher valent ions on flexible polyelectrolyte stiffness and counter-ion distribution”. In: *J. Chem. Phys.* 144.16 (Apr. 2016), p. 164904. ISSN: 0021-9606, 1089-7690. DOI: 10.1063/1.4947221.

[456] Janani Sampath and Lisa M. Hall. “Impact of ionic aggregate structure on ionomer mechanical properties from coarse-grained molecular dynamics simulations”. In: *J. Chem. Phys.* 147.13 (Oct. 2017), p. 134901. ISSN: 0021-9606, 1089-7690. DOI: 10.1063/1.4985904.

[457] Martin Blaško, Lukáš F. Pašteka, and Miroslav Urban. “DFT Functionals for Modeling of Polyethylene Chains Cross-Linked by Metal Atoms. DLPNO–CCSD(T) Benchmark Calculations”. In: *J. Phys. Chem. A* 125.34 (Sept. 2021), pp. 7382–7395. ISSN: 1089-5639. DOI: 10.1021/acs.jpca.1c04793.

[458] Axel D. Becke. “A new mixing of Hartree–Fock and local density-functional theories”. In: *J. Chem. Phys.* 98.2 (Jan. 1993), pp. 1372–1377. ISSN: 0021-9606. DOI: 10.1063/1.464304.

[459] Stefan Grimme et al. “A consistent and accurate ab initio parametrization of density functional dispersion correction (DFT-D) for the 94 elements H-Pu”. In: *J. Chem. Phys.* 132.15 (Apr. 2010), p. 154104. ISSN: 00219606. DOI: 10.1063/1.3382344.

[460] Florian Weigend and Reinhart Ahlrichs. “Balanced basis sets of split valence, triple zeta valence and quadruple zeta valence quality for H to Rn: Design and assessment of accuracy”. In: *Phys. Chem. Chem. Phys.* 7.18 (Aug. 2005), pp. 3297–3305. ISSN: 1463-9084. DOI: 10.1039/B508541A.

[461] Florian Weigend. “Accurate Coulomb-fitting basis sets for H to Rn”. In: *Phys. Chem. Chem. Phys.* 8.9 (Feb. 2006), pp. 1057–1065. ISSN: 1463-9084. DOI: 10.1039/B515623H.

[462] Benedetta Mennucci and Jacopo Tomasi. “Continuum solvation models: A new approach to the problem of solute’s charge distribution and cavity boundaries”. In: *J. Chem. Phys.* 106.12 (Mar. 1997), pp. 5151–5158. ISSN: 0021-9606. DOI: 10.1063/1.473558.

[463] Jeng-Da Chai and Martin Head-Gordon. “Systematic optimization of long-range corrected hybrid density functionals”. In: *J. Chem. Phys.* 128.8 (Feb. 2008), p. 084106. ISSN: 0021-9606. DOI: 10.1063/1.2834918.

[464] Stefan Grimme, Stephan Ehrlich, and Lars Goerigk. “Effect of the damping function in dispersion corrected density functional theory”. In: *J. Comput. Chem.* 32.7 (2011), pp. 1456–1465. ISSN: 1096-987X. DOI: 10.1002/jcc.21759.

[465] Walter H. Stockmayer. “Theory of Molecular Size Distribution and Gel Formation in Branched Polymers II. General Cross Linking”. In: *J. Chem. Phys.* 12.4 (Apr. 1944), pp. 125–131. ISSN: 0021-9606, 1089-7690. DOI: 10.1063/1.1723922.

[466] Scott P. O. Danielsen, Sergey Panyukov, and Michael Rubinstein. “Ion Pairing and the Structure of Gel Coacervates”. In: *Macromolecules* 53.21 (Oct. 2020), pp. 9420–9442. ISSN: 0024-9297. DOI: 10.1021/acs.macromol.0c01360.

[467] Scott P. O. Danielsen, Alexander N. Semenov, and Michael Rubinstein. “Phase Separation and Gelation in Solutions and Blends of Heteroassociative Polymers”. In: *Macromolecules* 56.14 (July 2023), pp. 5661–5677. ISSN: 0024-9297. DOI: 10.1021/acs.macromol.3c00854.

[468] Christopher Balzer, Puck Springintveld, and Glenn H. Fredrickson. “Phase Behavior of Reversibly Bonding Polymer Blends”. In: *Macromolecules* 58.13 (July 2025), pp. 6743–6752. ISSN: 0024-9297. DOI: 10.1021/acs.macromol.5c01173.

[469] Xinxiang Chen et al. “Dilute but Dense – Reversible Crosslinking Enables Water-Rich (Bio)polymer Condensates”. en. In: *Adv. Sci.* 13.20 (2026), e19636. ISSN: 2198-3844. DOI: 10.1002/advs.202519636.

[470] Xinxiang Chen, Lennart Hebestreit, and Friederike Schmid. *From real polymers to random graphs: percolation thresholds in associative polymer solutions*. arXiv:2607.25534 [cond-mat.soft]. July 2026. DOI: 10.48550/arXiv.2607.25534.

[471] Xinxiang Chen et al. “Sol–Gel Transition in Heteroassociative RNA-Protein Solutions: A Quantitative Comparison of Coarse-Grained Simulations and the Semenov–Rubinstein Theory”. In: *Macromolecules* 58.6 (Mar. 2025), pp. 3331–3342. ISSN: 0024-9297. DOI: 10.1021/acs.macromol.4c03065.

[472] W.G. Chapman et al. “SAFT: Equation-of-state solution model for associating fluids”. In: *Fluid Phase Equilib.* 52 (Dec. 1989), pp. 31–38. ISSN: 03783812. DOI: 10.1016/0378-3812(89)80308-5.

[473] Norman F. Carnahan and Kenneth E. Starling. “Equation of State for Nonattracting Rigid Spheres”. In: *J. Chem. Phys.* 51.2 (Sept. 2003), pp. 635–636. ISSN: 0021-9606. DOI: 10.1063/1.1672048.

[474] Bjørn Maribo-Mogensen, Georgios M. Kontogeorgis, and Kaj Thomsen. “Modeling of Dielectric Properties of Complex Fluids with an Equation of State”. In: *J. Phys. Chem. B* 117.12 (Mar. 2013), pp. 3389–3397. ISSN: 1520-6106, 1520-5207. DOI: 10.1021/jp310572q.

[475] Michael Rubinstein and Alexander N. Semenov. “Thermoreversible Gelation in Solutions of Associating Polymers. 2. Linear Dynamics”. In: *Macromolecules* 31.4 (Feb. 1998), pp. 1386–1397. ISSN: 0024-9297, 1520-5835. DOI: 10.1021/ma970617+.

[476] Lauren J. Abbott and John W. Lawson. "Effects of Side Chain Length on Ionic Aggregation and Dynamics in Polymer Single-Ion Conductors". In: *Macromolecules* 52.19 (Oct. 2019), pp. 7456–7467. ISSN: 0024-9297, 1520-5835. DOI: 10.1021/acs.macromol.9b00415.

[477] Alec Glisman et al. "Ca2+ mediated association between like charged polyelectrolytes". In: *In preparation* (2023).

[478] Wendy D. Cornell et al. "A Second Generation Force Field for the Simulation of Proteins, Nucleic Acids, and Organic Molecules". In: *J. Am. Chem. Soc.* 117.19 (May 1995), pp. 5179–5197. ISSN: 0002-7863. DOI: 10.1021/ja00124a002.

[479] Pengfei Li and Kenneth M. Merz. "Taking into Account the Ion-Induced Dipole Interaction in the Nonbonded Model of Ions". In: *J. Chem. Theory Comput.* 10.1 (Jan. 2014), pp. 289–297. ISSN: 1549-9618, 1549-9626. DOI: 10.1021/ct400751u.

[480] Brian K. Radak et al. "Constant-pH Molecular Dynamics Simulations for Large Biomolecular Systems". In: *J. Chem. Theory Comput.* 13.12 (Dec. 2017), pp. 5933–5944. ISSN: 1549-9618. DOI: 10.1021/acs.jctc.7b00875.

[481] Pavel Buslaev et al. "Best Practices in Constant pH MD Simulations: Accuracy and Sampling". In: *J. Chem. Theory Comput.* 18.10 (Oct. 2022), pp. 6134–6147. ISSN: 1549-9618. DOI: 10.1021/acs.jctc.2c00517.

[482] Bingrui Li et al. "Intrinsically Self-Healing Polymers: From Mechanistic Insight to Current Challenges". In: *Chem. Rev.* 123.2 (Jan. 2023), pp. 701–735. ISSN: 0009-2665. DOI: 10.1021/acs.chemrev.2c00575.

CONCLUDING REMARKS

Throughout this thesis, we have examined a broad range of thermodynamic and dynamic phenomena arising from electrostatic interactions in macromolecular and charge-containing systems. A recurring conclusion is that electrostatics cannot generally be incorporated as a simple pairwise correction to an otherwise neutral reference system. Owing to their long-ranged and collective nature, electrostatic interactions couple molecular conformation, ionic organization, solvent response, chemical equilibrium, and macroscopic material properties across multiple length and time scales. Nevertheless, by isolating these couplings in progressively more complex systems, we have developed simplified theoretical descriptions and transferable physical intuition for understanding their consequences.

The first part of this thesis established how electrostatic correlations reshape the equilibrium phase behavior of charge-containing materials. These effects were shown to depend not only on the magnitude of the charge, but also on molecular size, solvent polarization, charge sequence, and polymer topology. The second part extended this perspective to dynamic properties, demonstrating that conductivity, molecular transport, and mechanical response cannot generally be inferred from static measures such as ion-pair populations, equilibrium charge states, or crosslink densities alone. Instead, these properties emerge from collective motion, association and exchange kinetics, and competition among multiple relaxation pathways. Taken together, the results provide complementary thermodynamic and dynamic views of charged materials: one describing the states they may occupy, and the other describing how they move, respond, and relax within those states.

As is often the case, however, resolving one set of questions exposes several others. The findings of this thesis therefore suggest a number of natural directions for future work, particularly concerning explicit solvent effects, interfacial electrostatics, charge regulation, chemical specificity, and molecular design.

A particularly important insight from Chapter 2 is that the solvent cannot always be reduced to a passive dielectric background. The collective polarization of dipolar solvent molecules, especially when coupled to mobile ions and charged macromolecules, can qualitatively alter both the magnitude and temperature dependence of electrostatic interactions. The implications of this result extend well beyond the homogeneous bulk systems considered in that chapter. In particular, many con-

clusions drawn from implicit-solvent models of polyelectrolytes, electrolytes, and biomolecular condensates should be reconsidered when strong dielectric inhomogeneity or preferential solvent organization is expected.

One immediate extension would be to examine the interface between a coacervate and its surrounding supernatant. The two phases may differ substantially in polymer concentration, salt content, solvent density, and dielectric response. Their interface must therefore accommodate simultaneous gradients in composition, polarization, electrostatic potential, and molecular organization. Explicit-solvent molecular simulations could, in principle, resolve these profiles directly, but the computational cost of equilibrating large, slowly fluctuating interfaces would be considerable. A more tractable route would be to extend the explicit-solvent liquid-state theory developed in Chapter 2 to inhomogeneous systems, analogous to existing classical density-functional treatments of implicit-solvent electrolytes[483].

Such a theory could predict the spatial variation of the solvent density, polarization, dielectric response, ionic composition, and polyelectrolyte organization across the interface. It would also clarify whether the local dielectric constant varies smoothly between the bulk phases or exhibits nonmonotonic behavior caused by interfacial alignment and preferential partitioning. These quantities may be particularly important for understanding electrostatic potentials generated at biomolecular-condensate interfaces. Such potentials have been proposed as a means of concentrating reactants, orienting charged species, or modifying local reaction barriers[260], an effect that parallels the strong interfacial electric fields reported at aqueous microdroplet interfaces and their debated role in driving interfacial reaction chemistry[484, 485]. A molecularly resolved description of dielectric and compositional gradients would therefore provide a firmer basis for evaluating the potential catalytic functions of condensate interfaces.

Related questions arise at solid–liquid and membrane–liquid interfaces. Many conventional treatments assume a constant dielectric permittivity up to the charged surface, even though molecular packing, solvent orientation, and local ion concentration may differ strongly from their bulk values. Resolving the spatial decay of dielectric response away from an interface could improve our understanding of electric-double-layer structure, capacitive energy storage, interfacial ion association, and the formation or dissolution of salt aggregates. It could also clarify when continuum electrostatic boundary conditions remain valid and when molecular polarization must be treated explicitly.

Mixed solvents represent another natural, but substantially more challenging, extension. Differences in solvent polarity, molecular size, hydrogen-bonding character, and ion affinity can generate strong preferential solvation. In some mixtures, the addition of salt alone can induce or suppress liquid–liquid phase separation through a combination of dielectric contrast, ion partitioning, and changes in solvent chemical potentials. When combined with the nontrivial temperature and concentration dependence of the dielectric response identified in Chapter 2, these effects may produce phase behavior that cannot be captured by assigning a single composition-dependent dielectric constant to the mixture. An explicit treatment of each solvent species would make it possible to disentangle dielectric effects from preferential solvation and other chemically specific interactions.

Further complexity may arise from the internal charge distribution of the solvent molecules themselves. Our work on shifted-dipole Stockmayer fluids[10, 11] demonstrated that displacing a molecular dipole from the center of a particle introduces substantial changes in local structure, dielectric response, and phase behavior, even when the total dipole moment is held fixed. This additional molecular parameter is likely to influence the interfacial and mixed-solvent phenomena described above. At the same time, adding molecular asymmetry greatly enlarges the parameter space and may obscure the general physical principles sought through coarse-grained modeling. Future work should therefore adopt a targeted approach, introducing off-center dipoles only when they represent a specific molecular feature or address a clearly defined physical question.

A second major direction concerns charge regulation. Chapter 6 demonstrated that reversible changes in the charge state of a polymer network can alter ion transport in ways that cannot be reproduced by a fixed-charge description. Protonation, electrostatic binding, ion partitioning, and molecular diffusion are strongly coupled, and the resulting transport behavior reflects competition among these processes. Many questions remain regarding how these mechanisms operate in other responsive charged materials.

Chapter 7, for example, treated the charge state of the metallo-polyelectrolyte hydrogel using a fixed-charge approximation. A natural extension would be to repeat this analysis while explicitly accounting for charge regulation. Changes in protonation could alter the number of available metal-binding sites, the strength of local electrostatic attraction, the spatial distribution of crosslinks, and the exchange kinetics of metal ions. Conversely, metal coordination may shift the acid–base equilibrium

of nearby functional groups. The mechanical response would then arise from feedback among protonation, ion binding, network structure, and dynamic crosslink exchange.

The insights developed in Chapter 6 provide a useful strategy for addressing this complexity. Rather than attempting to interpret the full response through a single effective parameter, the competing mechanisms could be isolated through carefully chosen reference systems: fixed-charge networks, nonbinding counterions, permanently bound crosslinks, and independently varied protonation and metal concentrations. This decomposition would help determine which effects arise from equilibrium charge regulation, which arise from changes in network structure, and which depend on the kinetics of binding and unbinding. Such a study could yield design principles for pH-responsive hydrogels, selective ion-transport membranes, adaptive adhesives, and dynamically reconfigurable networks.

Combining explicit solvent polarization with charge regulation presents an even more fundamental challenge. Most theories of charge regulation treat the solvent as a homogeneous dielectric medium, allowing protonation equilibria to be coupled to a mean electrostatic potential without explicitly resolving the molecular response of the solvent. The results of Chapter 2, however, suggest that this approximation may fail in phase-separated systems, concentrated polymer networks, and interfacial environments. A change in protonation alters the local electric field and ionic composition, which modifies solvent polarization and the local dielectric response. That dielectric response then feeds back onto the free energy of ionization. Charge regulation and solvent polarization must therefore be treated as mutually coupled degrees of freedom rather than as independent corrections.

This coupling becomes particularly subtle in mixed-solvent environments. Even the operational definitions of pH and pK_a require care because proton activities, standard states, solvation free energies, and reference electrode responses depend on solvent composition. Preferential solvation may cause the microscopic environment of an ionizable group to differ substantially from the bulk solvent composition, especially within polymer-rich phases or near interfaces. A rigorous theoretical or simulation framework would therefore need to connect local proton solvation and chemical equilibrium to macroscopically measurable activities. Developing such a framework would provide a much-needed foundation for understanding charge regulation in solvent mixtures relevant to separations, catalysis, electrochemistry, and biomolecular formulations.

The results of this thesis and the extensions described above are intentionally formulated at a coarse-grained level. This reduction is a strength because it exposes general mechanisms that would be difficult to distinguish in a fully chemically detailed model. At the same time, many contemporary applications require quantitative predictions for specific molecules, solvents, ions, and polymer chemistries. Bridging the gap between transferable physical theory and chemical specificity is therefore one of the most important challenges for future work.

Chapter 1 demonstrated that the simplified theoretical frameworks developed here can be extended to represent chemically specific species. In practice, however, parameterizing these models solely through regression to experimental data is often difficult. Relevant measurements may be sparse, internally inconsistent, or confined to narrow ranges of temperature and composition. The challenge is especially severe for multicomponent charged systems, where the number of possible interactions grows rapidly and individual parameters may be poorly identifiable from bulk measurements alone.

Several complementary approaches could alleviate these limitations. Group-contribution methods can transfer parameters among chemically related molecules and reduce the amount of data required for each new species[486]. *Ab initio* quantum-chemical calculations can provide independent estimates of association energies, charge distributions, molecular volumes, polarizabilities, and solvation free energies. Data-driven approaches, including machine learning, can then be used to identify relationships between molecular structure and coarse-grained model parameters[487]. The most promising strategy is unlikely to be purely empirical. Rather, quantum chemistry, group-contribution models, and machine learning should be embedded within thermodynamic and transport theories that retain the essential constraints and collective physics of charged macromolecular systems.

Such physics-informed models would offer several advantages over direct prediction of macroscopic properties from molecular structure. They could enforce electroneutrality, thermodynamic consistency, correct limiting behavior, and known relationships between equilibrium and transport coefficients. They could also separate uncertainty arising from molecular parameters from uncertainty associated with the theoretical approximation itself. Most importantly, they would preserve interpretability, allowing a predicted change in phase behavior, conductivity, or mechanical response to be traced back to a molecular interaction or structural feature.

The resulting framework could ultimately be coupled to computer-aided molecular

and materials design. Potential applications include the design of battery electrolytes with balanced conductivity and stability[488], lipid-nanoparticle formulations for nucleic-acid delivery[489], selective membranes[440] and responsive hydrogels, and macromolecules that self-assemble into prescribed structures. Extending molecular-design methods to macromolecules will require confronting a much larger and more structured design space than is encountered for small molecules. In addition to chemical composition, the available variables include molecular weight, charge density, monomer sequence, branching, topology, crosslink density, and spatial patterning of functional groups. These variables are combinatorial, but they are not arbitrary: the physical principles developed in this thesis can be used to identify reduced descriptors and constrain the search to regions most likely to produce the desired behavior.

The broader opportunity is therefore not simply to construct increasingly detailed models, but to combine levels of description in a purposeful manner. Coarse-grained theory can identify the dominant physical mechanisms and relevant dimensionless variables; molecular simulation can test approximations and resolve correlations inaccessible to analytical theory; quantum chemistry can supply chemically specific microscopic information; and data-driven methods can interpolate efficiently across large chemical and architectural spaces. Together, these tools could provide predictive models that remain both chemically useful and physically interpretable.

The central lesson of this thesis is the importance of the long-range, many-body nature of electrostatic interactions on macromolecular systems. Its consequences depend on how charges are distributed, connected, solvated, regulated, and allowed to move. Electrostatic interactions couple these features over scales ranging from local molecular association to collective phase separation and network relaxation. By isolating these couplings, the work presented here has developed a set of principles for navigating both the thermodynamic landscape and the dynamic pathways of charge-containing macromolecular systems. Future progress will depend on extending these principles to interfaces, mixed solvents, adaptive charge states, and chemically specific materials while preserving the rigorous treatment of collective electrostatics on which they are founded.

References

[10] Samuel Varner et al. “Stockmayer fluid with a shifted dipole. II. Interfacial behavior”. en. In: *J. Chem. Phys.* 164.18 (May 2026). ISSN: 0021-9606. DOI: 10.1063/5.0331066.

[11] Pierre J. Walker et al. “Stockmayer fluid with a shifted dipole. I. Bulk behavior”. In: *J. Chem. Phys.* 164.18 (May 2026), p. 184512. ISSN: 0021-9606. DOI: 10.1063/5.0331053.

[260] Salman F. Banani et al. “Biomolecular condensates: organizers of cellular biochemistry”. en. In: *Nat. Rev. Mol. Cell Biol.* 18.5 (May 2017), pp. 285–298. ISSN: 1471-0080. DOI: 10.1038/nrm.2017.7.

[440] Elif Nur Durmaz et al. “Polyelectrolytes as Building Blocks for Next-Generation Membranes with Advanced Functionalities”. In: *ACS Appl. Polym. Mater.* 3.9 (Aug. 2021), pp. 4347–4374. ISSN: 2637-6105. DOI: 10.1021/acsapm.1c00654.

[483] Jian Jiang, Valeriy V. Ginzburg, and Zhen-Gang Wang. “Density functional theory for charged fluids”. en. In: *Soft Matter* 14.28 (July 2018), pp. 5878–5887. ISSN: 1744-6848. DOI: 10.1039/C8SM00595H.

[484] Hanqing Xiong et al. “Strong Electric Field Observed at the Interface of Aqueous Microdroplets”. In: *J. Phys. Chem. Lett.* 11.17 (Sept. 2020), pp. 7423–7428. DOI: 10.1021/acs.jpclett.0c02061.

[485] Hongxia Hao, Itai Leven, and Teresa Head-Gordon. “Can electric fields drive chemistry for an aqueous microdroplet?” In: *Nat. Commun.* 13.1 (Jan. 2022), p. 280. ISSN: 2041-1723. DOI: 10.1038/s41467-021-27941-x.

[486] Vasileios Papaioannou et al. “Group contribution methodology based on the statistical associating fluid theory for heteronuclear molecules formed from Mie segments”. In: *J. Chem. Phys.* 140.5 (2014), p. 054107. ISSN: 00219606. DOI: 10.1063/1.4851455.

[487] David Rosenberger. “Machine learning of consistent thermodynamic models using automatic differentiation”. In: *Phys. Rev. E* 105.4 (2022). DOI: 10.1103/PhysRevE.105.045301.

[488] Venkat Ganesan, Zidan Zhang, and Nico Marioni. “Dynamical Ion Correlations in Polymer and Membrane Electrolytes: Recent Advances and Open Questions”. In: *J. Phys. Chem. Lett.* 16.32 (Aug. 2025), pp. 8114–8124. DOI: 10.1021/acs.jpclett.5c02006.

[489] Yulia Eygeris et al. “Chemistry of lipid nanoparticles for RNA delivery”. In: *Acc. Chem. Res.* 55.1 (Jan. 2022), pp. 2–12. ISSN: 0001-4842. DOI: 10.1021/acs.accounts.1c00544.